Reconstruction Enhancements with Optical Scanning Holography

Kelly Katherine Dobson

Dissertation submitted to the faculty of the Virginia Polytechnic Institute and State University in partial fulfillment of the requirements for the degree of

Doctor of Philosophy
In
Electrical Engineering

Ting-Chung Poon, Chair
A. Lynn Abbott
William A. Davis
James R. Heflin
Ahmad Safaai-Jazi

April 21, 2016
Blacksburg, Virginia

Keywords: Optical scanning holography, spiral phase plate, optical sectioning

Reconstruction Enhancements with Optical Scanning Holography

Kelly Katherine Dobson

ABSTRACT

Optical scanning holography (OSH) [1] has the benefit of recording the entire three-dimensional (3-D) volume of a specimen in the form of a two-dimensional (2-D) hologram. Reconstruction of the original volume can be accomplished by applying digital reconstruction or decoding techniques to the recorded hologram. Accurate reconstruction of the 3-D volume and more specifically, the individual 2-D optical sections without artifacts such as out-of-focus haze from adjacent sections has been the focus of much work including algorithms, optical techniques, and combinations of the two. This dissertation presents several different techniques for enhancing the reconstruction of a recorded specimen and its optical sections including the use of optical coding and phase filtering techniques in the traditional OSH optical system.

ACKNOWLEDGEMENTS

This dissertation results from a lifetime of encouragement and support.

I would like to express my thanks to my advisor, Dr. Ting-Chung Poon, for his guidance, support and encouragement throughout this process. I am also very appreciative of Dr. A. Lynn Abbott, Dr. William Davis, Dr. Randy Heflin, and Dr. Ahmad Safaai-Jazi at Virginia Tech for their assistance throughout my degree program and for graciously serving on my advisory committee.

I have been fortunate to have the opportunity to work with many exceptional researchers at the Virginia Tech Optical Image Processing Laboratory and wish to thank them for their insightful comments and discussions. I would also like to recognize those individuals responsible for providing the equipment and laboratory space for the computer simulations and optical experiments.

Finally, my deepest appreciation is reserved for my family who provided me endless support and encouragement while on the journey to realizing my dreams.

TABLE OF CONTENTS

LIST OF FIGURES

LIST OF ABBREVIATIONS

2-D	Two-dimensional
3-D	Three-dimensional
4-f	Four-focal length
AOM	Acousto-optic Modulator
BE	Beam Expander
BPF	Band-pass filter
BS	Beam Splitter
CCD	Charge-coupled device
CDG	Circular Dammann Grating
CFZP	Cosine-Fresnel zone plate
CGH	Computer Generated Hologram
DC	Direct Current
DOE	Diffractive Optical Element
FINCH	Fresnel Incoherent Correlation Holography
FZP	Fresnel zone plate
L	Lens
LPF	Low-pass filter
M	Mirror, Mask
NA	Numerical Aperture
OSH	Optical Scanning Holography
OTF	Optical Transfer Function
PD	Photodetector
PSF	Point Spread Function
RPP	Random-Phase Pupil
SFZP	Sine-Fresnel zone plate
SLM	Spatial Light Modulator
SPP	Spiral Phase Plate
TDFZP	Time-dependent Fresnel Zone Plate
USAF	United States Air Force

1 INTRODUCTION

The main objective of this research is to investigate enhancements to the reconstruction of a specimen captured via holography, accomplished either by the addition of optical elements to change the optical recording of the specimen or in the digital processing of reconstruction techniques. In particular, the specific form of holographic recording presented in this dissertation is optical scanning holography (OSH) [1-4]. OSH which is based on optical-heterodyne image processing captures holographic information of a specimen with a single, two-dimensional (2-D) scan while preserving phase information [1].

The progression of this dissertation begins with a presentation on the basics of heterodyne image processing in Chapter 2. In Chapter 3, these processing techniques are then applied to a two-pupil optical system to capture the complex holographic information of a three-dimensional (3-D) specimen with a 2-D scan. A review and discussion of several applications using OSH are detailed in Chapter 4 including holographic-section reconstruction with random- phase pupil (RPP) and circular dammann grating (CDG). The fundamentals of optical vortices including several approaches to realize this phenomenon as well as results for using the component in a simulated optical system are presented in Chapter 5. The culmination of the dissertation is Chapter 6 where optical scanning holography is combined with a spiral phase plate (SPP) to illustrate edge enhancement of holographically reconstructed images in simulation and optical experiments. A preliminary extension of OSH with SPP for digital modulation of previously recorded holograms is presented with other future work in Chapter 7. A summary of the research and concluding remarks are found in Chapter 8.

The addition of circular dammann gratings, random-phase pupils, and spiral phase plates to the traditional OSH system is realized for the first time in computer simulation and optical experimentation in this research. The analysis and results presented throughout this dissertation include computer simulations conducted in MATLAB as well as experimental methods with optical systems for which the recorded data is extracted and digitally reconstructed in MATLAB.

The first investigation examines the ability to code and decode an object using a circular dammann grating. The author of this dissertation developed the numerical routines to simulate image coding using a traditional optical system, a planar object, and a CDG as the coding function.

Results demonstrating image coding and decoding in simulation and optical experiments were presented by Doh, Dobson, Poon, and Chung (2009) [5] and are summarized in Section 4.1.1. The resulting intensity-based optical coding system marked the first application of a CDG as a coding and decoding function in a traditional OSH system.

The familiarity gained from the previous demonstration contributed to the author's ability to aid in the formulation of an approach for inserting a CDG into an OSH system. While the optical experiment was being assembled, the author adapted code to produce simulated results for comparison to those from the optical experiment. The author took part in the campaign of observations and processed the data with the adapted code to produce results comparable to those by Shinoda, Liu, Chung, Dobson, Zhou, and Poon (2011) [6]. A summary of the simulated experiment via numerical routines and the optical experiment is presented in Section 4.1.2. These demonstrations are the first realization of 3-D complex coding and decoding with a CDG as the coding pupil in a traditional OSH system.

Further investigation into the effects of optical element choice on holographic reconstruction includes the addition of a random-phase pupil to the OSH system. This work leveraged prior experience in coding and decoding as the author verified the simulation results presented by Xin, Dobson, Shinoda, and Poon (2010) [7]. The results from the numerical routines for hologram, optical-section reconstruction are reviewed in Section 4.2.1. An extension of the random-phase pupil work by Wu, Zhou, Wang, Poon, Jiang, Xiao, and Dobson (2013) [8] included numerical routines to investigate the effects of lateral-deviation and pixel-error values on the holographic reconstruction quality. The reconstruction results from computer simulations for deviation and pixel errors can be found in Section 4.2.2.

The next chapter discusses the use of spiral phase plate as a filter in a standard, four-focal length (4-f) coherent imaging system for edge enhancement. The author developed numerical routines to simulate the introduction of a spiral phase plate (SPP) in a traditional imaging system. These simulation routines demonstrated isotropic and anisotropic edge enhancement by digital, spiral-phase modulation during processing as presented in Section 5.2.1 and 5.2.2, respectively. The ability to generate optical vortices with diffractive optics and spiral-phase kernel analysis for plane waves are discussed in Section 5.3 and 5.4, respectively. The chapter concludes in Section 5.5 and 5.6 with the generation of optical vortices with lenses and single or composite vortex illumination by Gaussian beam.

The culmination of the dissertation and final investigation adds a spiral phase plate to the OSH system to realize filtering techniques for edge enhancement. The author extended knowledge from OSH and SPP in a traditional imaging system to simulate changes in the optical recording of an OSH system. The optical system is changed by replacing one of the pupils with a spiral phase plate, thus inducing a helical reference wave as summarized in Section 6.1 for isotropic and Section 6.2 for anisotropic edge enhancement. The author leveraged this experience as the basis for the scheme to realize the optical system presented in Section 6.1.2. In Pan, Jia, Yu, Dobson, Zhou, Wang, and Poon (2014) [9], the author processed collected data from this optical experiment and demonstrated isotropic edge enhancement using previously developed numerical routines as discussed in Section 6.1.1. These simulated and experimental results are the first time that OSH has been used to record symmetric, edge-only information of a specimen holographically. The edge enhancement techniques were then extended by the author to simulate anisotropic filtering with OSH by digital reconstruction as discussed in Section 6.2.1-6.2.5 and summarized by Dobson, Jia, and Poon (2016) [10]. These simulated results mark the first applications of SPPs in OSH to control the degree and orientation of edge enhancement and thus record selective, edge-only information of a specimen holographically. The author makes some recommendations for future work and extensions of the research in Chapter 7 before providing final thoughts in Chapter 8.

2 OPTICAL-HETERODYNE IMAGE PROCESSING BACKGROUND AND MATHEMATICS

This chapter introduces Optical Scanning Holography (OSH) by covering the basics of optical-heterodyne scanning and the two-pupil optical system. A depiction of the two-pupil optical-heterodyne scanning system as well as the symbols, notations, and mathematical definitions used in subsequent sections is presented in Section 2.1. Sections 2.2 and 2.3 mathematically detail how pupil choice in the two-pupil system allows one to realize different coherency of the processor. Mathematical examples illustrating the ability to process an object in amplitude or intensity are presented in Sections 2.2.1 and 2.3.1, respectively. Section 2.4 concludes the chapter with the definition of the optical transfer function for the two-pupil optical heterodyne scanning system.

2.1 Two-pupil optical-heterodyne scanning: Introduction and Background

The two-pupil optical-heterodyne scanning system is an incoherent image processor or one that processes the intensity of the image in such a way that the point spread function (PSF) of the system is complex in general. Complex PSFs are obtained using the interferometric interaction of two-pupils with shifted temporal frequency [11-17]. It is this interaction which makes it possible to extract and process the holographic information of specimens using two-pupil optical heterodyne scanning as illustrated in Figure 1.

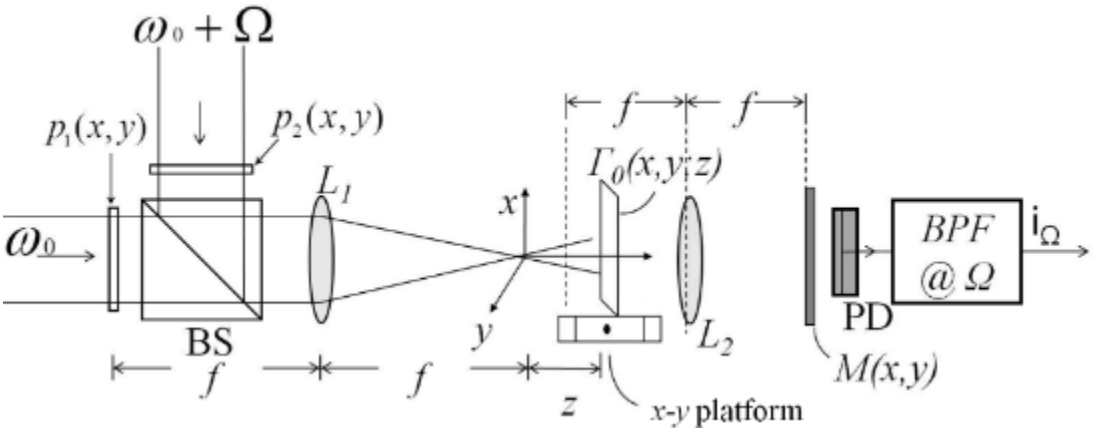

Figure 1 Two-pupil heterodyne scanning processor system. [Used with permission]

The pupil function $p_1(x,y)$ is located at the front focal plane of lens L_1 with focal length f and is illuminated by a collimated laser of temporal frequency ω_0. The other pupil, $p_2(x,y)$, is

located the same distance away from lens L_1 and is illuminated by a laser of temporal frequency $\omega_0 + \Omega$ where $\omega_0 \gg \Omega$ and the offset Ω results from an acousto-optic modulator (AOM). The laser beams are then combined by a beam splitter BS which projects the light onto a specimen with transparent function Γ_0. The specimen is placed on a two-dimensional $x - y$ scanning platform located at a distance z away from the back focal plane of L_1. The optical scanning field a distance z away from the focal plane of the lens is given by

$$\Psi_s(x, y; z) = P_1(x, y; z) \exp(j\omega_0 t) + P_2(x, y; z) \exp(j(\omega_0 + \Omega)t), \quad (1)$$

where $P_i(x, y; z)$ is the field distribution a distance z away from the focal plane of L_1 and through Fresnel diffraction [18-20] is given by

$$P_i(x, y; z) = P_i\left(\frac{k_0 x}{f}, \frac{k_0 y}{f}\right) \otimes h(x, y; z), i = 1, 2, \quad (2)$$

where the symbol $\otimes$ denotes the 2-D convolution operation defined as

$$g_1(x, y) \otimes g_2(x, y) = \int\int g_1\left(x', y'\right) g_2\left(x - x', y - y'\right) dx' dy'. \quad (3)$$

In Eq. (2) $P_i\left(\frac{k_0 x}{f}, \frac{k_0 y}{f}\right)$ is the field distribution at the back focal plane of L_1 and is given by

$$\begin{aligned} P_i\left(\frac{k_0 x}{f}, \frac{k_o y}{f}\right) &= \int\int p_i\left(x', y'\right) \exp\left[j\frac{k_0}{f}\left(xx' + yy'\right)\right] dx' dy' \\ &= \mathcal{F}\{p_i(x, y; z)\}_{k_x = \frac{k_0 x}{f}, k_y = \frac{k_0 y}{f}}, \end{aligned} \quad (4)$$

where $\mathcal{F}$ denotes the Fourier-transform operation defined as

$\mathcal{F}\{u(x, y)\}_{k_x, k_y} = \int\int u(x, y) \exp(jk_x x + jk_y y) dxdy$ with k_x and k_y denoting spatial frequencies associated with the variables x and y, and U denotes the transform of u. The 2-D free-space spatial impulse response in Fourier optics [20], $h(x, y; z)$, is given by

$$h(x, y; z) = \exp(-jk_0 z) \frac{jk_0}{2\pi z} \exp\left(\frac{-jk_0}{2z}\left(x^2 + y^2\right)\right) = h_e(x, y; z) \exp(-jk_0 z), \quad (5)$$

where $k_0 = 2\pi / \lambda$ is the wave number of the laser light.

The combined optical field or scanning pattern in Eq. (1) is used to 2-D scan a specimen $\Gamma_0(x, y; z)$, located a distance z away from the focal plane of L_1 resulting in [20]

$$\left\{P_1\left(x^{'},y^{'};z\right)\exp\left(j\omega_0 t\right)+P_2\left(x^{'},y^{'};z\right)\exp\left(j\left(\omega_0+\Omega\right)t\right)\right\}\Gamma_0\left(x+x^{'},y+y^{'};z\right), \quad (6)$$

where $x=x(t)$ and $y=y(t)$ represent the instantaneous 2-D position of the specimen with respect to the complex light amplitude distribution. This field then propagates through a Fourier transforms lens L_2 and reaches the mask $M(x,y)$ located at the back focal plane of L_2. The distribution exiting from the mask is [20]

$$\begin{aligned}\Psi\left(x,y;x_m,y_m\right)\propto\int&\left(P_1\left(x^{'},y^{'};z\right)\exp\left(j\omega_0 t\right)+P_2\left(x^{'},y^{'};z\right)\exp\left(j\left(\omega_0+\Omega\right)t\right)\right)\\&\times\Gamma_0\left(x+x^{'},y+y^{'};z\right)\exp\left[j\frac{k_0}{f}\left(x^{'}x_m+y^{'}y_m\right)\right]dx^{'}dy^{'}\\&\times\exp\left[-j\frac{k_0 z}{2f^2}\left(x_m^2+y_m^2\right)dz M\left(x_m,y_m\right)\right]\end{aligned}, \quad (7)$$

where x_m and y_m are the coordinates in the plane of the mask. The photodetector (PD) spatially integrates the intensity to give the output current $i(t)$ which consists of a baseband current and a heterodyne current at frequency Ω as

$$i(t)\propto\int|\Psi\left(x,y;x_m,y_m\right)|^2\,dx_m dy_m. \quad (8)$$

The heterodyne current $i_\Omega(t)$ at the output of a band-pass filter (BPF) is given by

$$\begin{aligned}i_\Omega(t)\propto\int&P_1\left(x^{'},y^{'};z^{'}\right)P_2^*\left(x^{''},y^{''};z^{''}\right)\exp\left(-j\Omega t\right)+P_2\left(x^{'},y^{'};z^{'}\right)P_1^*\left(x^{''},y^{''};z^{''}\right)\\&\times\exp\left(j\Omega t\right)\exp\left(j\frac{k_0}{f}\left[x_m\left(x^{'}-x^{''}\right)+y_m\left(y^{'}-y^{''}\right)\right]\right)\exp\left(-j\frac{k_0\left(z^{'}-z^{''}\right)}{2f^2}\right)\\&\times\left(x^2+y^2\right)\Gamma_0\left(x^{'}+x,y^{'}+y;z^{'}\right)\Gamma_0^*\left(x^{''}+x,y^{''}+y;z^{''}\right)\left|M\left(x_m,y_m\right)\right|^2\\&\times dx^{'}dx^{''}dy^{'}dy^{''}dz^{'}dz^{''}dx_m dy_m\end{aligned}, \quad (9)$$

where $[\,]^*$ stands for taking the complex conjugate.

Using the convention for phasor Ψ_p as $\Psi_p(x,y;t)=Re\left[\Psi_p(x,y)\exp\left(j\Omega t\right)\right]$ Eq. (9) can be simplified as

$$i_\Omega(t)\propto Re\left[i_{\Omega_p}(x,y)\exp\left(j\Omega t\right)\right], \quad (10)$$

where $Re[\cdot]$ is the real part of the content inside the brackets.

Sections 2.2 and 2.3 will show how in Eq. (9) the choice of pupils, $p_1(x,y)$ and $p_2(x,y)$, as well as the mask $M(x,y)$ allows different coherency of processing to be realized.

2.2 Coherent Processing

A special case of Eq. (9) arises when the mask is a pinhole centered on the axis, i.e. $M(x,y)=\delta(x,y)$. After integrating over the mask's coordinates Eq. (9) becomes [20]

$$i_{\Omega}(t) \propto \int P_1\left(x',y';z'\right) P_2^*\left(x'',y'';z''\right) \exp(-j\Omega t) + P_2\left(x',y';z'\right) P_1^*\left(x'',y'';z''\right) \times \exp(j\Omega t)\,\Gamma_0\left(x'+x,y'+y;z'\right)\Gamma_0^*\left(x''+x,y''+y;z''\right)dx'dx''dy'dy''dz'dz'', \quad (11)$$

and after some rearranging becomes

$$i_{\Omega}(t) \propto Re\int P_2\left(x',y';z'\right)\Gamma_0\left(x'+x,y'+y;z'\right)dx'dy'dz' \times P_1^*\left(x'',y'';z''\right)\Gamma_0^*\left(x''+x,y''+y;z''\right)dx''dy''dz''\exp(j\Omega t). \quad (12)$$

Letting $p_1(x,y)=\delta(x,y)$ and leaving $p_2(x,y)$ as is yields the situation where $\int P_1^*\left(x'',y'';z''\right)\Gamma_0^*\left(x''+x,y''+y;z''\right)dx''dy''dz''$ is a constant. Using the phasor relation in Eq. (10), Eq.(12) becomes

$$i_{\Omega_p}(x,y) = \int P_2\left(x'+x,y'+y;z\right)\Gamma_0\left(x'+x,y'+y;z\right)dx'dy'dz = \int P_2^*(x,y;z)\oplus\Gamma_0(x,y;z)\,dz, \quad (13)$$

where the symbol $\oplus$ denotes the 2-D correlation operation which is defined for x and y as $g(x,y)\oplus h(x,y)=\int\int g^*\left(x',y'\right)h\left(x+x',y+y'\right)dx'dy'$. Notice that Eq. (13) is processing the object's amplitude transmittance rather than intensity and the processing is only done by one pupil, namely $p_2(x,y)$. Thus, the 3-D coherent PSF for the system is

$$CPSF(x,y;z) = \mathcal{F}^{-1}\left\{\mathcal{F}^*\left\{P_2^*(x,y;z)\right\}\right\} = \mathcal{F}\left\{p_2(x,y)\right\}\otimes h(x,y;z), \quad (14)$$

where $\mathcal{F}^{-1}$ is the inverse Fourier transform defined as $\mathcal{F}^{-1}\{D(k_x,k_y)\} = d(x,y) = \frac{1}{4\pi^2}\int\int D(k_x,k_y)\exp(-jk_x x - jk_y y)\,dk_x dk_y$.

2.2.1 MATLAB Simulation: Coherent Processing

For coherent processing begin with Eq. (13) and let $p_2(x,y) = \delta(x,y)$ which is approximated in simulation using a small, circular aperture function. Plugging this into Eq. (4) yields $P_2(x,y;z)$ as

$$\begin{aligned} P_2(x,y;z) &= \mathcal{F}\{p_2(x,y)\}_{k_x=\frac{k_{0x}}{f},k_y=\frac{k_{0y}}{f}} \otimes h(x,y;z) \\ &\propto \mathcal{F}\{circ(x,y)\}_{k_x=\frac{k_{0x}}{f},k_y=\frac{k_{0y}}{f}} \otimes h(x,y;z) \end{aligned}. \quad (15)$$

Using the correlation operation and inserting Eq. (15) into Eq. (13) gives

$$\begin{aligned} i_{\Omega_p}(x,y) &= \int \mathcal{F}\{p_2(x,y)\}_{k_x=\frac{k_{0x}}{f},k_y=\frac{k_{0y}}{f}} \otimes h(x,y;z) \otimes \Gamma_0\left(x'+x, y'+y; z\right) \\ &\quad \times dx'dy'dz \\ &= \left[\mathcal{F}\{circ(x,y)\}_{k_x=\frac{k_{0x}}{f},k_y=\frac{k_{0y}}{f}} \otimes h(x,y;z)\right]^* \oplus \Gamma_0(x,y;z)\,dz \end{aligned}. \quad (16)$$

Based on the relationship expressing correlation in terms of convolution, $g(x,y) \oplus h(x,y) = g^*(-x,-y) \otimes h(x,y)$, the result in Eq. (16) can be written in terms of convolution as

$$i_{\Omega_p}(x,y) = \int \mathcal{F}\{circ(x,y)\}_{kx=\frac{k_{0x}}{f},ky=\frac{k_{0y}}{f}} \otimes h(x,y;z) \otimes \Gamma_0(x,y;z)\,dz. \quad (17)$$

For ease of calculation, the simulation of the expression under the integral in Eq. (17) will be implemented in MATLAB using the Fourier domain such that

$$\begin{aligned} i_{\Omega_p}(x,y) &= \mathcal{F}^{-1}\left\{\mathcal{F}\left\{\mathcal{F}\{circ(x,y)\}_{kx=\frac{k_{0x}}{f},ky=\frac{k_{0y}}{f}} \otimes h(x,y;z) \otimes \Gamma_0(x,y;z)\right\}\right\} \\ &= \mathcal{F}^{-1}\left\{\mathcal{F}\{\mathcal{F}\{circ(x,y)\}\}_{kx=\frac{k_{0x}}{f},ky=\frac{k_{0y}}{f}} \times \mathcal{F}\{(h(x,y;z)\} \times \mathcal{F}\{\Gamma_0(x,y;z)\}\right\} \\ &= \mathcal{F}^{-1}\{circ(x,y)\}_{kx=\frac{k_{0x}}{f},ky=\frac{k_{0y}}{f}} \times \mathcal{F}\{(h(x,y;z)\} \times \mathcal{F}\{\Gamma_0(x,y;z)\} \end{aligned}.$$

(18)

The full realization of Eq. (18) for the original object in Figure 2(a) under coherent recording is presented in the top of Figure 2(b). Inspecting this result as well as the row profile in

Figure 2(c) for pixel index at the red line one can see that the reconstruction contains speckle or ringing effects. The discussion of incoherent processing that follows will attempt to overcome these speckle artifacts.

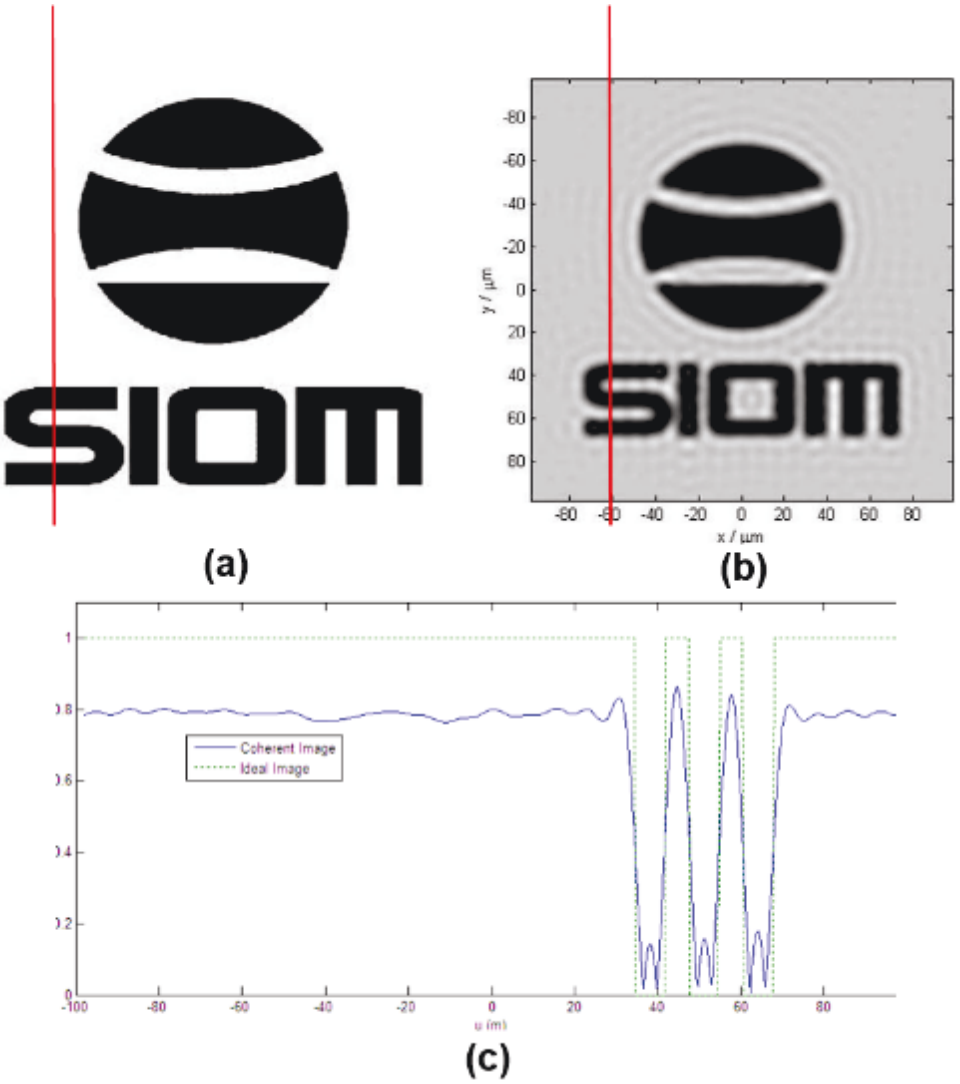

Figure 2 (a) Original image, (b) coherent recording, and (c) row profile.

2.3 Incoherent Processing

For incoherent processing Eq. (9) can be written as

$$
\begin{aligned}
i_{\Omega_p}(t) \propto \int & P_1\left(x^{'}, y^{'}, z^{'}\right) P_2^{*}\left(x^{''}, y^{''}, z^{''}\right) \exp\left(-j\Omega t\right) \\
& + P_2\left(x^{'}, y^{'}, z^{'}\right) P_1^{*}\left(x^{''}, y^{''}, z^{''}\right) \exp\left(j\Omega t\right) \\
& \times \Gamma_0\left(x^{'}+x, y^{'}+y, z^{'}\right) \Gamma_0^{*}\left(x^{''}+x, y^{''}+y, z^{''}\right) \Gamma\left(x^{'}-x^{''}, y^{'}-y^{''}, z^{'}-z^{''}\right) \\
& \times dx^{'} dy^{'} dz^{'} dx^{''} dy^{''} dz^{'} dz^{''}
\end{aligned}
\quad , \quad (19)
$$

where

$$
\begin{aligned}
\Gamma\left(x^{'}-x^{''}, y^{'}-y^{''}, z^{'}-z^{''}\right) = \int & \left|M\left(x_m, y_m\right)\right|^2 \exp\left[-j\frac{k_0\left(z^{'}-z^{''}\right)}{2f^2}\left(x_m^2+y_m^2\right)\right] \\
& \times \exp\left(j\frac{k_0}{f}\left[x_m\left(x^{'}-x^{''}\right)+y_m\left(y^{'}-y^{''}\right)\right]\right) dx_m dy_m
\end{aligned}
\quad .(20)
$$

The function $\Gamma\left(x^{'}-x^{''}, y^{'}-y^{''}, z^{'}-z^{''}\right)$ is a measure of the correlation field at $\left(x^{'}, y^{'}, z^{'}\right)$ and $\left(x^{''}, y^{''}, z^{''}\right)$ which plays the same role in scanning imaging as the coherent function in conventional coherent imaging [20]. If the mask becomes an open mask, $M\left(x_m, y_m\right) = 1$, Eq. (20) becomes

$$
\begin{aligned}
\Gamma\left(x^{'}-x^{''}, y^{'}-y^{''}, z^{'}-z^{''}\right) = \int & \exp\left(j\frac{k_0}{f}\left[x_m\left(x^{'}-x^{''}\right)+y_m\left(y^{'}-y^{''}\right)\right]\right) \\
& \times \exp\left(-j\frac{k_0\left(z^{'}-z^{''}\right)}{2f^2}\left(x_m^2+y_m^2\right)\right) dx_m dy_m
\end{aligned}
\quad . \quad (21)
$$

Note that the previous section used $M\left(x_m, y_m\right) = \delta\left(x_m, y_m\right)$ which leads to $\Gamma\left(x^{'}-x^{''}, y^{'}-y^{''}, z^{'}-z^{''}\right) = 1$. The quadratic term in Eq. (21) represents a spherical wave with a radius of curvature, $R = f^2 / \left(z - z^{'}\right)$, that can be made arbitrarily large thus, [20]

$$
\begin{aligned}
\Gamma\left(x^{'}-x^{''}, y^{'}-y^{''}, z^{'}-z^{''}\right) & \sim \frac{1}{z^{'}-z^{''}} \exp\left(j\frac{k_0\left[\left(x^{'}-x^{''}\right)^2+\left(y^{'}-y^{''}\right)^2\right]}{2\left(z^{'}-z^{''}\right)}\right) \\
& \sim \delta\left(x^{'}-x^{''}, y^{'}-y^{''}; z^{'}-z^{''}\right)
\end{aligned}
\quad . \quad (22)
$$

Substituting this into Eq. (19) yields

$$
\begin{aligned}
i_{\Omega_p}(x,y) &= \int P_1^*\left(x^{'},y^{'};z\right) P_2\left(x^{'},y^{'};z\right) \left|\Gamma_0\left(x^{'}+x,y^{'}+y;z\right)\right|^2 \\
&\quad \times dx^{'}dy^{'}dz \\
&= \int \left[P_1^*(x,y;z)\, P_2(x,y;z)\right]^* \oplus \left|\Gamma_0(x,y;z)\right|^2 dz
\end{aligned}
, \tag{23}
$$

and with the 3-D incoherent PSF is

$$
\begin{aligned}
IPSF(x,y;z) &= \mathcal{F}^{-1}\left\{\mathcal{F}^*\left\{P_1(x,y;z)\, P_2^*(x,y;z)\right\}\right\} \\
&= \mathcal{F}\left\{p_1(x,y)\, p_2^*(x,y) \otimes h(x,y;z)\right\}
\end{aligned}
. \tag{24}
$$

The result in Eq. (24) represents incoherent processing or processing by intensity values with two pupils.

2.3.1 MATLAB Simulation: Incoherent Processing

For incoherent processing, choose $p_1(x,y)=1$ and $p_2(x,y)$ thus, using Eq. (4) $P_1^*(x,y;z)$ and $P_2(x,y;z)$ become

$$
\begin{aligned}
P_1^*(x,y;z) &= \left[\mathcal{F}\left\{p_1(x,y)\right\}_{kx=\frac{k_0 x}{f} ky=\frac{k_0 y}{f}} \otimes h(x,y;z)\right]^* \\
&= \left[\mathcal{F}\left\{1\right\}_{kx=\frac{k_0 x}{f} ky=\frac{k_0 y}{f}} \otimes h(x,y;z)\right]^* \\
&= \left[4\pi^2\delta\left(\frac{k_0 x}{f},\frac{k_0 y}{f}\right) \otimes \left\{\exp\left[-jk_0 z\right]\frac{jk_0}{2\pi z}\right\}\right]^* \\
&\propto \left[\exp\left[-jk_0 z\right]\frac{jk_0}{2\pi z}\exp\left(\frac{-jk_0\left(x^2+y^2\right)}{2z}\right)\right]^* = h^*(x,y;z) \\
P_2(x,y;z) &= \left[\mathcal{F}\left\{p_2(x,y)\right\}_{kx=\frac{k_0 x}{f} ky=\frac{k_0 y}{f}} \otimes h(x,y;z)\right] \\
&= \left[\mathcal{F}\left\{\delta(x,y)\right\}_{kx=\frac{k_0 x}{f} ky=\frac{k_0 y}{f}} \otimes h(x,y;z)\right] \\
&= \int\int \delta(x,y)\exp\left(jk_x x + jk_y y\right)dxdy \otimes h(x,y;z) \\
&= \int \delta(x)\exp\left(jk_x x\right)dx \int \delta(y)\exp\left(jk_y y\right)dy \otimes h(x,y;z) \\
&= 1 \otimes h(x,y;z) \propto \exp\left[-jk_0 z\right]
\end{aligned}
. \tag{25}
$$

And Eq. (23) becomes

$$
\begin{aligned}
i_{\Omega_p}(x,y) &= \int \exp(jk_0 z)\frac{-jk_0}{2\pi z}\exp\left[\frac{jk_0\left(x^2+y^2\right)}{2z}\right]\exp(-jk_0 z) \\
&\times \mid \Gamma_0\left(x^{'}+x, y^{'}+y; z\right)\mid^2 dx^{'}dy^{'}dz \\
&= \int \left[\frac{-jk_0}{2\pi z}\exp\left[\frac{jk_0\left(x^2+y^2\right)}{2z}\right]\right]^{*} \oplus \mid \Gamma_0(x,y;z)\mid^2 dz \\
&= \int \frac{-jk_0}{2\pi z}\exp\left[\frac{jk_0\left(x^2+y^2\right)}{2z}\right] \otimes \mid \Gamma_0(x,y;z)\mid^2 dz
\end{aligned}
\quad . \qquad (26)
$$

The expression under the integral in Eq. (26) is implemented in the Fourier domain as previously for coherent processing. The recording under incoherent processing is presented in Figure 3(a). The improvements over coherent processing are enforced by examination of the row profile in Figure 3(b) where the speckle artifacts are not present.

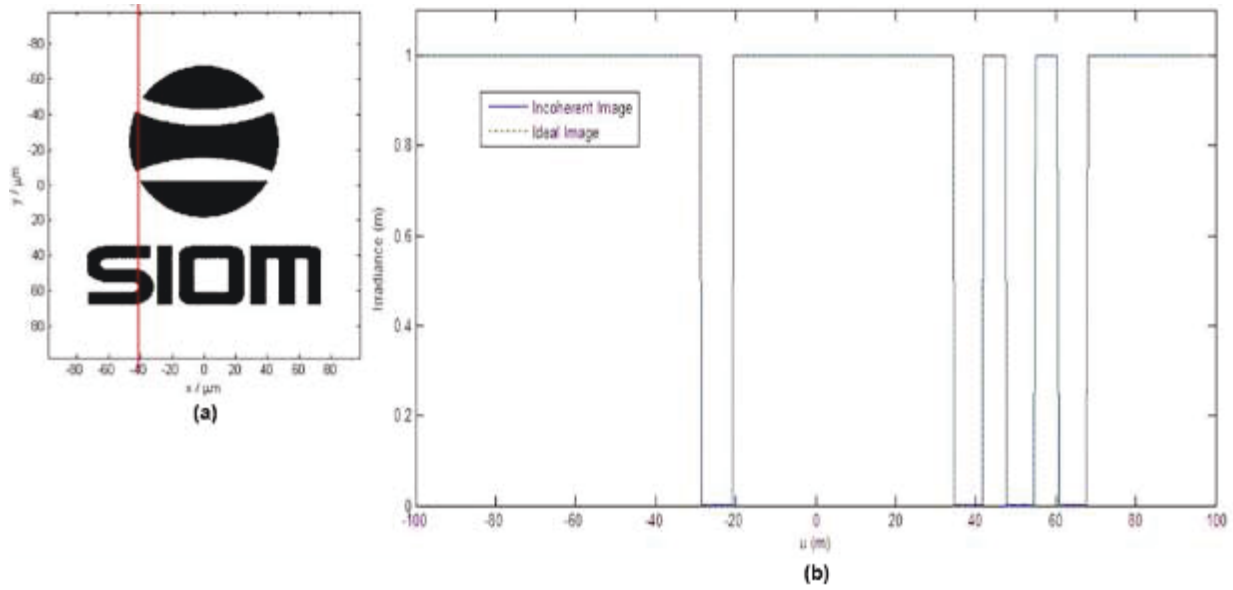

Figure 3 (a) Incoherent recording and (b) row profile.

2.4 Optical Transfer Function

Assuming the input object, $\Gamma_0(x,y;z)$, is an infinitely thin 2-D object located at a distance z away from the focal plane of L_1, the expression in Eq. (23) can be rewritten in terms of correlation as

$$
i_{\Omega_p}(x,y;z) = P_1(x,y;z)\,P_2^{*}(x,y;z) \oplus \mid \Gamma_0(x,y;z)\mid^2 . \qquad (27)
$$

The relation of input to output quantity in Eq. (27) allows for the definition of optical transfer function (OTF) of the system as

$$OTF_{\Omega}(k_x, k_y; z) = \mathcal{F}\{i_{\Omega_p}(x, y; z)\}\big|_{k_x,k_y} / \mathcal{F}\{|\Gamma_0(x, y; z)|^2\}\big|_{k_x,k_y}, \tag{28}$$

Taking the Fourier transform of Eq. (27) and combining it with Eq. (28) results in

$$OTF_{\Omega}(k_x, k_y; z) = \mathcal{F}\{P_1(x, y; z)P_2^*(x, y; z)\}\big|_{k_x,k_y}. \tag{29}$$

Writing Eq. (29) in terms of $p_1(x, y)$ and $p_2(x, y)$ by substituting Eq. (2) and (4) gives

$$\begin{aligned} OTF_{\Omega}(k_x, k_y; z) = \exp\left[j\frac{z}{2k_0}\left(k_x^2 + k_y^2\right)\right] \int\int p_1^*\left(x', y'\right) \\ \times p_2\left(x' + \frac{fk_x}{k_0}, y' + \frac{fk_y}{k_0}\right) \exp\left[j\frac{z}{f}\left(x' + \frac{fk_x}{k_0}, y' + \frac{fk_y}{k_0}\right)\right] dx' dy' \end{aligned} \tag{30}$$

Now using Eq. (28) and rewriting Eq. (10) in terms of OTF_{Ω} results in

$$\begin{aligned} i_{\Omega}(x, y; z) &= Re\left[i_{\Omega_p}(x, y; z)\exp[j\Omega t]\right] \\ &= Re\left[\mathcal{F}^{-1}\{\mathcal{F}\{|\Gamma_0(x, y; z)|^2\}\big|_{k_x,k_y} \times OTF_{\Omega}(k_x,\ k_y; z)\}\exp[j\Omega t]\right]. \end{aligned} \tag{31}$$

The spatial impulse response or point spread function of the optical-heterodyne scanning system can be defined as

$$h_{\Omega}(x, y; z) = \mathcal{F}^{-1}\{OTF_{\Omega}\}, \tag{32}$$

and Eq. (31) can be rewritten in the spatial domain as

$$i_{\Omega}(x, y; z) = Re\left[|\ \Gamma_0(x, y; z)\ |^2 \otimes h_{\Omega}(x, y; z)\exp[j\Omega t]\right]. \tag{33}$$

The demodulation unit in Figure 4 consists of a lock-in amplifier which electronically multiplies and low-pass filters the signal to demodulate the in-phase current $i_c(x, y)$ and quadrature current $i_s(x, y)$ as the following outputs in the frequency domain [20]

$$\begin{aligned} i_c(x, y; z) &= Re[\mathcal{F}^{-1}\{\mathcal{F}\{|\Gamma_0|^2\}\big|_{k_x,k_y} \times OTF_{\Omega}\}] \\ i_s(x, y; z) &= Im[\mathcal{F}^{-1}\{\mathcal{F}\{|\Gamma_0|^2\}\big|_{k_x,k_y} \times OTF_{\Omega}\}], \end{aligned} \tag{34}$$

where $Im[\cdot]$ denotes the imaginary part of the content inside the brackets. In the spatial domain, Eq. (34) is

$$i_c(x,y;z) = Re[\mathcal{F}^{-1}\{\mathcal{F}\{|\Gamma_0|^2\}\big|_{k_x,k_y} \times OTF_\Omega\}]$$
$$i_s(x,y;z) = Im[\mathcal{F}^{-1}\{\mathcal{F}\{|\Gamma_0|^2\}\big|_{k_x,k_y} \times OTF_\Omega\}] \quad (35)$$

Removing the assumption of an infinitely thin object and generalizing Eq. (34) over the depth of the 3-D object results in

$$i_c(x,y;z) = Re\left[\int \mathcal{F}^{-1}\{\mathcal{F}\{|\Gamma_0(x,y;z)|^2\}\big|_{k_x,k_y} \times OTF_\Omega\}dz\right]$$
$$i_s(x,y;z) = Im\left[\int \mathcal{F}^{-1}\{\mathcal{F}\{|\Gamma_0(x,y;z)|^2\}\big|_{k_x,k_y} \times OTF_\Omega\}dz\right], \quad (36)$$

and in the spatial domain

$$i_c(x,y;z) = Re\left[\int |\Gamma_0(x,y;z)|^2 \otimes h_\Omega(x,y;z)\right]dz$$
$$i_s(x,y;z) = Im\left[\int |\Gamma_0(x,y;z)|^2 \otimes h_\Omega(x,y;z)\right]dz \quad (37)$$

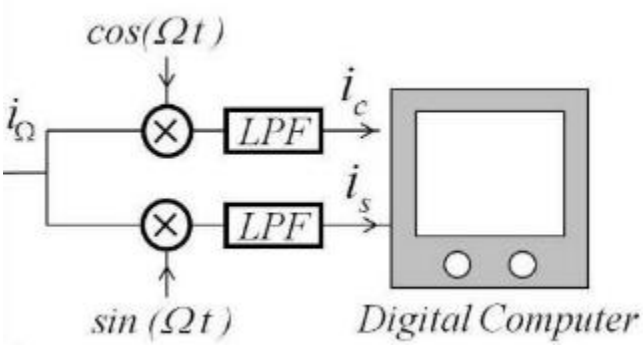

Figure 4 Electronic demodulation system (⊗ is electronic multiplier). [Used with permission]

In optical scanning holography, the pupils are chosen as $p_1(x,y) = \delta(x,y)$ and $p_2(x,y)$ so that the scanning beam on the specimen physically becomes the superposition of a plane wave of temporal frequency $\omega_0 + \Omega$ and a spherical wave of temporal frequency ω_0. This concept as illustrated in Figure 5 includes a point source and a plane wave as the two pupils. This generates a superposition of a plane wave and a spherical wave on the specimen with the intensity pattern of the scanning beam on the specimen at a distance z away from point C given by [20]

$$I_S(x,y;z,t) = A_z(x,y)\left|\exp\left[j(\omega_0+\Omega)t + \frac{j}{\lambda z}\exp\left[-j\frac{\pi}{\lambda z}(x^2+y^2)+j\omega_0 t\right]\right]\right|^2$$
$$= A_z(x,y)\left\{1+\left(\frac{1}{\lambda z}^2\right)+\frac{1}{\lambda z}\sin\left[\frac{\pi}{\lambda z}(x^2+y^2)+\Omega t\right]\right\}, \quad (38)$$

where $A_z(x,y)$ is the scanning pattern's spot size as determined by the numerical aperture (NA) of the scanning beam. The expression in Eq. (38) is a temporally-modulated Fresnel zone plate and is known as the time-dependent Fresnel zone plate (TDFZP). The phase information in Eq. (38) is preserved as z is encoded in the hologram by spatial variation of the sine function with quadratic spatial dependence. In Figure 6, the pattern of the scanning beam on the specimen is shown for a fixed time or a static Fresnel zone plate (FZP). As time progresses in Eq. (38) running zones would move towards the center of the zone pattern and it is this TDFZP that is used to 2-D scan a 3-D object to capture holographic information for the scanned specimen.

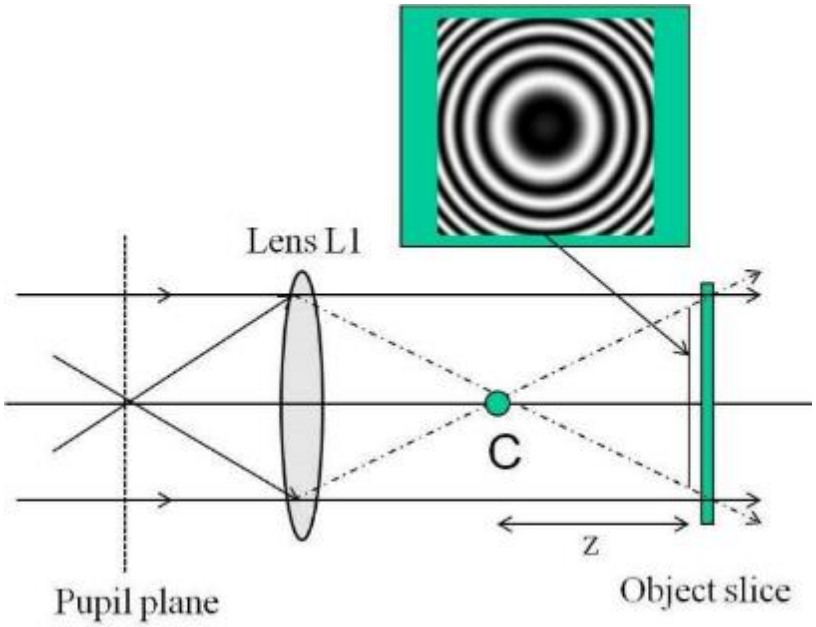

Figure 5 Principle of OSH: use of time-dependent Fresnel zone plate to scan over an object.

The spatial rate of change of the phase on the zone plate along the x-direction is

$$f_{local} = \frac{1}{2\pi}\frac{d}{dx}\left(\frac{k_0}{2z}x^2\right) = \frac{x}{\lambda_0 z}. \quad (39)$$

From Eq. (39) the local fringe frequency increases linearly with x thus, the further away from the origin of the zone the higher the local spatial frequency. Therefore, it is seen that the depth information, z, is encoded within the phase of the FZP. As seen in Figure 6 where the value of is

z doubled on the right, the further away from the recording film the lower the local fringe frequency of the recorded FZP.

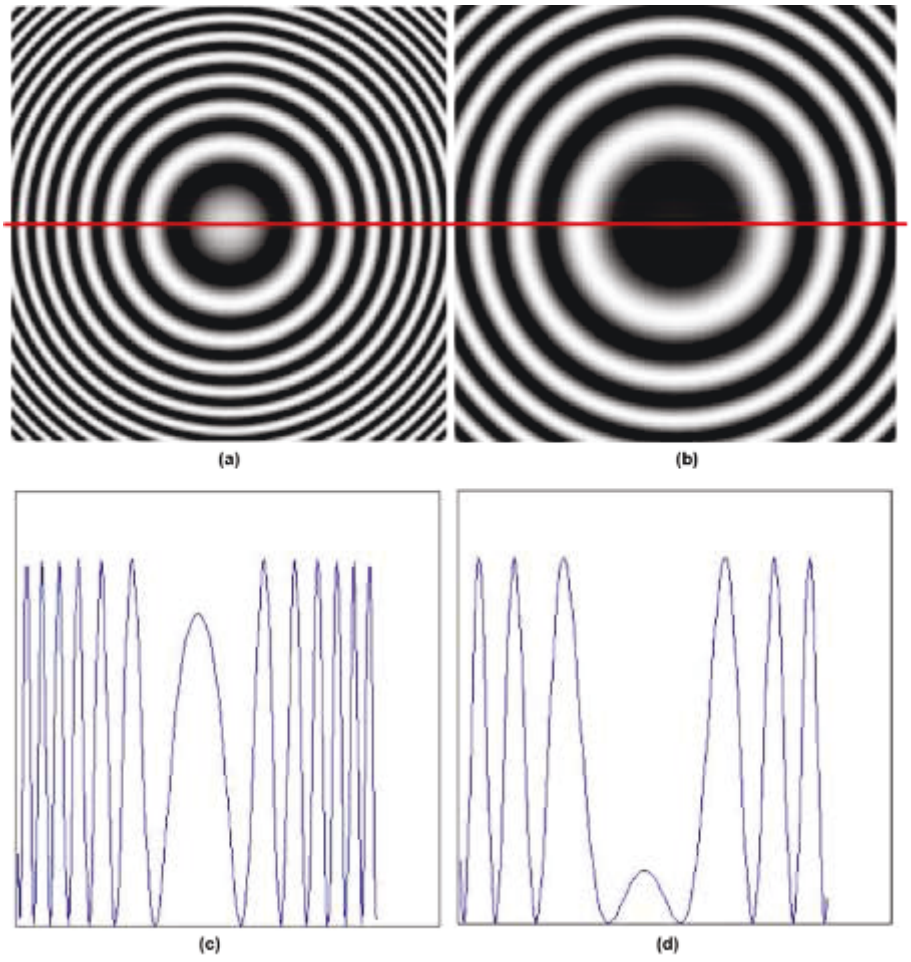

Figure 6 On-axis Fresnel zone plate (a) $z = 4z_0$ and (b) $z = 8z_0$, and (c) and (d) corresponding 1-D plot of Fresnel zone plate through center, respectively.

The specific OTF for the traditional-heterodyne scanning system that provides the foundation for the remainder of this dissertation is found by scanning an object with pupils $p_1(x,y) = \delta(x,y)$ and $p_2(x,y) = 1$ such that

$$OTF_{\Omega}(k_x, k_y; z) = \exp\left[-j\frac{z}{2k_0}\left(k_x^2 + k_y^2\right)\right] = OTF_{OSH}(k_x, k_y; z), \quad (40)$$

and similarly the corresponding spatial impulse response is

$$h_{\Omega}(x, y; z)\,|_{OSH} = -j\frac{k_0}{2\pi z}\exp\left[\frac{jk_0\left(x^2 + y^2\right)}{2z}\right]. \quad (41)$$

Note that the relation in Eq. (41) is similar to the spatial transfer function in Fourier optics in Eq. (5) except for a phase factor thus

$$h_{\Omega}(x,y;z)\mid_{OSH} = h^{*}(x,y;z), \tag{42}$$

and similarly

$$OTF_{OSH}(k_x,k_y;z) = H^{*}(k_x,k_y;z). \tag{43}$$

The next chapter will build upon these mathematical and optical relations to detail optical scanning holography principles such as holographic recording and reconstruction techniques.

3 PRINCIPLES OF OPTICAL SCANNING HOLOGRAPHY

The previous chapter covered the necessary background in mathematics and optics to provide a basic understanding of the components which can be used to realize real-time holographic recordings. This chapter will summarize the principles of optical scanning holography and demonstrate how an object can be two-dimensionally scanned to obtain holographic information. Section 3.1 begins the chapter by developing the principles of optical scanning holography including mathematical and graphical representations of a Fresnel zone plate (FZP). Section 3.1.1 features MATLAB simulation results for a sine and cosine hologram generated for a black and white planar object. In Section 3.2, holographic reconstructions are performed by digitally convolving the hologram with the free-space impulse response matched to the depth parameter. Simulations demonstrating digital reconstructions for a sine, cosine, and complex hologram are presented in Section 3.2.1. The mathematical concept of optical sectioning or focus at different reconstruction planes is realized in Section 3.3 where reconstructions are performed along the depth of the hologram. Simulations of reconstructions through different depths are presented in Section 3.3.1.

3.1 Scanning Holography

The optical-heterodyne scanning image processor analyzed in Chapter 2 can be used as a real-time holographic recording device. For the case of incoherent processing from Eq. (23), Eq. (34) can be written as

$$\begin{aligned} i_c(x,y) &\propto \int Re\left[P_1 P_2^*\right] \oplus |\,\Gamma_0\,|^2\, dz \\ i_s(x,y) &\propto \int Im\left[P_1 P_2^*\right] \oplus |\,\Gamma_0\,|^2\, dz \end{aligned} \quad . \tag{44}$$

Thus from Eq. (41) for scanning holography, the outputs of the system according to Eq. (44) are

$$
\begin{aligned}
i_c(x,y) &\propto Re\left[\int h^*(x,y;z)\right] \otimes |\,\Gamma_0(x,y;z)\,|^2\, dz \\
&= \int \frac{k_0}{2\pi z}\cos\left[\frac{k_0}{2\pi z}\left(x^2+y^2\right)\right] \otimes |\,\Gamma_0(x,y;z)\,|^2\, dz \\
&= H_{cos}(x,y) \\
i_s(x,y) &\propto Im\left[\int h^*(x,y;z)\right] \otimes |\,\Gamma_0(x,y;z)\,|^2\, dz \\
&= \int \frac{k_0}{2\pi z}\sin\left[\frac{k_0}{2\pi z}\left(x^2+y^2\right)\right] \otimes |\,\Gamma_0(x,y;z)\,|^2\, dz \\
&= H_{sin}(x,y)
\end{aligned}
\quad , \qquad (45)
$$

where $H_{sin}(x,y)$ and $H_{cos}(x,y)$ are the sine Fresnel zone plate (SFZP) hologram and cosine Fresnel zone plate (CFZP) hologram, respectively, of the specimen $|\,\Gamma_0(x,y;z)\,|^2$. Taking the specimen to be a point source, $|\,\Gamma_0(x,y;z)\,|^2 = \delta(x,y;z)$ then Eq. (45) becomes the hologram of a point source, $H_{sin}(x,y) \propto \sin\left[(k_0/2\pi z)\left(x^2+y^2\right)\right]$ and $H_{cos}(x,y) \propto \cos\left[(k_0/2\pi z)\left(x^2+y^2\right)\right]$. Similarly, a complex Fresnel zone plate hologram can be constructed as

$$
\begin{aligned}
H_{c+}(x,y) &= H_{cos}(x,y) + jH_{sin}(x,y) \\
&= \frac{k_0}{2\pi z}\exp\left[\frac{jk_0}{2\pi z}(x^2+y^2)\right] \otimes |\Gamma_0(x,\ y)|^2 \\
&= \mathcal{F}^{-1}\{OTF_{OSH}(k_x,k_y;z) \times \mathcal{F}\{|\Gamma_0(x,y)|^2\}\big|_{k_x,k_y}\}.
\end{aligned}
\qquad (46)
$$

3.1.1 MATLAB Simulations: Optical Scanning Holography

Using the OTF of optical scanning holography from Eq. (43) and Eq. (45) the sine hologram and cosine hologram in terms of spatial frequencies are

$$
\begin{aligned}
i_c(x,y) &\propto Re\left[\int \mathcal{F}^{-1}\{OTF_{OSH}(k_x,k_y;z) \times \mathcal{F}\{|\Gamma_0(x,y;z)|^2\}\big|_{k_x,k_y}\}dz\right] \\
&= H_{cos}(x,y) \\
i_s(x,y) &\propto Im\left[\int \mathcal{F}^{-1}\{OTF_{OSH}(k_x,k_y;z) \times \mathcal{F}\{|\Gamma_0(x,y;z)|^2\}\big|_{k_x,k_y}\}dz\right] \\
&= H_{sin}(x,y)
\end{aligned}
\quad . \qquad (47)
$$

For the simulations carried out in MATLAB, the text is a 2-D pattern $\left|\Gamma_0\left(x,y;z\right)\right|^2 = I\left(x,y\right)$ located at z from the back focal plane of lens L_1, where $I\left(x,y\right)$ is the planar intensity distribution of the text. Utilizing this, Eq. (47) becomes

$$\begin{aligned} i_c(x,y) &= Re\left[\mathcal{F}^{-1}\{OTF_{OSH}(k_x,k_y;z)\times\mathcal{F}\{|\Gamma_0(x,y;z)|^2\}\big|_{k_x,k_y}\}\right] \\ &= H_{cos}(x,\ y) \\ i_s(x,y) &= Im\left[\mathcal{F}^{-1}\{OTF_{OSH}(k_x,k_y;z)\times\mathcal{F}\{|\Gamma_0(x,y;z)|^2\}\big|_{k_x,k_y}\}\right] \\ &= H_{sin}(x,y) \end{aligned} \quad . \tag{48}$$

The original black and white, planar intensity object is the USAF bar chart presented in Figure 7. The simulated holograms for the object shown in Figure 8 (a) and (b), respectively where in Eq. (48) $z/2k_0 = 2$. The information in the original image is captured via the hologram in Figure 8 and the original image can be obtained from this using reconstruction techniques which are discussed next.

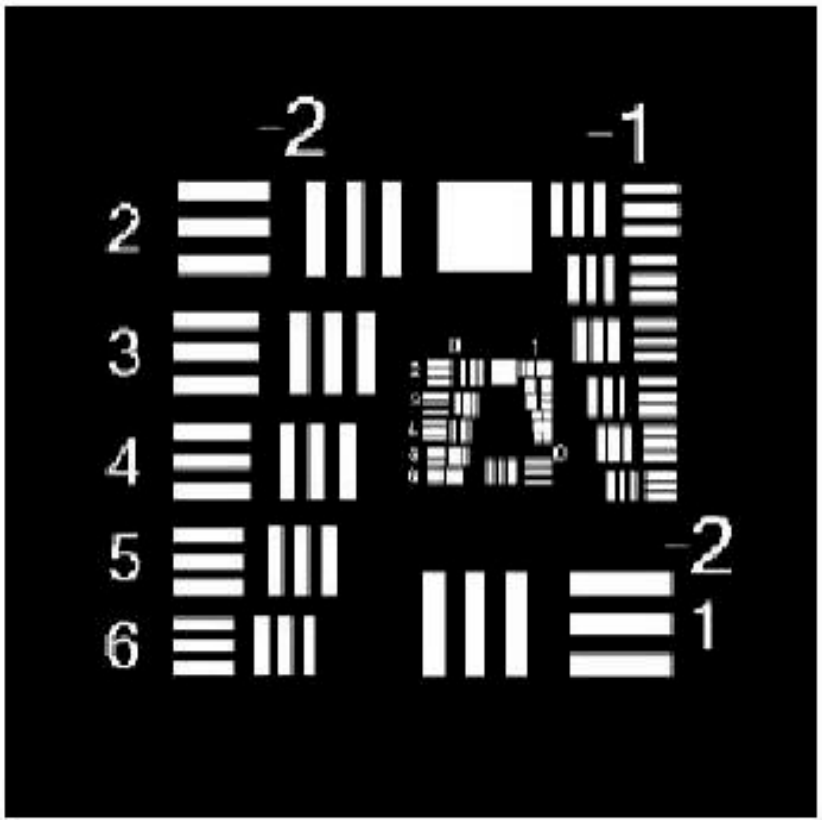

Figure 7 Original planar intensity object.

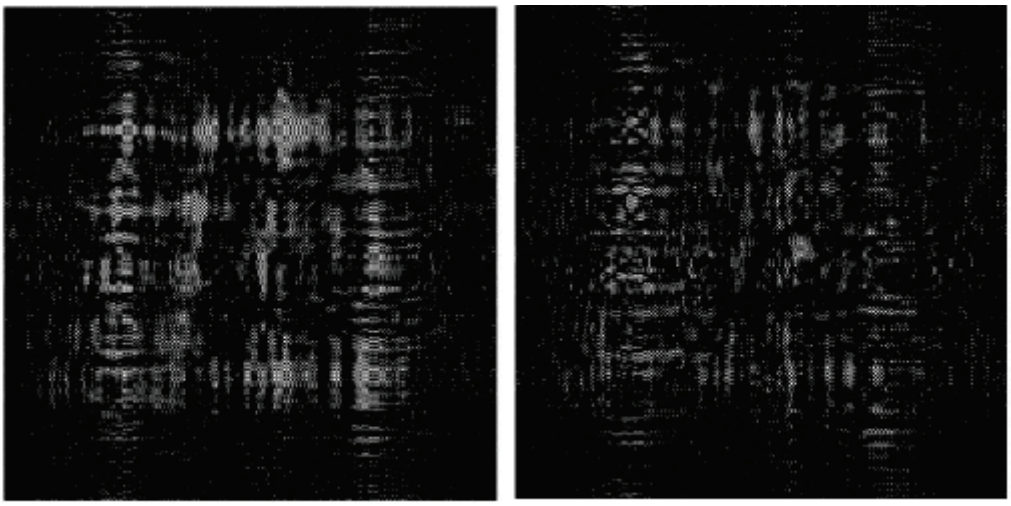

Figure 8 (a) Sine hologram and (b) cosine hologram of Figure 7.

3.2 Digital Reconstruction of Complex Hologram

Reconstruction of the hologram is completed by convolving the hologram with the free-space impulse response matched to the depth parameter $h(x, y; z)$ so as to simulate Fresnel diffraction for a distance z [1]. The reconstruction can be accomplished either optically by illuminating the hologram with a plane wave or digitally by performing the convolution given by

$$R(x, y; z) = H_i(x, y) \otimes h(x, y; z), \tag{49}$$

where $H_i(x, y)$ is the hologram under consideration and can be either a sine, cosine, or complex hologram.

3.2.1 MATLAB Simulation: Digital Reconstruction of Complex Hologram

Digital reconstructions are implemented in MATLAB using the Fourier domain based on

$$\begin{aligned} R &\propto \mathcal{F}^{-1}\{\mathcal{F}\{H_i(x,y) \otimes h(x,y;z)\}\big|_{k_x,k_y}\} \\ &= \mathcal{F}^{-1}\{\mathcal{F}\{H_i(x,y)\}\big|_{k_x,k_y} \times \mathcal{F}\{h(x,y;z)\}\big|_{k_x,k_y}\} \\ &= \mathcal{F}^{-1}\{\mathcal{F}\{H_i(x,y)\}\big|_{k_x,k_y} \times H(k_x,k_y;z)\} \\ &= \mathcal{F}^{-1}\{\mathcal{F}\{H_i(x,y)\}\big|_{k_x,k_y} \times OTF^*_{OSH}(k_x,k_y;z)\}. \end{aligned} \tag{50}$$

For reconstruction of a complex hologram in Eq. (46), it can be shown that

$$R \propto= \mathcal{F}^{-1}\{\mathcal{F}\{OTF_{OSH}(k_x,k_y;z)\} \times \mathcal{F}\{I(x,y)\}\big|_{k_x,k_y} \times OTF^{*}_{OSH}(k_x,k_y;z)\}, \quad (51)$$

as OTF_{OSH} is a phase function per Eq. (40). The reconstructed sine hologram, cosine hologram, and complex hologram are shown in Figure 9 (a), (b) and (c), respectively.

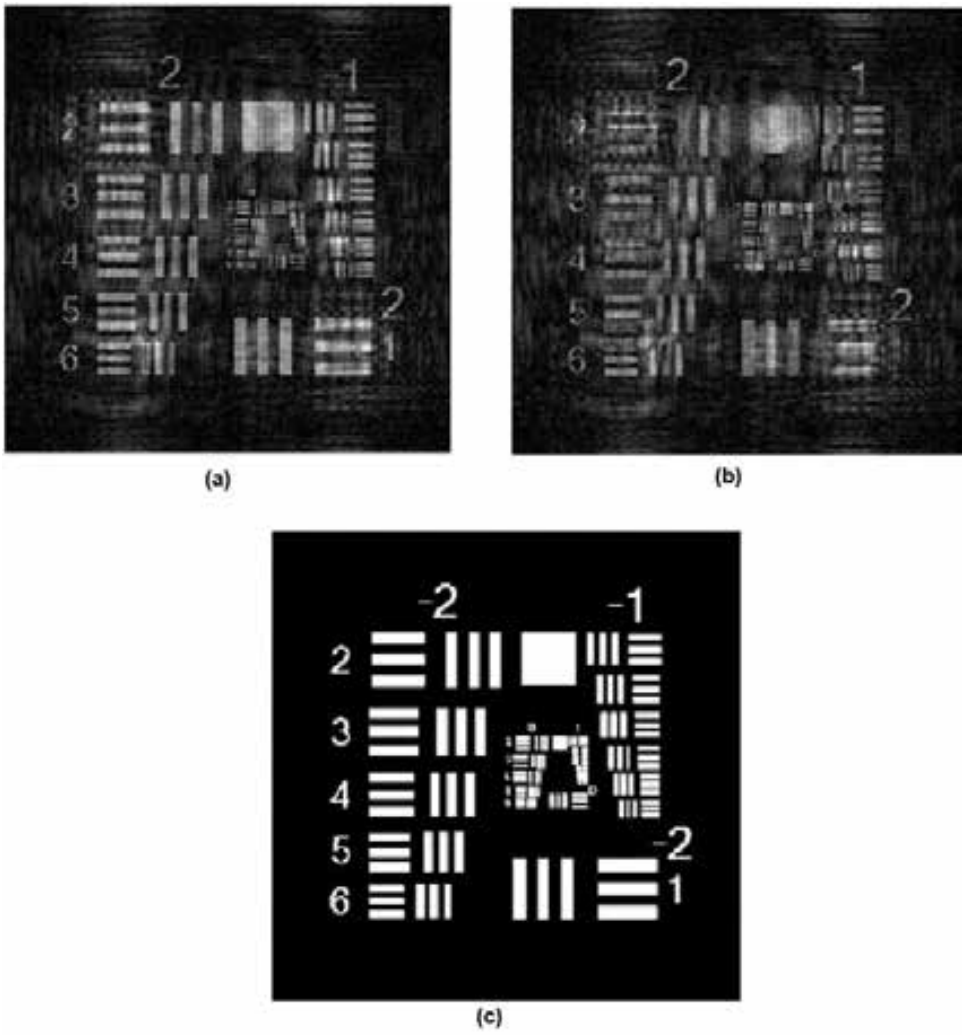

Figure 9 (a) Reconstruction of sine hologram [See Eq. (48)], (b) Reconstruction of cosine hologram [See Eq. (48)], and (c) Reconstruction of complex hologram constructed according to [See Eq. (46)].

3.3 Optical Sectioning

The results from complex hologram reconstruction shown in Figure 9 (c) illustrate the retrieval of the original 2-D pattern via Eq. (51) because

$$OTF_{OSH}(k_x,k_y;z) \times OTF^{*}_{OSH}(k_x,k_y;z) = 1, \quad (52)$$

for any z. In fact, $H_c(x,y)$ is the complex digital hologram of $|\Gamma_0(x,y;z|$ located at z from the back focal plane of lens L_1 so that when

$$OTF_{OSH}(k_x,k_y;z)\times OTF^{*}_{OSH}(k_x,k_y;z_i\neq z)\neq 1, \tag{53}$$

or

$$\mathcal{F}^{-1}\{OTF_{OSH}(k_x,k_y;z)\}\otimes\mathcal{F}^{-1}\{OTF^{*}_{OSH}(k_x,k_y;z_i\neq z)\}\neq\delta(x,y), \tag{54}$$

the reconstructed image is defocused due to the difference of the z_i parameter from z, where z_i is the reconstruction distance.

Thus for a 3-D object illuminated by a plane wave, reconstruction of a sectional image at a certain depth z_i is

$$\begin{aligned} R_{z_i} &= H_c(x,y)\otimes h(x,y;z_i) \\ &= |\Gamma_0(x,y;z_i)|^2+\int_{z\neq z_i}|\Gamma_0(x,y;z_i)|^2\otimes h(x,y;z-z_i)\,dz \end{aligned}, \tag{55}$$

where $|\Gamma_0(x,y;z_i)|^2$ is the sectional image at $z=z_i$ and $\int_{z\neq z_i}|\Gamma_0(x,y;z_i)|^2\otimes h(x,y;z-z_i)\,dz$ is the defocus noise on the $z=z_i$ plane. It is this defocus term that optical sectioning attempts to filter or reject while maintaining the clarity of the focused image $|\Gamma_0(x,y;z_i)|^2$. Efforts to maintain the clarity of the desired sectional reconstruction while suppressing the defocus noise contributions from the adjacent sections include algorithmic as well as hybrid optical and digital approaches. Recent algorithmic demonstrations include Wiener filtering [21], Wigner distribution function [22], and inverse imaging [23] but these approaches achieve noise suppression at the expense of computational intensity, optimality, and estimator bias. The evolution of a hybrid digital and optical system which obtains reconstructions of a similar quality without the additional expenses of these approaches will be presented in Chapter 4.

3.3.1 MATLAB Simulation: Optical Sectioning

For discretized sectional images, z can be denoted by $z_1, z_2, \cdots, z_n$ and Eq. (46) can be represented as

$$
\begin{aligned}
F\{H_c(x,y)\}\big|_{k_x,k_y} &= \mathcal{F}\{|\Gamma_0(x,y;z_1)|^2 \otimes h^*(x,y;z_1) + |\Gamma_0(x,y;z_2)|^2 \otimes h^*(x,y;z_2) \\
&\quad + |\Gamma_0(x,y;z_3)|^2 \otimes h^*(x,y;z_3)\}\big|_{k_x,k_y} \\
&= \mathcal{F}\{|\Gamma_0(x,y;z_1)|^2\}\big|_{k_x,k_y} \times OTF(k_x,k_y;z_1) + \mathcal{F}\{|\Gamma_0(x,y;z_2)|^2\}\big|_{k_x,k_y} \\
&\quad \times OTF(k_x,k_y;z_2) + \{|\Gamma_0(x,y;z_3)|^2\}\big|_{k_x,k_y} \times OTF(k_x,k_y;z_3)
\end{aligned}
\quad , \tag{56}
$$

such that when the plane of focus is z_2, then z_1 and z_3 are out of focus. Similarly, when you focus on z_1, z_2 and z_3 will be defocused. The original 3-D image as visualized in sectional image or planar form is presented in Figure 10. Using these as the $|\Gamma_0(x,y;z_i)|^2$ values in Eq. (56) produces the hologram in Figure 11.

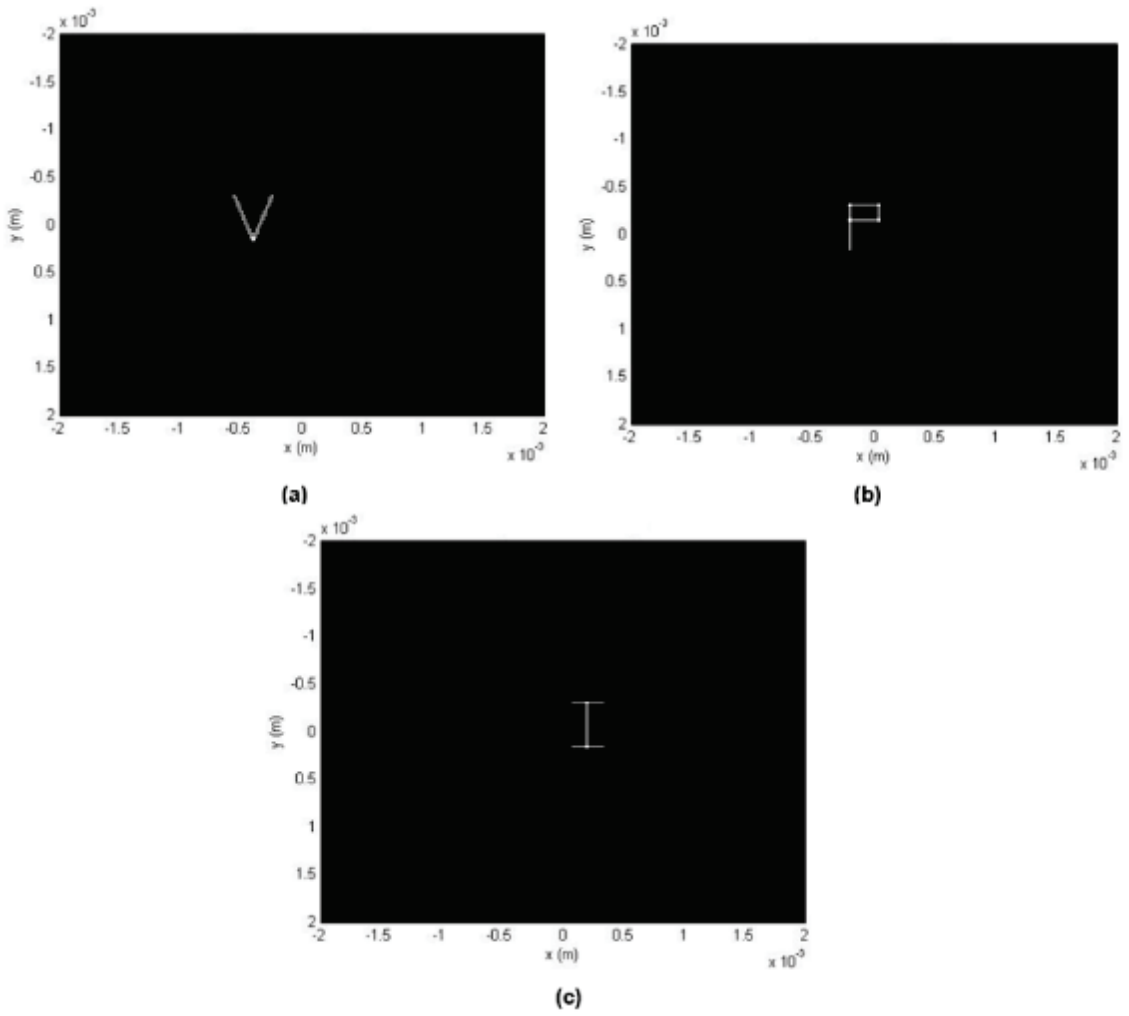

Figure 10 Original 3-D image.

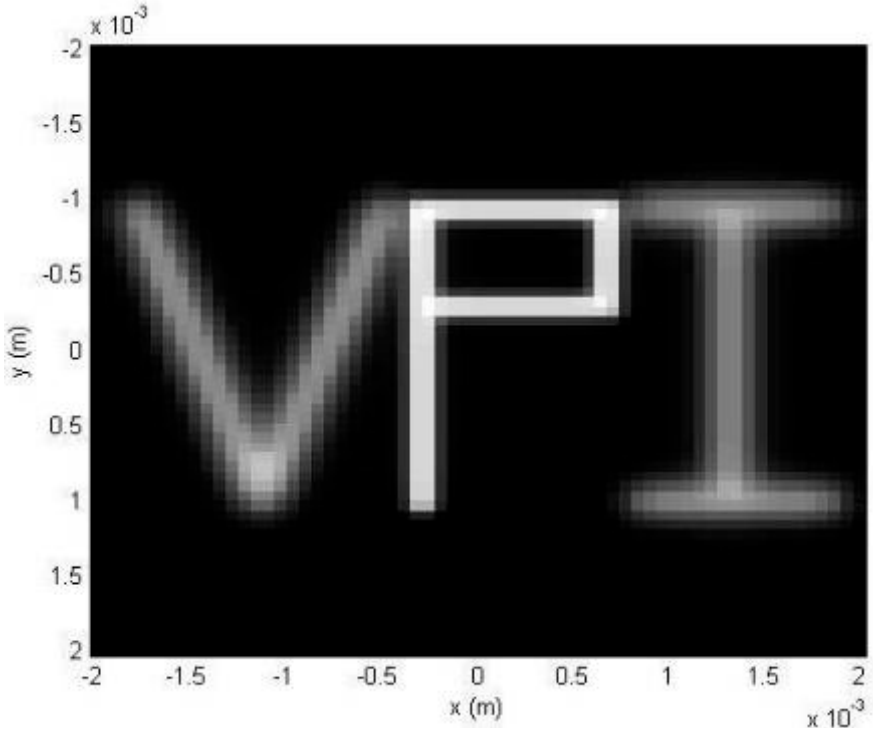

Figure 11 Simulated hologram implementation of Eq. (56) with original image in Figure 10.

Reconstruction at a particular plane of interest such as z_2 in Figure 11 is implemented in MATLAB as

$$\begin{aligned} R_{z_i} &\propto \mathcal{F}^{-1}\{\mathcal{F}\{H_c(x,y)\}\big|_{k_x,k_y} \times OTF^*(k_x,k_y;z_i)\} \\ &= \mathcal{F}^{-1}\{\mathcal{F}\{|\Gamma_0(x,y;z_1)|^2\}\big|_{k_x,k_y} \times OTF(k_x,k_y;z_1-z_2) \\ &+ \mathcal{F}\{|\Gamma_0(x,y;z_2)|^2\}\big|_{k_x,k_y} \times OTF(k_x,k_y;z_2)OTF^*(k_x,k_y;z_2) \\ &+ \mathcal{F}\{|\Gamma_0(x,y;z_3)|^2\}\big|_{k_x,k_y} \times OTF(k_x,k_y;z_3-z_2)\} \end{aligned} \quad . \qquad (57)$$

The experimental results for planar reconstruction for each of the three planes are shown in Figure 12. The presence of the defocus noise contributions from the nearby contributing planes is noticeable to the left or right of the focused plane. The next chapter will address applications of OSH including techniques to limit these defocus noise contributions.

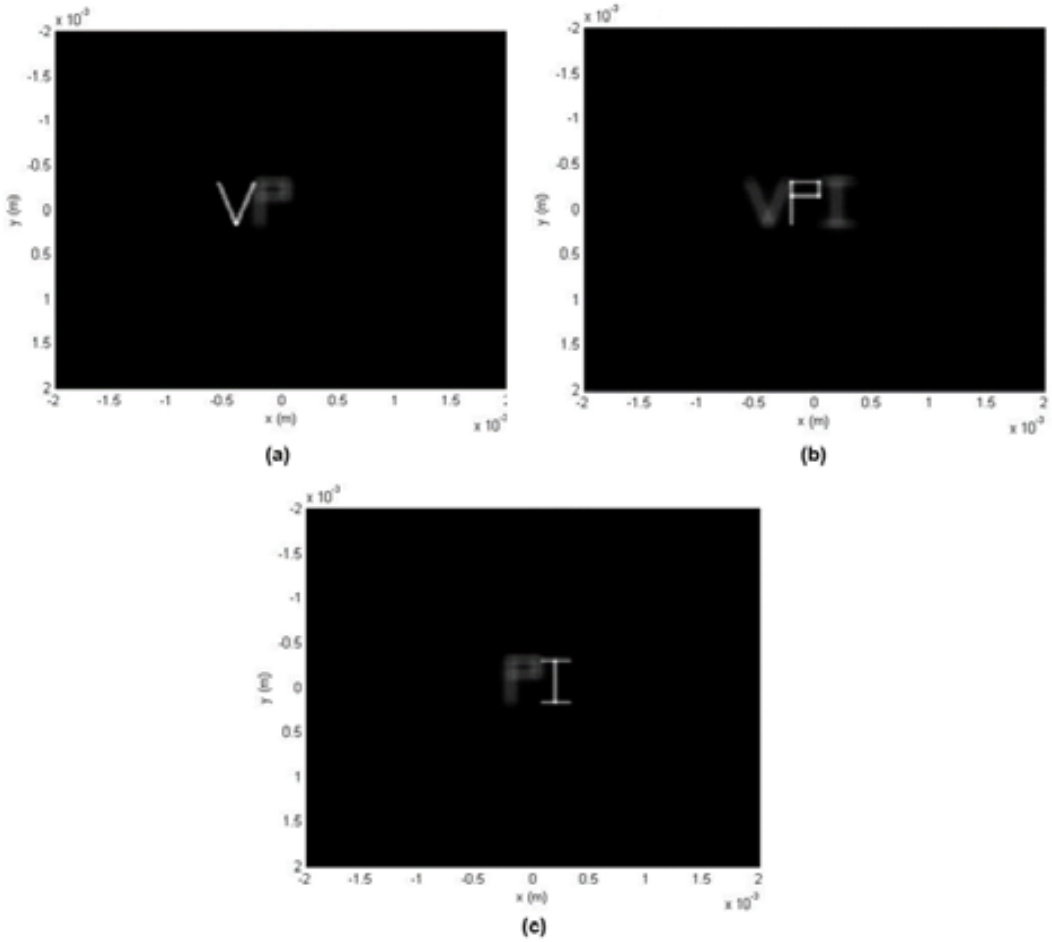

Figure 12 Reconstructed z_i planes in Eq. (59).

4 APPLICATIONS OF OPTICAL SCANNING HOLOGRAPHY

The optical system and concepts of OSH have been used in many applications in recent years including 3-D holographic microscopy, optical recognition of 3-D objects, 3-D optical remote sensing, 3-D holographic television and display, and 3-D optical scanning cryptography. The mathematics and principles of optical coding and decoding are presented in Section 4.1. A circular dammann grating is used as a coding pupil in a scanning imaging system to demonstrate optical coding of a planar object as simulated in Section 4.1.1. Section 4.1.2 presents the mathematical theory, computer simulation, and optical experiment scheme for achieving 3-D optical coding by adding a CDG to the traditional OSH system. The out-of-focus contributions from adjacent planes in the sectional-image reconstruction are attempted to be reduced through the introduction of a random pupil in the OSH system as discussed in Section 4.2. The mathematical concepts are then implemented in numerical routines for removal of out-of-focus noise in optical sections as presented in Section 4.2.1. Further analysis is conducted in Section 4.2.2 to investigate the influence of errors on the quality of the optical-section reconstruction.

4.1 Optical Coding

The previous chapter illustrated how the choice of pupil and mask results in different coherency properties. Similarly, the choice of aperture such that it has desirable autocorrelation or cross-correlation properties allows for a coded image to be decoded. Thus, the original image can be recovered in a hybrid system using digital techniques to process data recorded by the optical system. Encryption in the optical domain is intuitive as information such as images already exist in this domain and can be efficiently used for large volumes of information such as 3-D objects.

Assuming a coding function is given by $c(x,y)$ and the original object by $o(x,y)$ the two can be related into an equation for a coded image, $i_c(x,y)$ as

$$i_c(x,y) = o(x,y) \otimes c(x,y). \tag{58}$$

The image can be decoded by convolving the coded image with a decoding function given by $d(x,y)$ which results in

$$i_d(x,y) = i_c(x,y) \otimes d(x,y). \tag{59}$$

Substituting Eq. (59) into Eq. (58) gives

$$i_d(x,y) = i_c(x,y) \otimes d(x,y) = o(x,y) \otimes c(x,y) \otimes d(x,y). \tag{60}$$

In Eq. (60), $c(x,y) \otimes d(x,y)$ is the point spread function (PSF) of the overall system and when selected such that the Delta reconstruction condition applies

$$c(x,y) \otimes d(x,y) = \delta(x,y), \tag{61}$$

where $\delta(x,y)$ is the 2-D delta function then, Eq. (60) becomes

$$i_d(x,y) = o(x,y) \otimes \delta(x,y) = o(x,y). \tag{62}$$

Thus, via the convolution property of a delta function in Eq. (62) the original object $o(x,y)$ is recovered. The task of recovering the original object centers on designing the coding and decoding functions such that the condition in Eq. (61) is satisfied.

4.1.1 MATLAB Simulation: Optical Coding with Planar Object

An impulse ring was simulated by Doh et al. (2009) [5] for the coding and decoding functions where approximate satisfaction of the Delta reconstruction condition enabled successful demonstration of optical sectioning. This work also investigated the use of a circular dammann grating (CDG) as a means to implement the coding function in an optical system as it produces a set of uniform-intensity impulse rings at the focal plane [5]. The optical system used in this setup is in effect an idealized version of a conventional incoherent laser-scanning image processer as seen in Figure 13 [1].

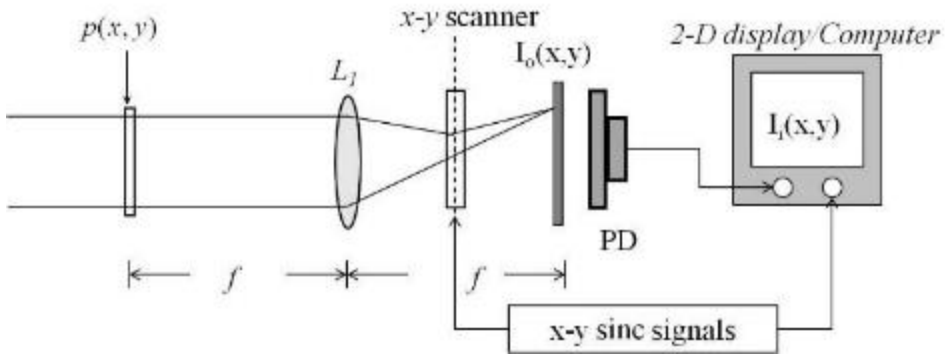

Figure 13 Conventional Incoherent laser-scanning image processor. [Used with permission]

The system relates the input intensity $I_i(x,y)$ to the output intensity $I_o(x,y)$ by [5]

$$I_i(x,y) = \mathrm{ipsf}(x,y) \otimes I_o(x,y), \tag{63}$$

where $\mathrm{ipsf}(x,y)$ is given by the absolute square of the Fourier transform of the pupil function, $p(x,y)$ i.e.

$$\mathrm{ipsf}(x,y) = \left|\mathcal{F}\{p(x,y)\}\right|^2 = \left|P\left(\frac{x}{\lambda f}, \frac{y}{\lambda f}\right)\right|^2. \tag{64}$$

In order to code $I_o(x,y)$ according to the image coding scheme discussed above, a scanning-impulse ring at the back focal plane of lens L_1 must be realized. A CDG placed in the pupil plane of the scanning system would accomplish this as it is a binary phase grating (0 and π) with circular symmetry that produces a set of uniform-intensity impulse rings at the focal plane as seen in Figure 14 [7].

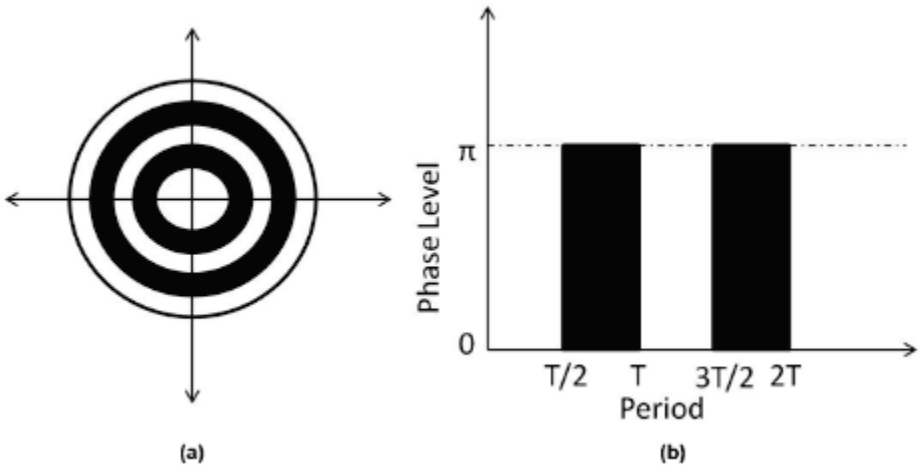

Figure 14 (a) Illustration of binary phase (0,π) CDG and (b) cross section.

A first-order CDG or one that produces only one uniform-intensity impulse ring in the focal plane is simulated in the system with a lens of focal length $f = 7.5cm$, a laser of wavelength $\lambda = 0.6318\mu m$, and a CDG with period $T = 80cm$ and limiting circular aperture diameter of $7mm$. The measured ring distribution in Figure 15 as measured by Doh et al. (2009) [5] was achieved by placing a pinhole of diameter approximately $0.038mm$ in front of the focal plane. The resulting uniform-intensity impulse ring is called an annular beam and is used to scan the input image in two dimensions to optically code the image.

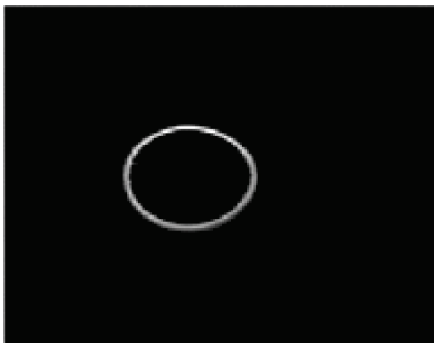

Figure 15 Annular beam (focal plane distribution due to the first-order CDG). [Used with permission]

A transparency of the letters “VT” of size $4mm \times 5mm$ on an opaque background is used as the input object by Doh et al. (2009) [5]. The size of the letters were designed to be smaller than the size of the scanning beam so as to minimize effects from the PSF of the overall system. Results from scanning the transparency by a sharply focused Gaussian laser beam are shown in Figure 16(a) and for comparison the coded output that results when the object is scanned by the annular beam are shown in Figure 16(b). The digitally decoded image using an annular beam for the coding and decoding function for the coded image given by Figure 16(b) is shown in Figure 16(c).

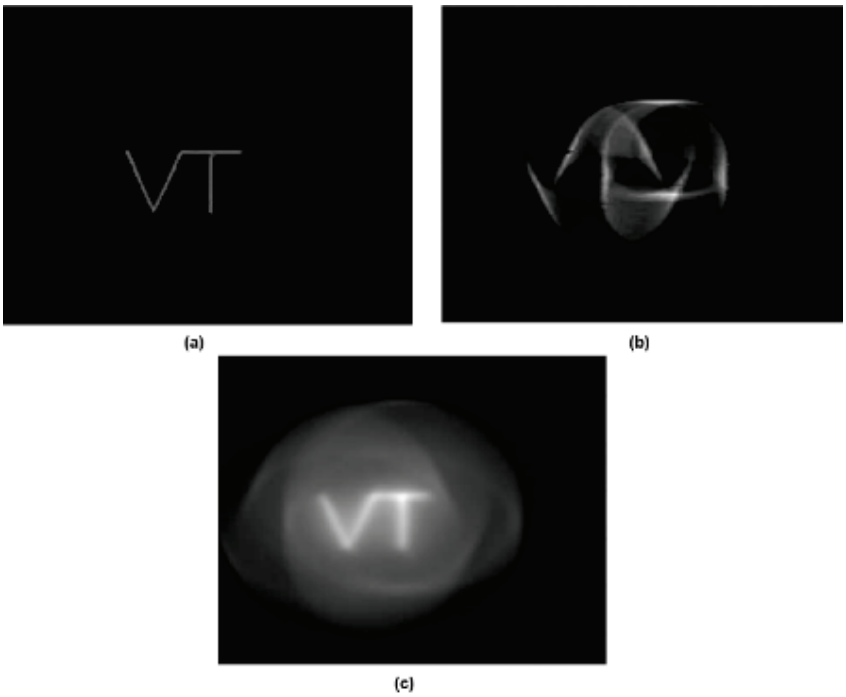

Figure 16 (a) Original "VT" image, (b) optically coded image and (c) digitally decoded image. [Used with permission]

The results indicate that the desired size of the coding ring is larger than the object however this comes at a cost of increased attenuation of information in the decoded image at higher frequencies. This can be compensated for using simple inverse filtering:

$$\text{inverse filtered decoded image} = \mathcal{F}^{-1}\left\{\mathcal{F}\left\{i_d\right\}/\mathcal{F}\left\{\text{ipsf}\right\} + \epsilon\right\}, \tag{65}$$

where ϵ is a small constant and the $\text{ipsf}\,(x, y)$ is known. The effectiveness of the proposed inverse filter is first demonstrated when a small ring is used for coding. From data captured by Doh et al. (2009) [5], the filtered, decoded image is presented in Figure 17(d) for an original image of Figure 17(a) and coded image of Figure 17(c).

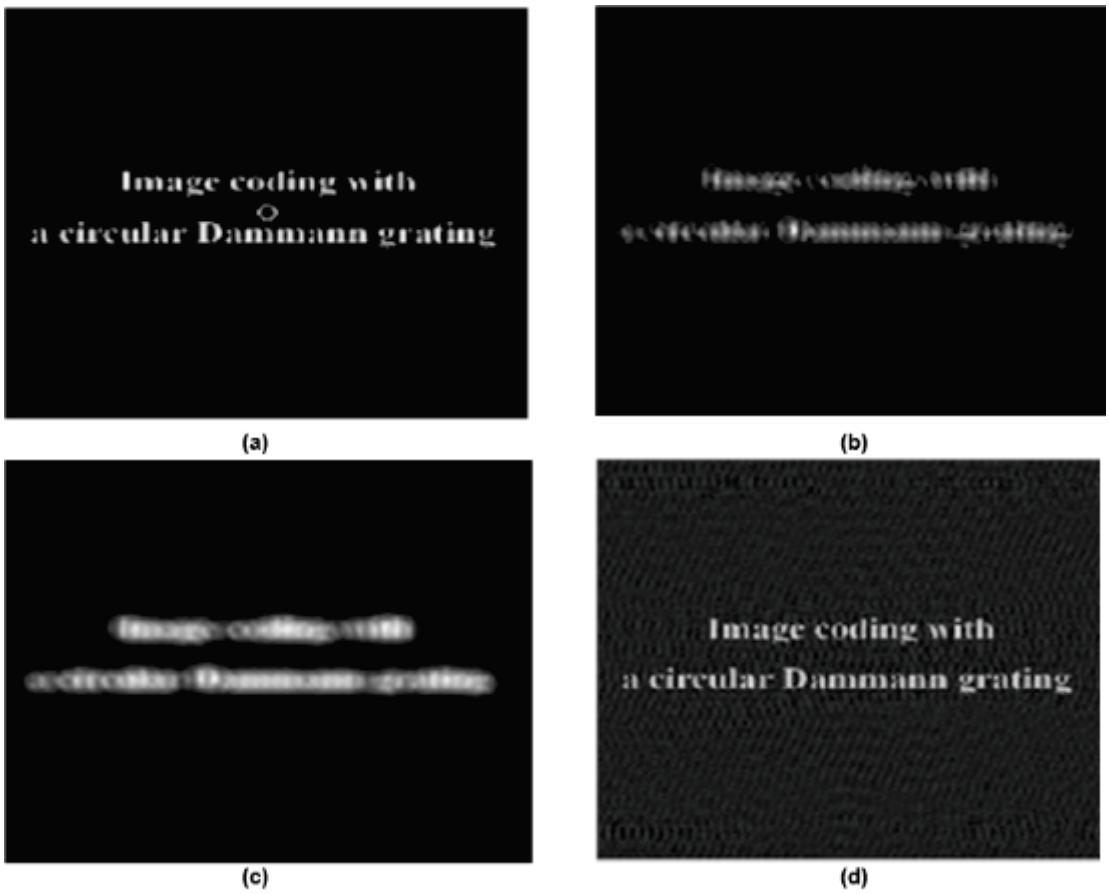

Figure 17 (a) Original image with small ring for scale, (b) coded image, (c) decoded image and (d) inverse filter of coded image shown in (c). [Used with permission]

The results in Figure 18 demonstrate filtering using data recorded by Doh et al. (2009) [5] when a larger ring is used in the coding process. Comparing the decoded images in Figure 17(c) and Figure 18(c) as the size of the ring increases the text the decoded image is restored and the edges of the image sharpened.

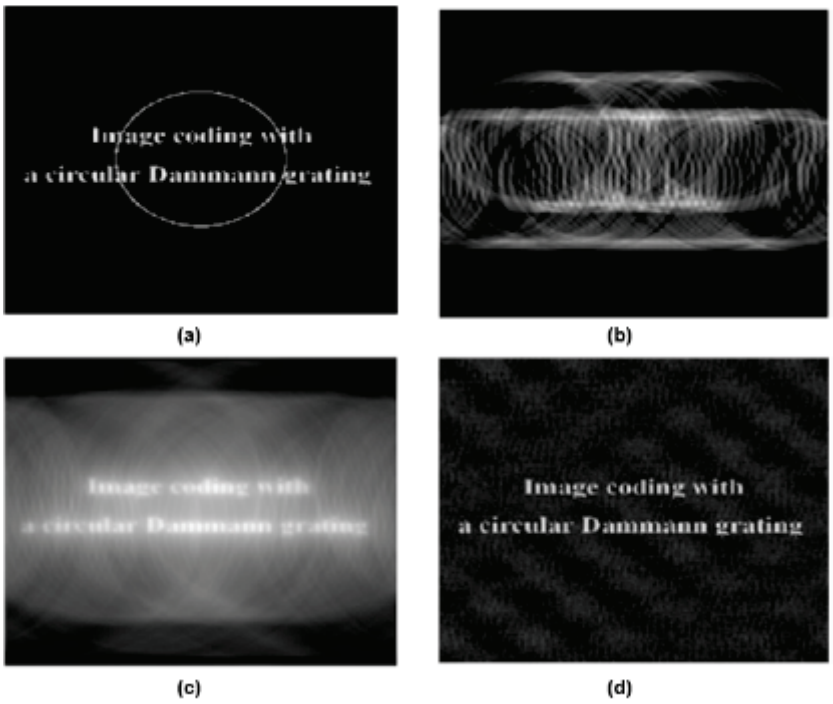

Figure 18 (a) Original image with big ring for scale, (b) coded image, (c) decoded image and (d) inverse filter of decoded image shown in (c). [Used with permission]

Applying the inverse filtering approach to the decoded image in Figure 16(c) produces the result in Figure 19. It is important to note that while using annular beams from a CDG as coding and decoding functions has been demonstrated in simulation, the realization in a physical system is limited by the resolution of the coding/decoding system which depends on how thin the ring can be made.

Figure 19 Inverse filter of Figure 16(c). [Used with permission]

4.1.2 Experiment: 3-D Optical Coding with Optical Scanning Holography

In order to extend the process mentioned above to three-dimensions, consider Eq. (63) and the use of OSH in the coding process [6]. The first pupil function $p_1(x,y)$ is assumed to be specified by the user while the second pupil $p_2(x,y)$ remains a delta function as in typical holographic systems. Thus, Eq.(40) becomes

$$\begin{aligned} OTF_{coding}\left(k_x,k_y;z\right) &= \exp\left[-j\frac{z}{2k_0}\left(k_x^2+k_y^2\right)\right]\times p_1^*\left(-\frac{fk_x}{k_0},-\frac{fk_y}{k_0}\right) \\ &= OTF_{OSH}\left(k_x,k_y;z\right)\times p_1^*\left(-\frac{fk_x}{k_0},-\frac{fk_y}{k_0}\right) \end{aligned} . \quad (66)$$

From Eq. (66), note that the first term is the OTF for holographic recording and the second term can be considered as the mechanism for coding the object's spectrum before the holographic recording process. In other words, when $p_1 = 1$ there is no coding and the process instead yields a holographic recording. A merit of optical encoding is that the object information can be disturbed optically so that it cannot be easily identified without the decoding process. For an arbitrary-encoding pupil function, $OTF_{coding}\left(k_x,k_y;z\right)\times OTF_{OSH}^*\left(k_x,k_y;z\right)$ is not unity and the object information cannot be decoded directly using the $OTF_{OSH}\left(k_x,k_y;z\right)$ in Eq. (51). Similar to the previous simulation, decoding the hologram could be accomplished by inverse filtering via Eq. (65) but this is not convenient as the denominator depends on the reconstructed distance z. This is particularly burdensome if the object target is 3-D when multiple decoding functions are necessary for accurate reconstruction. Moreover, inverse filtering will induce additional high spatial-frequency noise in the reconstructed image. Alternatively, the coding function can be directly used to retrieve the coded hologram provided the coded optical transfer function exhibits the property

$$OTF_{coding}\left(k_x,k_y;z\right)\times OTF_{coding}^*\left(k_x,k_y;z\right)\approx 1 . \quad (67)$$

These properties can be realized in an optical system by including a CDG as the first pupil function $p_1(x,y)$ with a decoding process that consists of two measurements from the OSH system in Figure 20. The first measurement is for coding the object and the second for measuring the impulse response for decoding. For the remainder of this discussion parameters in the coding stage will be denoted with a "c" subscript such as p_{1c} and p_{2c} with a "d" subscript for the decoding stage. Simulations were conducted by Shinoda et al. (2011) [6] and successfully demonstrated encoding

of a three-dimensional object using the circular dammann grating and decoding or reconstruction of the 3-D object using traditional digital holographic processes.

The experimental optical system as illustrated in Figure 20 includes laser frequency modulated by $\Omega/2\pi$ set at 50 KHz and the optical elements, $BE1$ and $BE2$, are two beam expanders to provide uniform laser beam for the circular dammann grating CDG and the object, respectively. The coding pupil is the CDG located at the front focal plane of lens L_1 and the other pupil is effectively a pinhole. Lens L_2 collects the light energy onto Photodetector 2 which provides the measured electrical signal, V_{meas}, as an input to the lock-in amplifier. The mirror shown in the bottom of the figure is used to direct the two laser beams combined by the BS just after Lens L_1 to Photodetector 1, which provides a reference heterodyne signal V_r at 50KHz. The band-pass filter rejects the DC electrical signal from Photodetector 1 and allows the heterodyne signal to go to the reference input of the lock-in amplifier.

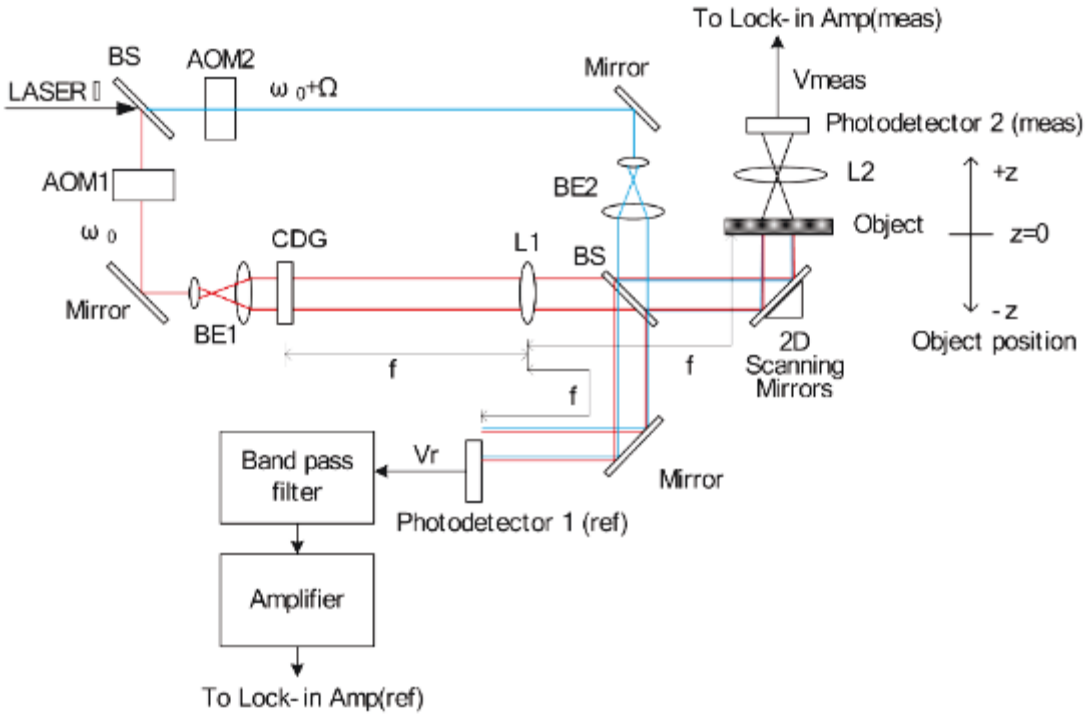

Figure 20 Optical system with CDG added to the optical path. [Used with permission]

The object used in this system are the letters "VT" located at $z_0 = 4.5cm$ and approximately $1in \times 1in$ on an opaque background with an opening linewidth of approximately $100\mu m$. Figure 21(a) and (b) show the real and imaginary part of a coded complex hologram, respectively from the recordings of Shinoda et al. (2011) [6], illustrating the outputs given by Eq.

(34) for the “VT” object. Figure 22 shows the Fresnel diffraction of the coded complex hologram recorded by Shinoda et al. (2011) [6] where the reconstruction of the coded complex hologram using traditional techniques yields an unrecognizable original object due to the coding process. Reconstruction results can be improved by measuring the impulse response of the system by placing a pinhole of diameter $0.28mm$ at the object position which is shown for data from Shinoda et al. (2011) [6] in Figure 23. This impulse response is then used to decode the complex hologram, the results of which are presented in Figure 24 featuring the original object clearly reconstructed at the correct location, $z_0 = 4.5cm$.

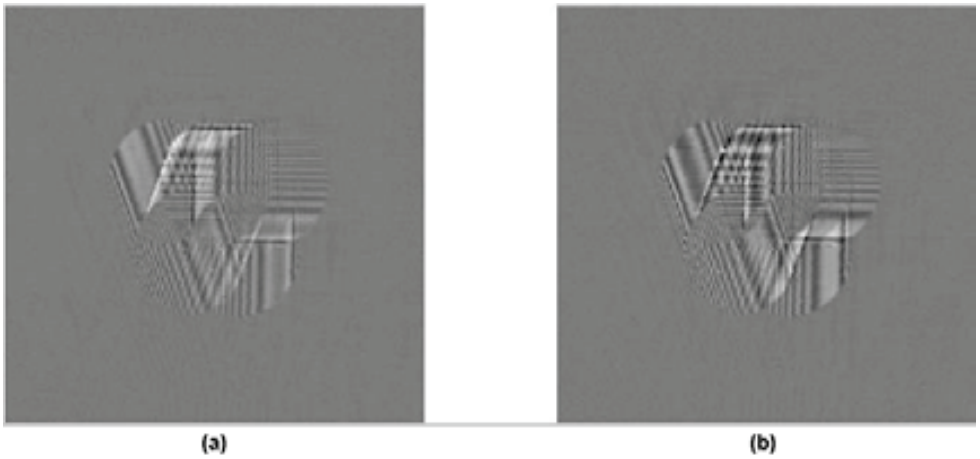

Figure 21 (a) Real and (b) Imaginary part of a coded complex hologram. [Used with permission]

Figure 22 Using Fresnel diffraction to reconstruct the coded complex hologram shown in Figure 21. [Used with permission]

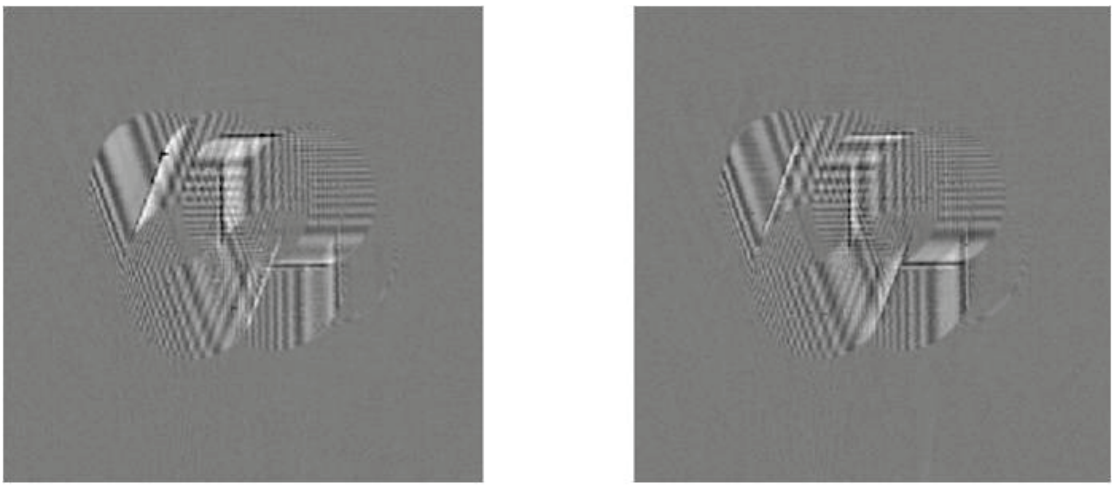

Figure 23 (a) Real and (b) Imaginary part of pinhole hologram. [Used with permission]

Figure 24 Reconstruction of the complex hologram shown in Figure 21 using the pinhole in Figure 23. [Used with permission]

This demonstrates decoding of a complex hologram but a 3-D complex coding capability to code a 3-D object in a single scan has yet to be seen. Instead of placing the "V" and "T" in the same plane, Shinoda et al. (2011) [6] made recordings placing the former at $z_0 = 0cm$ and the latter at $z_0 = 4.5cm$. These locations create a volume to be scanned instead of a plane. The coded hologram of the new object is shown in Figure 25. Previously the pinhole hologram was measured at $z_0 = 4.5cm$ which is used to reconstruct the "T" plane but in order to reconstruct the "V" plane

a measurement must also be taken at $z_0 = 0cm$which is shown in Figure 26. Figure 27 shows the decoded images using the Shinoda et al. (2011) [6] pinhole holograms shown in Figure 23 and Figure 26 such that the “V” and “T” are correctly decoded at their respective planes.

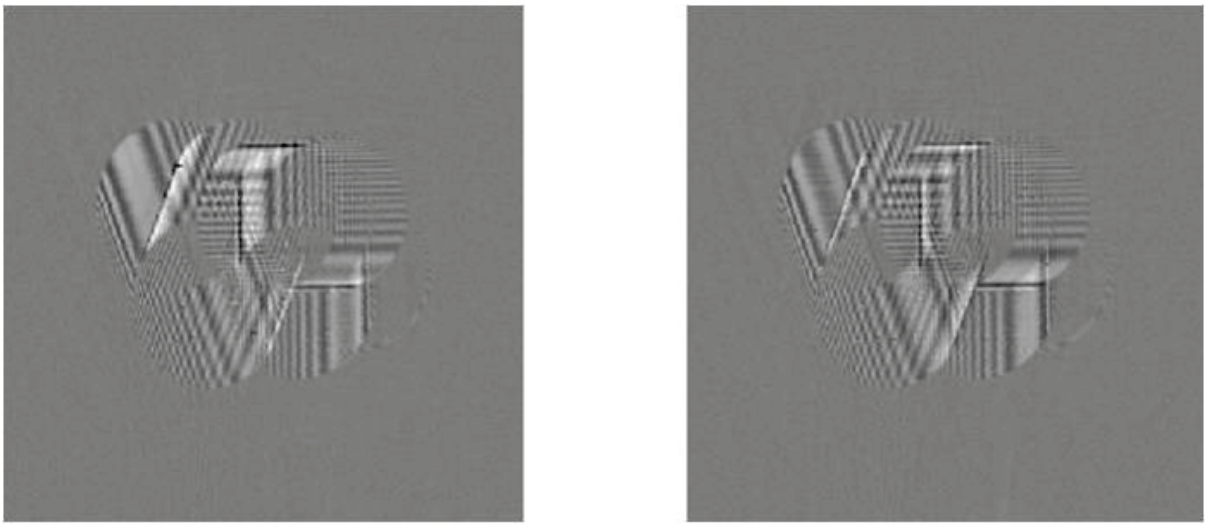

Figure 25 (a) Real and (b) Imaginary part of a coded complex hologram with “V” located at $z_0 = 0cm$ and “T” at $z_0 = 4.5cm$. [Used with permission]

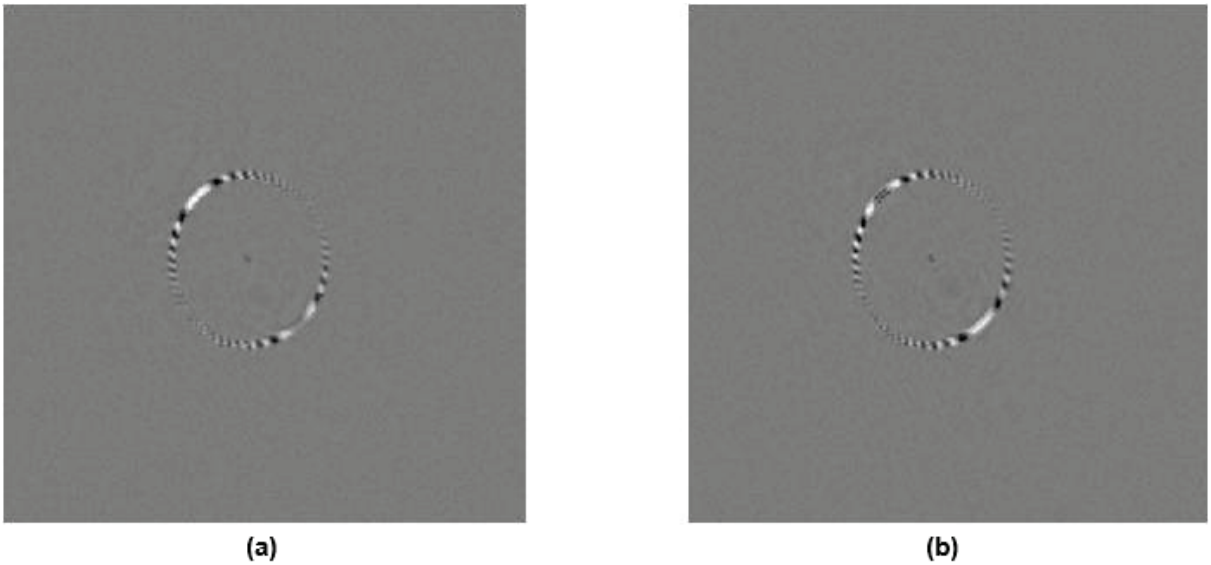

Figure 26 (a) Real and (b) imaginary part of the pinhole hologram measured at $z_0 = 0cm$. [Used with permission]

Figure 27 Reconstruction using the pinhole holograms shown Figure 23 and Figure 26 (a) Shows the "V" reconstructed correctly at $z_0 = 0cm$ and (b) Shows the "T" reconstructed correctly at $z_0 = 4.5cm$. [Used with permission]

Now that the ability to code and decode 3-D images using an OSH system and a pupil function different from those traditionally used in OSH has been demonstrated, it remains to parlay these results to demonstrate optical-section reconstruction without defocus noise.

4.2 Random Pupil and Optical Scanning Holography

The previous demonstration utilized a specific pupil, a CDG, in the OSH system to reconstruct optical sections from a hologram. However it remains to be seen how to achieve reconstruction of the sectional image such that it does not contain out-of-focus haze. The work by Xin et al. (2010) [7] proposed the use of a random-phase pupil in the OSH system so as to transfer the out-of-focus sectional images into speckle-like patterns which can then be suppressed by overlaying multiple section images. The authors found that the sectional separation can be adjusted by using lenses with different numerical aperture (NA), this is advantageous as compared to recent algorithmic approaches previously mentioned because it is not computationally intensive.

In the coding stage, the output of OSH system is related to the input object $I(x, y; z)$ located at a coding distance $z = z^c$ as follows [1,23]:

$$i(x, y) = \mathcal{F}^{-1}\left\{\mathcal{F}\left\{I(x, y; z = z^c)\right\}\Big|_{k_x, k_y} \times OTF_\Omega(k_x, k_y; z = z^c)\right\}, \tag{68}$$

where $OTF_\Omega(k_x, k_y; z = z^c)$ is the optical transfer function of the system given by Eq. (29).

For decoding, the same optical system shown in Figure 1 is used but a pinhole serves as the input object located at the decoding distance $z = z^d$ away from lens L_1 , i.e., let $I(x, y; z) = \delta(x, y; z^d)$ in Eq. (68). Thus the output of the OSH system, according to Eq. (68), is given by $\mathcal{F}^{-1}\{OTF_\Omega(k_x, k_y; z = z^d)\}$. The system output is the impulse response of the optical system when p_{1d} and p_{2d} are used which when coupled with Eq. (68) from the coding stage gives the final output of an overall two-stage system as

$$\Phi_{out}(x, y) = \mathcal{F}^{-1}\left\{\mathcal{F}\{I(x, y; z^c)\}\big|_{k_x,k_y} \times OTF_\Omega(k_x, k_y; z^c) \times OTF_\Omega(k_x, k_y; z^d)\right\}. \quad (69)$$

Recall that in traditional OSH, the pupils are chosen as $p_{1c}(x, y) = \delta(x, y)$ and $p_{2c}(x, y) = 1$ in the coding stage, and $p_{1d}(x, y) = 1$ and $p_{2d}(x, y) = \delta(x, y)$ for the decoding stage. With this selection of the pupils, Eq. (69) becomes [1,24]

$$\Phi_{out}(x, y) = \mathcal{F}^{-1}\left\{\mathcal{F}\{I(x, y; z^c)\}\big|_{k_x,k_y} \times \exp\left[j\frac{z^d - z^c}{2k_0}(k_x^2 + k_y^2)\right]\right\}. \quad (70)$$

It can thus be seen that the object image $I(x, y; z^c)$ can be recovered perfectly when the condition $z^d = z^c$ is met, such that when the pinhole is located at $z^d = z^c$ one measures the impulse response for decoding. However, if a multi-section object is placed in the coding stage of the system, only the sectional image located at $z^i = z^d$ will be recovered sharply with additional energy from the other sections manifesting as defocus haze given by

$$\Phi_{haze}(x, y) = \sum_{z^i \neq z^d} \mathcal{F}^{-1}\left\{\mathcal{F}\{I(x, y; z^i)\}\big|_{k_x,k_y} \times \exp\left[j\frac{z^d - z^i}{2k_0}(k_x^2 + k_y^2)\right]\right\}. \quad (71)$$

This haze exhibits as defocus images from other sections and is difficult to eliminate. If the defocus images can be transferred into speckle then, the noise may be easily eliminated by overlaying multiple section images. For this purpose, in the coding stage choose $p_{2c}(x, y) = 1$ and $p_{1c}(x, y) = \exp[j2\pi s(x, y)]$, where $s(x, y)$ denotes an independent random function uniformly distributed in the interval $[0, 1]$. Then in the decoding stage, choose $p_{1d}(x, y) = 1$ and $p_{2d}(x, y)$ such that the following condition is met

$$p_{1c}^*(-x, -y)\, p_{2d}(x, y) = 1. \quad (72)$$

Using these choices for pupils in Eq. (4) gives

$$\Phi_{out}(x)=\sum_i \mathcal{F}^{-1}\Bigg\{\mathcal{F}\{I(x,y;z^i)\}\big|_{k_x,k_y}\times\mathcal{F}^*\Bigg\{\Bigg[P_{1c}\left(\frac{-z^ik_x}{f}\right)P_{2d}^*\left(\frac{z^dk_x}{f}\right)$$
$$\times\exp\left(-j2\pi\frac{z^d}{f}k_xx_0\right)\Bigg]\otimes\Omega\text{sinc}\left(\Omega\frac{k_0x_0}{f}\right)\exp\left(j\frac{z^d-z^i}{2k_0}k_x^2\right)+R(k_x)\Bigg\}\Bigg\}. \quad (73)$$

Using phase retrieval algorithms $p_{1c}(x,y)$ and $p_{2d}(x,y)$ can be iteratively adjusted to meet Eq. (72) and the following [13, 14]:

$$P_{1c}\left(\frac{-z^ik_x}{f},\frac{-z^ik_y}{f}\right)P_{2d}^*\left(\frac{-z^dk_x}{f},\frac{-z^dk_y}{f}\right)=1. \quad (74)$$

From Eq. (73) and (74), it can be seen that the sectional image $(x,y;z^d)$ will be recovered perfectly when $z^i=z^d$. For $z^i\neq z^d$, the output of Eq. (73) will depend on the distribution of $P_{1c}\left(-z^ik_x/f,-z^ik_y/f\right)$and $P_{2d}\left(-z^dk_x/f,-z^dk_y/f\right)$. The threshold value of $|\,z^d-z^i\,|$ is estimated as

$$\left|z^d-z^i\right|=a\frac{N^2\lambda}{\pi D^2/f^2}, \quad (75)$$

where D is the pupil size for all the pupils used and N^2 is the sampling number of the pupil. When the difference between z^d and z^i is large enough and $a>1.0e-4$ for $N=512$,$f=7.5cm$, $D=2cm$, $k_0=2\pi/\lambda$, and $\lambda=0.6328\mu m$, the probability distribution becomes a Gaussian curve. Thus, $P_{1c}\left(\frac{-z^ik_x}{f},\frac{-z^ik_y}{f}\right)P_{2d}^*\left(\frac{-z^dk_x}{f},\frac{-z^dk_y}{f}\right)\exp\left[j\frac{z^d-z^i}{2k_0}\left(k_x^2+k_y^2\right)\right]$ will act as a random function and leads to the corresponding terms in Eq. (73) exhibiting as speckle-like noise as output [25, 26].

4.2.1 MATLAB Simulation: Random Pupil and Optical Scanning Holography

The threshold value in Eq. (75) represents the minimum sectional separation between image sections to retrieve one sectional image clearly using the system in Figure 20 such that there is no out-of-focus haze. The value of a may be determined depending on the random-phase pupil; however, for these demonstrations the value is set at $1.0e-4$. Simulations have shown that for a distance that is larger than that given by Eq. (75), the energy of the out-of-focus haze actually disperses over the entire in-focus plane forming speckle-like patterns. Using several independent random-phase pupils to obtain the speckle-like patterns and overlaying them, then the final grey

value on the whole plane will tend to be same everywhere because they are random with same probability [27, 28]. This means the speckle-like patterns can be eliminated by overlaying multiple section images.

The proposed methodology is used to demonstrate the reconstruction of sectional images encoded in a hologram. Figure 28 (a) shows a multi-section object which contains three elements at $z_1 = 9mm$, $z_2 = 10mm$, and $z_3 = 11mm$. A laser of wavelength $0.6328\mu m$ and a lens of focal length $7.5cm$ is used. The size of pupils are $2cm \times 2cm$ and the object images are sampled by 512×512 pixels. Reconstruction results from conventional holographic reconstruction focusing on section $z^d = z_2$ and $z^d = z_3$ with data from Xin et al. (2010) [7] are shown in Figure 28 (b) and (c), respectively.

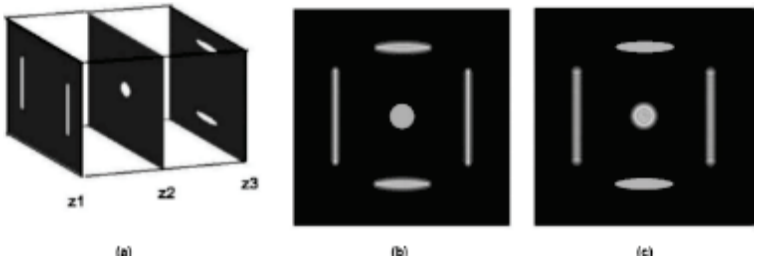

Figure 28 (a) Multi-section object used in the system, (b) reconstruction with image section z_2 in focus and (c) reconstruction with section image z_3 in focus. [Used with permission]

The reconstruction results from the proposed random-phase pupil method for $z^d = z_2$ and $z^d = z_3$ are shown in Figure 29 (a) and (c), respectively. Note that the out-of-focus haze shown in Figure 28 (b) has been dispersed into speckle-like patterns over the focused plane shown in Figure 29 (a) and (c). Figure 29 (b) and (d) are the results from overlaying 10 section images obtained from 10 independent random-phase pupils and illustrates how overlaying multiple-section images can effectively eliminate the speckle-like patterns from the in-focus plane.

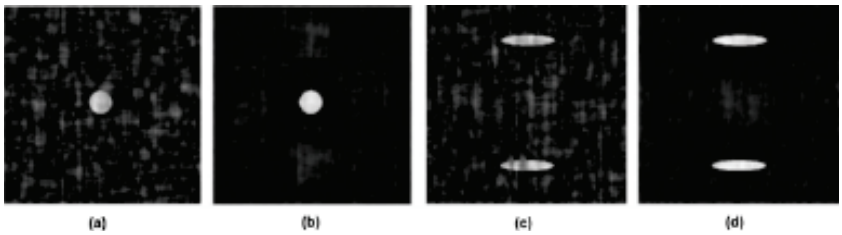

Figure 29 (a) Reconstruction by proposed method with image section z_2 in focus, (b) average results for section z_2, (c) reconstruction by proposed method with image section z_3 in focus and (d) average results for section z_3. [Used with permission]

From the previous discussion, the introduction of a random-phase pupil into OSH has great impact on the sectional image reconstruction through the matching of the decoding and encoding pupil functions. However, for actual application, the decoding and encoding pupil functions are usually not strictly matched due to the sensitivity of the random-phase pupil and the need to take separate encoding and decoding measurements. Two kinds of deviation errors are common, the first occurs in the lateral-pixel position and the second in the pixel value of the decoding pupil function. Wu et al. (2013) [8] analyzed the characteristics of the recovered image when the decoding pupil function results in errors either in the position of lateral direction or in the value of the pixels.

A depiction illustrating lateral-orientation deviation in the OSH system is shown in Figure 30. For simplicity, one-dimensional notation will be used in the following discussion. Denote a shift to the random-phase pupil $p_{2d}(x)$, for example, a landscape-orientation shift x_0 as $p_{2d}^{\Delta}(x)$. The limit of pupil size in the x direction is $rect(x/\Omega)$ such that $p_{2d}^{\Delta}(x)$ can be expressed as:

$$p_{2d}^{\Delta}(x) = p_{2d}(x - x_0)\, rect(x/\Omega), \tag{76}$$

where $\Omega \leq 1$.

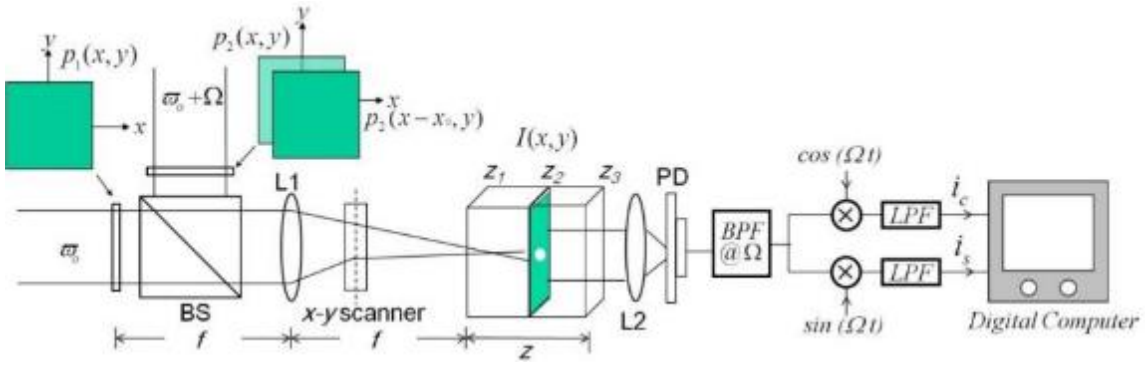

Figure 30 Schematic of OSH system when a lateral-orientation deviation occurs. $p_{1d}(x)$ and $p_{2d}(x)$ are decoding pupil functions; $p_{2d}(x - x_0)$ is $p_{2d}(x)$ with a landscape-orientation shift x_0.

According to the shift characteristics of the Fourier transform,

$$P_{2d}^{\Delta}\left(\frac{z^d k_x}{f}\right) = \left[P_{2d}\left(\frac{z^d k_x}{f}\right)\exp\left(-j2\pi\frac{z^d}{f}k_x x_0\right)\right] \otimes \Omega\mathrm{sinc}(\Omega k_x). \tag{77}$$

The sectional-image reconstruction during a shift to the random-phase pupil $p_{2d}(x)$ from Eq. (75) and Eq. (73) is then:

$$\Phi_{out}(x)=\sum_i \mathcal{F}^{-1}\Bigg\{\mathcal{F}\{I(x,\ y;z^i)\}\big|_{k_x,k_y}\times\mathcal{F}^*\Bigg\{P_{1c}\Big(\frac{-z^ik_x}{f}\Big)P_{2d}^{\triangle *}\Big(\frac{z^dk_x}{f}\Big)\times\exp\Big(j\frac{z^d-z^i}{2k_0}k_x^2\Big)\Bigg\}\Bigg\}$$
$$=\sum_i \mathcal{F}^{-1}\Bigg\{\mathcal{F}\{I(x,y;z^i)\}\big|_{k_x,k_y}\times\mathcal{F}^*\Bigg\{P_{1c}\Big(\frac{-z^ik_x}{f}\Big)\Big[P_{2d}^{*}\Big(\frac{z^dk_x}{f}\Big)\times\exp\Big(-j2\pi\frac{z^d}{f}k_xx_0\Big)\Big]\otimes\Omega\mathrm{sinc}(\Omega k_x)\exp\Big(j\frac{z^d-z^i}{2k_0}k_x^2\Big)\Bigg\}\Bigg\}$$
$$=\sum_i \mathcal{F}^{-1}\Bigg\{\mathcal{F}\{I(x,y;z^i)\}\big|_{k_x,k_y}\times\mathcal{F}^*\Bigg\{P_{1c}\Big(\frac{-z^ik_x}{f}\Big)\sum_\zeta\Big[P_{2d}^{*}\Big(\frac{z^dk_x}{f}\Big)\times\exp\big(-j2\pi\frac{z^d}{f}k_xx_0\big)\Big]\otimes\Omega\mathrm{sinc}(\Omega[k_x-\zeta])\exp\Big(j\frac{z^d-z^i}{2k_0}k_x^2\Big)\Bigg\}\Bigg\}. \quad (78)$$

Removing the term for $\zeta=k_x-(k_0x_0/f)$ from the summation $\sum_\zeta$ in the brackets $\{\cdot\}$ [29, 30], Eq. (78) can be expressed as:

$$\Phi_{out}(x)=\sum_i \mathcal{F}^{-1}\Bigg\{\mathcal{F}\{I(x,y;z^i)\}\big|_{k_x,k_y}\times\mathcal{F}^*\Bigg\{\Big[P_{1c}\Big(\frac{-z^ik_x}{f}\Big)P_{2d}^{*}\Big(\frac{z^dk_x}{f}\Big)\times\exp\Big(-j2\pi\frac{z^d}{f}k_xx_0\Big)\Big]\otimes\Omega\mathrm{sinc}\Big(\Omega\frac{k_0x_0}{f}\Big)\exp\Big(j\frac{z^d-z^i}{2k_0}k_x^2\Big)+R(k_x)\Bigg\}\Bigg\}. \quad (79)$$

The term $R(k_x)$ represents the term for $\zeta\neq k_x-(k_0x_0/f)$ and its inverse Fourier transform is $r(x)$. Since $p_{1c}(x)$ and $p_{2d}(x)$ are random functions $r(x)$ is a random function. When $z^i=z^d$ the reconstructed sectional image is

$$\Phi_{out}(x)=\sum_i \mathcal{F}^{-1}\Bigg\{\mathcal{F}\{I(x,y;z=z^d)\}\big|_{k_x,k_y}\times\mathcal{F}^*\Bigg\{\Big[P_{1c}\Big(\frac{-z^dk_x}{f}\Big)P_{2d}^{*}\Big(\frac{z^dk_x}{f}\Big)\times\exp\Big(-j2\pi\frac{z^d}{f}k_xx_0\Big)\Big]\otimes\Omega\mathrm{sinc}\Big(\Omega\frac{k_0x_0}{f}\Big)+R(k_x)\Bigg\}\Bigg\}$$
$$=\Omega\mathrm{sinc}\Big(\Omega\frac{k_0x_0}{f}\Big)I\big(x-x_0;z^d\big)+r(x) \quad .(80)$$

Thus, the energy of the reconstructed sectional image can be expressed as:

$$\left|\Phi_{out}\left(x\right)\right|^2 = \Omega^2 \mathrm{sinc}^2\left(\Omega\frac{k_0 x_0}{f}\right)\left|I\left(x-x_0;z^d\right)\right|^2 + r^{'}\left(x\right), \tag{81}$$

where $r^{'}(x)$ is a uniformly-distributed white noise[25, 30].

From Eq. (80) and Eq. (81), it can be seen that as the decoding random-phase pupil lateral-deviation distance, x_0, increases the image can still be decrypted, but the intensity of the reconstruction sectional image is attenuated. Moreover, from Eq. (80) the reconstructed image is shifted by x_0 relative to the original image.

4.2.2 MATLAB Simulation: Errors in Random Pupil and Optical Scanning Holography

The numerical simulations that follow illustrate the influence of the sectional-image reconstruction when the decoding random-phase pupil has a shift. The character "O", as shown in Figure 31 (a), is a binary image of pixels 256×256 and size $2cm \times 2cm$. The OSH system features lens L_1 of focal length $f = 7.5cm$. The sectional image at $z_d = 5mm$ is reconstructed with data from Wu et al. (2013) [8] in Figure 31 (b), (c), (d), and (e) where the decoding pupil have shifts with $(x_0 = 2mm, y_0 = 0mm)$, $(x_0 = 10mm, y_0 = 0mm)$, $(x_0 = 0mm, y_0 = 2mm)$ $(x_0 = 0mm, y_0 = 10mm)$, respectively. From this figure, observe that when the decoding pupil function has a small, lateral shift x_0 or y_0, the reconstructed sectional image will also shift x_0 or y_0 in the lateral direction. Additionally, as the lateral deviation of the decoding pupil increases, the reconstructed image sharpness decreases until the original object can no longer be easily identified.

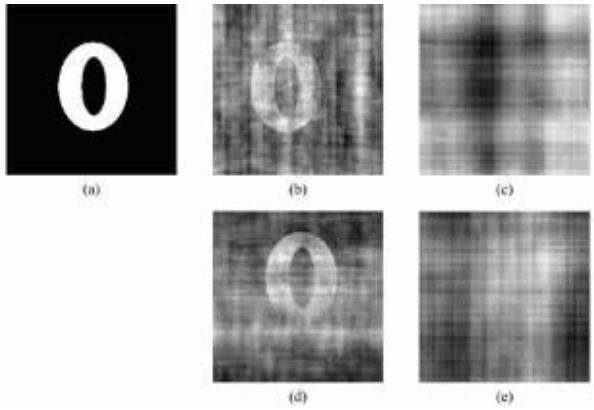

Figure 31 Sectional-image reconstruction with the decryption pupil function lateral deviation. (a) original image, (b) $(x_0 = 2mm, y_0 = 0mm)$, (c) $(x_0 = 10mm, y_0 = 0mm)$, (d) $(x_0 = 0mm, y_0 = 2mm)$, and (e) $(x_0 = 0mm, y_0 = 10mm)$. [Used with permission]

The other reconstruction error that can occur is in the pixel value of the decoding random-phase pupil. The phase function of the decoding pupil can be given by:

$$p_{2d}^{\Delta}(x) = p_{2d}(x) + p_{3d}(x), \tag{82}$$

where $p_{3d}(x)$ is a random function. According to the linear superposition properties of the discrete Fourier transform, it is known that

$$P_{2d}^{\Delta}\left(\frac{z^d k_x}{f}\right) = P_{2d}\left(\frac{z^d k_x}{f}\right) + P_{3d}\left(\frac{z^d k_x}{f}\right). \tag{83}$$

Using Eq. (73) and Eq. (83), the reconstructed sectional image can be obtained:

$$\begin{aligned}\Phi_{out}(x) = \sum_i \mathcal{F}^{-1}\Bigg\{ & \mathcal{F}\{I(x,y;z^i)\}\big|_{k_x,k_y} \times \mathcal{F}^*\Bigg\{ P_{1c}\left(\frac{-z^i k_x}{f}\right) P_{2d}^{\Delta *}\left(\frac{z^d k_x}{f}\right) \\ & \times \exp\left(-j2\pi \frac{z^d - z^i}{2k_0} k_x^2\right)\Bigg\}\Bigg\} \\ = \mathcal{F}^{-1}\Bigg\{ & \mathcal{F}\{I(x,y;z^i)\}\big|_{k_x,k_y} \times \mathcal{F}^*\Bigg\{ P_{1c}\left(\frac{-z^i k_x}{f}\right)\Bigg[P_{2d}^*\left(\frac{z^d k_x}{f}\right) \\ & + P_{3d}^*\left(\frac{z^d k_x}{f}\right)\Bigg] \exp\left(-j2\pi \frac{z^d - z^i}{2k_0} k_x^2\right)\Bigg\}\Bigg\} \end{aligned}, \tag{84}$$

and when $z^d = z^i$,

$$\Phi_{out}(x) = I(x;z^d) + I(x;z^d) \otimes p_{1c}(-x;z^d) \otimes p_{3d}^*(x;z^d). \tag{85}$$

Note that in Eq. (84) $I(x;z^d)$, $p_{1c}^*(-x;z^d)$, and $p_{3d}(x;z^d)$ are independent with each other, so their mutual convolution can be considered as random noise dependent on the original image. The same original image, variable parameters, and recordings from from Wu et al. (2013) [8] as presented in Figure 31 (a) are used for this simulation as well. Figure 32 (a), (b) and (c) show the reconstructed images for the pixel-error ratios of 1/196, 1/16 and 1/4, respectively. The sectional image can be reconstructed when errors occur in the pixel value of the decoding random-phase pupil, but as the number of pixel errors gradually increases the inductive random noise increases. As a result, the original object in the reconstructed image becomes mostly unidentifiable.

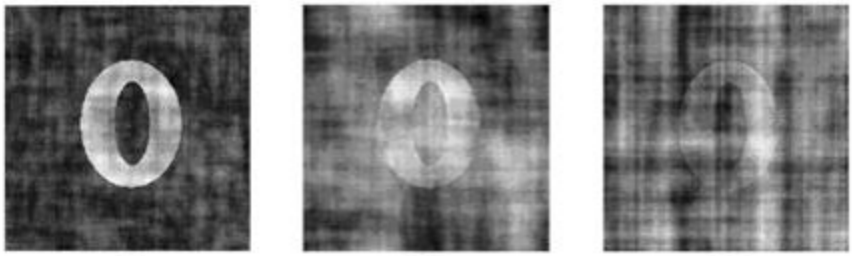

Figure 32 Reconstructed images with error pixels of decoding pupil. (a) 1/196; (b) 1/16; (c) 1/4. [Used with permission]

By adopting a random-phase pupil in the OSH sectional-image reconstruction, the sensitivity issue of traditional OSH can be effectively solved and the out-of-focus sectional image no longer manifests in the in-focus sectional image. When a small, lateral deviation occurs in the decoding pupil function, the reconstructed image will be shifted by this same amount and its intensity reduces as a function of the deviation. Additionally, the quality of the recovered image depends on the ratio of the number of pixel errors in the phase pupil and the value of the pixel error. The next chapter will provide background and mathematics for another pupil function, optical vortices.

5 OPTICAL VORTEX: CREATION AND APPLICATION

In this chapter optical vortices are introduced as a means of spatial filtering to obtain isotropic and anisotropic edge enhancement. A brief introduction to optical vortices is provided in Section 5.1 and is followed by Sections 5.2 and 5.3 which detail two common means to produce optical vortices with plane waves: spiral phase plates (SPPs) and computer-generated holograms (CGHs), respectively. The former features numerical routines to simulate isotropic and anisotropic filtering for a simple planar object. The chapter continues in Section 5.4 with a discussion of the spiral phase-kernel and a numerical routine comparing the spiral phase-kernel to a circular amplitude point spread function. Section 5.5 includes a discussion of optical vortex with Gaussian beam illumination including a MATLAB simulation implementing the filtering technique in Section 5.5.1. The final section of the chapter, Section 5.6, introduces composite vortices with MATLAB simulations. Sections 5.6.1 and 5.6.2 present and analyze the implementation of filtering techniques for various phase, topological charge, and displacement of composite vortices.

5.1 Optical Vortices and Laguerre-Gaussian Beams

The study of properties of light beams with a helical phase structure and their interference along the beam axis received much attention after the paper from Nye and Berry (1974) [31] including experimental demonstration that an optical vortex could be intentionally produced within optical fields by Vaughan and Willets (1979) [32]. The term optical vortex was introduced by Coullet, Gil, and Rocca (1989) [33] to describe the light field in a laser cavity and now finds wide use in optical science.

An optical vortex is a zero point of intensity or optical singularity of an optical field where the phase circulates around these points such that the line integral of the gradient of phase over a closed line around these points is equal to an integer multiple of 2π [34]. This can be mathematically expressed as

$$\oint_c \nabla\Phi dq = 2\pi m, \tag{86}$$

where Φ represents the local phase, $\nabla\Phi$ represents the gradient of the phase function, q is the line on a closed loop c enclosing the vortex , and m is an integer known as the topological charge or strength of the vortex.

Based on this definition, a simple case of an optical vortex is the Laguerre-Gaussian mode LG_m^0 [34]. The beam cross section under the representation of the electromagnetic field of a paraxial beam through a slowly varying complex amplitude $u(r,\theta;z)$ is

$$E(r,\theta;z) = u(r,\theta;z)\exp(jkz), \tag{87}$$

where r is the polar radius so that (r,θ) forms a polar coordinate frame, k is the wave number, and z is the propagation axis. Using Eq. (87) the LG_m^0 can be expressed by

$$u(r,\theta;z) = \frac{E_0}{\sqrt{|\,m\,|\,!}}\frac{w_0}{w}\left(\frac{r}{w}\right)^{|m|}\exp\left(-\frac{r^2}{w^2}\right) \times \exp\left(j\left[\frac{kr^2}{2R} + m\theta - (|\,m\,|+1)\arctan\frac{z}{z_R}\right]\right), \tag{88}$$

where E_0 is the amplitude, $w = w_0\sqrt{1+z_R^2/z^2}$ is the beam radius at z, w_0 is the beam radius at the $z=0$ plane, $R = z\left(1+z_R^2/z^2\right)$ is the wavefront-curvature radius, and $z_R = kw_0^2/2$ is the Rayleigh range [35].

There are a variety of approaches to impose a spiral-phase distribution on an input beam and thus generate an optical vortex beam including spiral phase plate [36-39], deformable mirror [40], diffractive optical elements (DOEs) [41], spatial light modulators (SLMs) [42], and optic fiber [43]. This dissertation explores two common means to produce optical vortices: spiral phase plates and computer-generated holograms (CGH). The SPP directly imposes the vortex structure on the incident beam by linearly varying the optical path length around the circumference of the device. CGHs are created by mathematically interfering an oblique plane wave with an optical vortex and function by diffracting a plane wave into multiple orders of optical vortices of distinct topological charge.

5.2 Generating Optical Vortex with Lenses and Spiral Phase Plate

Allen, Beijersbergen, Spreeuw, and Woerdman (1992) [44] recognized that light beams with helical wavefronts carry mechanical angular momentum or orbital angular momentum with respect to the propagation axis. Beijersbergen, Allen, van der Veen, and Woerdman (1993) [45] then pursued a new approach via optical components termed spiral phase plates for the generation of vortex-carrying beams. The components are made of glass or plastic and have refractive index n and optical thickness Δt that increases with azimuthal angle according to $\Delta t = \theta\,(n-1)\,m\lambda/2\pi$ as seen in Figure 33. The transmission of a plane wave through a spiral phase plate results in the acquisition of an $\exp(jm\theta)$ phase term and induces an optical vortex along the beam axis.

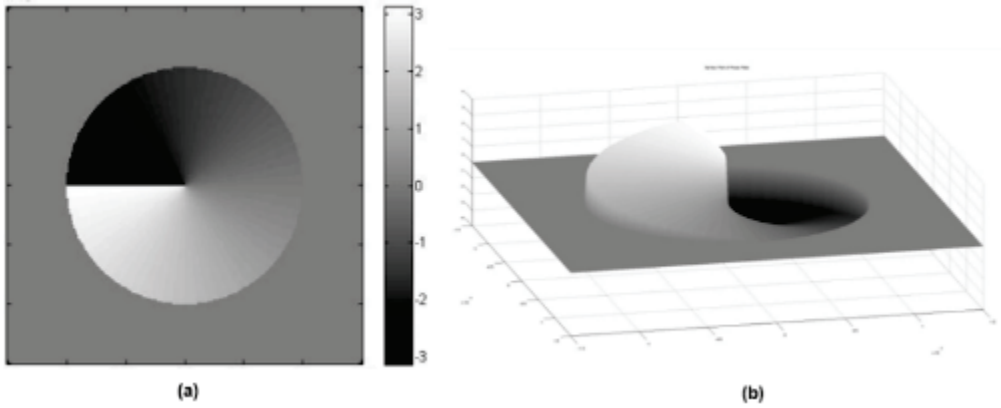

Figure 33 Spiral Phase Plate $m = 1$ (top view) and (c) side view.

By inspecting the plots in Figure 34, one can see how changing the topological charge affects the phase output of the SPP where the gray-scale values correlate to the phase modulation π in black to $-\pi$ in white.

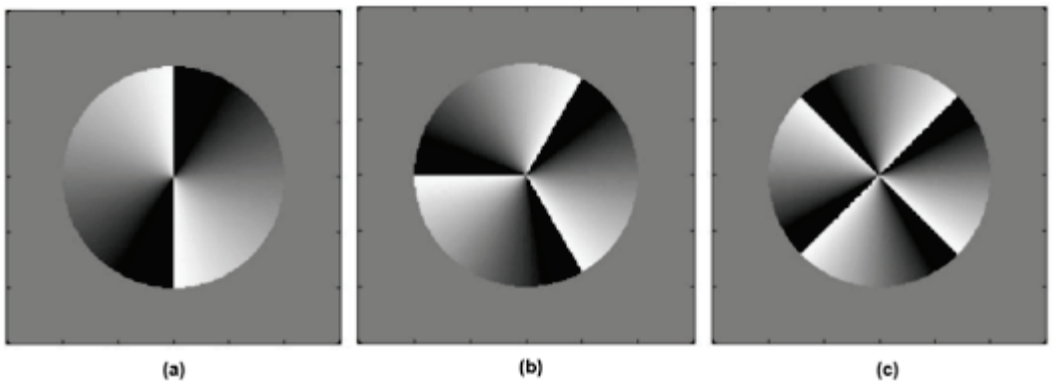

Figure 34 Spiral Phase Mask (a)$m = 2$, (b)$m = 3$, and (c)$m = 4$.

Davis *et al*. used a vortex-phase mask $\exp(jm\theta)\, 0 < \theta < 2\pi$ as a spatial filter in a 4-focal length optical system to achieve isotropic edge enhancement with $m = 1$ and anisotropic edge enhancement with fractional or non-integer m [46]. The enhancement results are due to the phase profile of the vortex mask which redistributes the intensity in a symmetric manner due to the phase difference of $m\pi$ at symmetric positions in any radial line with respect to the vortex core. These characteristics can also be found in the one-dimensional Hilbert transform [47-49]. Using the spiral phase plate characterized by $\exp(jm\theta)$ for spiral phase filtering, can be regarded as a radial Hilbert phase mask with m as the order of the radial Hilbert transform.

For isotropic enhancement an SPP is used as a radial Hilbert mask which effectively works as vortex spatial filtering by redistributing the intensity in a symmetric manner. Using this property if one desires to enhance selective edges in a particular direction one has to break the symmetry.

Before discussing selective and symmetric edge enhancement with analytical expressions and simulated results, a mathematical background on spiral phase filtering is provided. Generally the edge enhancement effects are realized by Fourier transforming the object and then manipulating it with the help of a filter function before taking the inverse Fourier transform. The general case of filtering in a standard, 4-f coherent imaging system uses a spatial filter $S(r,\theta)$ is defined as

$$S(r,\theta) = circ\left(\frac{r}{R}\right)\exp(jm\theta), \tag{89}$$

where (r,θ) represent polar coordinates in the Fourier plane, m is the topological charge, and $circ(r/R)$ is a circular aperture function of radius R.

Consider the optical system in Figure 35 where a plane wave is used to illuminate the input pattern $g(x,y)$ placed at P_1 the front of a lens,L_1, then at the back focal plane one obtains the Fourier transform as

$$G(\xi,\eta) = \mathcal{F}\{g(x,y)\}, \tag{90}$$

where $(\xi = \rho\cos\theta, \eta = \rho\sin\theta)$ are the coordinates at the back focal plane. The field after the SPP is

$$T(\rho,\theta) = G(\rho,\theta) \times S(\rho,\theta) = \mathcal{F}\{g(x,y)\} \times S(\rho,\theta), \tag{91}$$

and using L_2 as a Fourier transform gives the output image field at the rear focal plane P_2 as

$$t(r,\phi) = \mathcal{F}\{T(\rho,\theta)\} = g(r,\phi) \otimes \mathcal{F}\{S(\rho,\theta)\} \\ = g(r,\phi) \otimes s(r,\phi) \quad , \tag{92}$$

where (r,ϕ) represent the polar coordinates in the CCD plane, respectively $(x = r\cos\phi, y = r\sin\phi)$ with $s(r,\phi)$ representing the Fourier transform of the filter function in Eq. (89). From Eq. (92) one can develop an understanding of how edge enhancement occurs by analyzing the Fourier transform of the spiral phase filter, which acts as the point spread function (PSF) of the system.

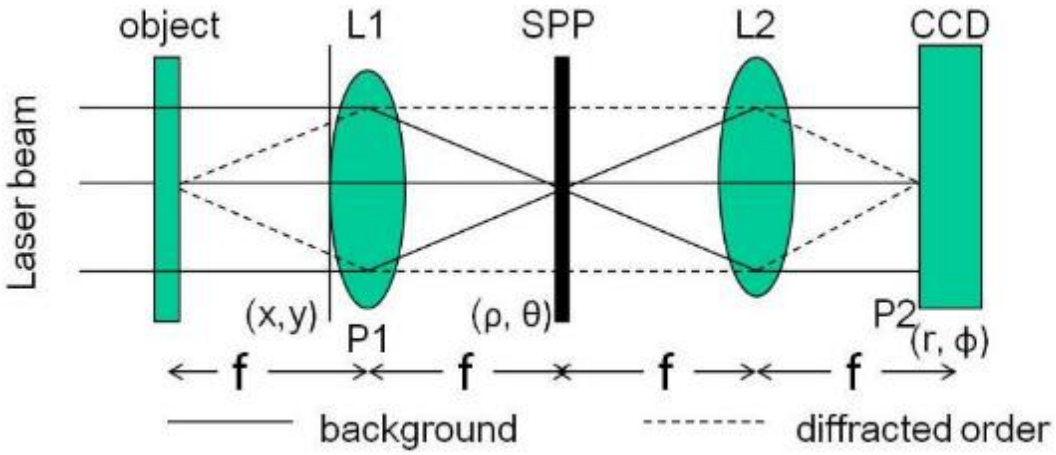

Figure 35 4-f system for spiral phase filtering.

5.2.1 Isotropic Spatial Vortex Filtering

The ability to use optical vortices for isotropic edge enhancement of an object is important because often in identification an image is understood by enhancing its edges. This is realized by radial Hilbert transform of an input pattern $g(x,y)$ which from Eq. (92) can also be expressed as a convolution of the input pattern with a 2-D kernel $s(r,\phi)$. The filter function is separable in polar coordinates, $S(\rho,\theta) = q_R(r)\, q_\Theta(\theta)$ such that the Fourier transform is given by [50]

$$s(r,\phi) = \sum_{-\infty}^{\infty} c_p (-j)^p \exp(jp\phi)\, H_p\{q_R(r)\} \quad , \tag{93}$$

where the coefficients are given as

$$c_p = \frac{1}{2\pi}\int_a^b q_\Theta(\theta)\exp(-jp\phi)\, d\phi \quad , \tag{94}$$

and $H\{\cdot\}$ represents the Hankel transform given as

$$H_P\left\{q_R\left(r\right)\right\} = 2\pi \int_0^\infty r q_R\left(r\right) J_1\left(2\pi\rho r\right) dr \tag{95}$$

For the vortex-phase mask $S\left(\rho,\theta\right) = \exp\left(j\theta\right)$, letting $c_p = c_1 = 1$ and radially restricting the mask function from 0 to R, the Hankel transform in the Fraunhofer zone becomes [50]

$$\begin{aligned} H_1\left\{S_R\left(r\right)\right\} &= 2\pi \int_0^R r S_R\left(r\right) J_1\left(2\pi\rho r/\lambda f\right) dr \\ &= 2\pi \int_0^R r J_1\left(2\pi\rho r/\lambda f\right) dr \\ &= \frac{\pi R}{2\rho}\left[J_1\left(x\right) H_0\left(x\right) - J_0\left(x\right) H_1\left(x\right)\right], \end{aligned} \tag{96}$$

where $x = 2\pi r R/\lambda f$, λ is the wavelength of light illuminating the input pattern $g\left(x,y\right)$, f is the focal length of the Fourier transform lens, J_0 and J_1 are the zero and first-order Bessel functions, respectively, and H_0 and H_1 are the Struve functions of the zero- and first-order, respectively. The Fourier transform of the filter function can be written as

$$s\left(r,\phi\right) = -j\exp\left(j\phi\right)\frac{\pi R}{2r}\left[J_1\left(x\right) H_0\left(x\right) - J_0\left(x\right) H_1\left(x\right)\right]. \tag{97}$$

Thus one can obtain the output from Eq. (92) by convolving Eq. (97) with the input field. The next section will discuss simulations accomplished in MATLAB to show edge enhancement using this isotropic vortex function.

5.2.1.1 MATLAB Simulation: Isotropic Spatial Vortex Filtering

The numerical simulation of edge enhancement is performed in MATLAB by Fourier transforming the circular amplitude object sampled at 512×512 pixels then multiplied element by element with the filter function and inverse Fourier transformed. The results are presented in Figure 36 where (a) is the original input image, (b) is the resulting edge enhancement, and (c) and (d) are the horizontal linear intensity distribution profile of the output in (a) and (d), respectively. One can inspect either the filtered image or the intensity distribution profile to see the edges of the input object have been enhanced. The intensity distribution profile of the filtered image has amplitude lower than the original image, the filtered output is not as symmetric, and rather than having a sharp transition as the input object has more of a gradual transition before and after the edge.

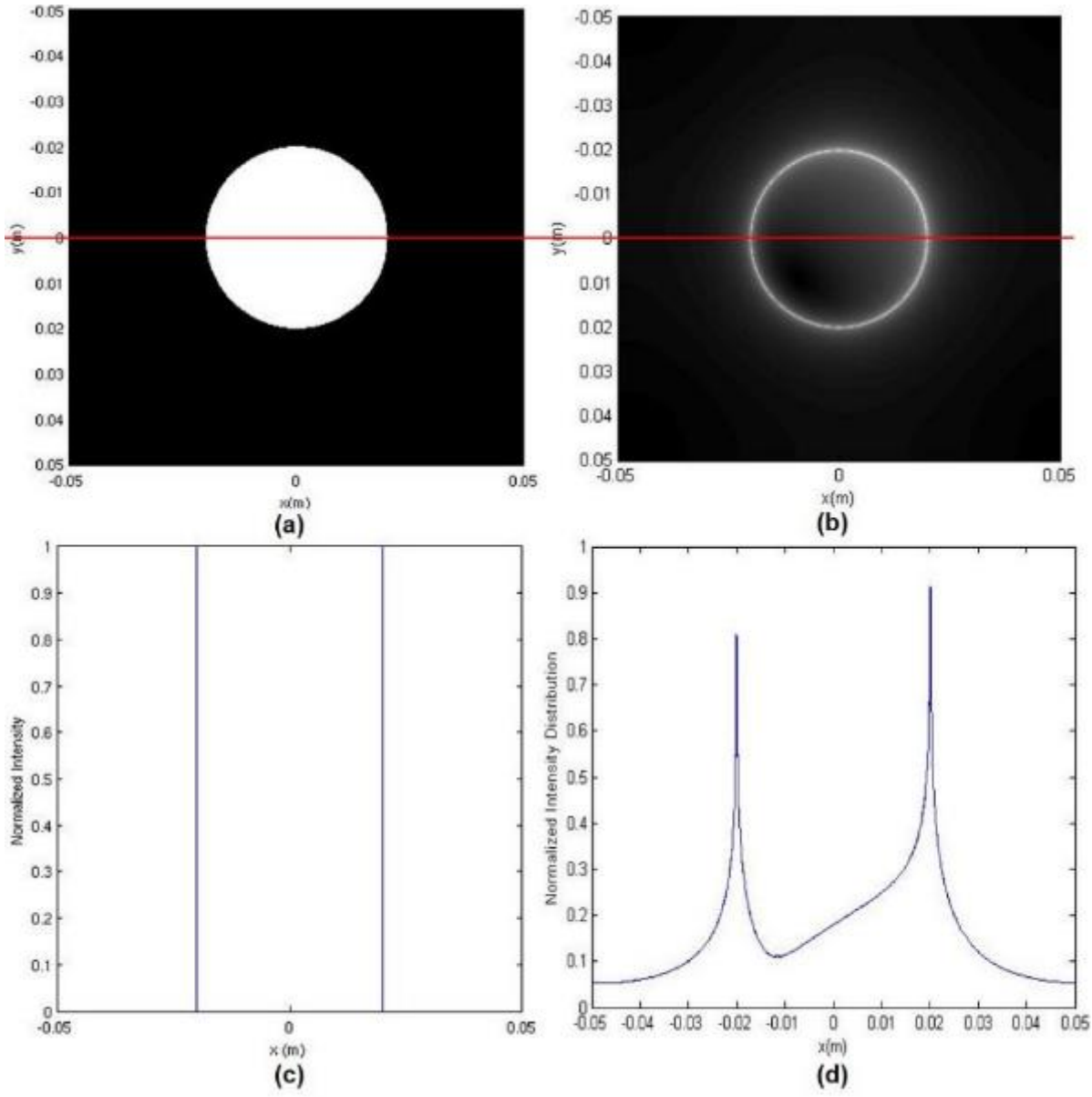

Figure 36 (a) Original image, (b) filtered output, (c) horizontal linear intensity distribution profile for (a), and (d) horizontal linear intensity distribution profile for (b).

A more challenging input object is used as represented by the USAF bar chart in (a) of Figure 37, the resulting filter output in (b), and the intensity distribution profile (c). Visual inspection of the filtered output and intensity distribution profile again show that the edges of the input image have been enhanced but perhaps not as distinctly as one would like.

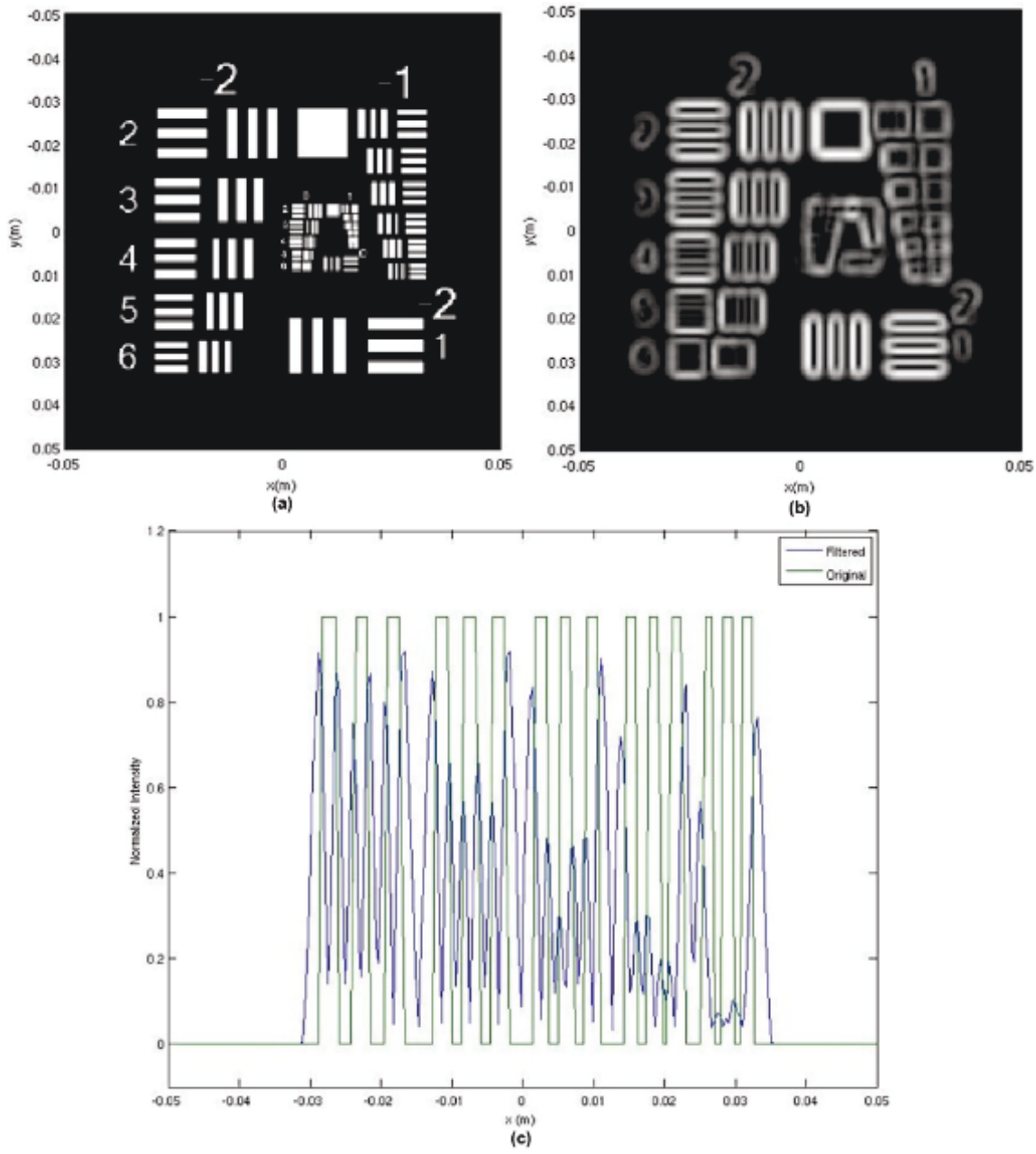

Figure 37 (a) Input image, (b) filtered output, and (c) intensity distribution profile.

In either example, the convolution of the filter with the input object suppresses the zeroth-order frequency component in an almost symmetric fashion. If the zeroth-order frequency component could be partially suppressed by changing the vortex core, then one could filter certain frequency components and achieve selective edge enhancement. A discussion of several methods to achieve selective enhancement is discussed next.

5.2.2 Anisotropic Spatial Vortex Filtering

Generally, the enhancement effect is isotropic such that regardless of orientation, each edge of the input pattern is enhanced uniformly. However, in some cases the feature information around certain orientations and edges is of greater interest and therefore requires anisotropic edge enhancement to emphasize these edges. Methods reported for selective edge enhancement include changing the power and offset angle in the vortex distribution [51], fractional [46,52-54] or shifted vortex filters [54,55], superposed vortex amplitude filter [56], and introduction of aberrations in the vortex filter [57]. Expressions for fractional vortex mask and anisotropic vortex phase mask to perform the Hilbert transform [51] will be shown and selective edge enhancement simulated using MATLAB.

An isotropic optical vortex can be defined by the complex field

$$\widetilde{V_i}(x,y) = x + jy = r\exp(j\theta), \tag{98}$$

where r is the distance from the vortex center and $\theta = \tan^{-1}(y/x)$ is the azimuthal angle. The phase distribution is $\psi(r,\theta) = \theta$ which makes the rate of change of the phase around the vortex $d\psi/d\theta = 1$. This is not the case for an anisotropic optical vortex as will be shown next.

Begin with an anisotropic vortex given by [58]

$$\widetilde{V_a}(x,y) = x + j\sigma y = r\exp(j\psi(x,y)), \tag{99}$$

where the phase is defined as

$$\psi(x,y) = \tan^{-1}\left(\sigma\frac{y}{x}\right) = \tan^{-1}\left(\sigma\frac{\sin\theta}{\cos\theta}\right), \tag{100}$$

and σ is the anisotropy parameter which determines the internal structure of the optical vortex. From Eq. (100), the rate of change of the phase of anisotropic vortex is

$$\frac{d\psi}{d\theta} = \frac{\sigma}{\cos^2\theta + \sigma\sin^2\theta}. \tag{101}$$

The phase profile for isotropic and anisotropic vortices is shown in Figure 38. The phase plot for an isotropic vortex $\sigma = 1$ and anisotropic vortex $\sigma = 5$ are shown in Figure 39. A plot of the rate of change of phase for isotropic and anisotropic vortices is shown in Figure 40. From Figure 40 and Eq. (101) one can see that for an anisotropic vortex the rate of change of the phase is a function of θ and not a constant as for an isotropic vortex. This change of phase is one of the characteristics that will be leveraged to enable selective edge enhancement.

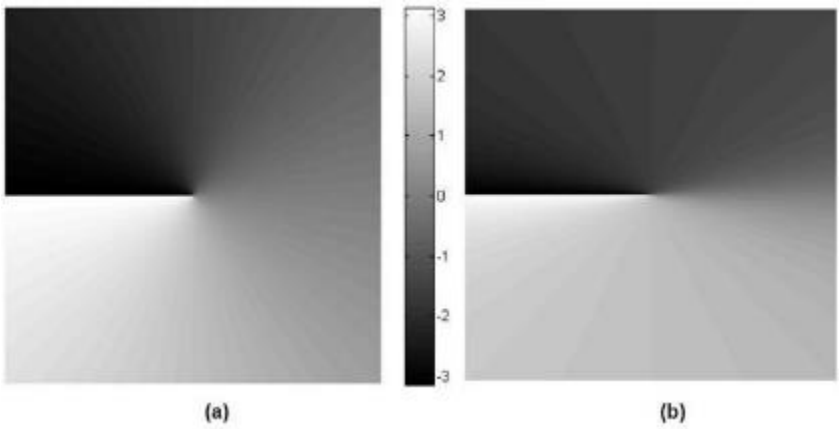

Figure 38 (a) Isotropic vortex and (b) anisotropic vortex.

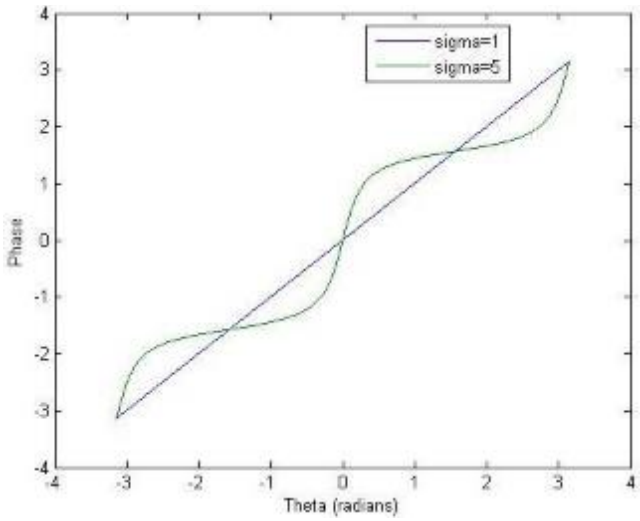

Figure 39 Phase plot for isotropic vortex ($\sigma = 1$) and anisotropic vortex ($\sigma = 5$).

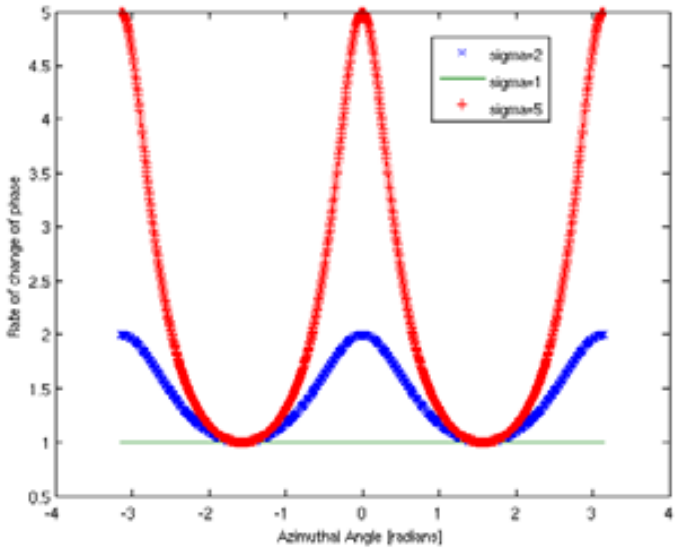

Figure 40 Rate of change of phase for isotropic and anisotropic vortices.

Anisotropic filtering has been discussed and introduced, the remaining sections will discuss specific anisotropic techniques either by making changes to the physical phase plate itself or its position in the optical system.

5.2.2.1 Anisotropic Spatial Vortex Filtering: Method 1 Superposed Vortex Filter

While optical vortices perform isotropic edge enhancement, it was shown by Sharma, Joseph, and Senthilkumaran (2014) [56] that a new filter which is made up of the superposition of two optical vortices can perform directional edge enhancement. The noise reduction and contrast enhancement of the azimuthal amplitude variations for this filter make it a more appropriate choice over the one-dimensional Hilbert filter for applications such as fingerprint filtering [59].

The filter function is given by

$$S(\rho,\theta) = (1/2) + (1/2)\cos\theta, \tag{102}$$

where the second term is the superposition of a positive and negative vortex as $2\cos\theta = \exp(j\theta) + \exp(-j\theta)$. Leveraging Eq. (96) and (97) the Fourier transform for the negative vortex, $S_1(\rho,\theta) = \exp(-j\theta)$, is

$$s_1(r,\phi) = -j\exp(-j\phi)\frac{\pi R}{2r}\left[J_1(x)H_0(x) - J_0(x)H_1(x)\right], \tag{103}$$

and similarly for the positive vortex, $S_2(\rho,\theta) = \exp(j\theta)$,

$$s_2(r,\phi) = j\exp(j\phi)\frac{\pi R}{2r}\left[J_1(x)H_0(x) - J_0(x)H_1(x)\right]. \tag{104}$$

Combining Eq. (103) and (104) the transfer function or the Fourier transform of the superposed filter in Eq. (102) can be expressed as

$$\mathcal{F}\left\{\frac{1}{2} + \frac{1}{2}\left(e^{j\theta} + e^{-j\theta}\right)\right\} = \frac{1}{2}\left[\delta(0,0) - j\frac{\pi R}{2r}\left[J_1(x)H_0(x) - J_0(x)H_1(x)\right]2\sin\phi\right]. \tag{15}$$

Comparing Eq. (105) and Eq. (97) one can see that the latter provides symmetric edge enhancement due to the phase term $\exp(j\phi)$ whereas for the former the angle dependent amplitude variation results from the $\sin\phi$ terms which leads to directional edge enhancement. Instead of the transfer functions one can inspect the filter transmittance functions in Figure 41 where the phase variation in one direction from the second term of the filter function in Eq. (105) is apparent in (c) with the vortex filters from Eq. (103) and Eq. (104) in (a) and (b), respectively. This is further emphasized by plotting the Fourier transform of the superposed vortex function using Eq. (107) with its three-dimensional (3D) view shown in Figure 42 (a) and the similar view for the vortex

function in Eq. (30) shown in Figure 42 (b). The intensity distribution for each of these is provided in Figure 42 (c) and (d), respectively for comparison. The symmetry of the vortex function about the center can be seen in Figure 42 (b) while the asymmetric nature caused by the $\sin\phi$ term is seen in Figure 42 (a).

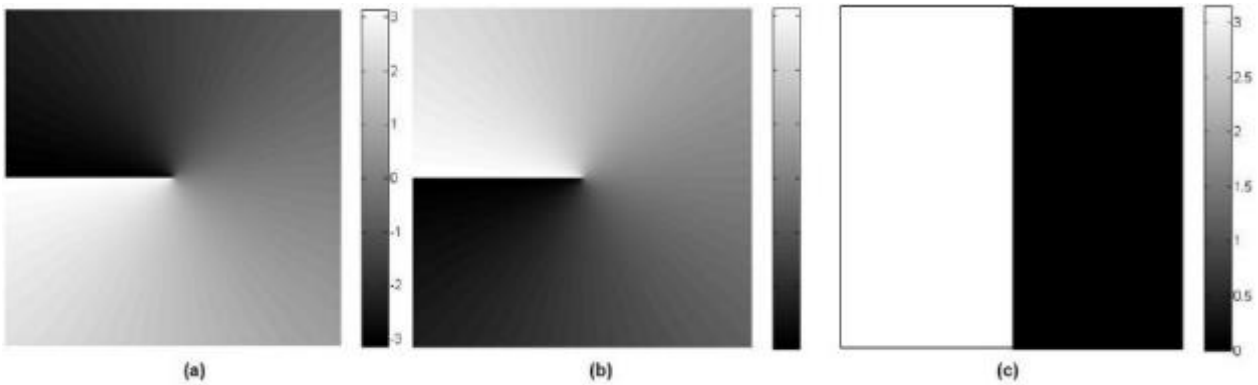

Figure 41 Phase distribution corresponding to (a) positive vortex, (b) negative vortex, and (c) superposition of positive and negative vortex.

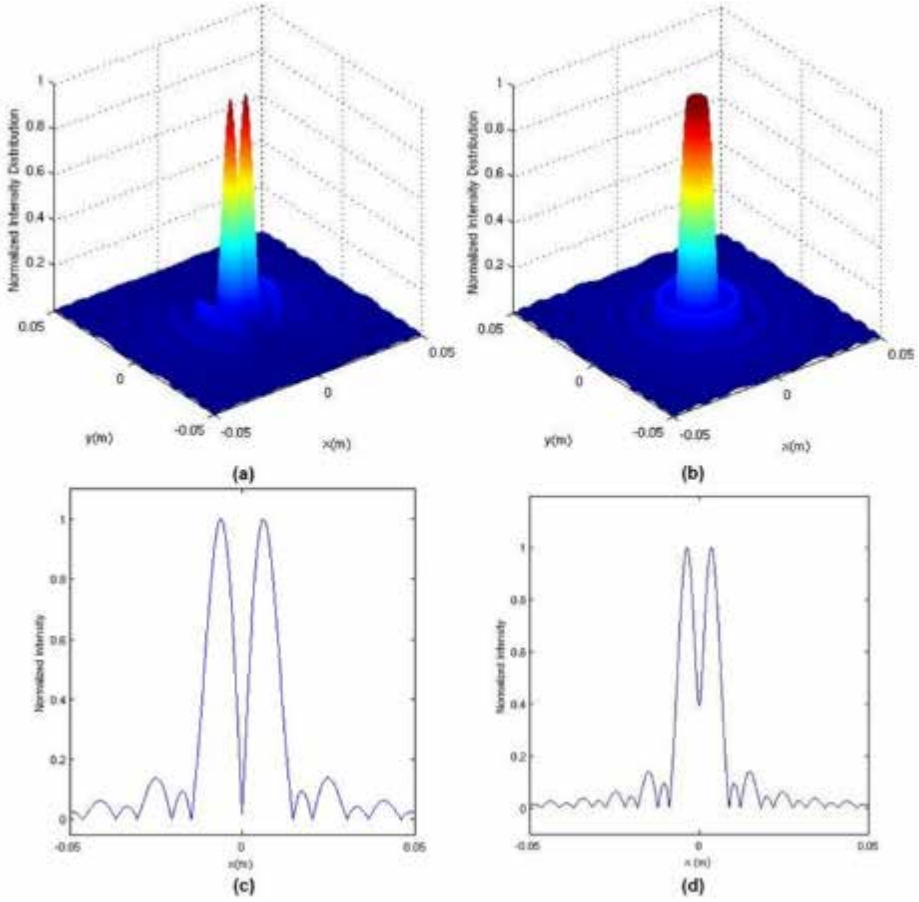

Figure 42 3D view of modulus of Fourier transform for (a) superposed vortex filter and (b) vortex filter, and intensity distribution profile for (c) superposed vortex filter and (d) vortex filter.

The amplitude distribution of the superposed filter in Eq. (102) is shown in Figure 43 where one can see that the anticipated edge enhancement will be in the lighter areas while the darker areas are those that will not be enhanced. Thus, one can expect edge enhancement in an asymmetric fashion.

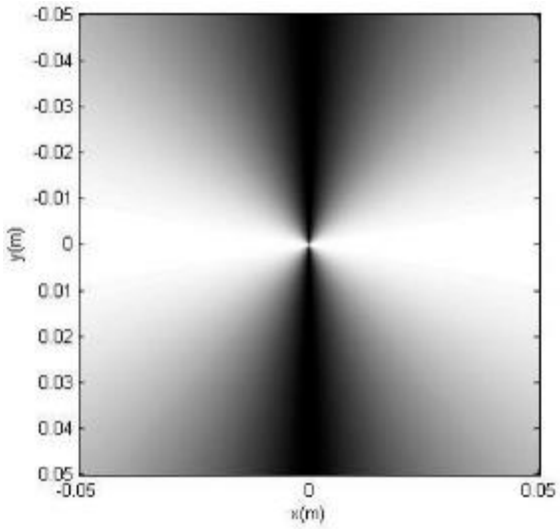

Figure 43 Amplitude of superposed vortex filter.

The simulated filter output for superposed vortex filter in Eq. (102) is provided in Figure 44. When compared to the output and the intensity distribution in Figure 36 (b) and (d) one can see that the result is in fact anisotropic edge enhancement. The right and left edges in the figure where the amplitude was nonzero are enhanced while the top and bottom edges where the amplitude was darker are not enhanced.

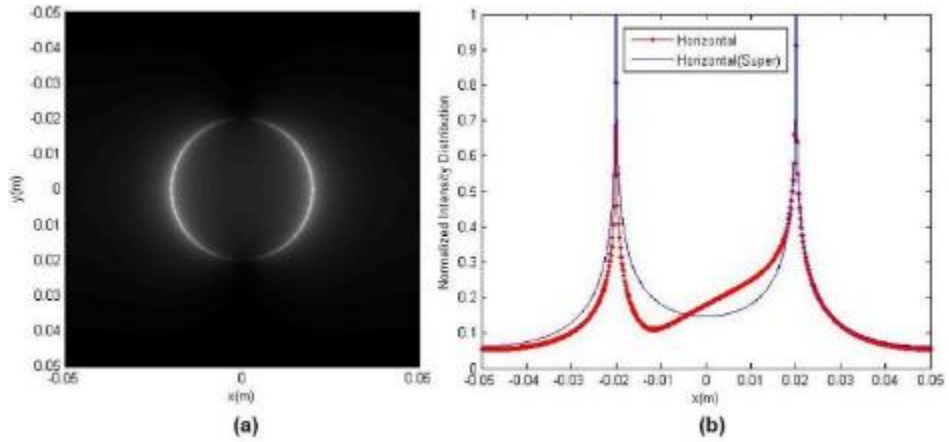

Figure 44 Simulation results for edge enhancement by superposed vortex filter (a) anisotropic edge enhancement and (b) intensity distribution profile.

As has been illustrated, the superposed vortex filter produces directional edge enhancement as a result of amplitude filtering. Sharma, Joseph, and Senthilkumaran (2013) [60] proposed an

extension to their superposed vortex amplitude filter as a complex filter of superposed vortices with relative phase between them. The filter considers two vortex beams with topological charge of ± 1 and relative phase difference β and no change to the position of the vortex core. The complex transmittance of the filter is given as [60]

$$S_c(\rho,\theta) = \frac{1}{2}\left(\exp(j\theta) + \exp(-j(\theta+\beta))\right). \tag{106}$$

The amplitude and phase of the superposed filter in Eq. (106) with different phases β is shown in Figure 45 (a-d) and (e-h), respectively. From the figure it can be seen that as the phase between the two beams changes, the orientation of the filter changes in a similar fashion. Thus, one expects to see directional edge enhancement in different radial directions using these filters.

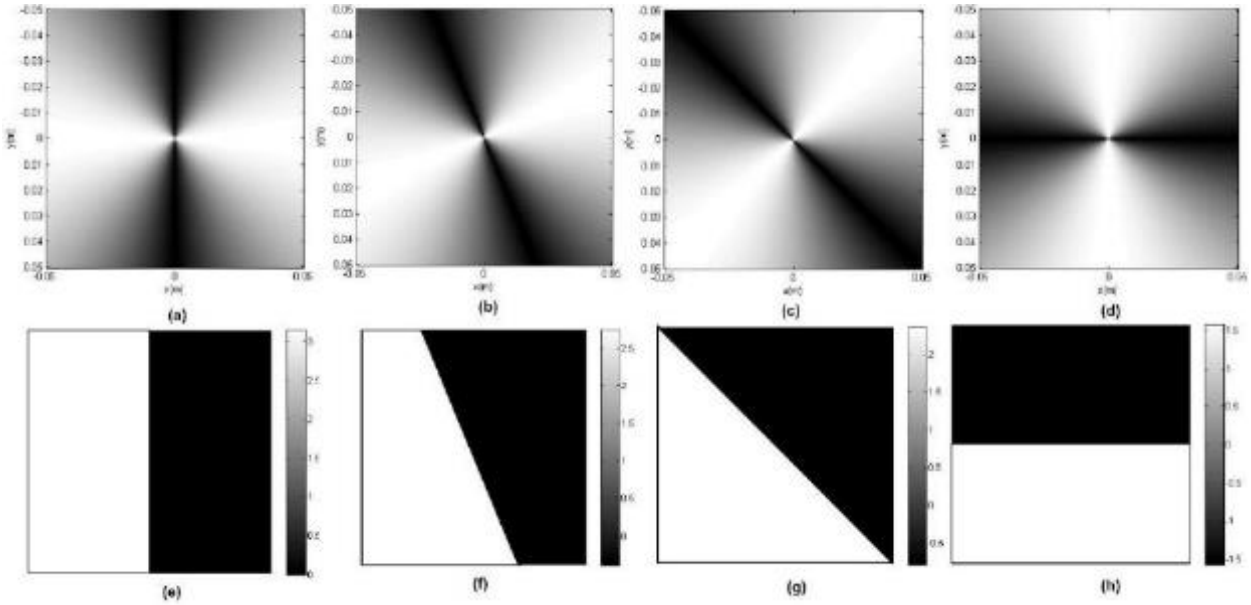

Figure 45 Amplitude of superposed vortex filter for β (a)$0°$, (b)$45°$, (c)$90°$, and (d)$180°$ with the corresponding phases shown in (e), (f), (g), and (h), respectively.

The simulated filtered output that results from using the superposed vortex filter in Eq.(106) are shown in Figure 46 (a-d) for $\beta = 0°, 45°, 90°, \text{and } 180°$, respectively. From the figure it is clear that the filtered output produces edge enhancement in different directions with the orientation of the enhancement at β. A further illustration of the edge enhancement effects can be seen in Figure 47 where the horizontal intensity distributions are graphed for no rotation, $90°$ rotation, and $180°$ rotation. The figure illustrates that the filtered output decreases in intensity or contrast and sharpness as the rotation increases.

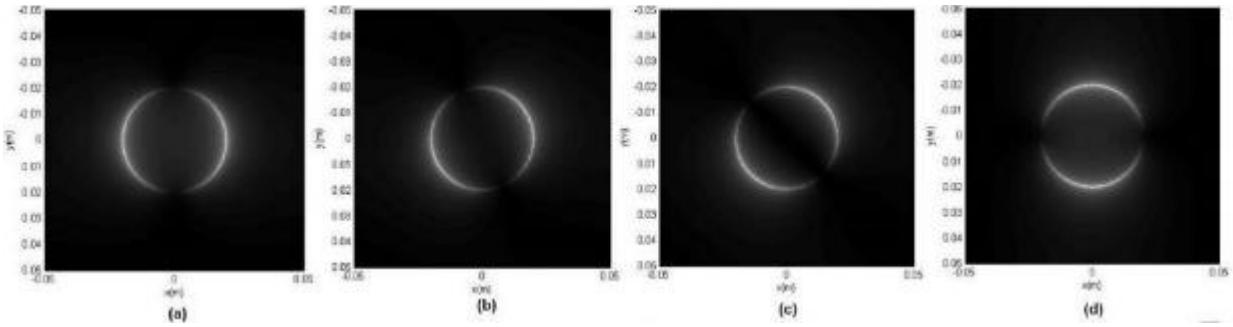

Figure 46 Simulation results for edge enhancement by superposed vortex filter for β(a)$0°$, (b)$45°$, (c)$90°$, and (d)$180°$.

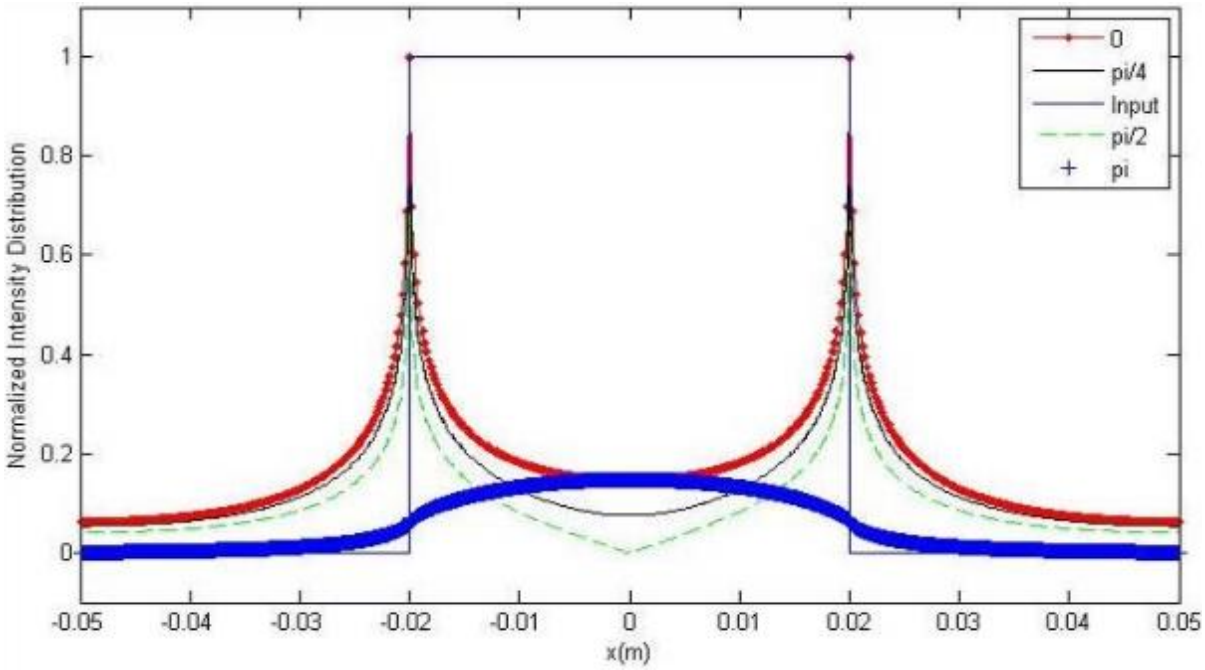

Figure 47 Intensity distribution for original image and superposed filter for β(a)$0°$, (b)$45°$, (c) $90°$, and (d)$180°$.

The next section will discuss how aberrations in the optical system can lead to anisotropic edge enhancements.

5.2.2.2 Anisotropic Spatial Vortex Filtering: Method 2 Siedel Aberrations

Aberrations are an inherent part of optical systems and it is thus important to study the effects of aberrations on the radial Hilbert mask. For rotationally symmetric optical systems the general aberration function is [61]

$$W(\rho,\theta) = A_s\rho^4 + A_c\rho^3\cos\theta + A_a\rho^2\cos^2\theta + A_f\rho^2 + A_d\rho\cos\theta, \qquad (107)$$

where (ρ, θ) are the polar coordinates at the exit pupil of the imaging system and A_s, A_c, A_a, A_f, and A_d are the coefficients for spherical aberration, coma, astigmatism, field curvature or defocus, and tilt or distortion, respectively. A general representation for an aberrated-vortex beam is

$$S_{ab}(\rho, \theta) = \exp(jm\theta) \exp(jkW(\rho, \theta)), \tag{108}$$

where $W(\rho, \theta)$ is the aberration function representing the wave aberration and $k = 2\pi/\lambda$ is the propagation constant as before.

Spherical aberrations result from rays focusing at two different axial points with the distance between these two foci a measure of the spherical aberration in the lens. The spherical aberration function is $W(\rho, \theta) = A_s \rho^4$ where A_s is the spherical aberration coefficient. Plugging this into Eq. (108) gives the vortex filter with spherical aberration as

$$S_{sp}(\rho, \theta) = \exp(j\theta) \exp\left(jkA_s \rho^4\right). \tag{109}$$

The spherical aberration vortex mask, the filtered output, and the horizontal profile of the output intensity pattern for a circular object are shown in Figure 48 (a-c), respectively. Inspection of this figure reveals that the filtered output is not as crisp as in isotropic filtering. Additionally by inspecting the intensity profile the enhanced edges become less in the presence of spherical aberrations because the edges are more spread out.

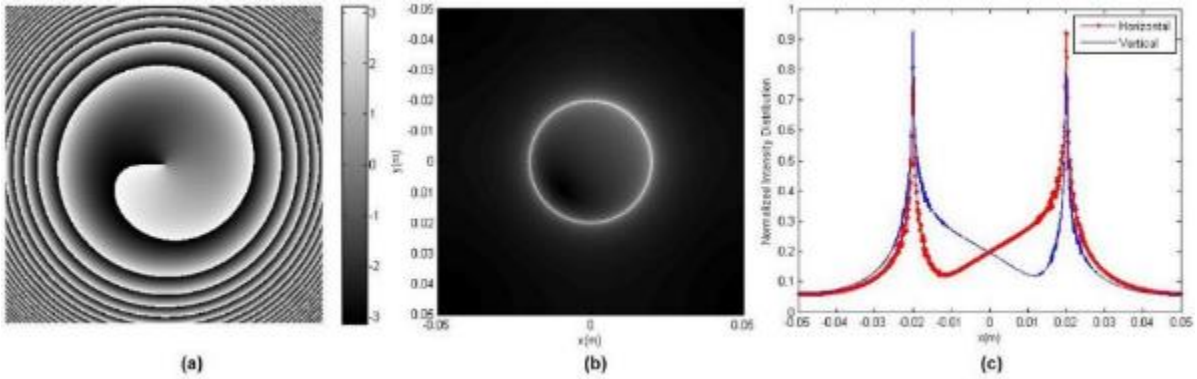

Figure 48 (a) Phase profile of the vortex beam with spherical aberration, (b) corresponding filtered output, and (c) plot of the horizontal and vertical intensity profile $A_s = 0.5$.

Distortion or tilt in an imaging system results from various components of the system having different focal lengths and different magnifications which leads to misshaping of the image. The aberration function is $W(\rho, \theta) = A_d \rho \cos\theta$ and plugging into Eq. (108) gives the distortion aberrations as

$$S_d(\rho, \theta) = \exp(j\theta) \exp(jkA_d \rho \cos\theta). \tag{110}$$

The phase of the distorted vortex mask takes the shape of a fork as seen in Figure 49 (a) with the corresponding enhanced edges filter output appearing as different orders of the fork grating. In Figure 49 (c) one can see that the output intensity is slightly greater in the vertical direction as compared to the isotropic output whereas in the horizontal direction it is more comparable to the isotropic case. The intensity has been redistributed in the two directions of the imaging plane and the incremental increase is in the direction parallel to the fork fringes.

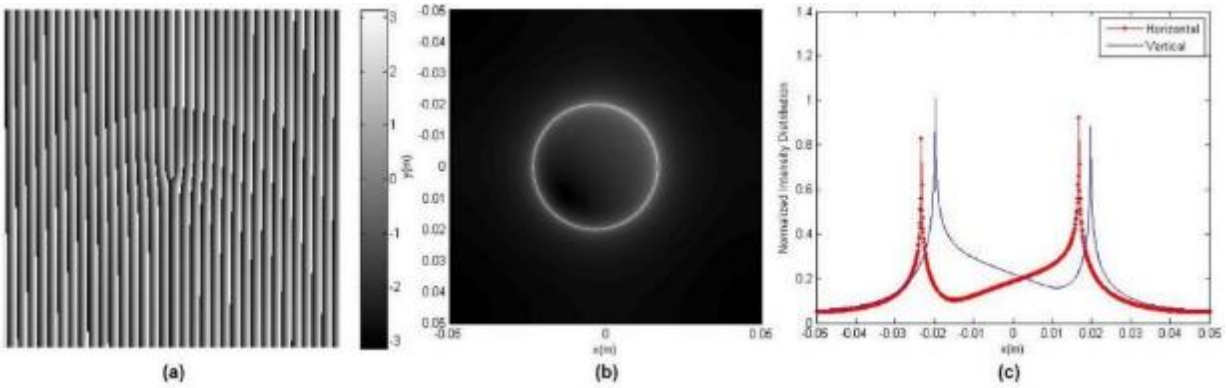

Figure 49 (a) Phase profile of the vortex beam with distortion, (b) corresponding filtered output, and (c) plot of the horizontal and vertical intensity profile $A_d = 1.25$.

Astigmatism is an off-axis wavefront aberration that results from incident light rays striking a lens asymmetrically which modifies the focal plane intensity distribution function of a singular beam. The aberration function for astigmatism is given by $W(\rho, \theta) = A_a \rho^2 \cos^2 \theta$ and from Eq. (108) the astigmatic vortex filter is

$$S_a(\rho, \theta) = \exp(j\theta) \exp\left(jkA_a \rho^2 \cos^2 \theta\right). \tag{111}$$

The astigmatic aberration in the vortex phase leads to edge enhancement as well as edge blurring. This effect is further analyzed by varying the astigmatic coefficient in Eq. (111). The astigmatic vortex mask for $A_a = 0.003$ and $A_a = 0.007$ values are shown in Figure 50 (a) and (b), respectively, with the corresponding filtered output with selectively enhanced edges in Figure 50 (c) and (d). In Figure 50 (e) and (f), the increase in astigmatism coefficient decreases the anisotropy and increases the blur of the edges in other directions. The intensity in the vertical direction for the output is increased whereas the horizontal direction is decreased and blurred as a result of redistributing the intensity in different radial directions.

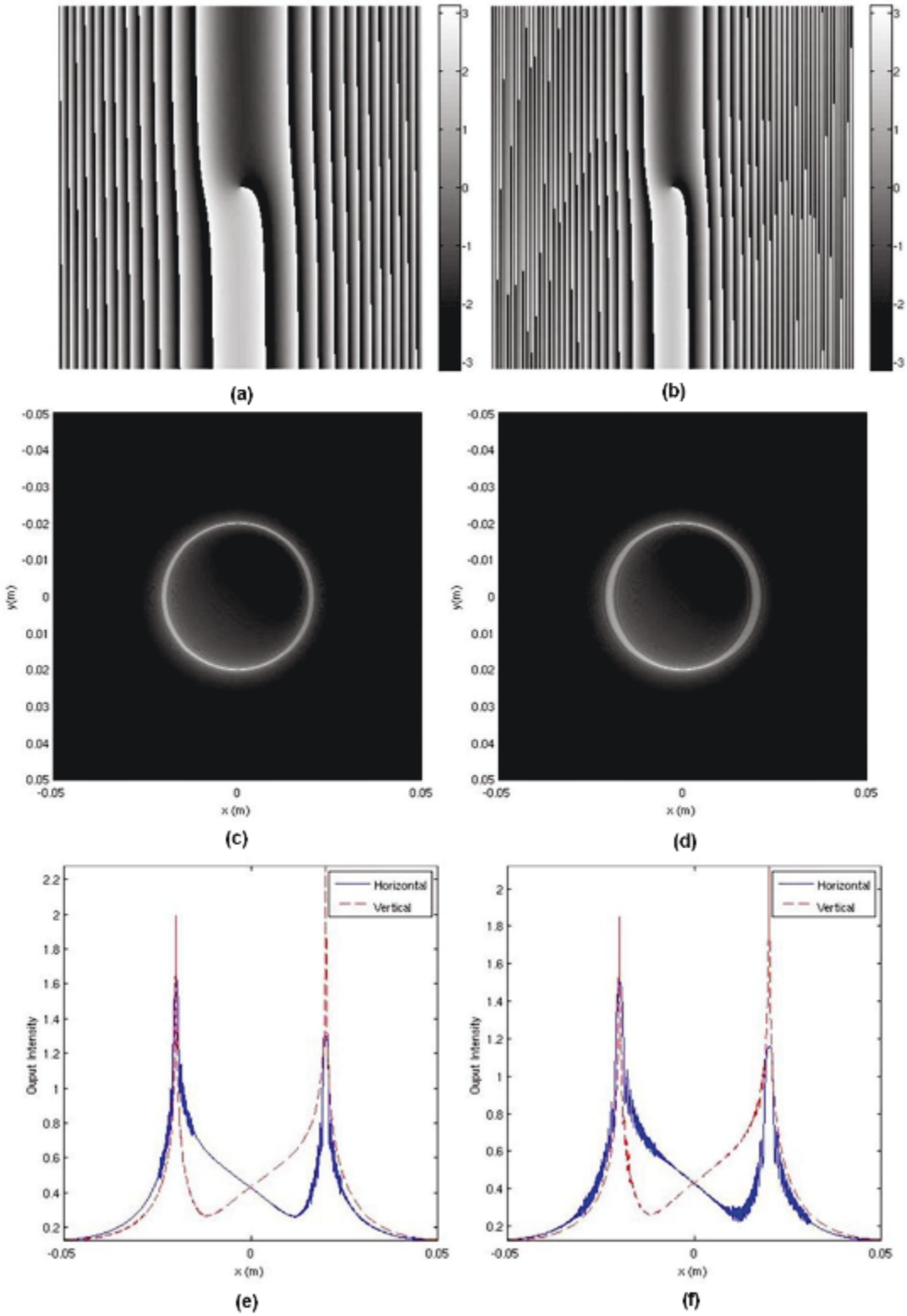

Figure 50 (a-b) Phase profile of the astigmatic vortex beam $A_a = 0.003$ and $A_a = 0.007$, (c-d) corresponding filtered output, and (e-f) output intensity for horizontal and vertical directions.

Coma is an off-axis aberration where the magnifications from different zones of an optical system are different. The aberration function is given by $W(\rho,\theta) = A_c\rho^3\cos\theta$ and the vortex filter for coma aberration from Eq. (108) is

$$S_c(\rho,\theta) = \exp(j\theta)\exp\left(jkA_c\rho^3\cos\theta\right). \tag{112}$$

The phase profile, corresponding output, and the horizontal and vertical intensity profile are shown in Figure 51 (a-c), respectively. The outer portion of the phase mask has changed in relation to typical vortex filtering while the center is less changed. The effects of the coma aberration on the output are not as clearly seen as in the intensity profile. Inspecting the intensity profile one sees that the vertical direction is most like the isotropic case while the horizontal direction is non-symmetric and in fact has some ringing.

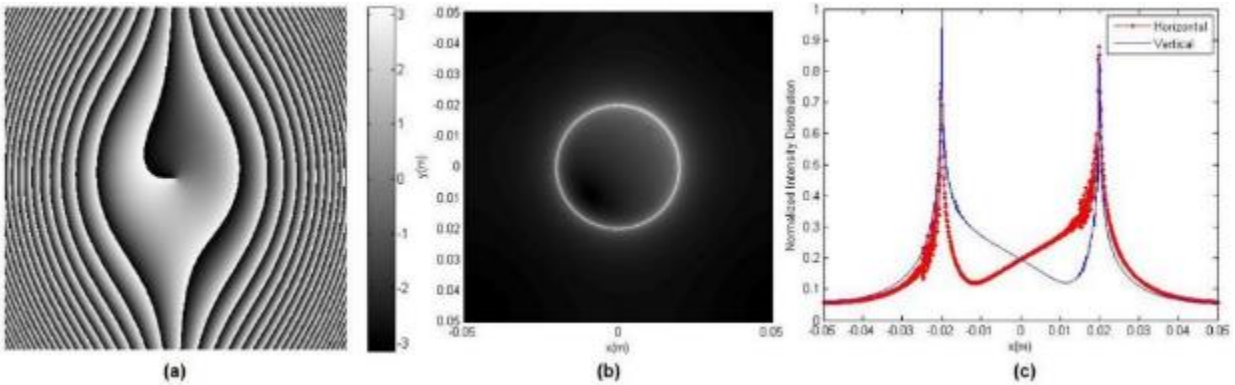

Figure 51 (a) Phase profile of the vortex beam with coma aberration, (b) corresponding filtered output, and (c) plot of the horizontal and vertical intensity profile $A_c = 0.05$.

The defocus or field of curvature aberration causes the imaging surface to be curved even without astigmatism. The aberration function is $W(\rho,\theta) = A_f\rho^2$ and the vortex filter is

$$S_f(\rho,\theta) = \exp(j\theta)\exp\left(jkA_f\rho^2\right). \tag{113}$$

In Figure 52 (a-c) the phase profile, the filtered output, and intensity distribution profile are plotted. The phase profile is a more evenly spaced throughout as compared to Figure 48 (a) as a result the output intensity profile shows symmetric distribution about the center of the input circular object. The filtered output and intensity distribution show defocus effects in the slight broadening of the edges.

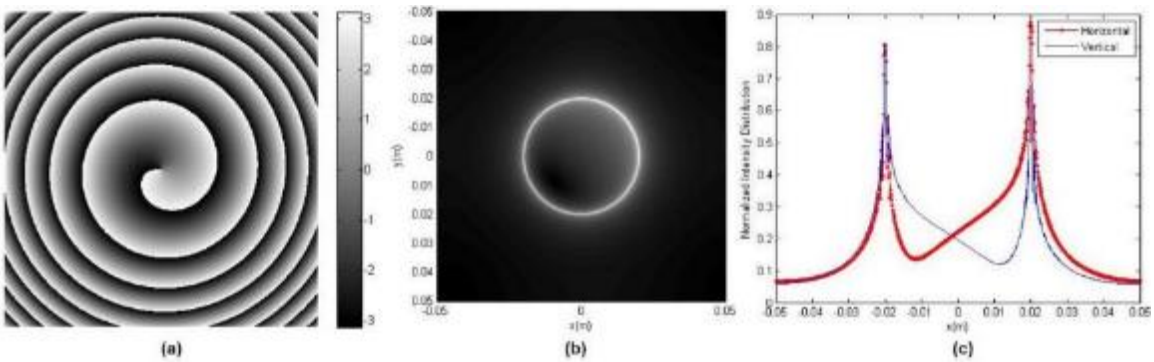

Figure 52 (a) Phase profile of the defocused vortex beam, (b) corresponding filtered output, and (c) plot of the horizontal and vertical intensity profile $A_f = 0.001$.

The next section investigates how changes to the topological charge of the phase plate can produce anisotropic filtering effects.

5.2.2.3 Anisotropic Spatial Vortex Filtering: Method 3 Fractional Spiral Phase Filter

Instead of Eq. (91) consider the spiral phase filter as

$$S_m(\rho,\theta,\tau) = \exp(jm(\theta+\tau)), \tag{114}$$

where τ is a constant angle denoting the orientation of the edge of discontinuity with respect to the positive ξ axis [53]. If the topological charge m is a fractional or non-integer number then, the phase of Eq. (114) is no longer continuous and has a discontinuity along τ. This is best illustrated by expanding Eq. (114) as a Fourier series

$$S_m(\rho,\theta,\tau) = \frac{\exp(jm\pi)\sin m\pi}{\pi}\sum_{n=-\infty}^{\infty}\frac{S_n(\rho,\theta,\tau)}{m-n}. \tag{115}$$

The Fresnel transform of Eq. (115) is [54]

$$s_m'\left(\rho',\theta',\tau,z\right) = \frac{\exp(jm\pi)\sin m\pi}{\pi}\sum_{n=-\infty}^{\infty}\frac{s_n'\left(\rho',\theta',\tau,z\right)}{m-n}. \tag{116}$$

From Eq. (116) one can see that there is no vortex core at the origin and the only nonzero contribution comes from $s_0'\left(\rho',\theta',\tau,z\right)$ so that

$$s_m'\left(\rho'=0,\theta',\tau,z\right) = \frac{\exp(jm\pi)\sin m\pi}{\pi}s_0'\left(\rho',\theta',\tau,z\right). \tag{117}$$

In Eq. (117) the vortex core is not located at the origin but instead is at position

$$\rho' \approx 1.3293\sqrt{\frac{8z}{k\pi}}(1-m), \tag{118}$$

when m is close to 1 and z is on the scale size of the spiral phase filter. One can see from Eq. (118) that the location of the vortex core depends on the value of m and thus by choice of this value one can control edge enhancement.

As Eq. (116) propagates to the Fraunhofer domain, the field has a vortex core on a radial line orthogonal to the τ direction [62]

$$s_m(r,\phi,\tau) = \frac{k}{2\pi f}\sum_{p=-\infty}^{\infty}(-j)^p \exp[jp(\phi+\tau)]\frac{\exp[j2\pi(m-|p|-1)]}{m-|p|}\int_0^R J_{|p|}\frac{kr\rho}{f}d\rho, \tag{119}$$

where the contribution of $\int_0^R J_{|p|}kr\rho/fd\rho$ to $s_m(r,\phi,\tau)$ depends on the value of the factor

$$c_p = \left|\frac{\exp[j2\pi(m-|p|)]-1}{m-|p|}\right|. \tag{120}$$

The coefficient in Eq. (120) has a contribution to Eq. (119) when p is an integer value close to m and in particular when m itself approaches an integer value. This is illustrated in Figure 53 where the distribution of c_p is plotted versus p for m equal to 0.2, 0.5 and 0.85, respectively.

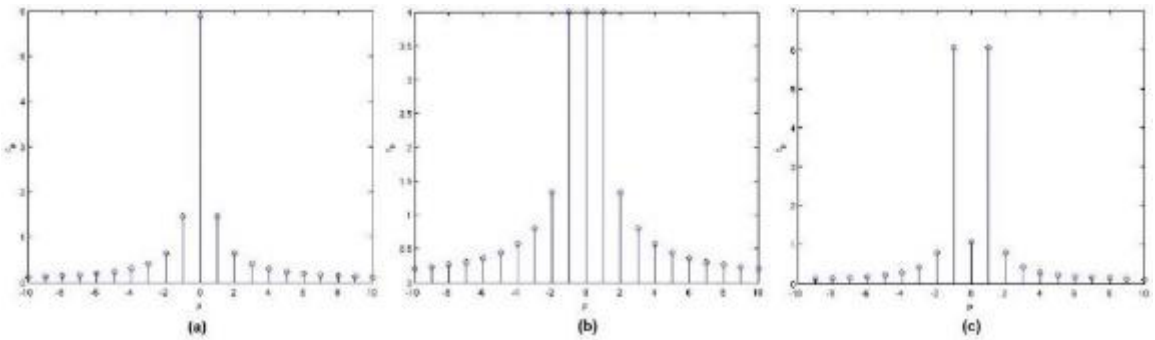

Figure 53 Plot of c_p versus p for $m =$ (a) 0.2, (b) 0.5, and (c) 0.85.

As discussed above, the degree of enhancement can be controlled by the value of m this can be further demonstrated by examining the density plot of Eq. (119) for $m = 0.2, 0.5, \text{and } 0.8$ and $\tau = 0$ seen in Figure 54. The figure illustrates how as the vortex moves toward the origin the enhancement of directional edges becomes more symmetric as illustrated by the movement of the lighter and darker rings.

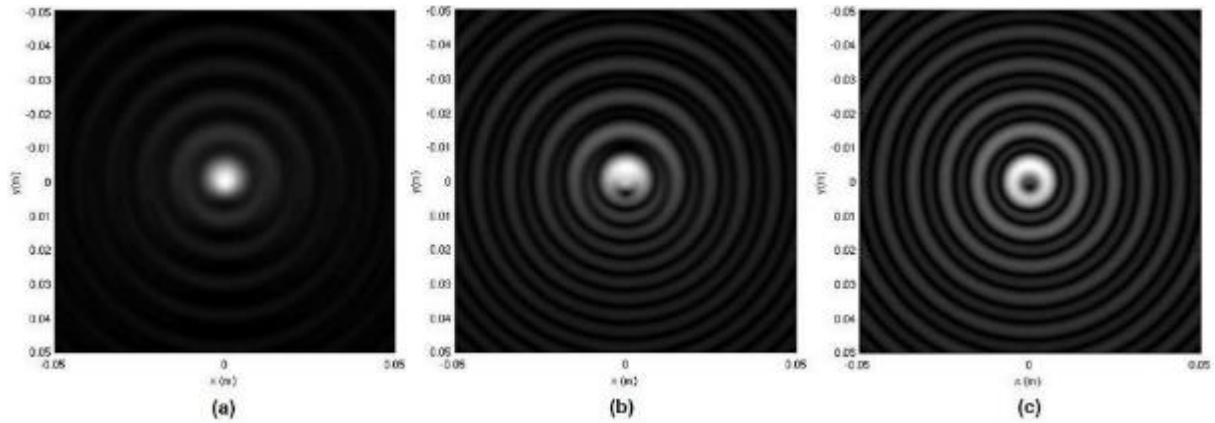

Figure 54 Density plot of $s_m\left(r,\phi,\tau_{=0}\right)$ with $m =$ (a) 0.2, (b) 0.5, and (c) 0.8.

While degree of enhancement can be controlled by the value of m, the orientation of the vortex in Eq. (119) is determined by τ. As an example the density plot of s_m with $m = 0.5$ and $\tau = -\pi/2$ is presented in Figure 55. Upon comparison to Figure 54 (b) it can be seen that the vortex has rotated counterclockwise through the angle $\pi/2$.

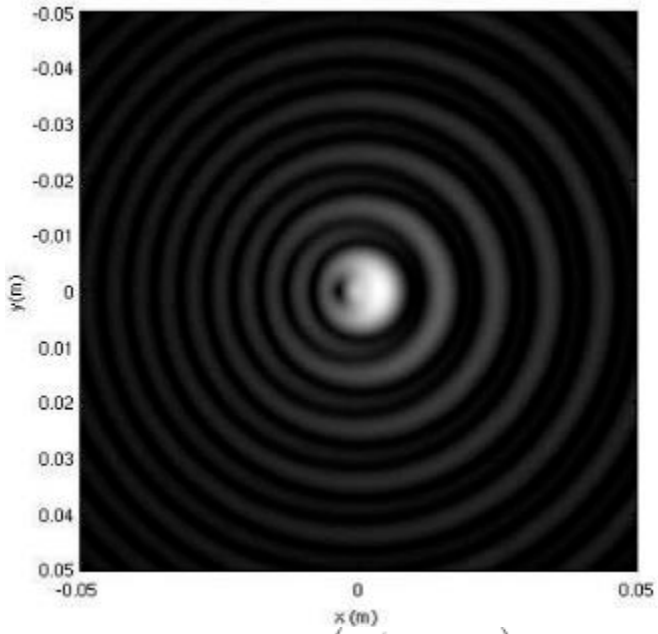

Figure 55 Density plot of $s_m\left(r,\phi,\tau_{=-\pi/2}\right)$ with $m = 0.5$.

The simulated filter output for $m = 0.5, 0.7, \text{and } 0.8$ and $\tau = 0$ is shown in Figure 56 (a-c) with the corresponding intensity distribution plot in (d-f). The figure illustrates how as the value of m increases the amount of contrast between enhanced edges decreases such that the enhancement is nearly symmetric.

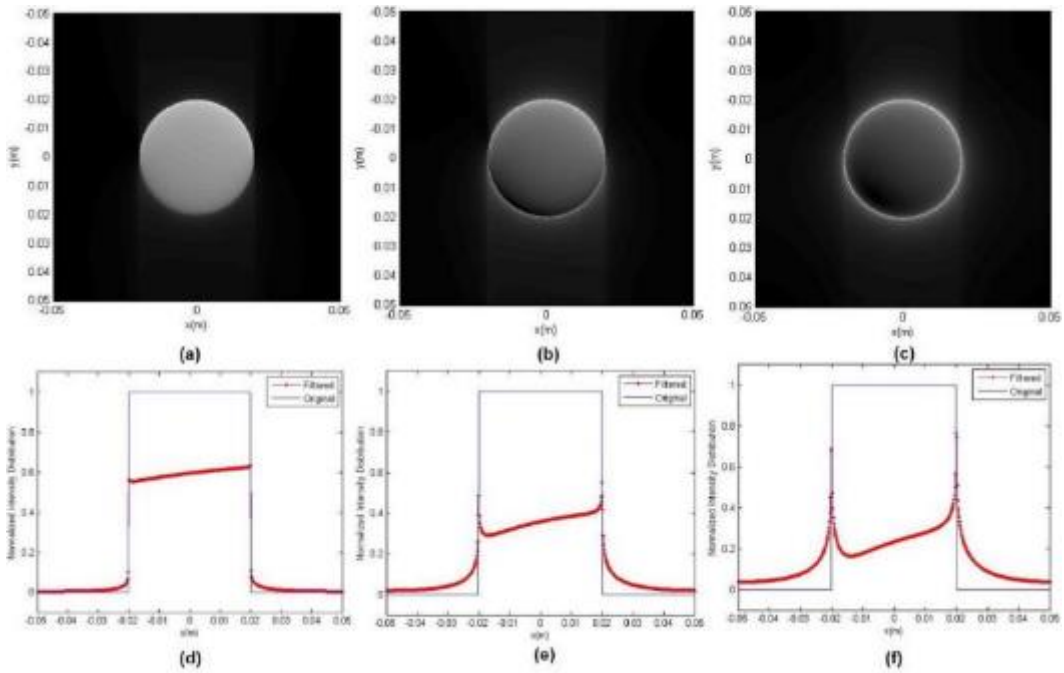

Figure 56 Filtered output for $\tau = 0$ (a) $m = 0.5$, (b)$m = 0.7$, and (c)$m = 0.8$, intensity distribution shown in (d), (e), and (f), respectively.

The simulated filter output for $m = 0.6, 0.8, \text{and } 0.9$ and $\tau = 5\pi/4, \pi, \text{and } \pi/2$ is shown in Figure 57 (a-c) with the corresponding intensity distribution plot in (d-f). The figure illustrates how as the value of τ changes so does the orientation of the enhanced edge.

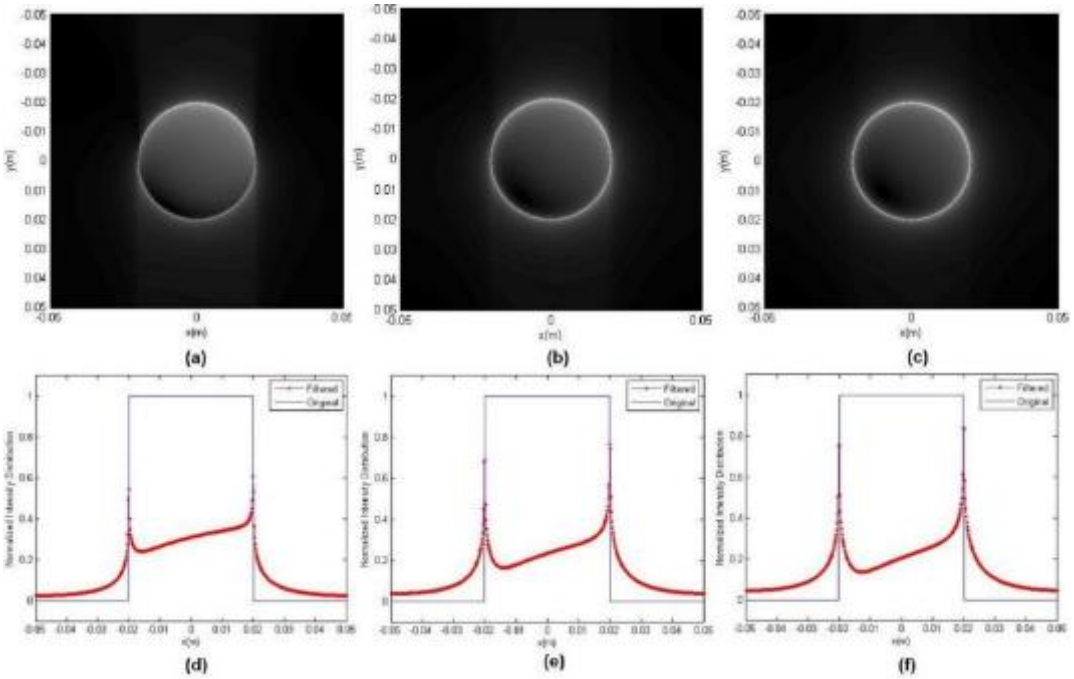

Figure 57 Filtered output for (a)$m = 0.6, \tau = 5\pi/4$, (b)$m = 0.8, \tau = \pi$, and (c) $m = 0.9, \tau = \pi/2$, intensity distribution shown in (d), (e), and (f), respectively.

The next section discusses anisotropic filtering as a result of shifting the spiral phase plate in the optical system.

5.2.2.4 Anisotropic Spatial Vortex Filtering: Method 4 Shifting Filter Singularity

Another approach to break the symmetry of the vortex filter is to shift the singularity away from the origin to a user specified position in polar coordinates (ρ_0, θ_0) where $\rho_0 < R$ and $\theta_0 \epsilon [0, 2\pi]$. The transmission function of this spiral phase plate is given by

$$S(\rho, \theta, \rho_0, \theta_0) = \exp(j\theta_s), \tag{121}$$

where the subscript $_s$ represents shifting, $\theta_s = \tan^{-1}(y - y_0/x - x_0), y_0 = \rho_0 \sin\theta_0$, $x_0 = \rho_0 \cos\theta_0$, and $\rho_s = \sqrt{(x - x_0)^2 + (y - y_0)^2}$. The position of the vortex is determined by ρ_0 so that when it is very small the vortex is located close to the origin and as it becomes larger the vortex moves increasingly further away from the origin.

The filtered output can again be expressed as the convolution of the input object $g(x, y)$ and Eq. (121). The edge enhancement of the filtered output with $\rho_0 = 0.001, 0.0025, 0.0075, \text{and } 0.01$ and $\theta_0 = 0$ becomes less significant as the value of ρ_0 increases until eventually no high-contrast enhancement is achieved due to the vortex disappearing as seen in Figure 58 (a-d). The exact value for the high-contrast enhancement crossover is unknown but is suspected to be tied to the area where the Fourier spectrum has significant value [54]. The distance between the vortex and the origin can be seen by examining the state of the filter for $\rho_0 = 0.001, 0.0025, 0.0075, \text{and } 0.01$ and $\theta_0 = 0$, respectively, as shown in Figure 58 (e-h).

Using the value for $\rho_0 = 0.001$ and varying the angle $\theta_0 = 0, \pi/4, \pi/2, \text{and } 3\pi/4$ one can see that orientation enhancement is achieved as seen in Figure 59 (a-d). As the angle is varied around the circular input object the filtered output has edge enhancement in the direction of the angle θ_0. It has thus been demonstrated that the orientation of the enhancement results from θ_0 and the degree of enhancement by the distance ρ_0.

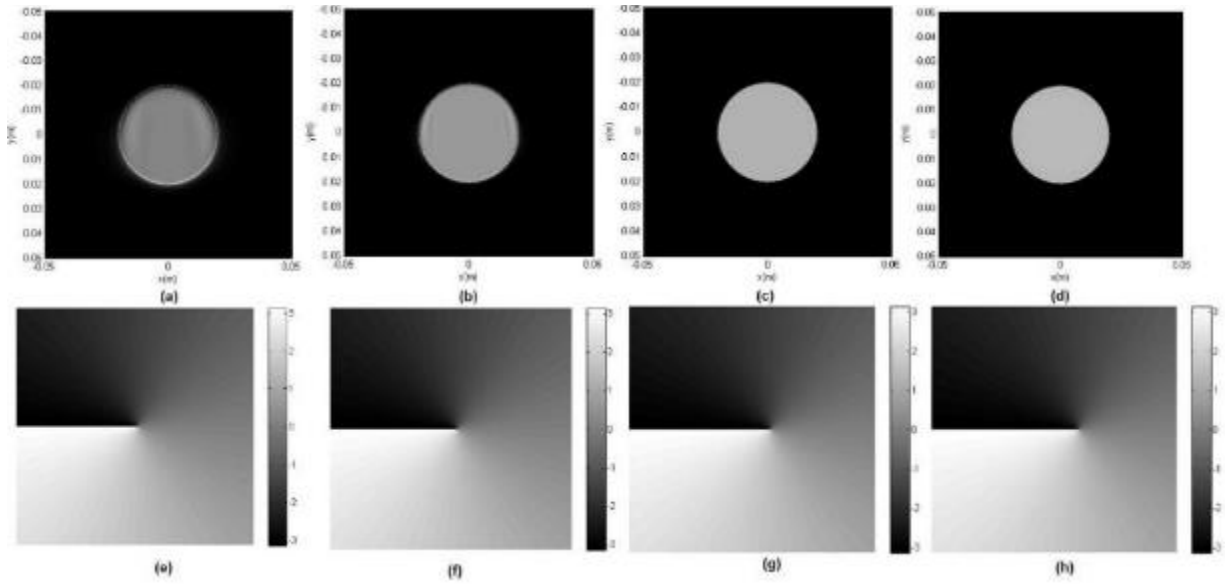

Figure 58 Simulation results for edge enhancement by shifted vortex (a-d) anisotropic edge enhancement and (e-h) filter status for $\rho_0 = 0.001, 0.0025, 0.0075, \text{and } 0.01$ and $\theta_0 = 0$, respectively.

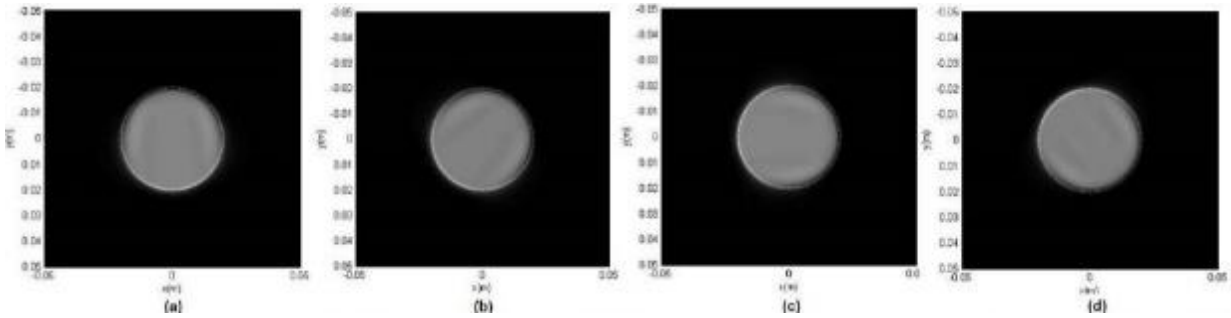

Figure 59 Simulation results for edge enhancement by shifted vortex (a-d) anisotropic edge enhancement for $\rho_0 = 0.001$ and $\theta_0 = 0, \pi/4, \pi/2, \text{and } 3\pi/4$, respectively.

In the next section, anisotropic filtering results from changing the power and offset angle of the spiral phase plate are presented.

5.2.2.5 Anisotropic Spatial Vortex Filtering: Method 5 Power and Offset Angle

An anisotropic vortex function for selective edge enhancement on amplitude objects starts with a similar form to that for isotropic vortex functions and can be expressed as [55]

$$S(\rho, \theta) = \exp\left(j\theta \left| \sin^m(\theta/2) \right|\right) = \exp(j\psi_s), \tag{122}$$

where ψ_s is the phase function similar to Eq. (100) corresponding to the anisotropic vortex function $S(\rho, \theta)$, the modulus of the sine function is to preserve the helical shape of the vortex, and m is an integer. The modulo 2π operation is used to wrap the phase, θ, between $-\pi$ and π. The rate of change of phase is

$$\frac{d\psi_s}{d\theta} = \left| \sin^{m-1}(\theta/2) \left[\sin(\theta/2) + \frac{m\theta}{2} \cos(\theta/2) \right] \right| . \tag{123}$$

The phase profile plot for the vortex function in Eq. (122) is shown in Figure 60 (a) with (b) showing the monotonic nature of the phase variation as function of θ. The plot of rate of change of phase of function $S(\rho, \theta)$ as a function of azimuthal angle θ is shown in Figure 61. One can see from Figure 61 that the variation of phase with the azimuthal angle is not uniform and this non-uniformity is key for selective edge enhancement. Figure 61 also contains two values for m such that one sees that upon increasing the value the rate of change of phase becomes steeper and thus enhancement is more selective.

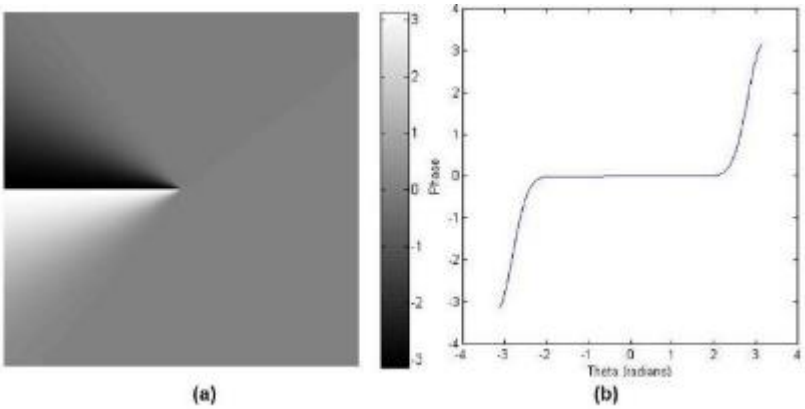

Figure 60 (a) Phase profile of function $S_{m=30}$ and (b) plot of phase of $S_{m=30}$ as function of $m\theta$.

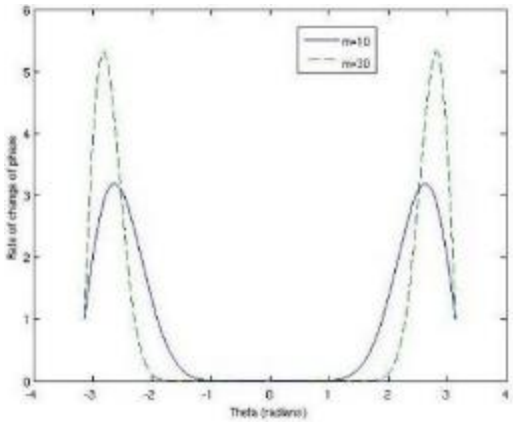

Figure 61 Plot of rate of change of phase of function S for $m = 10$ and $m = 30$ as a function of θ.

From Figure 60 and Figure 61 it has been shown that phase variation is the key enabler to selectively enhancing edges. Using the anisotropic vortex field $S(\rho, \theta)$ in Eq. (122) define its

corresponding Fourier transform as $s(r,\phi)$ such that the output of the 4-f system is given by the convolution of the input object with $s(r,\phi)$.

As the function is separable in polar coordinates, the Fourier transform of 4-f can be written using Eq. (93) where now

$$\begin{aligned} c_p &= \frac{1}{2\pi}\int_0^{2\pi} q_\Theta(\theta)\exp(-jp\phi)\,d\phi \\ &= \frac{1}{2\pi}\int_0^{2\pi} \exp\left(j\phi\left[\left|\sin^m(\phi/2)-p\right|\right]\right)d\phi \end{aligned}. \tag{124}$$

An analytic solution to the integral in Eq. (126) exists only if $p=\sin^m(\phi/2)$ where p is an integer and the function $\sin^m(\phi/2)$ assumes all values between 0 and 1. A plot of $\sin^m(\phi/2)$ is presented in Figure 62 which shows that for ϕ ranging between 0 to ϕ_1 and ϕ_2 to 2π the value is approximated to 0 and for ϕ ranging between ϕ_1 and ϕ_2 is approximated to 1. Thus approximating $|\sin^m(\phi/2)|$ as binary integer valued function one can find coefficients c_p in Eq. (124).

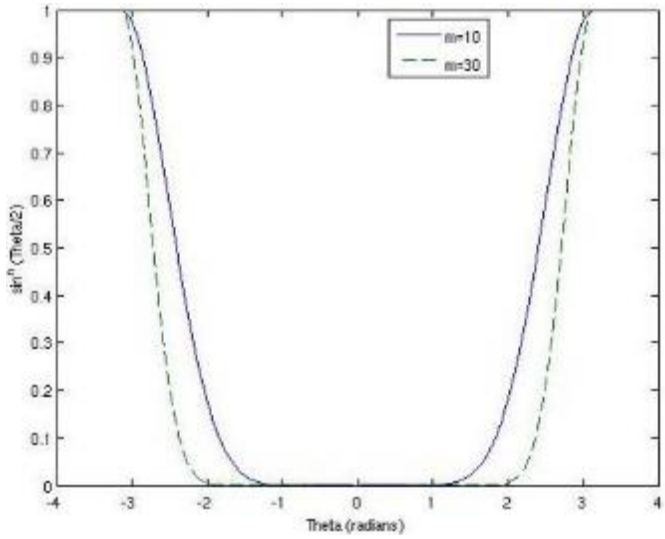

Figure 62 Plot of $|\sin^m(\phi/2)|$ for $m=10$ and $m=30$.

Restricting the vortex phase mask radially from 0 to R, the first-order Hankel transform can be calculated as in Eq. (96) and the zeroth-order Hankel transform is

$$H_0\{S_R(r)\} = 2\pi\int_0^\infty rS_R(r)\,J_0(2\pi\rho r/\lambda f)\,dr = xJ_1(x), \tag{125}$$

The expression for the Fourier transform of $S(\rho,\theta)$ can now be rewritten as

$$s(r,\phi) = c_0 H_0\{S_r(r)\} + c_1(-j)\exp(j\phi)\,H_1\{S_R(r)\}, \tag{126}$$

where

$$
\begin{aligned}
c_0 &= \frac{1}{2\pi}\int_0^{\phi_1} d\phi + \frac{1}{2\pi}\int_{\phi_2}^{2\pi} d\phi \\
&= \frac{1}{2\pi}\left(2\pi + \phi_1 - \phi_2\right) \text{for } 0 < \phi < \phi_1 \text{and } \phi_2 < \phi < 2\pi \\
&= 0 \text{ otherwise}
\end{aligned}
\quad , \tag{127}
$$

and

$$
\begin{aligned}
c_1 &= \frac{1}{2\pi}\int_{\phi_1}^{\phi_2} d\phi = \frac{1}{2\pi}\left(\phi_1 - \phi_2\right) \text{ for } \phi_1 < \phi < \phi_2 \\
&= 0 \text{ otherwise}
\end{aligned}
\quad . \tag{128}
$$

Plugging Eqs. (127) and (128) into Eq. (126) gives

$$
s\left(r,\phi\right) = \frac{2\pi + \phi_2 - \phi_1}{2\pi} x J_1\left(x\right) - j\exp\left(j\phi\right)\frac{\left(\phi_2 - \phi_1\right)}{2\pi}\frac{\pi R}{2\rho}\left[J_1\left(x\right)H_0\left(x\right) - J_0\left(x\right)H_1\left(x\right)\right], \tag{129}
$$

where ϕ_1 and ϕ_2 represent numerical values of the azimuthal angle. Thus from Eq. (129) one can see that $s\left(r,\phi\right)$ depends on the angular difference $\left(\phi_2 - \phi_1\right)$ which covers the region where the Fourier transform coefficients are nonzero or where $\left|\sin^m\left(\phi/2\right)\right|$ is approximated to 1. One can see in Figure 62 that upon increasing the value of m, $\left(\phi_2 - \phi_1\right)$ covers a smaller region and thus enhancement selectivity is obtained. Region-selective edge enhancement has thus been analytically illustrated with $S\left(\rho,\theta\right)$ and edge enhancements in smaller regions result by increasing the power m of the sine function.

While selective edge enhancement has been discussed using this approach, the ability to enhance edges by orientation angle has not. Orientation selection can be accomplished via the proposed function $S\left(\rho,\theta\right)$ in Eq. (124) by adding θ_0 such that

$$
S\left(\rho,\theta\right) = \exp\left[j\left(\theta + \theta_0\right)\left|\sin^m\left(\theta + \theta_0/2\right)\right|\right]. \tag{130}
$$

The addition of θ_0 in Eq. (130) rotates the orientation of the radial signum function of the vortex mask and thus selective edge enhancement in different azimuthal directions can be achieved. For the function in Eq. (132) the phase difference between two radially opposite directions is not π but varies from 0 to π and thus edge enhancement results at the positions where the phase difference is π. The phase difference results from the weighting of the Hankel transform where it is a maximum when the signum function exists. A plot of the phase difference for radially opposite positions of the proposed function is shown in Figure 63. One can see from Figure 63 that the phase difference in radially opposite directions for the proposed anisotropic function is a quantity

that varies according to orientation via azimuth angle whereas for the isotropic vortex phase function it is π for all orientations. The plot reaffirms that wherever the orientation is π the edge is enhanced and for the remaining values the signum function does not exist and thus the edges are not enhanced.

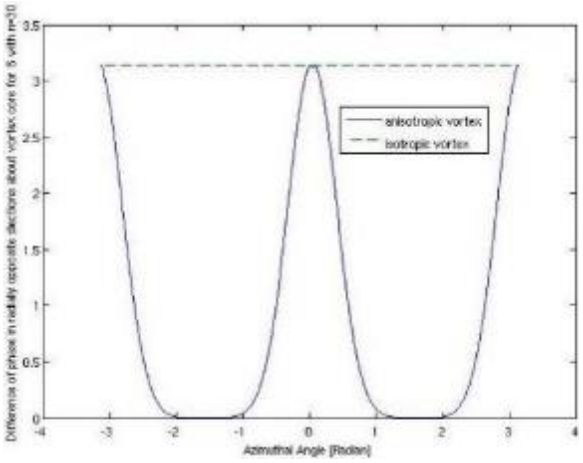

Figure 63 Phase difference between two radially opposite points about the phase singularity for function S with $m = 30$ and for an isotropic vortex.

The first set of results in Figure 64 display selective edge enhancement using the function $S(\rho, \theta)$ in Eq. (130) with the value of $m = 10$ fixed and varying the value of $\theta_0 = 0, \pi/4, \pi/2, \text{and } 3\pi/4$. One can see in the figure that as the value of θ_0 changes the enhanced region moves accordingly. The set of results in Figure 65 are simulations with $\theta_0 = 0$ to show the effect of increasing the power m in the function $S(\rho, \theta)$ to narrow the selected edge enhancement. A further examination by taking a cross section as indicated by the red line in Figure 65 and plotting intensity distribution is provided in Figure 66. The plots in this figure further emphasize how for smaller power m as in Figure 66 (a) the edge is broader than for larger power as in Figure 66 (d). Thus, it has been shown that the function can achieve orientation and region selective edge enhancement for a simple object.

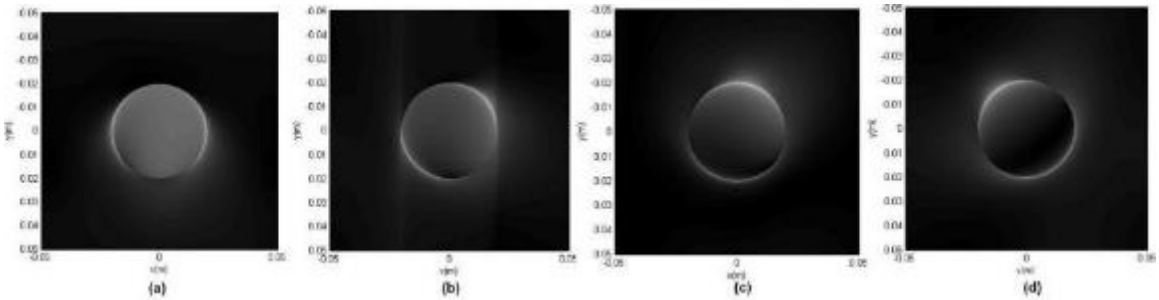

Figure 64 Simulation results of selective edge enhancement for a circular aperture using the anisotropic vortex function S when $m = 10$ and $\theta_0 = 0, \pi/4, \pi/2, \text{and } 3\pi/4$ (a-d), respectively.

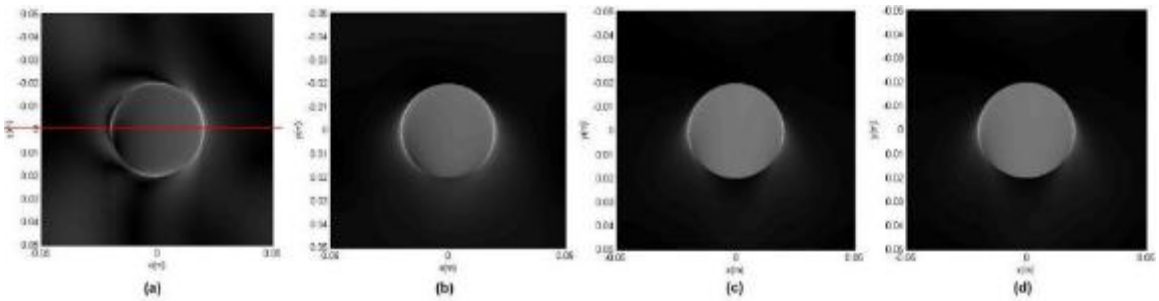

Figure 65 Simulation results to show the effect of increasing m in the function S on selectivity (a-d) show that the region of edge enhancement narrows with the power of $m = 5, 10, 30, \text{and } 50$ respectively.

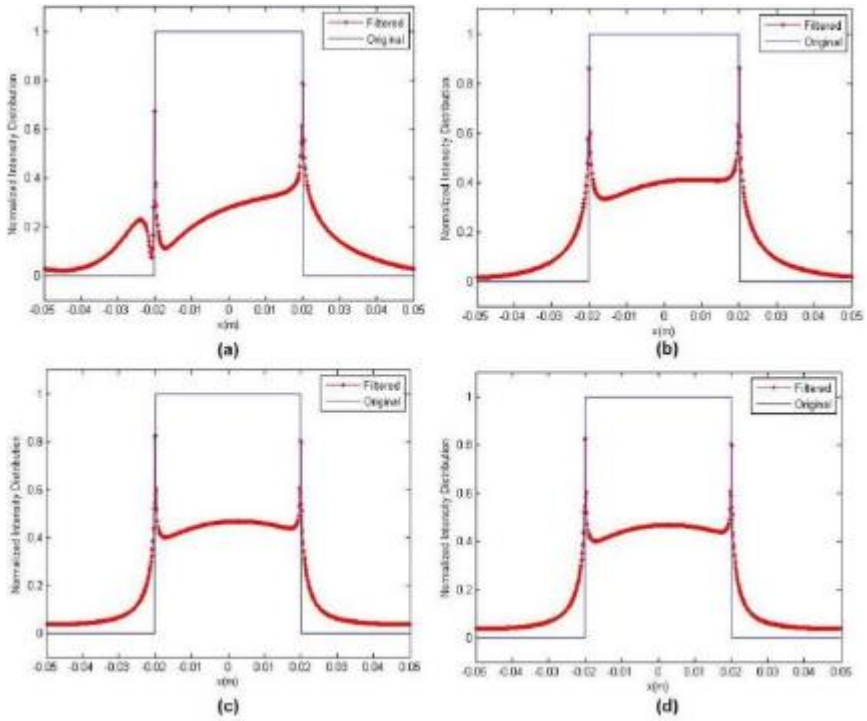

Figure 66 Cross section of Figure 65 (a-d) to further show edge enhancement narrowing for increasing power m.

5.3 Generating Optical Vortex with Diffractive Optics for Plane Wave

A computer generated hologram can theoretically be produced by recording the interference pattern between a plane wave and an optical vortex on a photoplate such that when a plane reference wave illuminates the grating it would produce an optical vortex identical to the former. The phase dependence in the azimuthal direction results in the splitting of the central fringe into $|m|$ new fringes with formation of the fork structure as seen in Figure 67 (c). The first CGH grating with this fork structure was realized by Bazenhov, Vasnetsov, and Soskin (1990) [63] and can be

implemented either as an amplitude or phase grating calculated as the addition modulo 2π of a helical phase $\exp(jm\theta)$ with a diffraction grating.

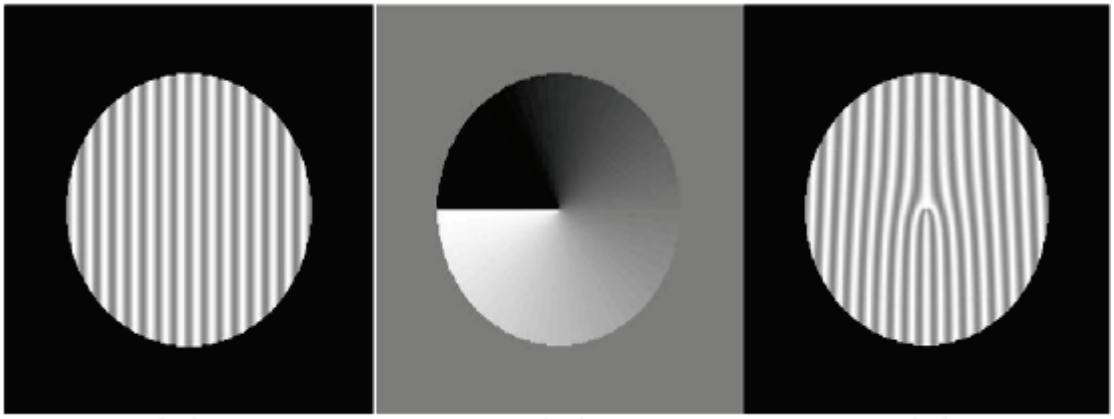

Figure 67 Combining the (a) binary grating and (b) spiral phase mask produces a (c) fork grating.

The pattern of the fork hologram is the interferogram of two waves, a planar reference wave and an object wave that contains the holographic image. The object wave is the simplest representation of an optical vortex on an infinite background field of amplitude C_1 as

$$E_{obj} = C_1 \exp(jm\theta) \exp(-jkz), \tag{131}$$

where m again is the topological charge and θ is an angle in the plane transverse to the direction of propagation. Assume the recording device is located at $z = 0$ and the point vortex is of unit charge, $m = 1$, Eq. (131) becomes

$$E_{obj} = C_1 \exp(j\theta). \tag{132}$$

The reference wave of amplitude C_0 has a wave vector that subtends the optical axis at angle ψ_1

$$E_{ref} = C_0 \exp\left(\frac{-j2\pi x}{\Lambda}\right), \tag{133}$$

where $\Lambda = \lambda / \sin\psi_1$ is the spatial period of the plane wave in the transverse plane. Unity contrast, $((I_{max} - I_{min})(I_{max} = 1))$, is achieved by letting $C_0 = C_1$ such that the resulting interferogram can be expressed as

$$I_{z=0}(x, \theta) = |E_{ref} + E_{obj}|^2_{z=0} = 2C_0^2 [1 + \cos(2\pi x/\Lambda + \theta)]. \tag{134}$$

Alternatively, one can express the transmission function in terms of a power spectrum of the Fourier series [64]

$$T(x,\phi) = \sum_{-\infty}^{\infty} C_m \exp(jm\phi) \exp\left(\frac{j2\pi mx}{\Lambda}\right). \tag{135}$$

Building the hologram to maximize the efficiency of diffraction in a particular order of diffraction results in a transmission function expressed by

$$T(x,\phi) = C_0 \exp\left[j\alpha \cos\left(m\phi - \frac{2\pi}{\Lambda} r\cos\phi\right)\right], \tag{136}$$

where α is the amplitude of the phase modulation, C_0 is the constant absorption coefficient of the hologram, and Λ is the period of the grating (fringe spacing).

The interference pattern between the plane wave and optical vortices are characterized by a fork in the center. The charge of the vortex can be found by counting the number of forks or subtracting one from the number of prongs as seen in Figure 68.

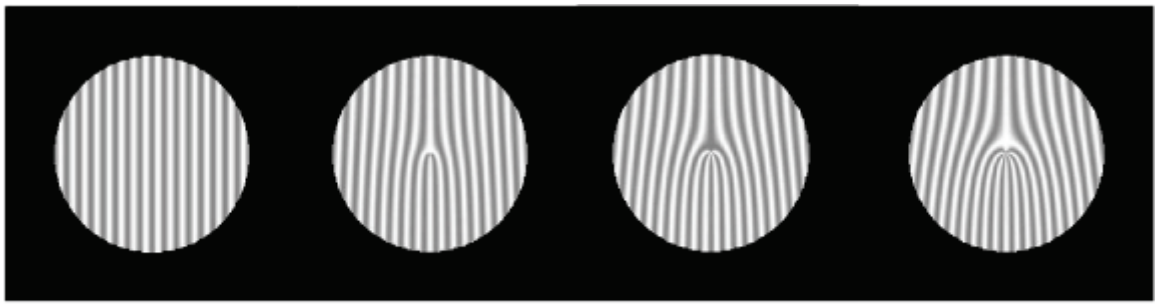

Figure 68 An (a)$m = 0$, (b)$m = 1$, (c)$m = 2$, and (d)$m = 3$ fork grating.

5.4 Spiral Phase-Kernel Analysis for Plane Wave

In Section 5.2.1 it was demonstrated that the result of the vortex filter process can be derived by a convolution of the original object function $g(x,y)$ with the vortex kernel, which corresponds to the Fourier transform of the mirrored filter function $\exp(j\theta)$ as

$$s(r,\phi) = \frac{-1}{\lambda f} \int\int_{\text{Aperture}} \exp[j\phi(\mu,\nu)] \exp\left(-j\frac{2\pi}{\lambda f}(x\mu + y\nu)\right) d\mu d\nu, \tag{137}$$

where in polar coordinates $x = r\sin\phi$ and $y = r\sin\phi$, $\mu = \rho\cos\theta$ and $\nu = \rho\cos\theta$. Using the trigonometric sum formula, Eq. (137) becomes

$$s(r,\phi) = \frac{\exp(j\phi)}{\lambda f}\int_{\rho=0}^{\rho_{max}}\int_{\theta=0}^{2\pi}\rho\exp(-j\theta)\exp\left(-j\frac{2\pi}{\lambda f}r\rho\cos\theta\right)d\rho d\theta \quad (138)$$

Using the integral representation of Bessel functions of the first kind [65], $J_m(x) = j^{-m}/2\pi\int_{2\pi}^{\theta=0}\exp(jz\cos\theta)\exp(jm\theta)\,d\theta$, Eq. (138) can be simplified as

$$s(r,\phi) = \frac{2\pi}{\lambda f}j\exp(j\phi)\int_{\rho=0}^{\rho_{max}}\rho J_1\left(\frac{2\pi}{\lambda f}r\rho\right)d\rho \quad (139)$$

where J_1 is the Bessel function of the first kind, λ the light wavelength, and f the focal length of the two lenses which perform the Fourier transform.

The explicit integrated, analytical form of Eq. (139) which is related to the field distribution of a doughnut mode is [66]

$$s(r,\phi) = j\exp(j\phi)\frac{\pi\rho_{max}}{2r}\left[J_1\left(\frac{2\pi}{\lambda f}r\rho\right)H_0\left(\frac{2\pi}{\lambda f}r\rho\right) - J_0\left(\frac{2\pi}{\lambda f}r\rho\right)H1\left(\frac{2\pi}{\lambda f}r\rho\right)\right]. \quad (140)$$

For comparison consider the convolution kernel of a simple two-lens imaging system without vortex filter

$$s_s(r,\phi) = \frac{2\pi}{\lambda f}\int_{\rho=0}^{\rho_{max}}\rho J_0\left(\frac{2\pi}{\lambda f}r\rho\right)d\rho = \frac{\rho_{max}}{r}J_1\left(\frac{2\pi}{\lambda f}r\rho_{max}\right), \quad (141)$$

where $s_s(r,\phi)$ is the point spread function of a circular aperture with radius ρ_{max}.

Comparing Eqs. (138) and (141) the primary differences are in the orders of the Bessel functions and the vortex phase factor $\exp(j\phi)$, which causes the vortex kernel to be ϕ-dependent [67].

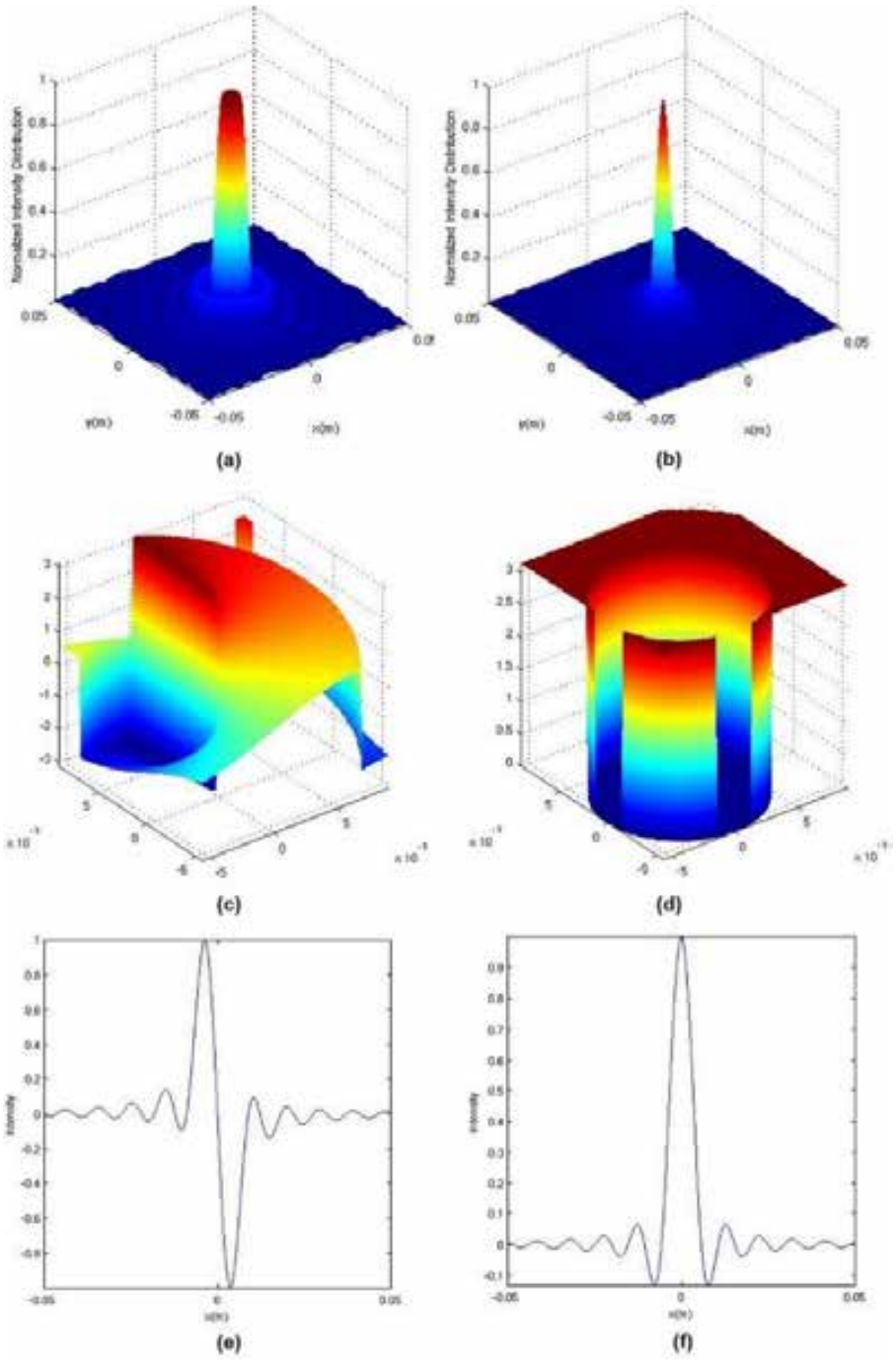

Figure 69 (a) Spiral kernel amplitude, (b) circular aperture transfer function amplitude, (c) and (d) phase of (a) and (b), respectively, and (e) and (f) real part of kernel cross section, respectively.

One can see from Figure 69 (a) and (b) as well as (e) and (f) that the spiral kernel has a doughnut shape and is broader than the PSF which suggests potential decrease in resolution as a

result of vortex filtering. In (c) and (d) the previously mentioned azimuthal dependence of the spiral kernel is shown where as there is none for the circular aperture.

The next section will discuss and simulate the generation of optical vortices with lenses and spiral phase plate under Gaussian beam illumination.

5.5 Generating Optical Vortex with Lenses and Spiral Phase Plate for Gaussian Beam

Analysis and results to this point have centered on the diffraction of a plane wave by a spiral phase plate however, Saks, Rozas, and Swartzlander (1998) and Peele and Nugent (2003) [68, 69] derived an analytical expression to describe diffraction a Gaussian beam by a SPP. In this situation the complex amplitude at $z = 0$ is represented as [70]

$$S_m^0(\rho,\theta) = \exp\left[-(\rho/w)^2 + jm\theta\right], \tag{142}$$

where ω is the width of the beam waist and as before (ρ,θ) represent polar coordinates. The paraxial approximation of the light field's complex amplitude at a distance d via Fresnel diffraction is given by [71-73]

$$\begin{aligned} s_m(r,\phi;d) &= \frac{-jk}{2\pi d}\int_0^{\infty}\int_0^{2\pi} s_m^0(r,\phi)\exp\left(\frac{jk}{2d}\left[r^2+\rho^2-2r\rho\cos(\phi-\theta)\right]\right) r dr d\phi \\ &= \frac{(-j)^{m+1}}{2}\frac{{d_0}^2}{d}\frac{\rho}{\omega}\left[1+\left(\frac{{d_0}^2}{d}\right)\right]^{-3/4} \\ &\times \exp\left(\frac{3j}{2}\tan^{-1}\frac{d_0}{d} - \frac{jk\rho^2}{2R_0(d)} + \frac{jk\rho^2}{2d} - \frac{\rho^2}{\omega^2(d)} + jm\phi\right) \\ &\times \left(I_{m-1/2}\left\{\rho^2\left[\frac{1}{\omega^2(d)}+\frac{jk}{2R_0(d)}\right]\right\} - I_{m+1/2}\left\{\rho^2\left[\frac{1}{\omega^2(d)}+\frac{jk}{2R_0(d)}\right]\right\}\right), \end{aligned} \tag{143}$$

where I_ν is the Bessel function of the second kind and νth order and $\omega^2(d) = 2\omega^2\left[1+(d/d_0)^2\right]$, $R_0(d) = 2d\left[1+(d/d_0)^2\right]$, and $d_0 = \frac{k\omega^2}{2}$.

5.5.1 MATLAB Simulation: Spiral Phase Plate Filtering for Gaussian Beam

A vortex is simulated in MATLAB using the expression in Eq. (143) for a spiral phase plate with a Gaussian beam. The parameters for the implementation are $d = 138.15mm$, $f = 300mm$, $\omega = 2mm$, and $\lambda = 633nm$. The input image is a slightly larger diameter white circle black background than before sampled at 1024×1024 with the filtered output result presented in Figure 70 (a) and (b) for $d = 0mm$ and $d = 138.15mm$, respectively. One can see from the filtered outputs how the edges have been enhanced leaving almost a negative relief of the original image but with slightly decreased intensity as seen in the intensity distributions of Figure 70 (c). The results for $d = 0mm$ in (d) are less symmetric with varying intensity values at the two edges and different side-lobe width for the left and right side of each edge.

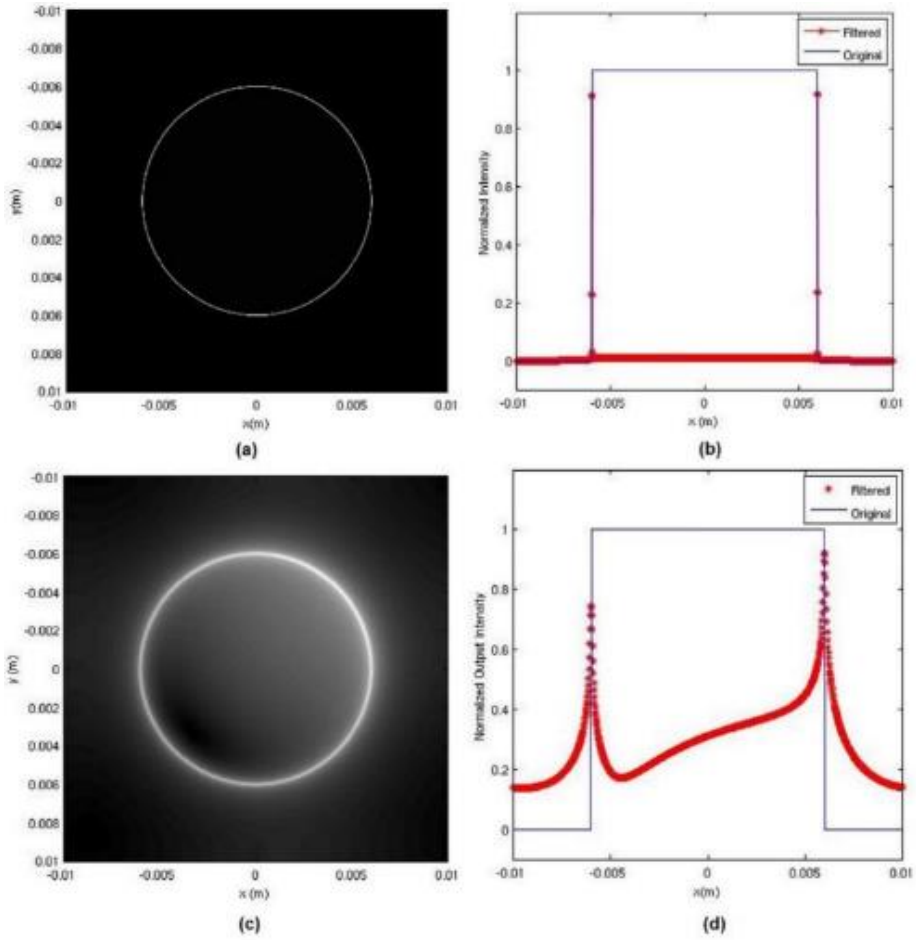

Figure 70 (a) Spiral phase filtering result $d = 0mm$, (b) corresponding intensity distribution, (c) spiral phase filtering result $d = 138.15mm$, and (d) corresponding intensity distribution.

The next section will discuss and simulate optical vortices with lenses and different variations of composite spiral phase plates under Gaussian beam illumination.

5.6 Generating Optical Vortex with Lenses and Composite Spiral Phase Plate for Gaussian Beam

In Section 5.2.2.1 it was shown that a filter made up of the superposition of two optical vortices can perform directional edge enhancement. In this section the idea is extended to investigate enhancement effects that result from shifting symmetric optical vortices of the same charge and opposite charge.

The results for the composite vortices will be compared to a single optical vortex shifted to center (ρ_0, θ_0) illuminated by a Gaussian beam expressed as [60,74]

$$S_m^0(\rho, \theta, \rho_0, \theta_0) = \exp\left[-(\rho_{s+}/\omega)^2 + jm\theta_{s+}\right], \tag{144}$$

where $\theta_{s+} = \tan^{-1}(y - y_0/x - x_0)$ and $\rho_{s+} = \sqrt{(x - x_0)^2 + (y - y_0)^2}$.

The complex amplitude for two symmetric optical vortices as depicted in Figure 71 adds a second vortex to Eq. (144) with a phase shift of π expressed as [10,74]

$$S_{+m}^0(\rho, \theta, \rho_0, \theta_0) = \exp\left[-(\rho_{s+}/\omega)^2 + jm\theta_{s+}\right] + \exp\left[-(\rho_{s-}/\omega)^2 + jm\theta_{s-}\right], \tag{145}$$

where $\rho_{s-} = \sqrt{(x + x_0)^2 + (y + y_0)^2}$ and $\theta_{s-} = \tan^{-1}(y + y_0/x + x_0)$.

The complex amplitude for two symmetric optical vortices of opposite charge changes one of the charges in Eq. (145) expressed as [10, 74]

$$S_{+m}^0(\rho, \theta, \rho_0, \theta_0) = \exp\left[-(\rho_{s+}/\omega)^2 + jm\theta_{s+}\right] + \exp\left[-(\rho_{s-}/\omega)^2 - jm\theta_{s-}\right]. \tag{146}$$

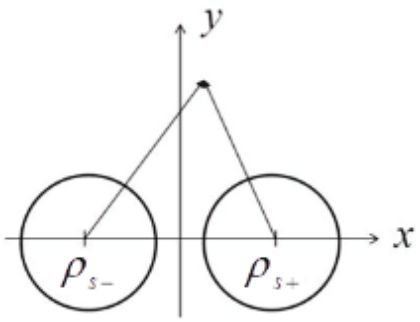

Figure 71 Composite spiral phase plate separated by ρ_s.

5.6.1 MATLAB Simulation: Composite Spiral Phase Plate Filtering for Gaussian Beam

The MATLAB simulation uses the same input image and parameters as Section 5.5.1. The intensity distribution and filtered output using Eq. (144) for $\rho_0 = 0, 0.0025, \text{and } 0.005$ and $\theta_0 = 0$ are shown in Figure 72 (a-c) and (d-f), respectively. As expected, as ρ_0 is closer to the origin the filtering is more isotropic and as ρ_0 moves further away from the origin the filtering is more selective.

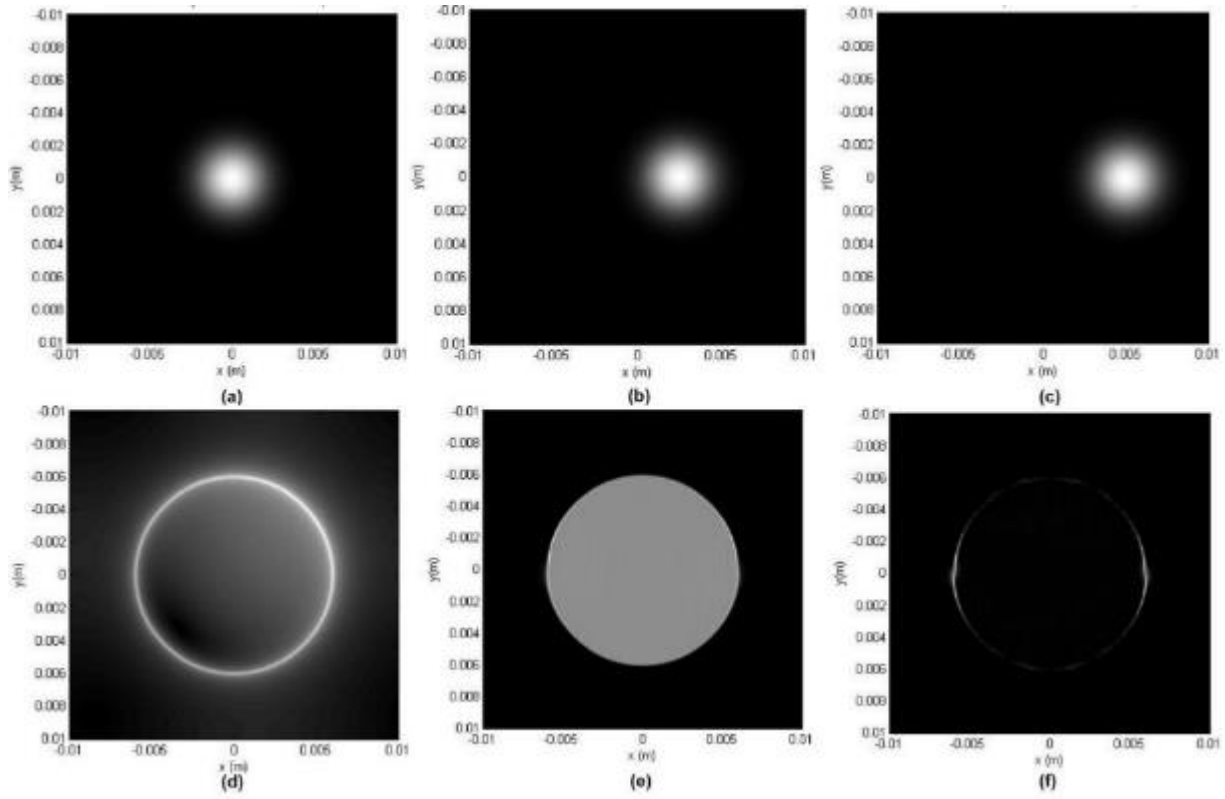

Figure 72 Vortex profile for single optical vortex with Gaussian beam shifted $\theta_0 = 0$ and $\rho_0 = 0, 0.0025, \text{and } 0.005$ (a-c), and corresponding filtered output (d-f).

The intensity distribution and filtered output for composite same charge vortices using Eq. (145) for $\rho_0 = 0.0025 \text{ and } 0.005$ and $\theta_0 = 0$ are shown in Figure 73 (a-b) and (c-d), respectively. As the shift and separation distance increases, the filtered output is noisier at the extracted edge which becomes more and more prominent. This effect results because the two symmetrically offset SPP corresponds to double-sided filtering which gives a second-order derivative [75]. The double-sided filtering gives zero-crossing detection on the edge and is the reason a double-line is observed at the edge location in the filtered output.

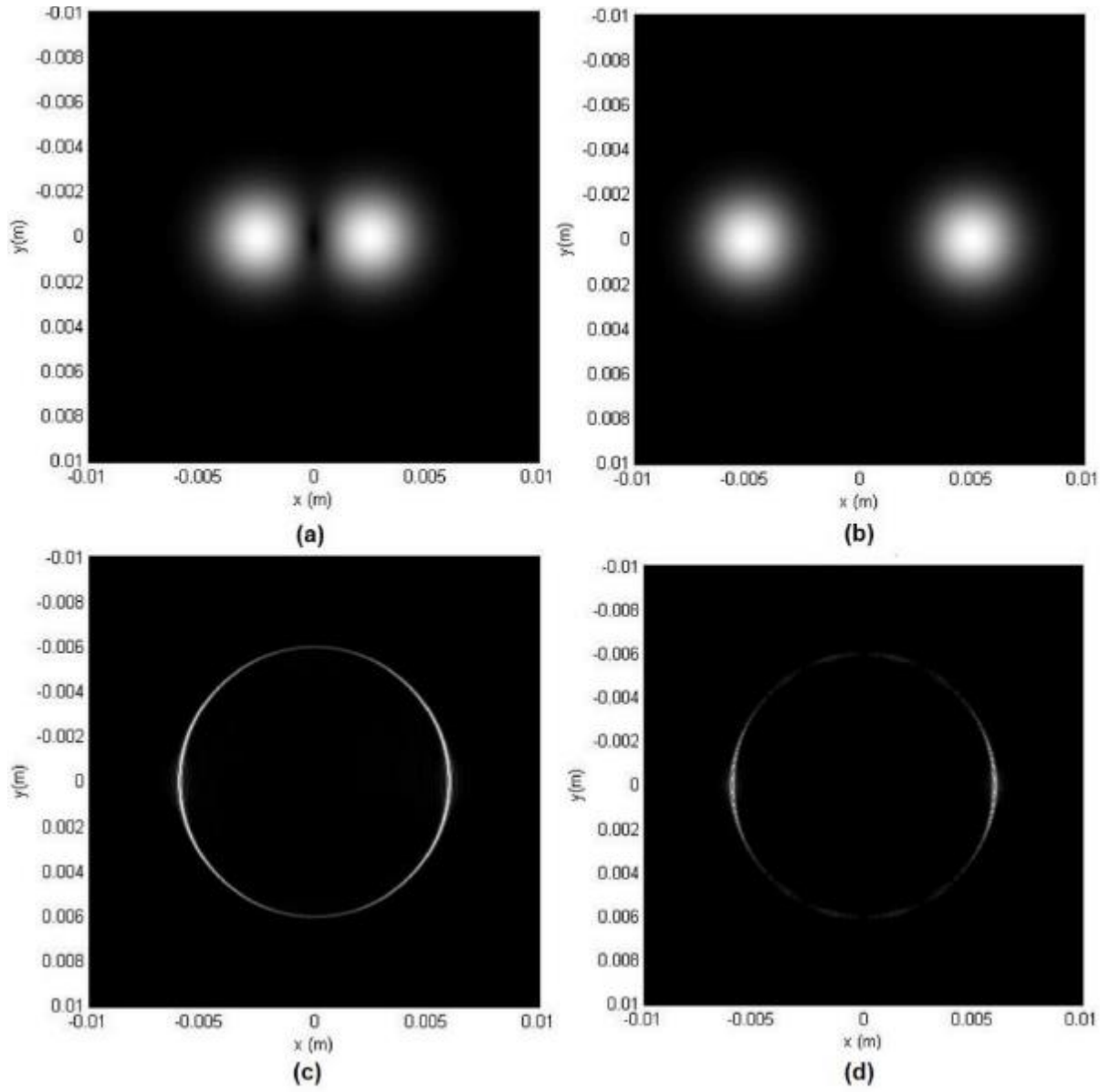

Figure 73 Vortex profile for double optical vortex with Gaussian beam shifted $\theta_0 = 0$ and $\rho_0 = 0.0025 \text{ and } 0.005$ (a-b), and corresponding filtered output (c-d).

The intensity distribution and filtered output for composite opposite charge vortex using Eq. (146) for $\rho_0 = 0.0025 \text{ and } 0.005$ and $\theta_0 = 0$ are shown in Figure 74 (a-b) and (c-d), respectively. The filtered output demonstrates that selective edge enhancement is maintained even as displacement is increased.

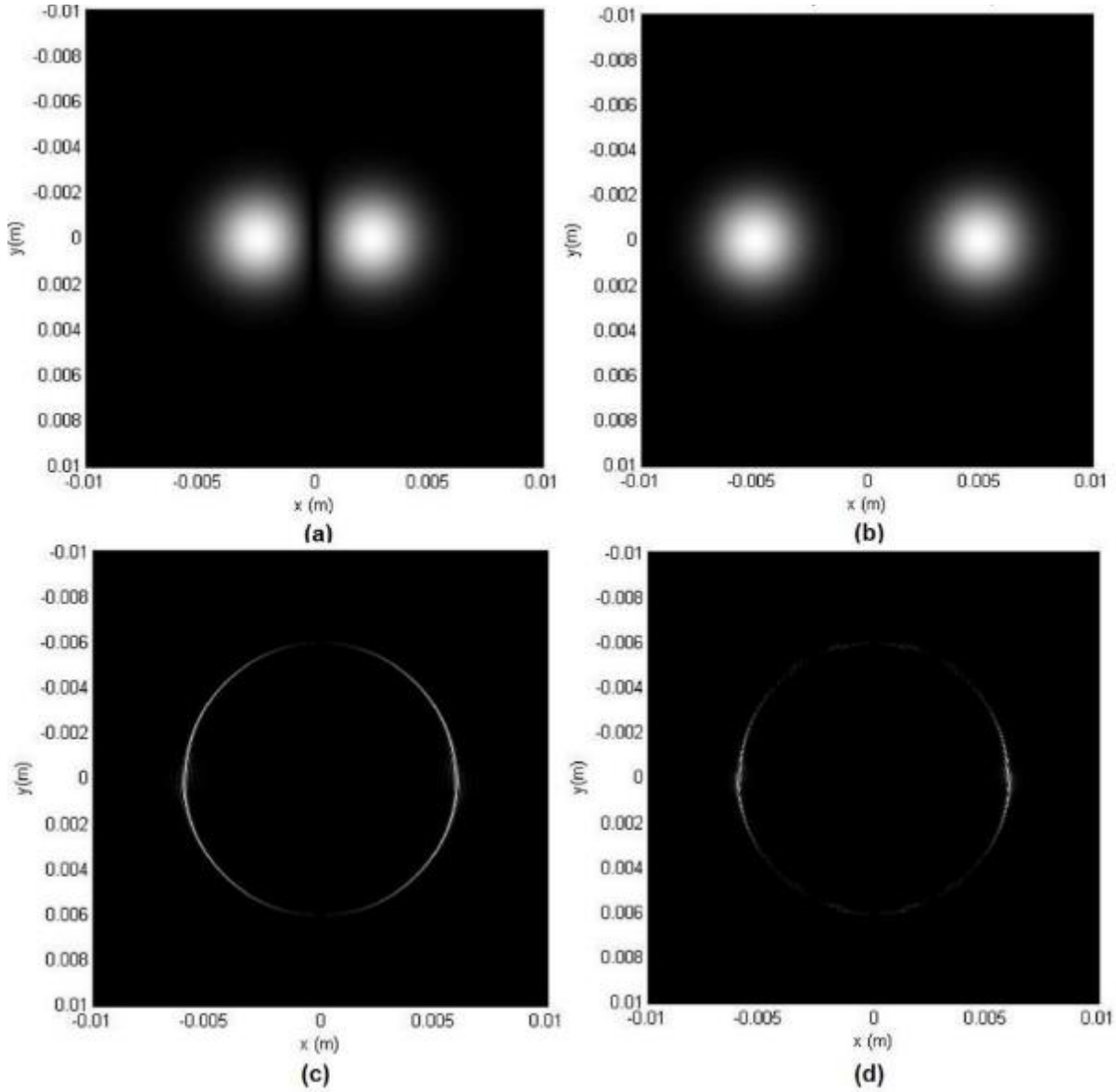

Figure 74 Vortex profile for opposite charge double optical vortex with Gaussian beam shifted $\theta_0 = 0$ and $\rho_0 = 0.0025$ and 0.005(a-b), and corresponding filtered output (c-d).

The intensity distribution and filtered output for composite same charge vortices using Eq. (145) for $\rho_0 = 0.0025$ and $\theta_0 = 0$ and $\theta_0 = \pi/2$ are shown in Figure 75 (a-b) and (c-d), respectively. These results illustrate how changing the filter orientation from horizontal to vertical retains edge enhancement but this time in the orientation of the filter.

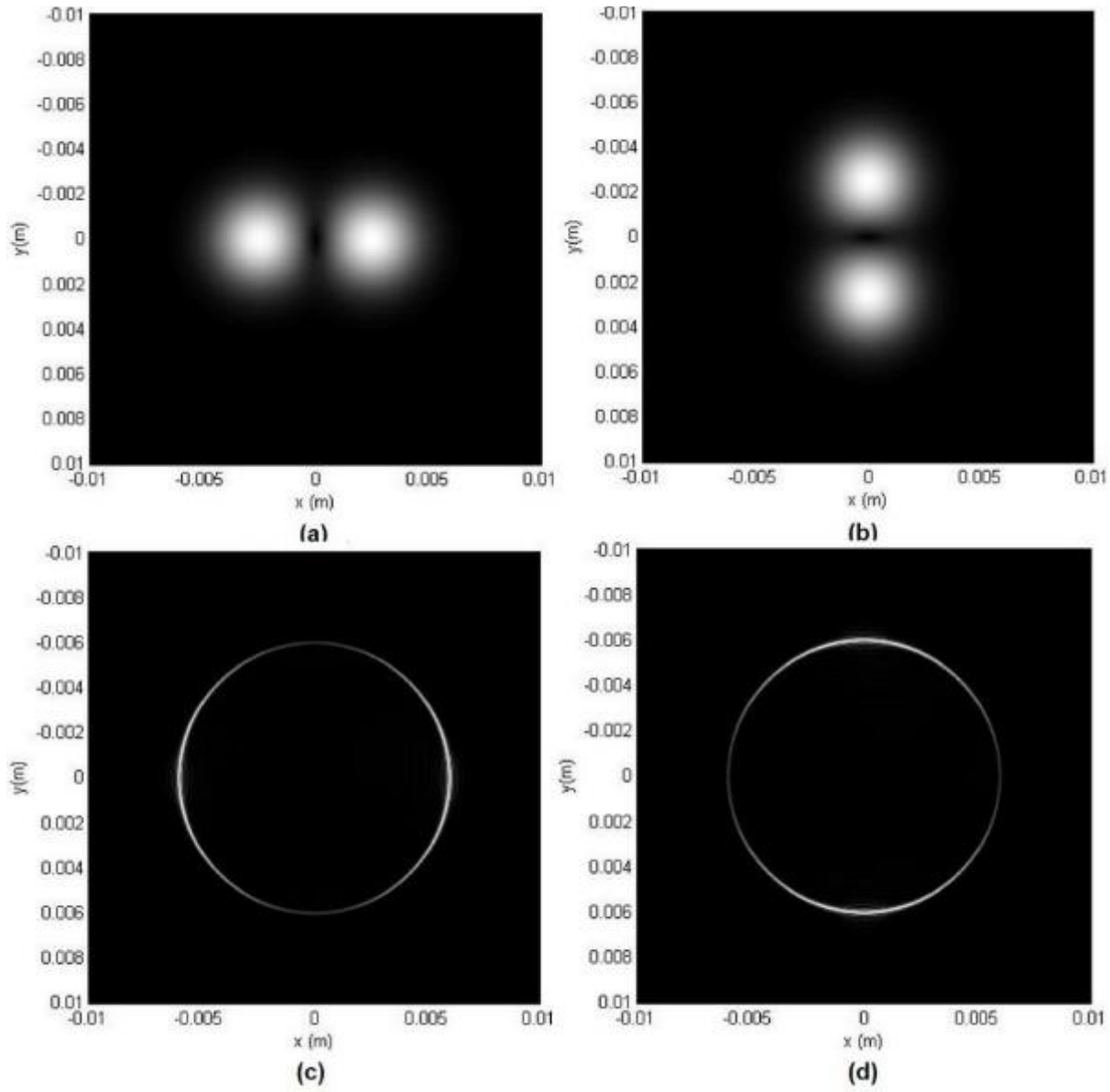

Figure 75 Vortex profile for double optical vortex with Gaussian beam shifted $\rho_0 = 0.0025$ and $\theta_0 = 0 \text{ and } \pi/2$ (a-b), and corresponding filtered output (c-d).

The intensity distribution and filtered output for composite same charge vortices using Eq. (145) for $\rho_0 = 0, 0.0025, 0.005, \text{and } 0.0075$ and $\theta_0 = 3\pi/4$ are shown in Figure 76 (a-d) and (e-g), respectively. The edges in the direction of orientation are enhanced for all values of ρ_0 such that as the distance from the origin increases the contribution from all edges decreases.

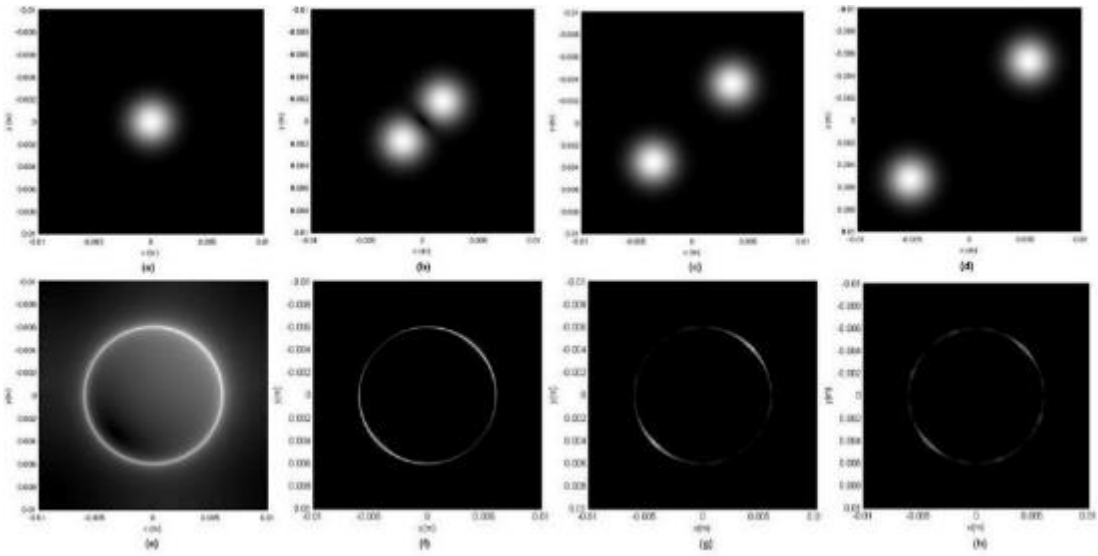

Figure 76 Vortex profile for double optical vortex with Gaussian beam shifted $\rho_0 = 0, 0.0025, 0.005, \text{and } 0.0075$ and $\theta_0 = 3\pi/4$ (a-d), and corresponding filtered output (e-g).

The intensity distribution and filtered output for composite opposite charge vortices using Eq. (146) for $\rho_0 = 0, 0.0025, 0.005, \text{and } 0.0075$ and $\theta_0 = 3\pi/4$ are shown in Figure 77 (a-d) and (e-g), respectively. The filtered output contains edge enhancement with contribution from the center for $\rho_0 = 0.0025$ but as ρ_0 increases the selective enhancement effects increase in the orientation of θ_0 such that contributions from the center are no longer present.

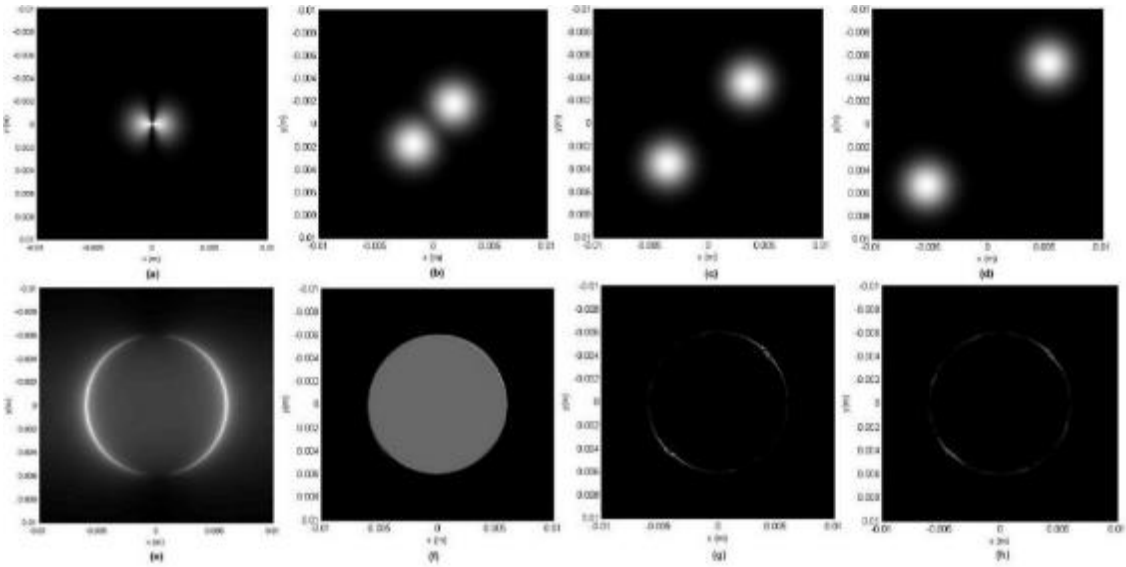

Figure 77 Vortex profile for opposite charge double optical vortex with Gaussian beam shifted $\rho_0 = 0, 0.0025, 0.005, \text{and } 0.0075$ and $\theta_0 = 3\pi/4$ (a-d), and corresponding filtered output (e-g).

5.6.2 Analysis: Composite Spiral Phase Plate Filter for Gaussian Beam

The previous section investigated the ability to tailor the amplitude and phase of the composite beam by adjusting the relative amplitude, phase, and displacement of the composite beams. This section investigates how the loss of symmetry results from violating the central singularity and angular symmetry of the spiral-phase function leading to topographic images with relief-like shadow effect [76]. The investigation focuses on the phase profile for amplitude, phase, displacement, and charge changes of composite beams.

When analyzing phase profiles there are two possible types of singularities, the first is a shear and the second is a vortex. A vortex singularity or screw dislocation is a spiral-phase ramp of 2π around the point of the phase singularity which is where the phase of the wave is undefined causing its amplitude to vanish [77]. A shear singularity or edge dislocation is π-phase shift so that instead of the phase being undefined along a point as in the vortex case, it is undefined along a line lying on a plane perpendicular to the direction of propagation [77].

The phase profile for the single optical vortex using Eq. (144) with $\rho_0 = 0$ and $\theta_0 = 0$ or $\theta_0 = \pi/2$ is shown in Figure 78. The cross-section along the x-axis shown in (b) contains one phase dislocation exists with the cross-section along the y-axis shown in (c) indicating that phase dislocation is an optical vortex of charge $+1$, in accordance with the phase singularity sign principle defined by Freund and Shvartsman (1994) [78]. Similar results are obtained for $\theta_0 = 0$ and $\rho_0 = 0.0025$ or $\rho_0 = 0.005$ with the phase dislocation shifted by ρ_0 as seen in Figure 79 (b) and (e), respectively. Likewise for $\theta_0 = \pi/2$ the cross-section along the y-axis contains an optical vortex shifted by either $\rho_0 = 0.0025$ or $\rho_0 = 0.005$ with a cross-section along the x-axis similar to the $\rho_0 = 0$ as seen in Figure 80 (c) and (f), respectively.

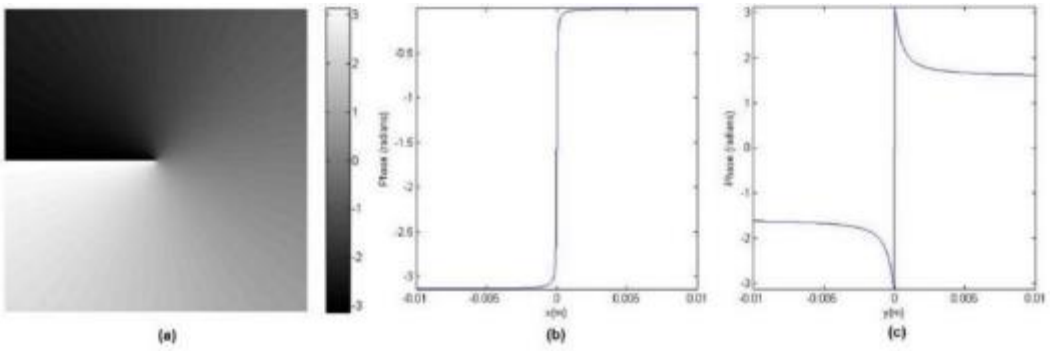

Figure 78 Single optical vortex for $\rho_0 = 0$ and $\theta_0 = 0$ or $\theta_0 = \pi/2$ a) phase profile, (b) cross-section along x-axis, and (c) cross-section along y-axis.

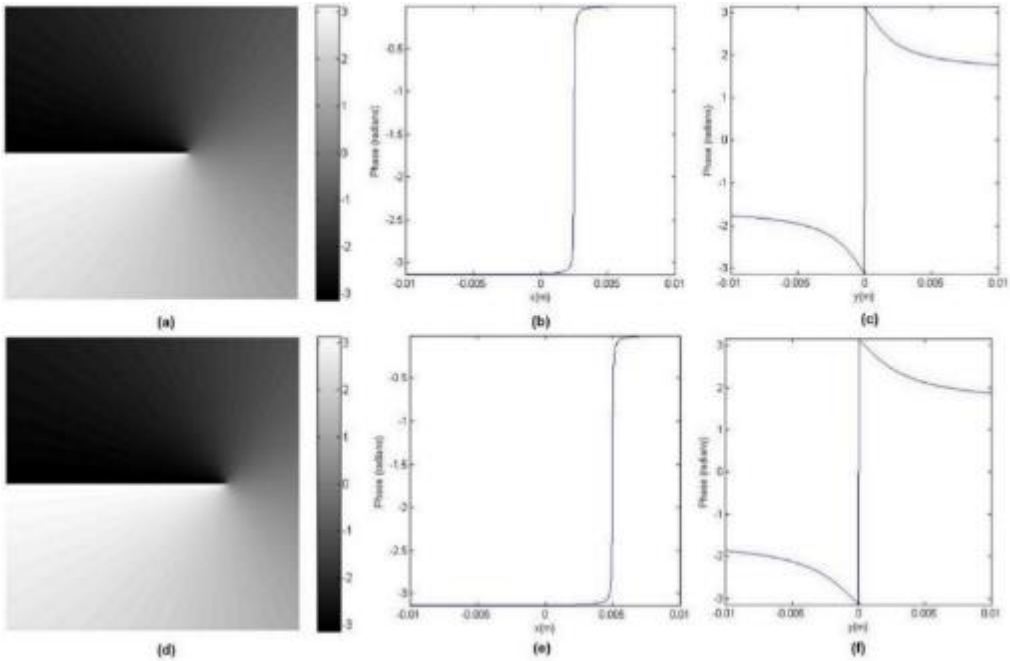

Figure 79 Single optical vortex for $\theta_0 = 0$ and $\rho_0 = 0.0025$ (a) phase profile, (b) cross-section along x-axis, (c) cross-section along y-axis and $\theta_0 = 0$ and $\rho_0 = 0.005$ (d) phase profile, (e) cross-section along x-axis, (f) cross-section along y-axis.

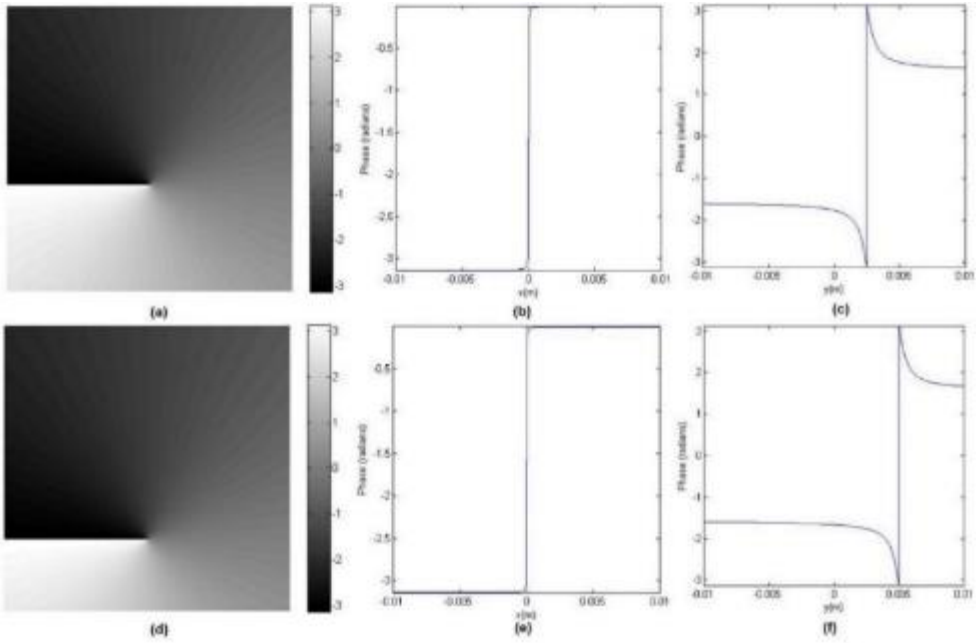

Figure 80 Single optical vortex for $\theta_0 = \pi/2$ and $\rho_0 = 0.0025$ (a) phase profile, (b) cross-section along x-axis, (c) cross-section along y-axis and $\theta_0 = \pi/2$ and $\rho_0 = 0.005$ (d) phase profile, (e) cross-section along x-axis, (f) cross-section along y-axis.

Generally, for finite separation new phase dislocations appear when the phases of the two beams do not match up such as in the region between them. This phase mismatch is a minimum

when the component beams have topological charge of opposite sign therefore one would not expect to see dislocations [76]. The phase mismatch is a maximum when the topological charge has the same sign such that dislocations form in the region between the two beams. Further discussion on anticipated results using opposite and same topological charge follows.

When the beams are collinear and their charges are opposite, $m_1 = -m_2$, only the center of the beam has a vortex, if any [79]. Using Eq. (146) $m_1 = 1$ and $\theta_0 = 0$ or $\theta_0 = \pi/2$, the phase profile of the collinear beams contains no vortices and one shear singularity at $\rho_0 = 0$ as seen in Figure 81 (b) and (c), respectively.

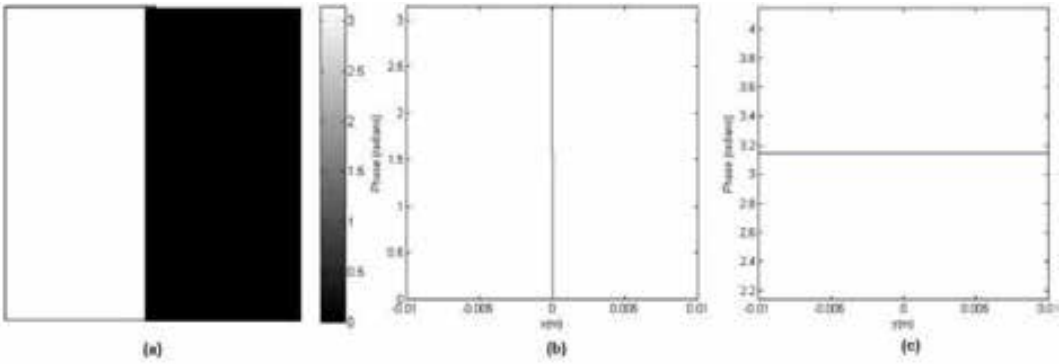

Figure 81 Collinear opposite charge optical vortices $\rho_0 = 0$ and $\theta_0 = 0$ or $\theta_0 = \pi/2$ (a) Phase profile, (b) cross-section along x-axis, and (c) cross-section along y-axis.

As the displacement increases vortices appear at the same angular locations as the shear singularities for the collinear case [80]. The vortices form as the displacement between the two beams increases because the beams stop sharing regions of equal phase such that the regions of destructive interference are no longer lines but instead become points. For the case of $m_1 = -m_2$ where $m_1 = 1$, there is expected to be two vortices, one of charge m_1 and one of charge m_2 [79]. Additionally, the region between the component beams is expected to have a phase that increases smoothly.

For $\theta_0 = 0$ and $\rho_0 = 0.0025$ the phase profile and cross-section along the x-axis shown in Figure 82 (a) and (b), respectively contain three phase dislocations. Examining the cross-section along the y-axis in Figure 82 (c) and (d) provides further insight into the three phase dislocations such that there is a vortex singularity of charge -1 at $\rho_0 = -0.0025$, a vortex singularity of charge $+1$ at $\rho_0 = 0.0025$, and a shear singularity of charge -1 at $\rho_0 = 0$. The additional shear singularity at the origin filters out the zeroth-order component of the Fourier transformed image and it is expected that edge enhancement will be strongest on the edges in the direction of $\theta = 0$ as was demonstrated in Figure 74 (c).

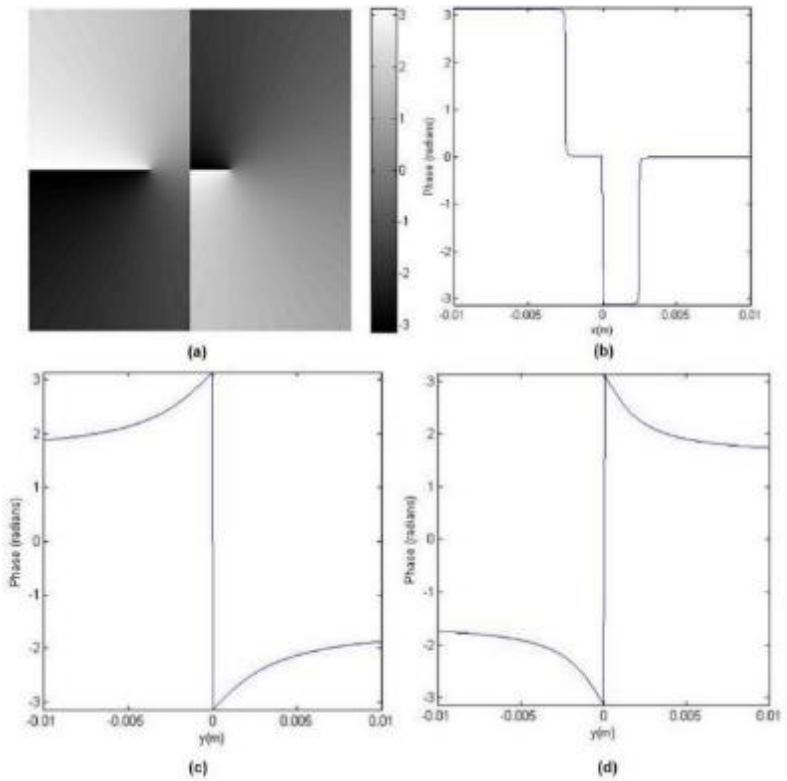

Figure 82 Displaced opposite charge optical vortices $\rho_0 = 0.0025$ and $\theta_0 = 0$ (a) phase profile, (b) cross-section along x-axis, (c) cross-section along y-axis $\rho_0 = -0.0025$, and (d) cross-section along y-axis $\rho_0 = 0.0025$.

In the case $\rho_0 = 0.0025$ and $\theta_0 = \pi/2$ the phase profile and cross-section along the x-axis are shown in Figure 83 (a) and (b), respectively indicate two phase dislocations. These phase dislocations are two are vortex singularities of charge ∓ 1 at $\rho_0 = \mp 0.0025$.

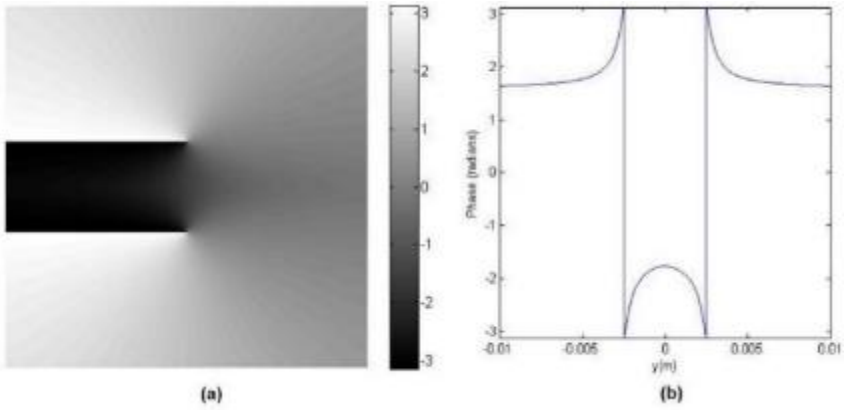

Figure 83 Displaced opposite charge optical vortices $\rho_0 = 0.0025$ and $\theta_0 = \pi/2$ (a) phase profile and (b) cross-section along x-axis.

Neither of the dislocations is aligned with the zeroth-order component of the Fourier transformed image as seen in Figure 84 (b) and the amplitude is non-zero between the two vortices as seen in Figure 84 (a). It is therefore expected that the filtered output at best the output will only

be partially suppressed and have a relief like appearance [81] which is consistent with results for $\theta_0 = 3\pi/4$ in Figure 77 (a) and (d).

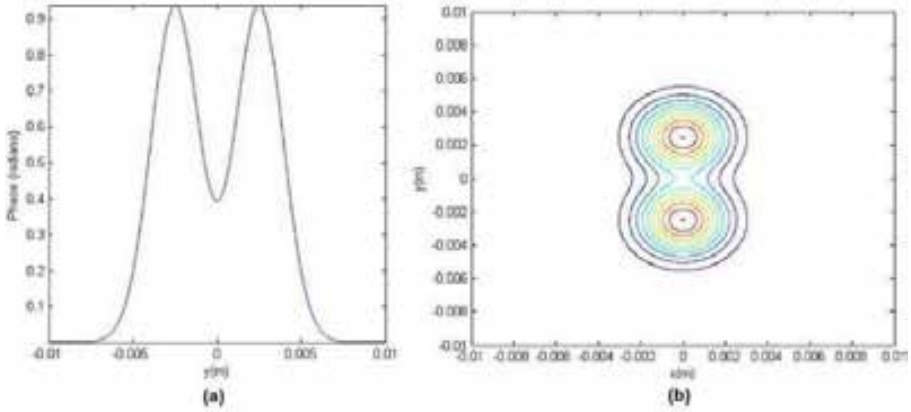

Figure 84 Displaced opposite charge optical vortices $\rho_0 = 0.0025$ and $\theta_0 = \pi/2$cross-section along y-axis (a) normalized intensity and (b) contour.

Increasing the separation to $\rho_0 = 0.005$, the phase profiles for $\theta_0 = 0$ and $\theta_0 = \pi/2$ produce the same number of vortex singularities and shear singularities as the $\rho_0 = 0.0025$ case as seen in Figure 85 and Figure 86, respectively. The filtered output for the $\theta_0 = 0$ case again contains orientation dependent enhancement as seen in Figure 74(d).

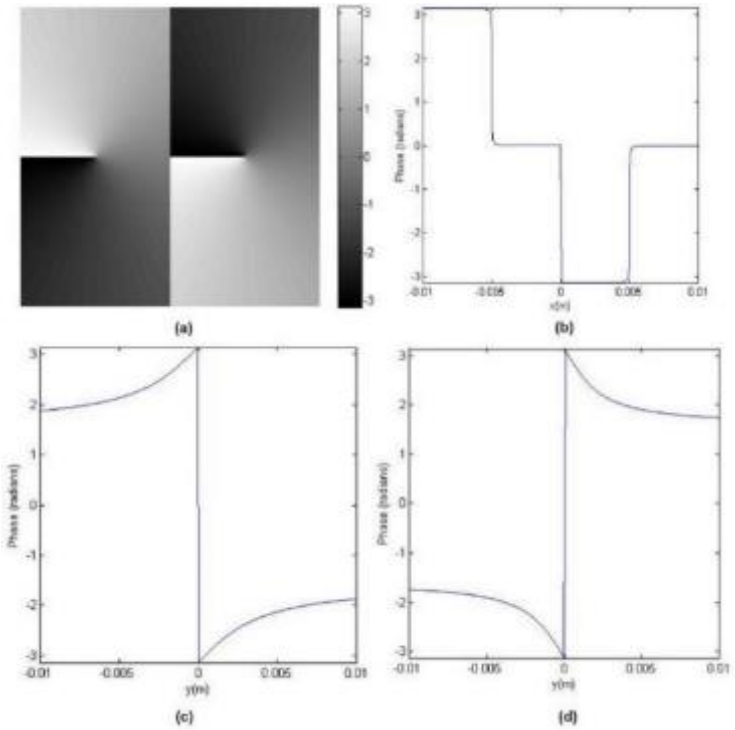

Figure 85 Displaced opposite charge optical vortices $\rho_0 = 0.005$ and $\theta_0 = 0$ (a) phase profile, (b) cross-section along x-axis, (c) cross-section along y-axis $\rho_0 = -0.005$, and (d) cross-section along y-axis $\rho_0 = 0.005$.

For the $\theta_0 = \pi/2$ case, the regions where the beams have similar phase are increased as seen in Figure 87 (b) but the corresponding region has some amplitude of zero as seen in Figure 87 (a). It is this zero amplitude which is anticipated to lead to filtering effects as demonstrated for $\theta_0 = 3\pi/4$ in Figure 77 (e).

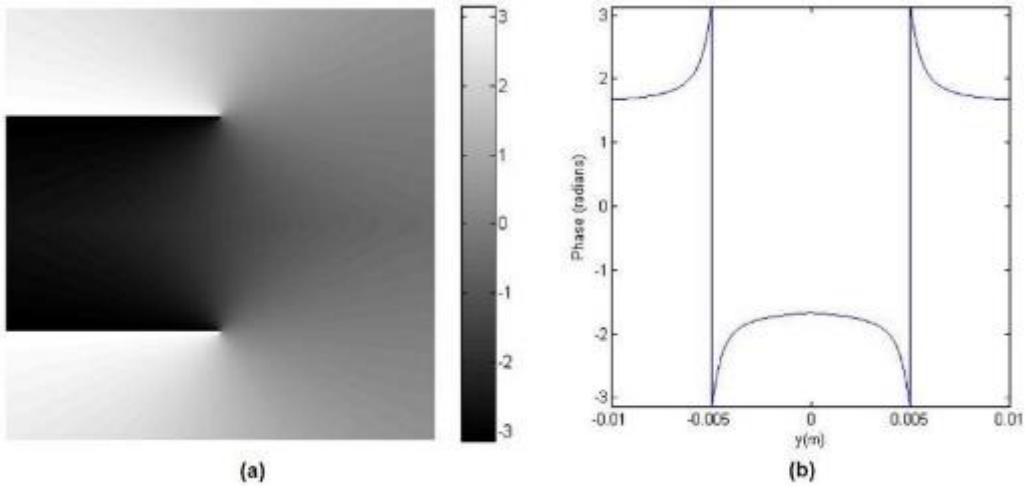

Figure 86 Displaced opposite charge optical vortices $\rho_0 = 0.005$ and $\theta_0 = \pi/2$ (a) phase profile and (b) cross-section along x-axis.

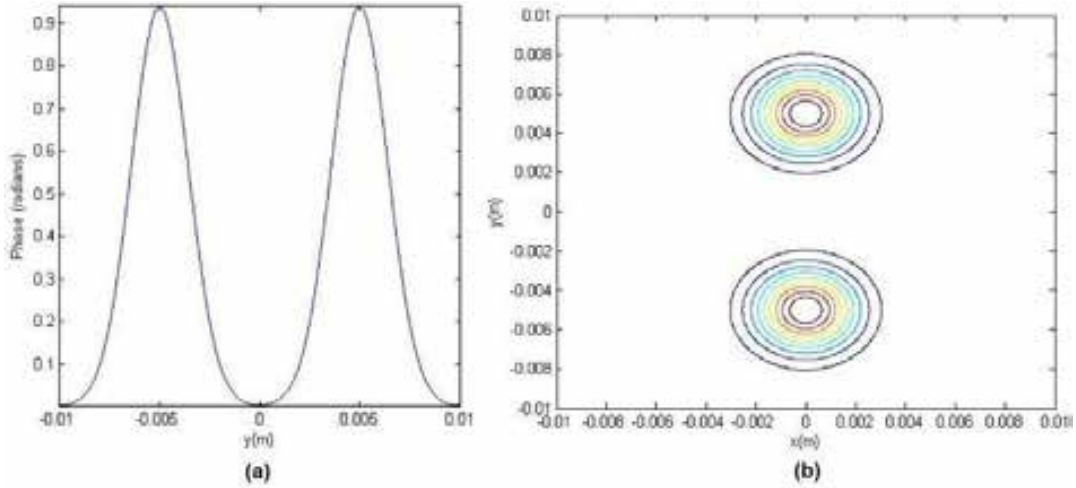

Figure 87 Displaced opposite charge optical vortices $\rho_0 = 0.005$ and $\theta_0 = \pi/2$ cross-section along y-axis (a) normalized intensity and (b) contour.

In the case where the component beams have topological charges of the same sign, $m_1 = m_2$, the composite pattern evolves from one central vortex and zero peripheral vortices to two vortices when the beams are displaced [80]. The collinear case using $m_1 = 1$ and $\theta_0 = 0$or $\theta_0 = \pi/2$ in Eq. (145) produces a $+1$ vortex singularity at $\rho_0 = 0$ as seen in Figure 88.

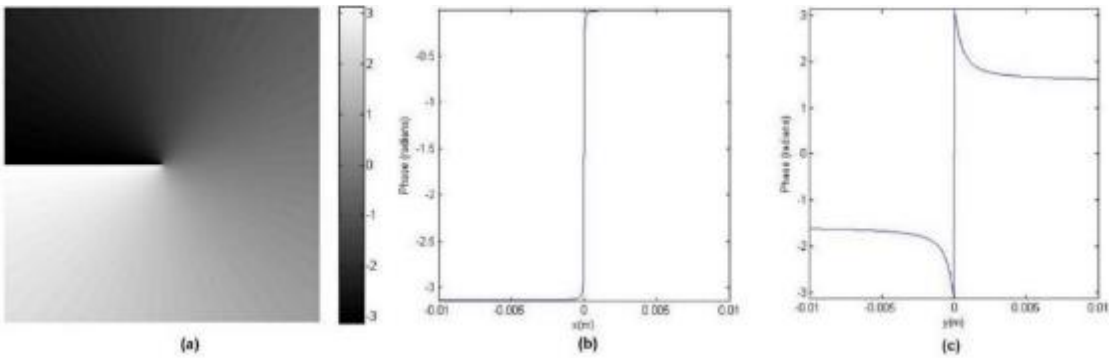

Figure 88 Collinear same charge optical vortices $\rho_0 = 0$ and $\theta_0 = 0$or $\theta_0 = \pi/2$ (a) phase profile, (b) cross-section along x-axis, and (c) cross-section along y-axis.

As the separation distance increases the composite pattern evolves from initially contains one vortex to two vortices and a shear singularity in the transition [80]. Using $\rho_0 = 0.0025$ and $\theta_0 = 0$ in Eq. (145) the results in Figure 89 (a) and (b) indicate three singularities. Further analysis reveals a shear singularity at $\rho_0 = 0$ and two vortex singularities of charge $+1$ at $\rho_0 = \mp 0.0025$. Due to the existence of a singularity at the origin, the zeroth-order component of the Fourier transformed image is expected to be filtered out and selective edge enhancement in the angle of orientation achieved as demonstrated in Figure 75 (c).

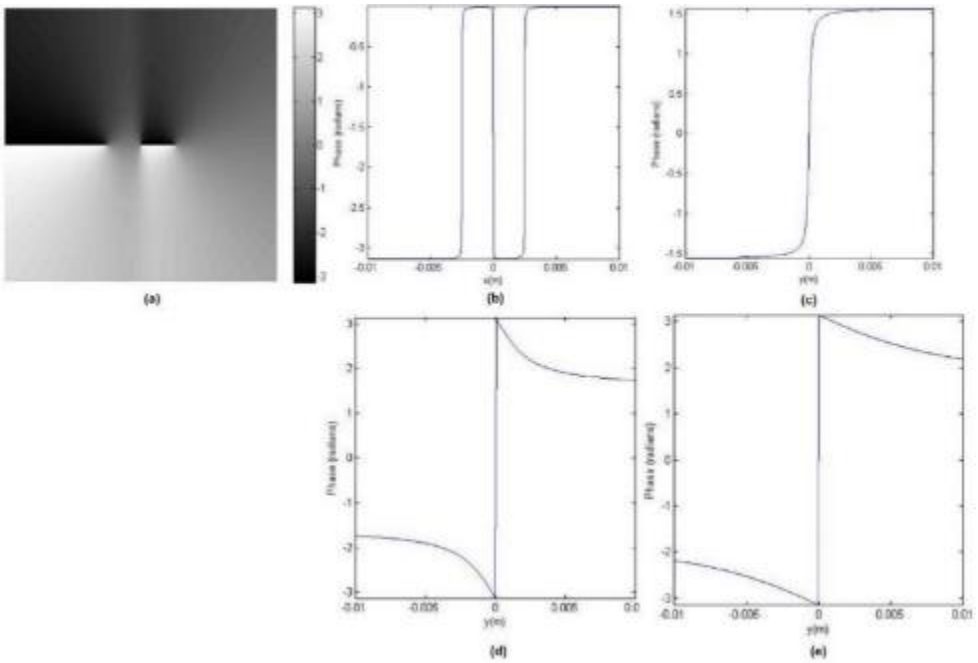

Figure 89 Displaced same charge optical vortices $\rho_0 = 0.0025$ and $\theta_0 = 0$ (a) phase profile, (b) cross-section along x-axis, (c) cross-section along y-axis $\rho_0 = -0.0025$, and (d) cross-section along y-axis $\rho_0 = 0.0025$.

Changing the orientation to $\theta_0 = \pi/2$ results in three singularities as seen in Figure 90 (a) and (b). There is a vortex singularity at $\rho_0 = 0$ and two vortex singularities of charge $+1$ at

$\rho_0 = \mp 0.0025$. While this phase profile contains an additional vortex singularity instead of a shear singularity, the zeroth-order component of the Fourier transformed image is expected to be filtered and selective edge enhancement in the angle of orientation achieved as demonstrated in Figure 75 (d).

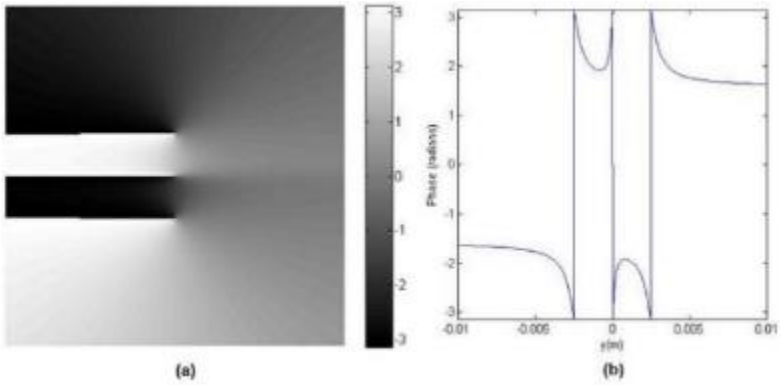

Figure 90 Displaced same charge optical vortices $\rho_0 = 0.0025$ and $\theta_0 = \pi/2$ (a) phase profile and (b) cross-section along x-axis.

As the displacement is increased to $\rho_0 = 0.005$ with $\theta_0 = 0$, three singularities are seen in the phase profile in Figure 91 (a) and (b). The singularities are one shear singularity at $\rho_0 = 0$ and two vortex singularities of charge $+1$ at $\rho_0 = \mp 0.005$. The increased displacement is anticipated to maintain the filtering on the zeroth-order component and therefore yield selective edge enhancement in the angle of orientation achieved as demonstrated in Figure 72 (d).

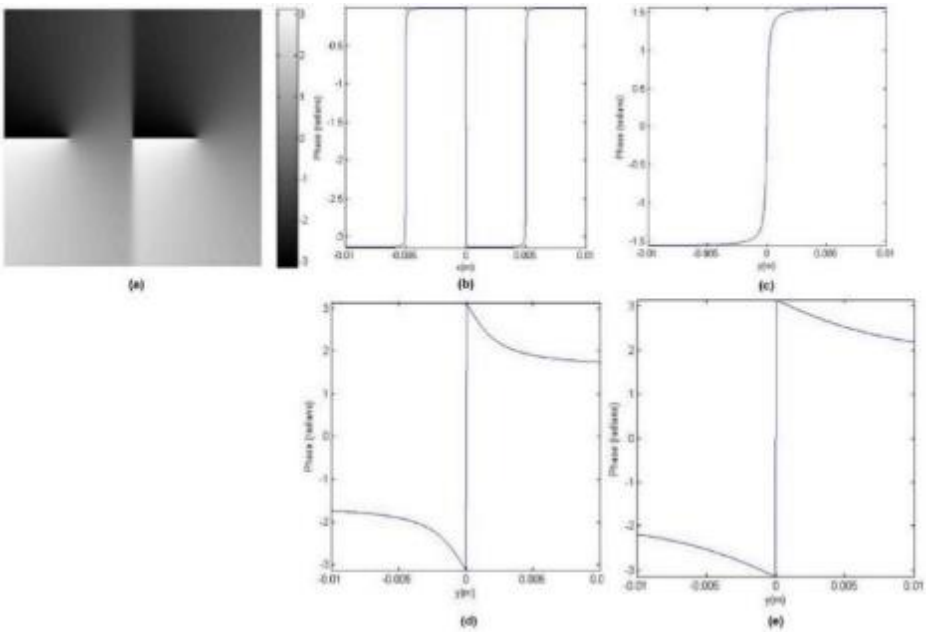

Figure 91 Displaced same charge optical vortices $\rho_0 = 0.005$ and $\theta_0 = 0$(a) phase profile, (b) cross-section along x-axis, (c) cross-section along y-axis$\rho_0 = -0.005$, and (d) cross-section along y-axis $\rho_0 = 0.005$.

An orientation change to $\theta_0 = \pi/2$ maintains the same number of singularities as previously and presented in Figure 92 (a) and (b). The singularities are all vortex singularities, one of charge -1 at $\rho_0 = 0$ and two of charge $+1$ at $\rho_0 = \mp 0.005$. The change in orientation is reflected in the selective edge enhancement in the angle of orientation as demonstrated for in $\theta_0 = 3\pi/4$ Figure 76 (c).

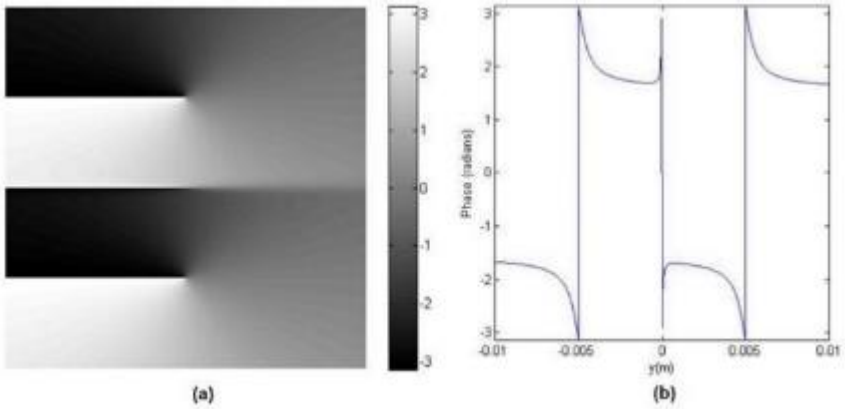

Figure 92 Displaced same charge optical vortices $\rho_0 = 0.005$ and $\theta_0 = \pi/2$ (a) phase profile and (b) cross-section along x-axis.

This chapter demonstrated and analyzed optical vortices for uniform or selective edge enhancement. The next chapter focuses on the spiral phase plate as a pupil choice in the OSH system so as to enhance edges in the reconstruction of original specimens captured by holography.

6 ADVANCES IN OPTICAL SCANNING HOLOGRAPHY WITH SPIRAL PHASE PLATE

This chapter details the novel combination of theories and concepts from previous chapters into numerical routines and experimental demonstration. The optical system and mathematics for using a spiral phase plate in an OSH system are presented in section 6.1. In Section 6.1.1 the discussion focuses on simulating isotropic enhancement in the OSH system with the experimental realization of the optical system in Section 6.1.2. The chapter includes several simulations demonstrating anisotropic filtering with OSH in Sections 6.2.1 to 6.2.5. Additional simulations demonstrating edge enhancement effects for two symmetrically offset vortices conclude the chapter in Section 6.3.1.

6.1 Optical Scanning Holography with Spiral Phase Filtering

As seen in Chapter 5, the spiral phase plate can be used as a filter to enhance the edges of an object. Edge enhancement has found utility in a variety of image processing applications where detecting the edge or shape is of interest such as in industrial inspection [82-85] and finger print identification [86,87]. This is desirable in OSH applications such as microscopy where one seeks to improve resolution and specificity of features within cells. The inclusion of SPP in holography was first demonstrated by Bouchal and Bouchal (2012) [88] which modified Fresnel incoherent correlation holography (FINCH) techniques to operate with vortex imaging. The switch between standard FINCH and spiral contrast imaging operations as proposed by Bouchal and Bouchal (2012) [88] could be achieved either by changing the optical recording based on application of a helical reference wave or digital spiral-phase modulation during processing of standard FINCH recordings. The SPP used in the FINCH method was based upon using a pure SPP. This is disadvantageous to that presented in Section 5.5 in terms of filter suppression as the lower image quality is due to a DC offset and the presence of ringing around the reconstructed edges. The approach is based on self-interference and requires the capture of three phase-shifted recordings sequentially which could introduce bias build-up when using complex objects. It is therefore proposed to use a different SPP with OSH in an attempt to overcome these biases. This chapter will detail the application of the SPP proposed in Chapter 5 to achieve edge enhancement either by insertion of the SPP in the holographic recording of a traditional OSH system.

The addition of the SPP in a traditional OSH system begins with an optical system much like that in Figure 20 but replaces the CDG with the SPP as shown in Figure 93 [9].

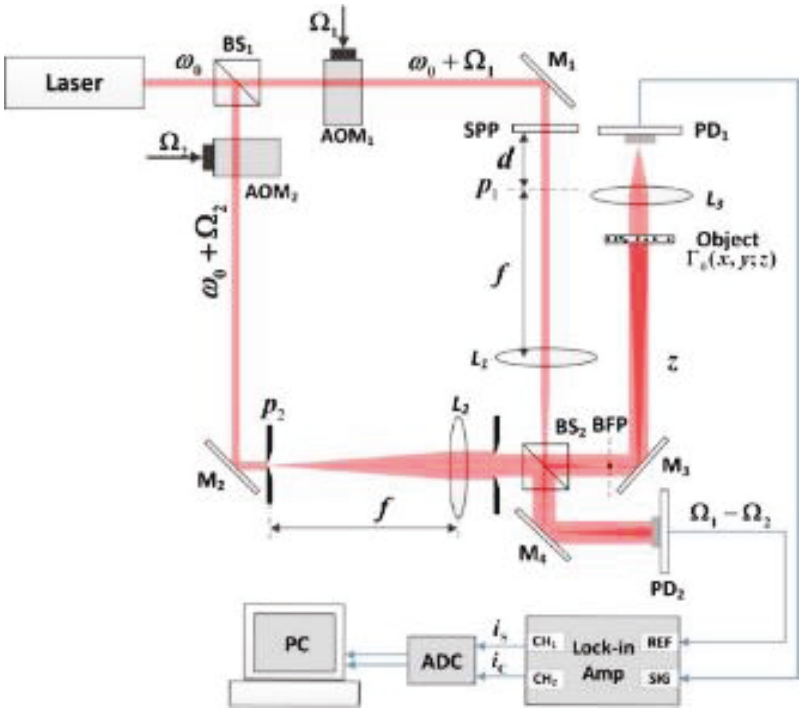

Figure 93 Optical system. [Used with permission]

As in traditional OSH, for the reference arm $p_2(x,y) = \delta(x,y)$ and using Eq. (25) $P_2^*(x,y;z) = \exp(jk_0 z)$. For the information arm using $p_1(x,y) = S(\rho,\theta,d)$ as the spiral phase plate, the Fresnel diffraction of the spiral phase gives

$$P_1(x,y) = \mathcal{F}\{S(\rho,\theta,d)\}\big|_{k_x,k_y} \otimes h(x,y;z). \tag{147}$$

Using this in Eq. (29) gives the OTF for this system as

$$\begin{aligned} OTF_\Omega(k_x,k_y;z+d) &= \mathcal{F}^*\left\{\mathcal{F}\{S(\rho,\theta,d)\}\big|_{k_x,k_y} \otimes h(x,y;z) \times \exp(jk_0 z)\right\}\big|_{k_x,k_y} \\ &= S^*(\rho,\theta,d) \times \mathcal{F}^*\{h_c(x,y;z)\}\big|_{k_x,k_y} \end{aligned} \tag{148}$$

and using $|\Gamma_0|^2 = I(x,y)$ in Eq. (50), the reconstruction equation becomes

$$\begin{aligned} R(x,y;z+d) &= H_c(x,y;z+d) \otimes h(x,y;z) \\ &= \mathcal{F}^{-1}\{OTF_{SPP}(k_x,k_y;z+d) \times \mathcal{F}\{I(x,y)\}\big|_{k_x,k_y}\} \otimes h(x,y;z) \\ &\propto \mathcal{F}^{-1}\{S^*(\rho,\theta,d) \times \mathcal{F}\{I(x,y)\}\big|_{k_x,k_y}\} \end{aligned} \tag{149}$$

6.1.1 MATLAB Simulation: Optical Scanning Holography with Isotropic Spiral Phase Filter

The realization of the simulation begins with generation of the pupil function $p_1(x,y)$ from Eq. (147) as shown by the amplitude of the filter and normalized amplitude of the filter through the center in Figure 94.

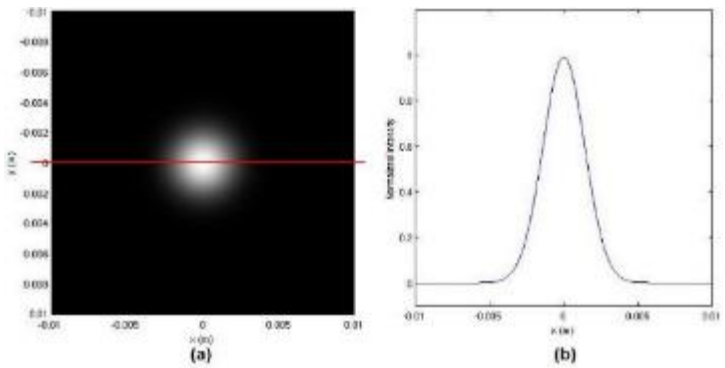

Figure 94 (a) Amplitude distribution and (b) normalized amplitude across the center.

The application of the proposed SPP to OSH begins by inserting a $m=1$ SPP into a traditional OSH system via recording in Figure 93 by moving L_1 forward and letting $d=0mm$ such that $z=1066mm$ and the pupil function reduces to

$$p_1(x,y)\big|_{d=0,m=1} = S(\rho,\theta,0) = \exp\left(-\left(\frac{\rho}{\omega}\right)^2 + j\theta\right). \tag{150}$$

The original image, $I(x,y)$ in Eq. (149), is the black and white face of a pig sampled at 1024×1024 shown in Figure 95(a) with the normalized cross-section intensity distribution through the middle of image as indicated by the red line is shown in Figure 95 (b). The cosine and sine holograms using the spiral phase plate as a pupil are shown in Figure 96 (a) and (b), respectively with the corresponding results for the reconstruction in Figure 96 (c) and (d). The intensity reconstruction shown in Figure 97 illustrates the viability for the use of SPP to achieve edge enhancement in the OSH optical system as compared to holograms reconstructed without the filter as presented in Figure 98 and Figure 99 for cosine and sine holograms, respectively.

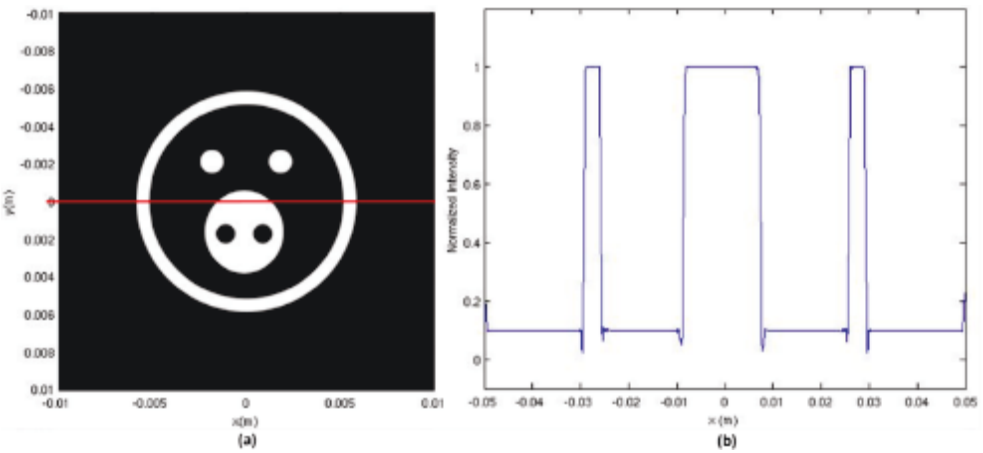

Figure 95 (a) Original pig image and (b) normalized intensity distribution.

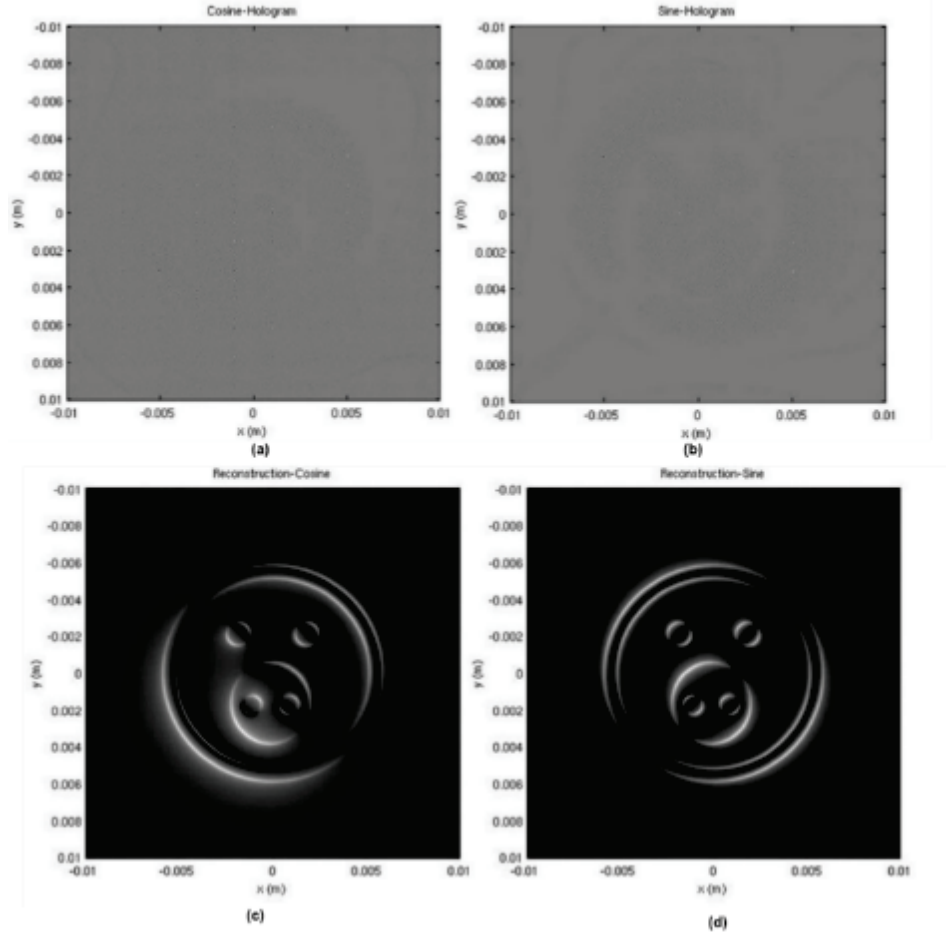

Figure 96 Traditional SPP (a) cosine hologram, (b) sine hologram, (c) cosine reconstruction, and (d) sine reconstruction.

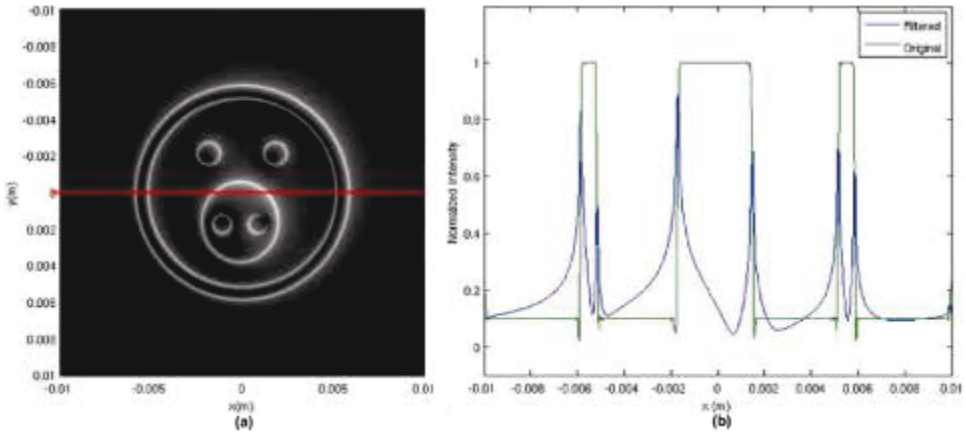

Figure 97 (a) Traditional SPP reconstruction and (b) corresponding intensity distribution.

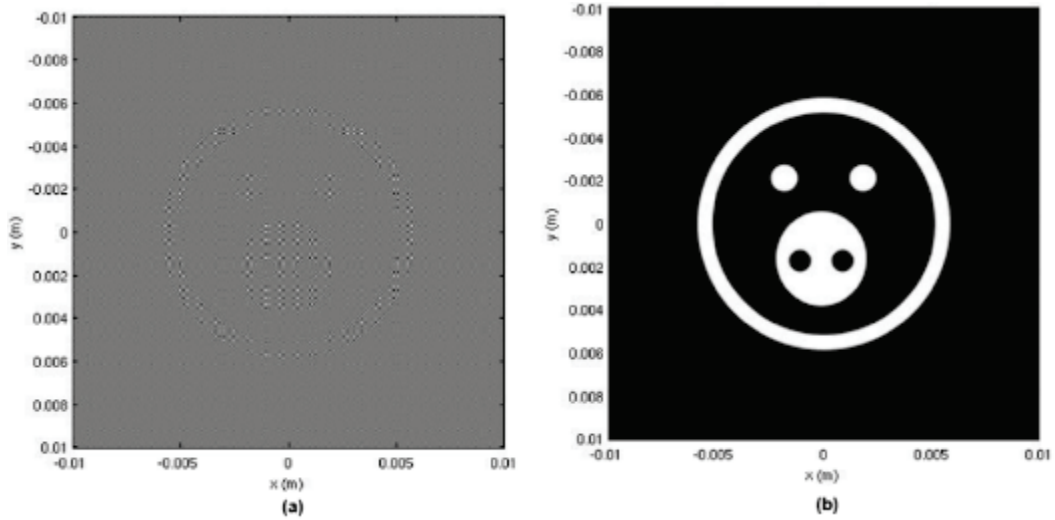

Figure 98 (a) Traditional cosine hologram and (b) reconstruction.

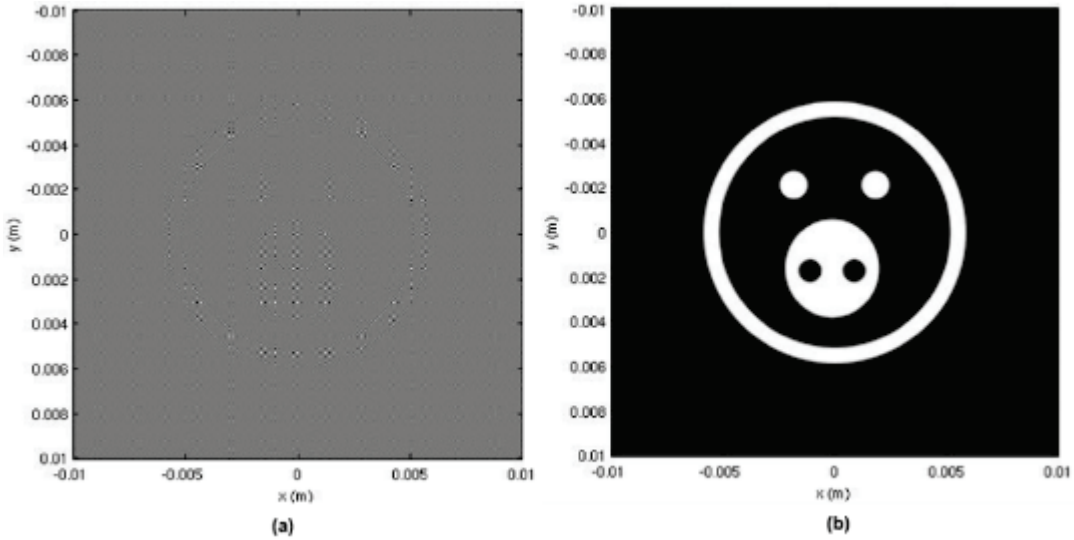

Figure 99 (a) Traditional sine hologram and (b) reconstruction.

The proposed SPP in Chapter 5 is realized by moving L_1 back in Figure 93 such that $d = 138.15mm$ and $z = 868mm$ in Eq. (143). The simulated cosine and sine hologram are shown in Figure 100 (a) and (b), respectively with the results for the reconstruction for the holograms shown in Figure 101 (a) and (b), respectively. The numerical reconstruction of the complex hologram is shown in Figure 102 (a) and the horizontal intensity distribution for the center of the image shown in Figure 102 (b).

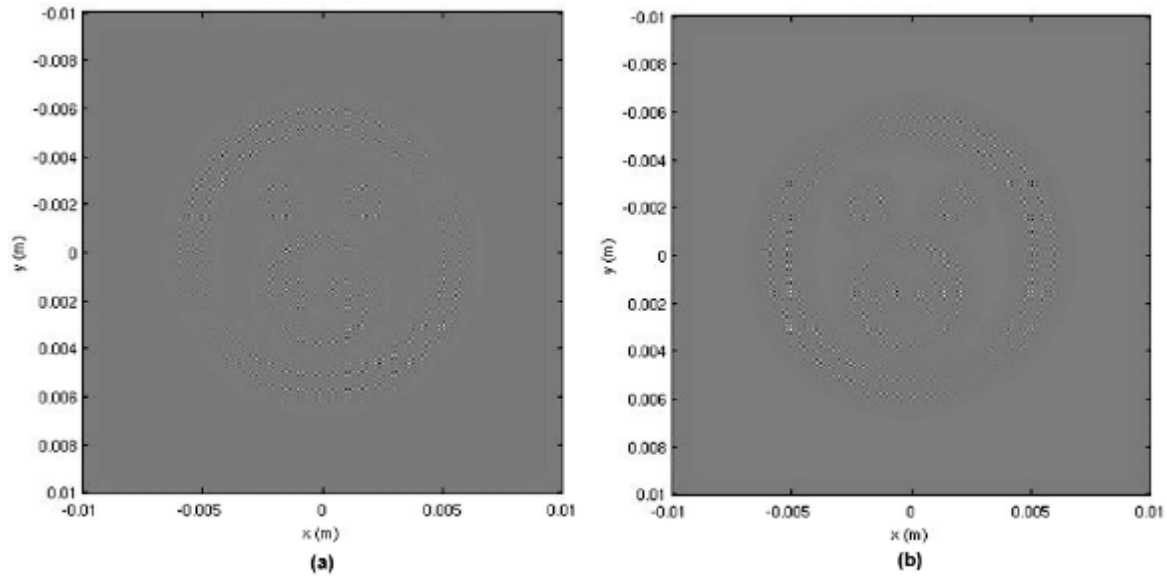

Figure 100 (a) Cosine and (b) sine hologram for input image in Figure 70 (a).

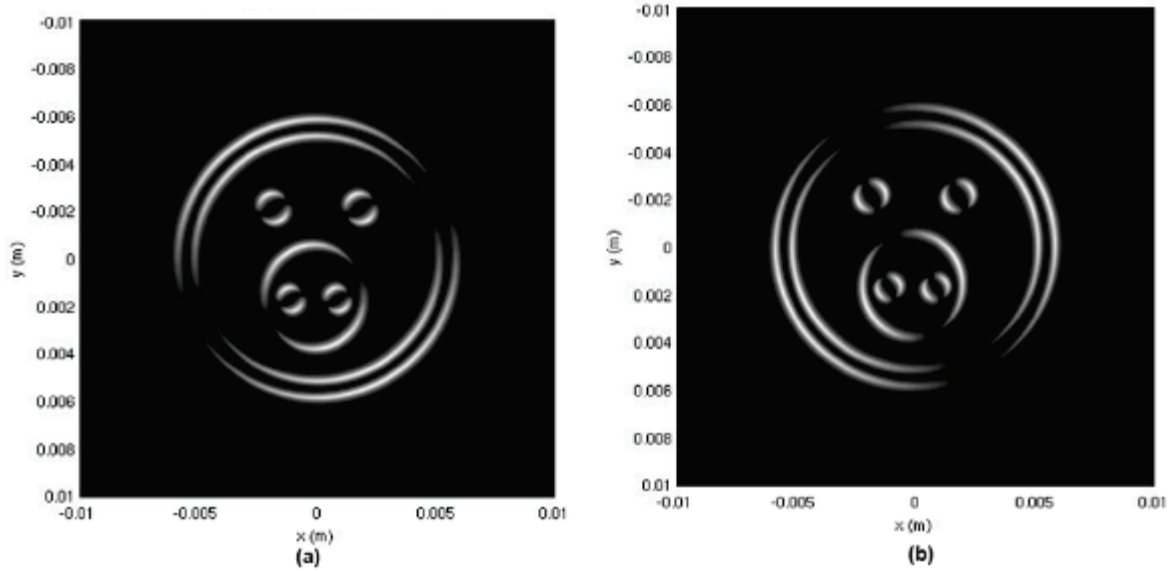

Figure 101 (a) Reconstructed cosine hologram and (b) reconstructed sine hologram.

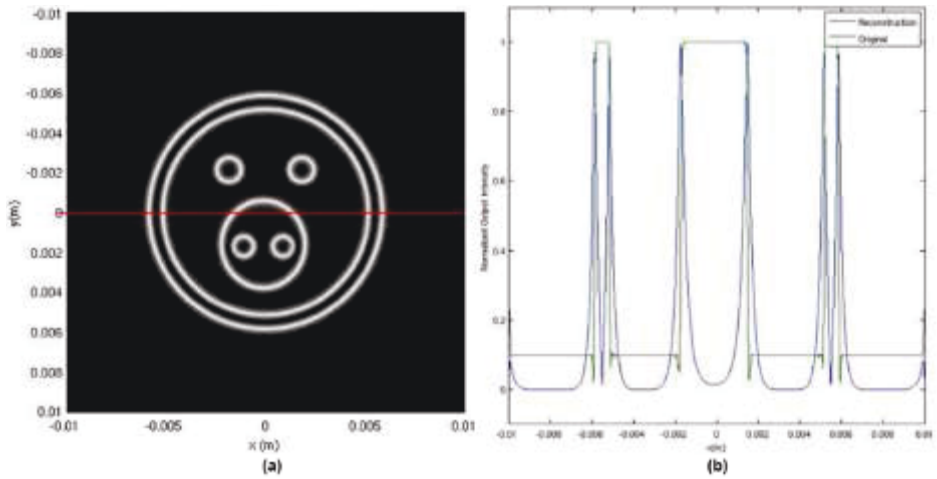

Figure 102 (a) Intensity of reconstruction and (b) intensity distribution.

The filtered output for SPP in the OSH system when compared to those results presented in Figure 70 (c) and (d) for spatial filtering with Gaussian beam has little deviation aside from broader edges. Comparing the results in Figure 97 to those in Figure 102 (a) one notes that the result from the SPP $d = 0mm$ is much weaker than the SPP $d = 138.15mm$ and that the edge enhancement is not as uniform. Further insight into these differences is gleaned by comparing the normalized horizontal intensity distribution as seen in Figure 103 where the blue line represents the traditional SPP and the red line the proposed SPP. One can see that the SPP $d = 0mm$ has a strong DC bias as well as sharper side-lobes which are not present in the SPP $d = 138.15mm$ and thus might account for edge enhanced differences.

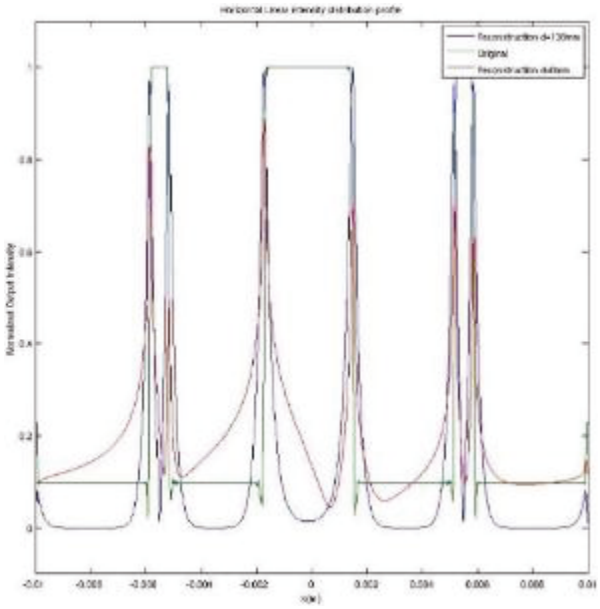

Figure 103 Normalized intensity distribution (blue) reconstruction at $d = 138.15mm$, (green) original, and (red) reconstruction $d = 0mm$.

The previous results demonstrated via numerical simulation that edge enhancement capabilities can be realized with optical scanning holography by directly changing the recording process. The next section features optical experimentation with an optical scanning holography system as in Figure 93 where one of the traditional pupils has been replaced by a spiral phase plate.

6.1.2 Experiment: Optical Scanning Holography with Spiral Phase Filtering

The optical system in Figure 93 was realized by Pan et al. (2014) [9] with a He-Ne laser with specifications of 15mW, $\lambda = 632.8nm$, and $\omega = 0.6mm$; two lenses of focal length $f = 300mm$; and a $2mm \times 2mm$ SPP whose topological charge $m = 1$. The interference pattern of a Gaussian vortex at the p_1 plane of distance $d = 138.15mm$ from data collected by Pan et al. (2014) [9] is shown in Figure 104 (a) and the interference pattern between a diffracted Gaussian vortex and a plane wave in (b).

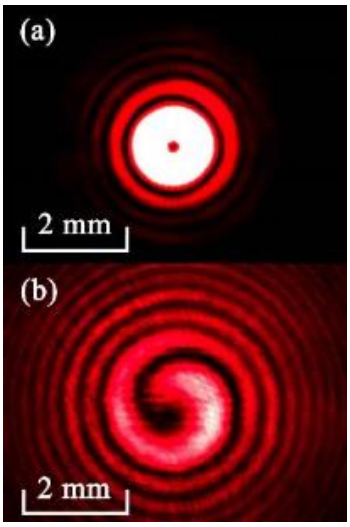

Figure 104 (a) Intensity of the beam at the pupil plane and (b) the interference pattern between diffracted Gaussian vortex and a plane wave.

The two-dimensional amplitude transparency used as the input object is similar to that in Figure 70 (a) with physical dimensions $20mm \times 20mm$. Applying the method proposed in Eq. (149) with the pupil function related to Eq. (143), the holograms were captured and their visualizations as well the reconstructions accomplished in MATLAB from data collected by Pan et al. (2014) [9]. The cosine and sine hologram are shown in Figure 105 (a) and (b) respectively with the intensity reconstruction shown in Figure 105 (c). For comparison the results obtained by numerical reconstruction are included in Figure 105 (d).

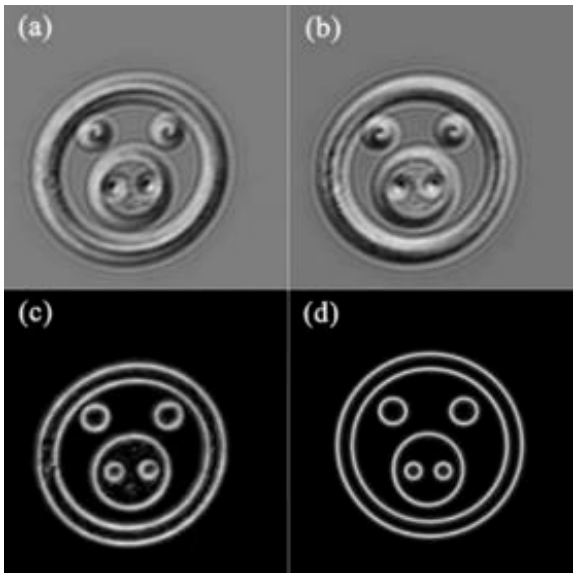

Figure 105 Experimental realization of proposed SPP (a) cosine hologram, (b) sine hologram, (c) intensity reconstruction and (d) numerical simulation result. [Used with permission]

The reconstruction via optical measurement and numerical simulation in Figure 105 (c) and (d) respectively, are in fact quite similar in appearance with artifacts from the imaging system and a slight stretch in the horizontal appearing in the former. These artifacts and stretching are prevalent in holographic recordings captured using the standard OSH method as seen in Figure 106. The traditional OSH optical system was realized as in Section 6.1.1 simply by removing the SPP from the setup in Figure 93 with the corresponding hologram and reconstruction results illustrated in Figure 106.

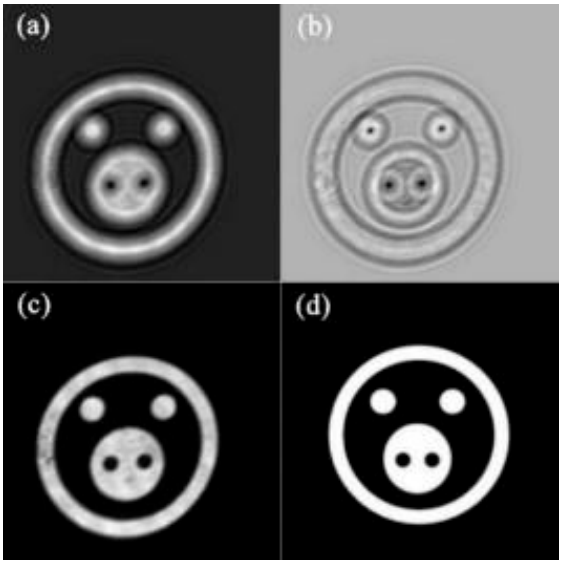

Figure 106 Experimental realization of standard OSH (a) cosine hologram, (b) sine hologram, (c) intensity reconstruction, and (d) numerical simulation result.

Thus, from Figure 105 (c) and Figure 106 (c) one can see that using the optical results from an experimental setup with the SPP that both edge preservation and enhancement are realized. Results from inserting the SPP at $d = 0mm$ into the previously setup optical system produces the results in Figure 107. While the experimental realization does illustrate some edge enhancement similar to the numerical simulation results in Section 6.1.1, the edge enhancement is much thinner and less evenly distributed making any task relying on edge preservation more difficult.

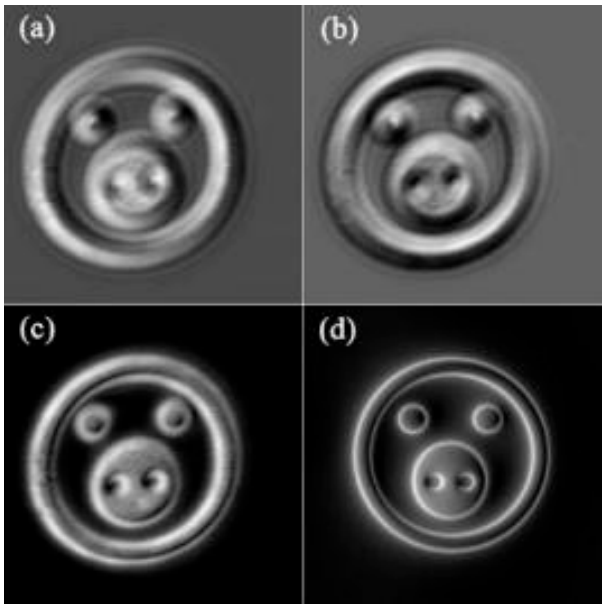

Figure 107 Experimental realization of traditional SPP (a) cosine hologram, (b) sine hologram, (c) intensity reconstruction, and (d) numerical simulation result. [Used with permission]

The edge enhancement effects of using an SPP as a pupil in the traditional OSH optical system have thus been demonstrated for a planar object. However, the results depend on parameters of the optical setup such as placement and topological charge of the SPP. These results can be extended via simulation to further examine edge enhancement with a SPP with different topological charge, orientation, or aberration.

6.2 Optical Scanning Holography with Anisotropic Spiral Phase Filter

The results presented thus far have demonstrated the ability to achieve isotropic edge enhancement by inserting a SPP with unity topological charge as a pupil in the OSH system. However, the SPP might not always have unity charge, aberrations might be present in the optical system, or the SPP might be oriented in a different direction. It is anticipated that the edge enhancements of the

reconstructed hologram under these alterations will be less symmetric and more selective similar to the filtering results in Chapter 5. The sections that follow aim to demonstrate selective edge enhancement via computer simulation using these altered SPPs via $S(\rho,\theta)$ in the information arm of the optical scanning holography system in Eq. (144).

6.2.1 Anisotropic Spatial Vortex Filtering: Method 1 Superposed Vortex Filter

Utilizing the black and white pig image as the input, the simulated cosine and sine reconstructed holograms that result from using a superposed vortex filter as calculated using Eq. (102) in the information arm of an OSH system are presented in Figure 108 (a) and (b), respectively. The reconstruction of the complex hologram using Figure 108 (a) and (b) is shown in Figure 108 (c). The intensity distribution across the $y=0$ plane is shown in Figure 108 (d) for both the original and reconstructed hologram images. Inspecting Figure 108 (c) and (d) one can see that edge enhancement different from that in Figure 107 (d) has been achieved following the holographic reconstruction. The results are similar to those in Figure 44 (a) in that edges appear to be enhanced in one direction. Thus, direction dependent edge enhancement has been simulated with the reconstructed hologram.

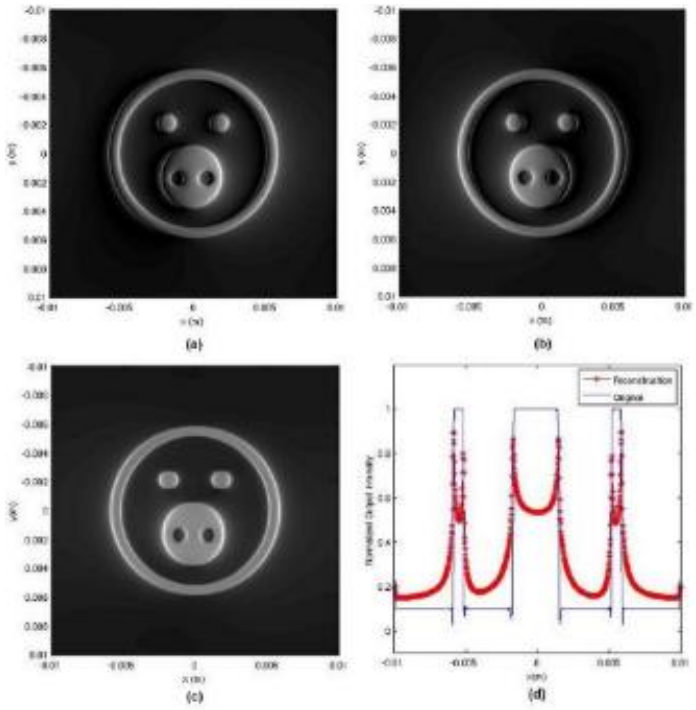

Figure 108 Superposed vortex filter (a) cosine hologram reconstruction, (b) sine hologram reconstruction, (c) complex hologram reconstruction, and (d) intensity distribution.

6.2.2 Anisotropic Spatial Vortex Filtering: Method 2 Siedel Aberrations

The simulated, reconstructed complex holograms that result from using an astigmatism aberration as calculated using Eq. (111) are presented in Figure 109 (a) for $A_a = 0.3$ and (c) for $A_a = 0.7$ and the corresponding intensity distribution profile for each in (b) and (d), respectively. As the astigmatism coefficient increases the blurring increases and the contrast decreases.

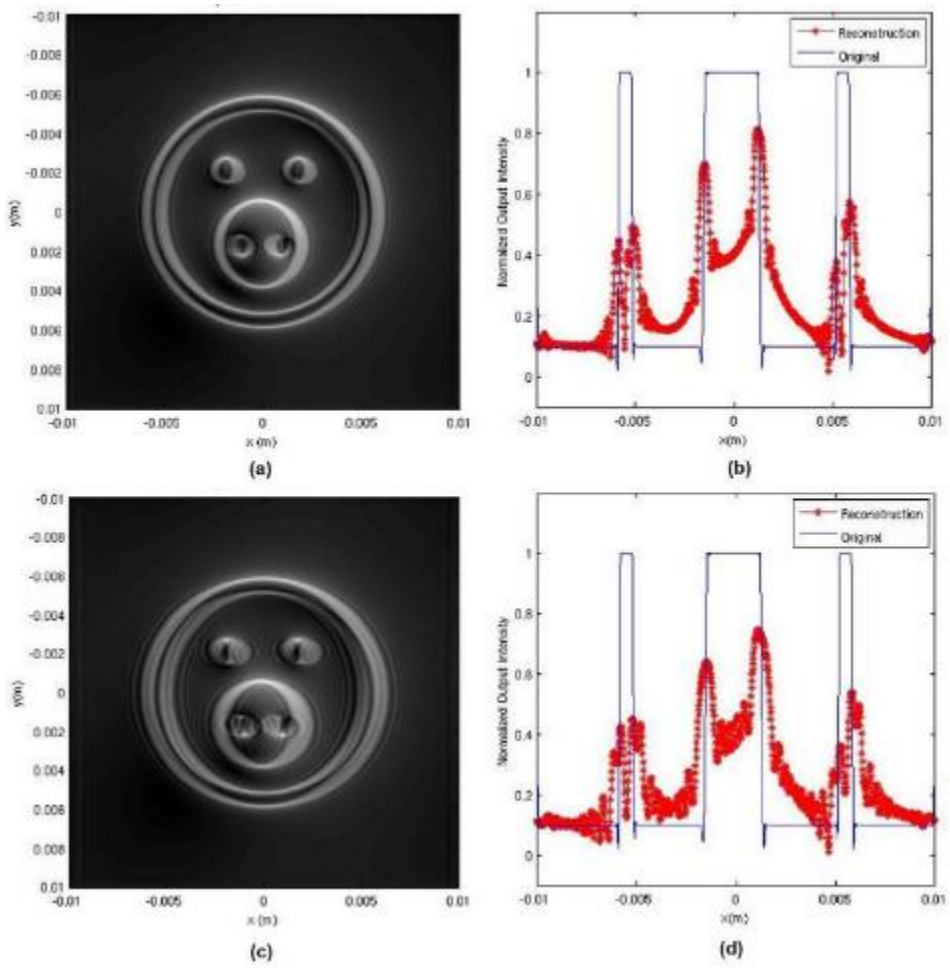

Figure 109 Astigmatism aberration (a) reconstructed complex hologram $A_a = 0.3$, (b) corresponding horizontal intensity distribution profile, (c) reconstructed complex hologram $A_a = 0.7$, and (d) corresponding horizontal intensity distribution profile.

The simulated, reconstructed complex holograms that result from using an coma aberration as calculated using Eq. (112) are presented in Figure 110 (a) for $A_c = 50$ and the corresponding intensity distribution profile in (b). The reconstructed hologram has an increased intensity as compared to other aberration effects but has increased ringing about the enhanced edges.

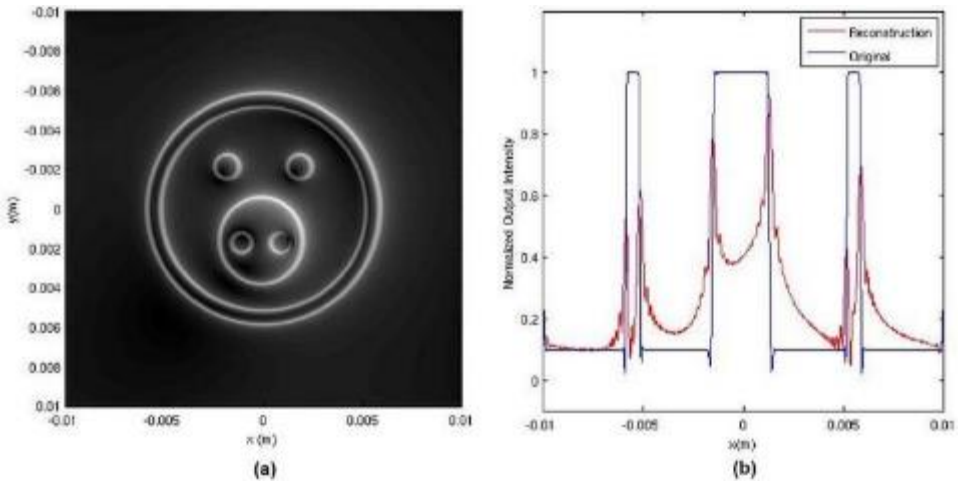

Figure 110 Coma aberration (a) reconstructed complex hologram $A_c = 50$, (b) corresponding horizontal intensity distribution profile.

The simulated, reconstructed complex holograms that result from using a distortion aberration as calculated using Eq. (110) are presented in Figure 111 (a) for $A_d = 0.03$ and the corresponding intensity distribution profile in (b). The reconstructed hologram has an intensity redistribution in the horizontal plane as seen by shift in the profile plot in (b).

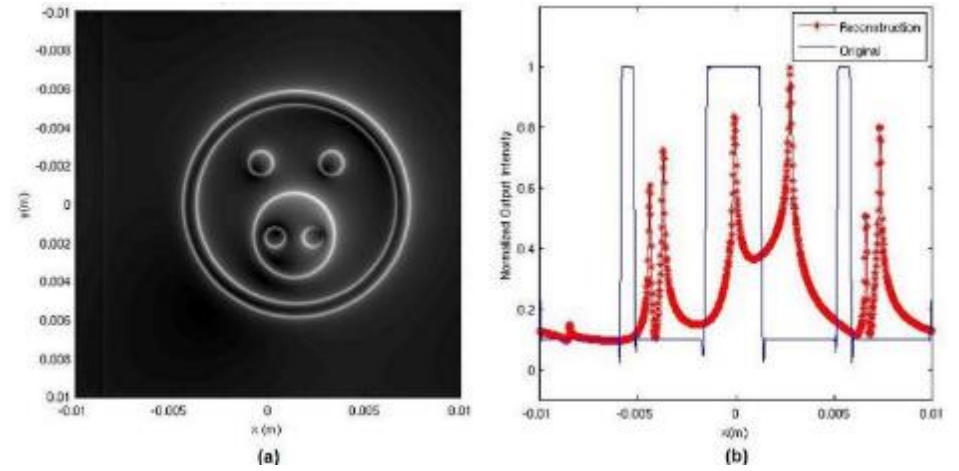

Figure 111 Distortion aberration (a) reconstructed complex hologram $A_d = 0.03$, (b) corresponding horizontal intensity distribution profile.

The simulated, reconstructed complex holograms that result from using an defocus aberration as calculated using Eq. (113) are presented in Figure 112 (a) for $A_f = 10^{-1}$ and the corresponding intensity distribution profile in (b). The reconstructed hologram has broadened edges as a consequence of the defocus effects.

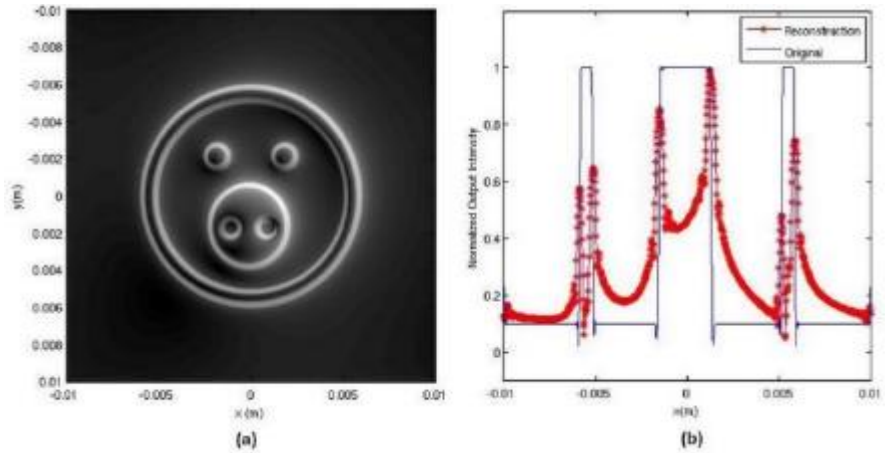

Figure 112 Defocus aberration (a) reconstructed complex hologram $A_f = 10^{-1}$, (b) corresponding horizontal intensity distribution profile.

The simulated, reconstructed complex holograms that result from using an spherical aberration as calculated using Eq. (109) are presented in Figure 113 (a) for $A_s = 10^4$ and the corresponding intensity distribution profile in (b). The reconstructed hologram has some edges which have wider intensity distribution spread due to ringing but their intensity is more enhanced than in the filtered isotropic reconstruction.

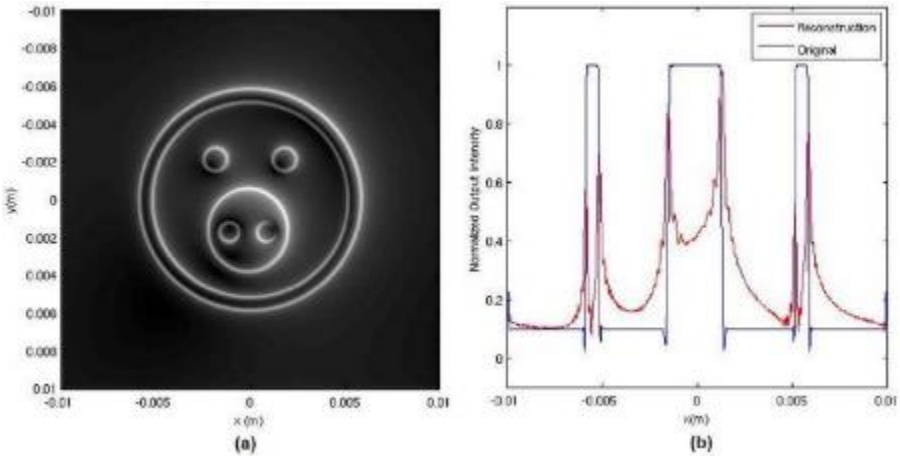

Figure 113 Spherical aberration (a) reconstructed complex hologram $A_s = 10^4$, (b) corresponding horizontal intensity distribution profile.

It has been shown that the complex hologram reconstructions retain anisotropic filtering effects in the presence of aberrations that result as part of optical systems. The selectiveness and type of edge enhancement can be controlled by aberration type and aberration coefficient.

6.2.3 Anisotropic Spatial Vortex Filtering: Method 3 Fractional Spiral Phase Filter

The simulated complex hologram realized with a fractional spiral phase filter in Eq. (114) with $m = 0.6$ and $\tau = 7\pi/4$ is presented in Figure 114 (a) with the corresponding intensity distribution in (b). The difference in edge contrast as one traverses the horizontal direction is apparent with visual inspection of the results or by further analysis of the intensity distribution. Orientation selective edge enhancement was realized with a fractional spiral phase filter of $m = 0.8$ and $\tau = \pi/4$. The reconstructed complex hologram and corresponding intensity distribution are shown in Figure 114 and show both orientation selective edge enhancement as compared to Figure 115. The enhancement is more symmetric due to the increase m in such that the vortex core is more toward the origin the enhancement is more symmetric. Anisotropic filtering of the reconstructed hologram has been simulated by fractional charge and orientation of the spiral phase filter in the OSH system.

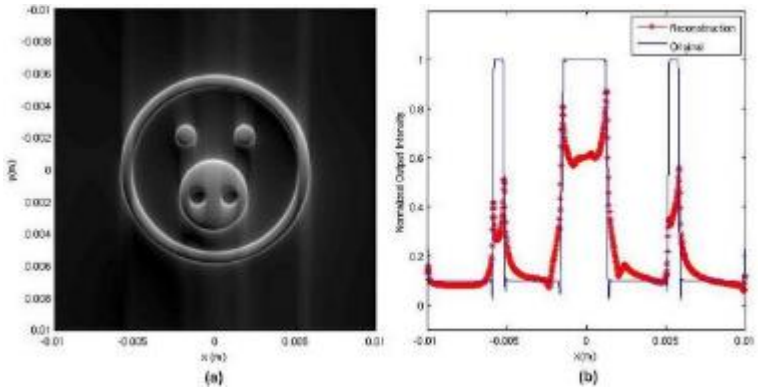

Figure 114 (a) Reconstructed complex hologram with fractional spiral phase filter with $m = 0.6$ and $\tau = 7\pi/4$ and (b) corresponding intensity distribution.

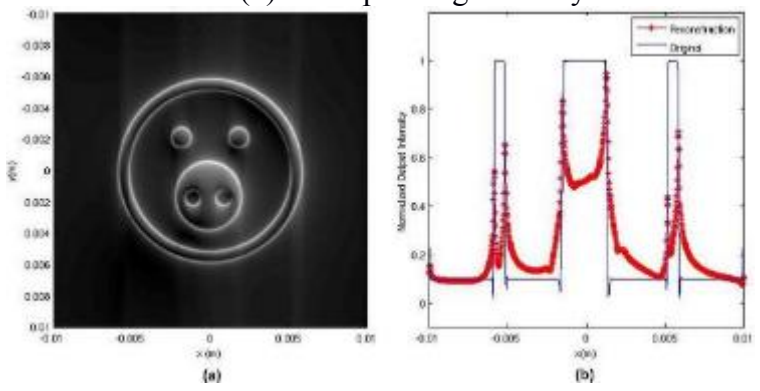

Figure 115 (a) Reconstructed complex hologram with fractional spiral phase filter with $m = 0.8$ and $\tau = \pi/4$ and (b) corresponding intensity distribution.

6.2.4 Anisotropic Spatial Vortex Filtering: Method 4 Shifting Filter Singularity

The reconstructed cosine and sine holograms that result from shifting a vortex filter via Eq. (121) with $\rho_0 = 0.005$ and $\theta_0 = 3\pi/4$ in the information arm of an OSH system are presented in Figure 116 (a) and (b), respectively. The reconstruction of the complex hologram as calculated in Eq. (49) is shown in Figure 116 (c) where after the reconstruction, the edges in the direction of θ_0 have the greatest enhancement. The orientation based enhancement that results from changing θ_0 is seen in Figure 117 (a-c) for the filter position in Figure 117 (d-f). Keeping $\theta_0 = 3\pi/4$ and varying $\rho_0 = 0, 0.0025, 0.005, \text{and } 0.0075$ as seen in Figure 118 (d-f) the degree of edge enhancement starts off small at first before increasing as seen in Figure 118 (a-c). Orientation edge enhancement and degree of direction enhancement have been simulated in the reconstructed hologram.

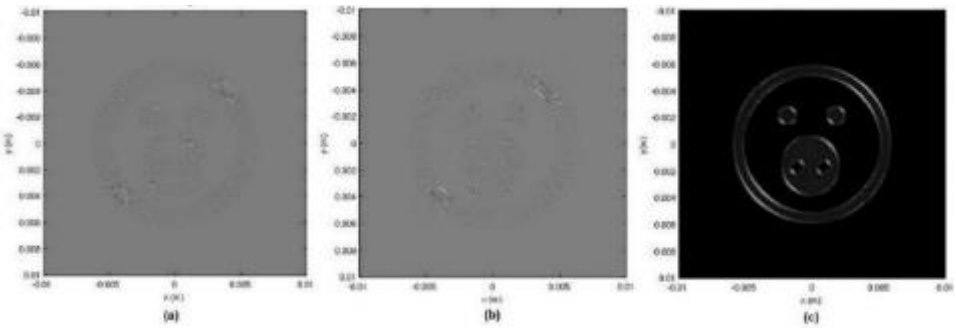

Figure 116 Shifted vortex filter (a) cosine hologram, (b) sine hologram, and (c) complex hologram reconstruction for $\rho_0 = 0.005$ and $\theta_0 = 3\pi/4$.

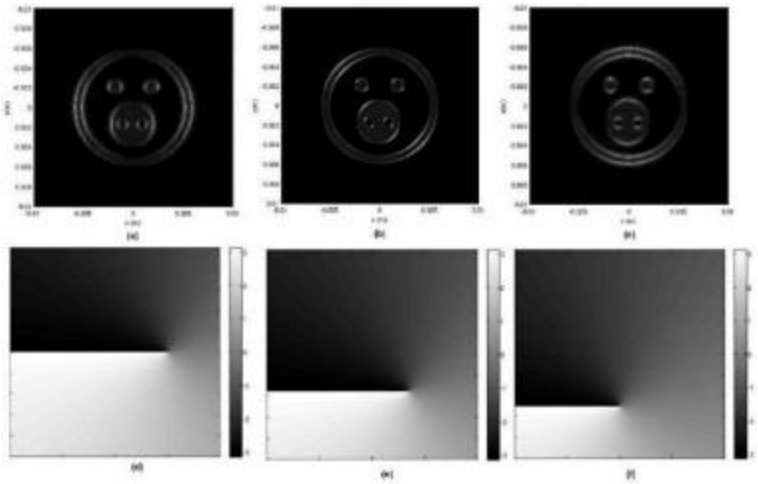

Figure 117 Shifted vortex filter (a)-(c) complex hologram reconstruction, and (d-f) phase distribution for $\rho_0 = 0.005$ and $\theta_0 = 0, \pi/4, \text{and } \pi/2$, respectively.

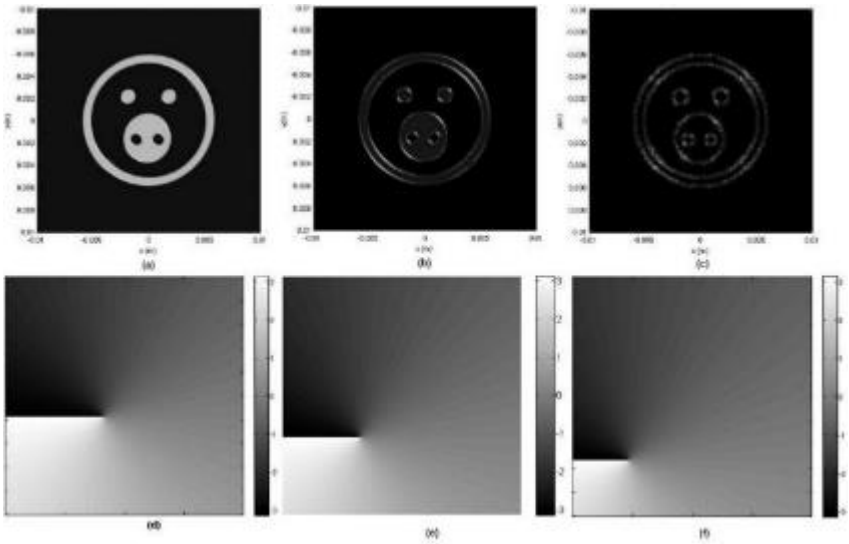

Figure 118 Shifted vortex filter (a-c) complex hologram reconstruction and (d-f) phase distribution for $\theta_0 = 3\pi/4$ and $\rho_0 = 0.0025, 0.005, \text{and } 0.0075$, respectively.

6.2.5 Anisotropic Spatial Vortex Filtering: Method 5 Power and Offset Angle

The simulated complex hologram reconstruction for edge enhancement using Eq.(130) with a fixed value of m are shown in Figure 119 where the position of the enhanced region is based on the value of θ_0. The results in (a-c) are as one should expect from Figure 59 with the orientation change resulting from the reconstruction process.

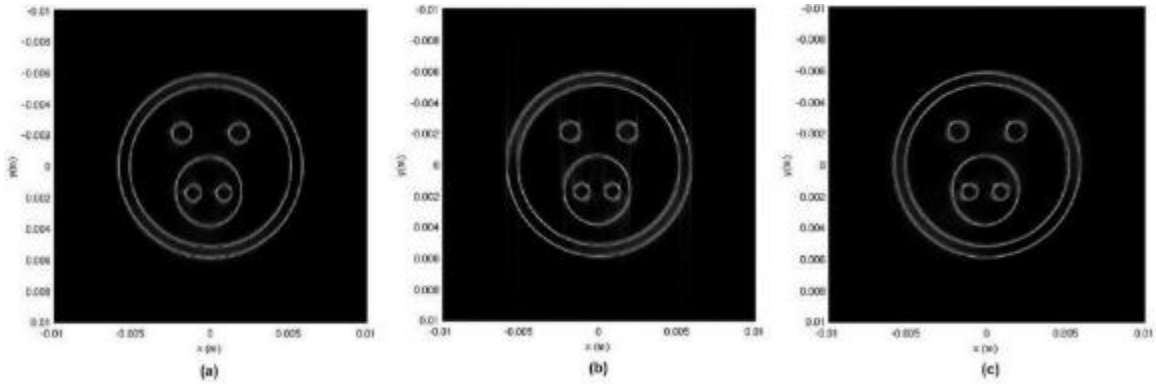

Figure 119 (a-c) Complex hologram reconstruction for $m = 10$ and $\theta_0 = 0, \pi/4, \text{and } 3\pi/4$, respectively.

The reconstructed complex hologram in Figure 120 shows that as the power of m increase the less pronounced the selective enhancement and the blur or smearing overtakes the reconstruction. Further investigation via the intensity distribution in Figure 120 (d-f) shows that $m = 5$ has an almost uniform enhancement while $m = 10$ has the highest intensity with selective

or non-uniform enhancement more on the left half of the object. Thus controllable anisotropy by choice of power m and orientation θ_0 has been simulated on a reconstructed complex hologram.

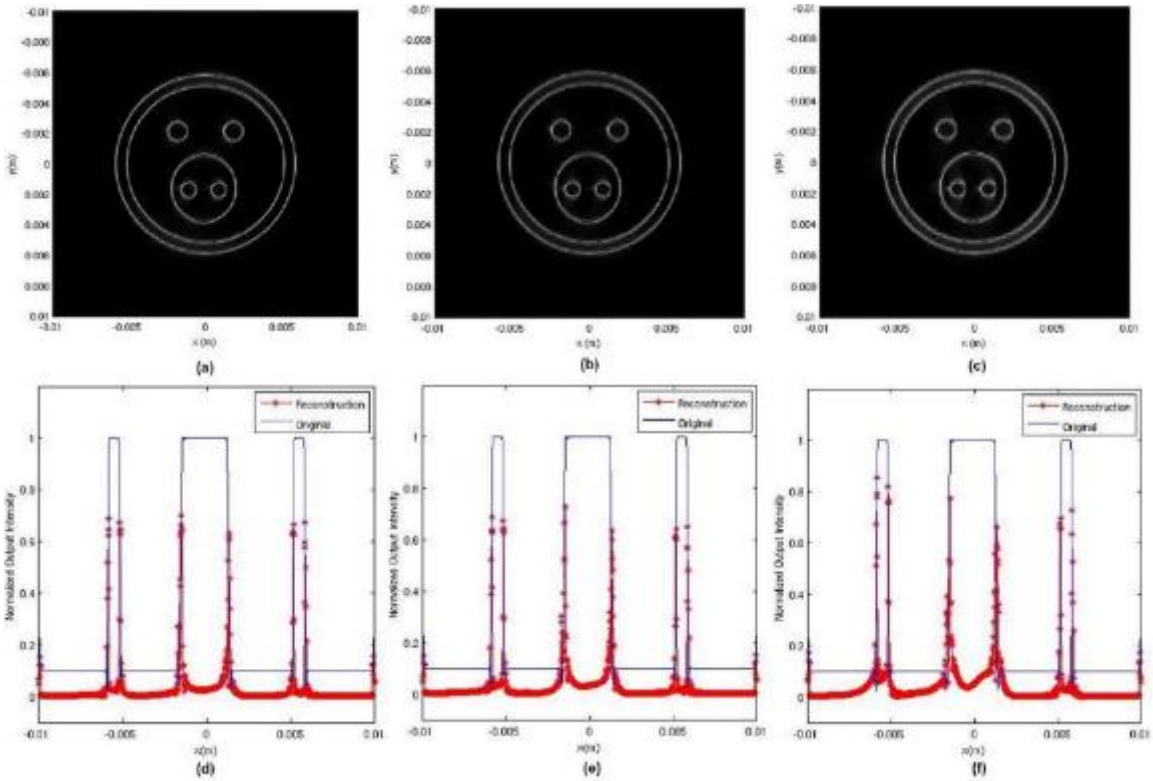

Figure 120 (a-c) Complex hologram reconstruction for $\theta_0 = \pi$ and $m = 5, 10, \text{and } 30$, respectively and (d-f) corresponding intensity distribution.

The anisotropic edge enhancement that results from using an SPP with different topological charge, orientation, or aberration as a pupil in the traditional OSH optical system have been simulated for a planar object. The next section will extend some of these attributes to two symmetrically opposite spiral phase plates under Gaussian beam illumination.

6.3 Optical Scanning Holography with Composite Spiral Phase Plate for Gaussian Beam

This section combines one or more of the properties from the previous section on anisotropic spatial vortex filtering to realize edge enhancement for two combined optical vortices as $S(\rho, \theta)$ in the information arm of the optical scanning holography system via Eq. (147).

6.3.1 Anisotropic Spatial Vortex Filtering: Composite Spiral Phase Plate Filter for Gaussian Beam

The intensity distribution and filtered output using Eq. (144) for a single shifted vortex with $\rho_0 = 0, 0.0025, \text{and } 0.005$ and $\theta_0 = 0$ are shown in Figure 121 (a-c) and (d-f), respectively. As expected, as ρ_0 is closer to the origin the filtering is more isotropic and as ρ_0 moves further away from the origin the filtering is more selective.

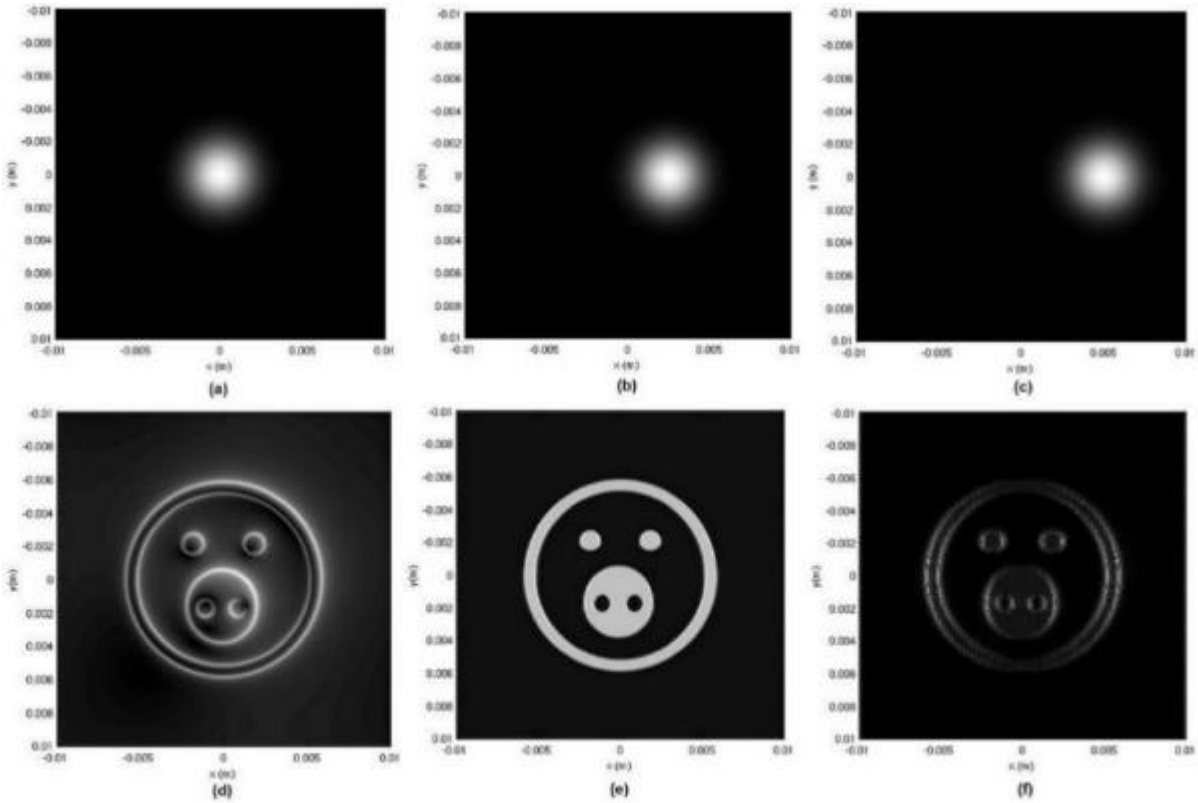

Figure 121 Vortex profile for single optical vortex with Gaussian beam shifted $\rho_0 = 0, 0.0025, \text{and } 0.005$ and $\theta_0 = 0$ (a-c), and corresponding reconstruction (d-f).

The intensity distribution and filtered output for composite vortices of the same charge using Eq. (145) for $\rho_0 = 0.0025 \text{ and } 0.005$ and $\theta_0 = 0$ are shown in Figure 122 (a-b) and (c-d), respectively. As the shift and separation distance increases, the filtered output is noisier at the extracted edge which becomes more and more prominent.

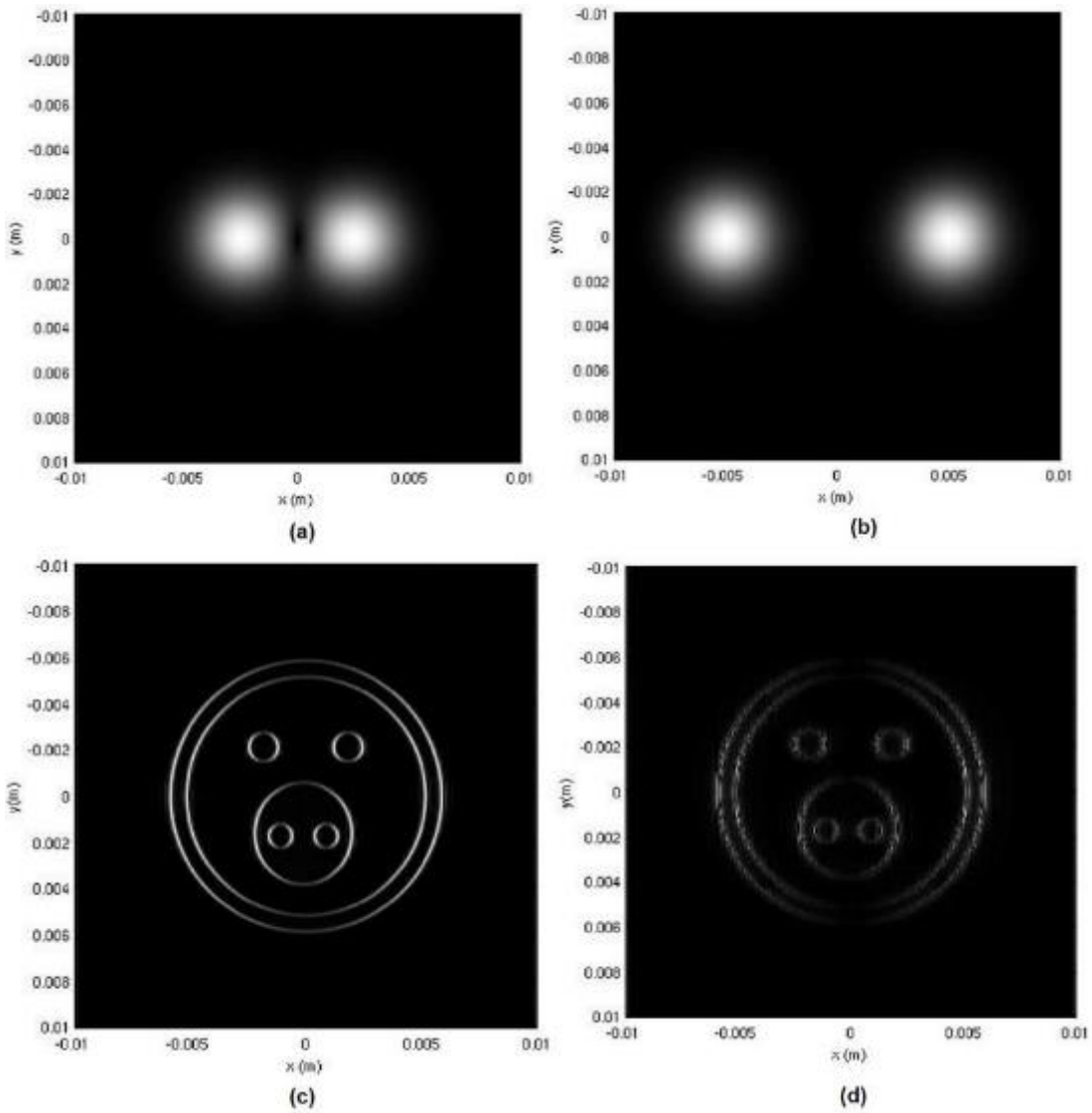

Figure 122 Vortex profile for same charge optical vortex with Gaussian beam shifted $\rho_0 = 0.0025$ and 0.005 and $\theta_0 = 0$ (a) and (b), and corresponding reconstruction (c) and (d), respectively.

The intensity distribution and filtered output for composite vortices of opposite charge using Eq. (146) for $\rho_0 = 0.0025$ and 0.005 and $\theta_0 = 0$ are shown in Figure 123 (a-b) and (c-d), respectively. As the shift and separation distance increases, the filtered output edges are less strong.

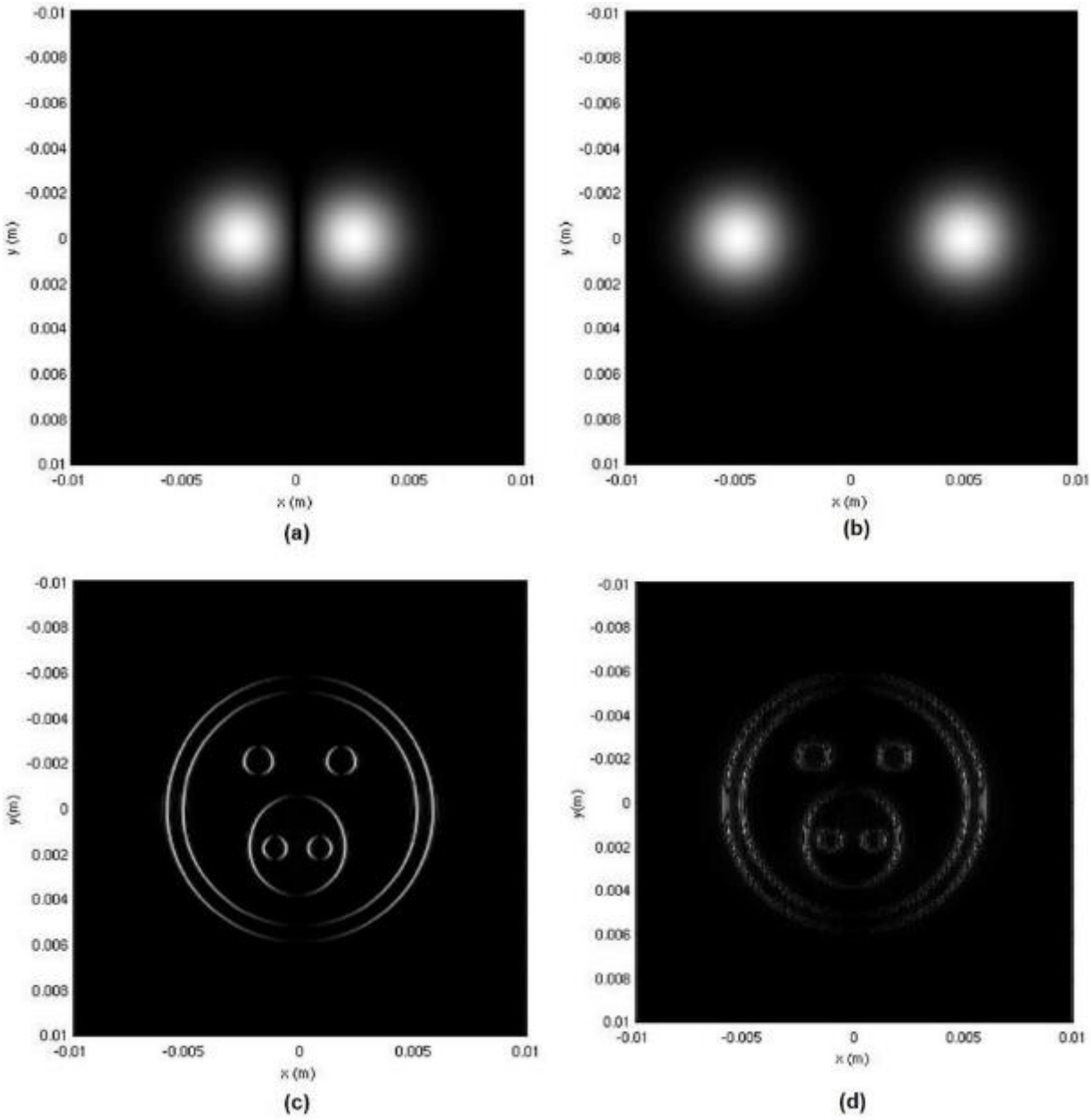

Figure 123 Vortex profile for opposite charge optical vortex with Gaussian beam shifted $\rho_0 = 0.0025 \text{ and } 0.005$ and $\theta_0 = 0$ (a) and (b), and corresponding reconstruction (c) and (d).

The intensity distribution and filtered output for composite vortices of same charge using Eq. (145) for $\rho_0 = 0.0025 \text{ and } 0.005$ and $\theta_0 = \pi/2$ are shown in (a-b) and (c-d), respectively. These results illustrate how changing the filter orientation from horizontal to vertical leads to no edge enhancement due to the increased amount of low frequency information as seen in Figure 124 (a).

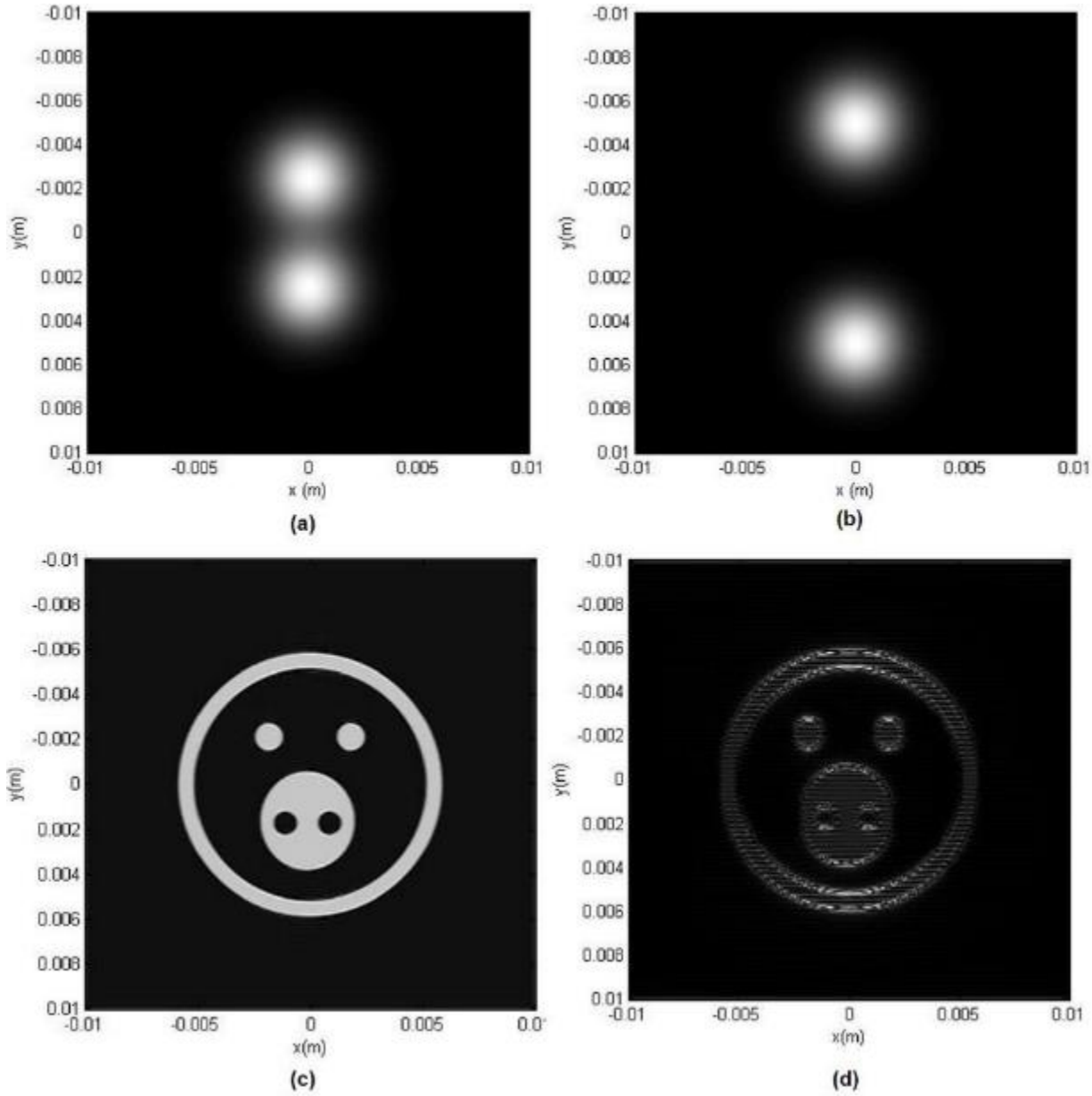

Figure 124 Vortex profile for same charge optical vortex with Gaussian beam shifted $\rho_0 = 0.0025$ and 0.005 and $\theta_0 = \pi/2$ (a) and (b), and corresponding reconstruction output (c) and (d).

The intensity distribution and filtered output for composite vortices of same charge using Eq. (145) for $\rho_0 = 0, 0.0025, 0.005, \text{and } 0.0075$ and $\theta_0 = 3\pi/4$ are shown in Figure 125 (a-d) and (e-h), respectively. The edges in the direction of orientation are enhanced for all values of ρ_0 and as the distance from the origin increases, the contribution from all edges decreases.

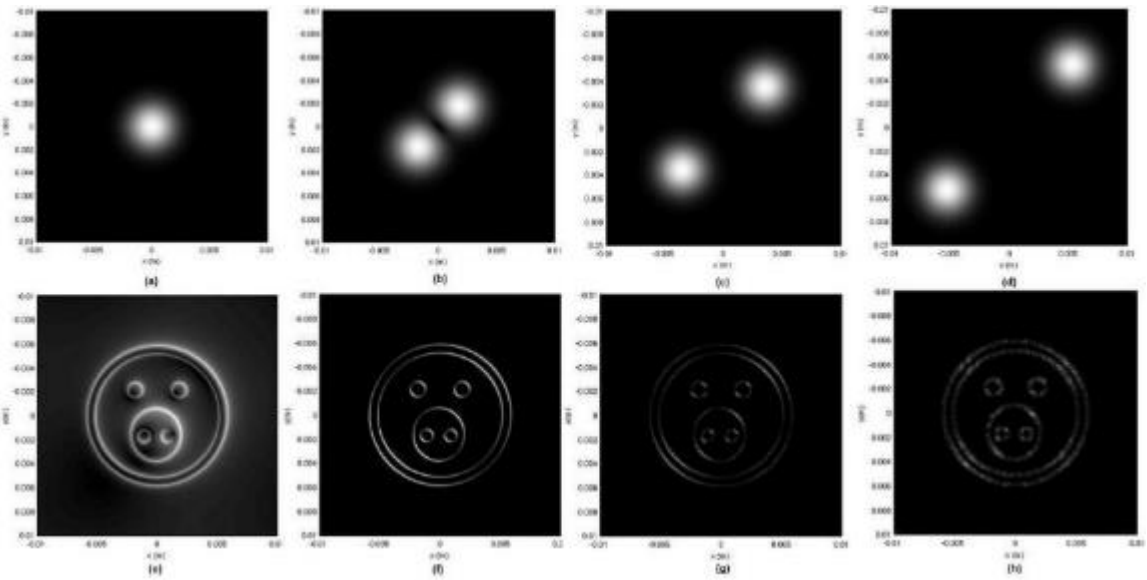

Figure 125 Vortex profile for same charge optical vortex with Gaussian beam shifted $\rho_0 = 0, 0.0025, 0.005, \text{and } 0.0075$ and $\theta_0 = 3\pi/4$ (a-d), and corresponding filtered output (e-h).

The intensity distribution and filtered output for composite vortices of opposite charge using Eq. (146) for $\rho_0 = 0, 0.0025, 0.005, \text{and } 0.0075$ and $\theta_0 = 3\pi/4$ are shown in Figure 126 (a-d) and (e-h), respectively. As expected, the filtered output contains only slight edge enhancement for $\rho_0 = 0.0025$ but as ρ_0 increases the enhancement effects increase in the orientation of θ_0.

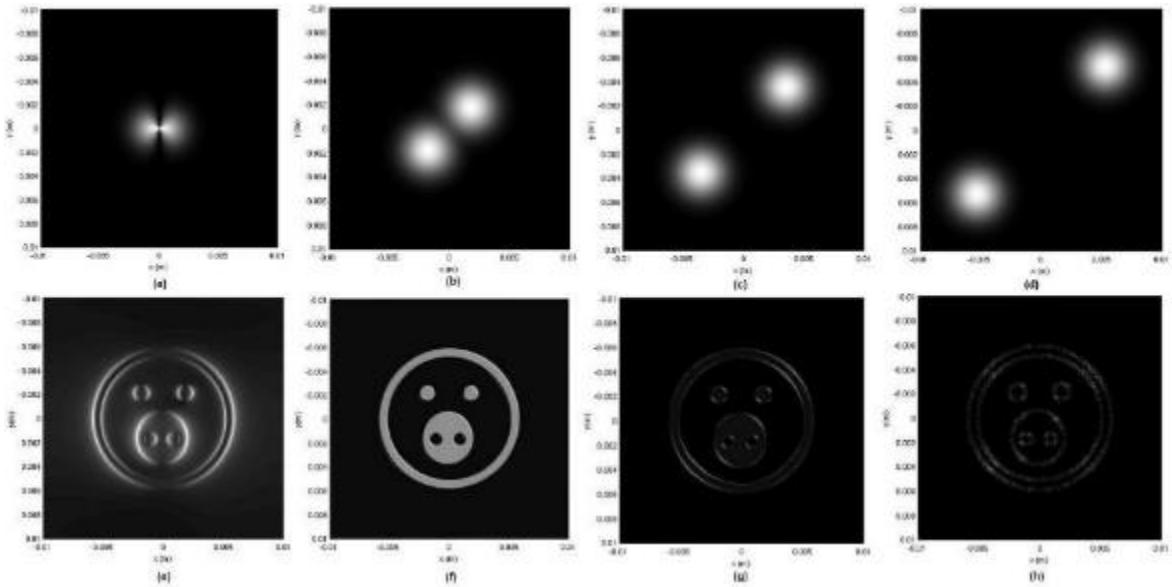

Figure 126 Vortex profile for opposite charge optical vortex with Gaussian beam shifted $\rho_0 = 0, 0.0025, 0.005, \text{and } 0.0075$ and $\theta_0 = 3\pi/4$ (a-d), and corresponding filtered output (e-h).

The anisotropic edge enhancement that results from spiral phase filtering via spiral phase plate in an optical scanning holography system have been demonstrated via computer simulation

for a simple planar object. These results can be extended for a more complex or three-dimensional object and used for comparison to those from optical experimentation.

7 FUTURE WORK

Recently the spiral phase plate was extended to three-dimensional hologram reconstruction in an optical scanning holography system [89]. The authors applied the spiral phase plate in simulation and optical experimentation to improve the depth resolution of the reconstructed hologram. Future extensions include the ability to enhance the edges of individual optical sections in the reconstructed three-dimensional hologram.

For instance, consider the application of the SPP in the holographic recording of a traditional OSH system via digital processing for hologram reconstruction. Application of the SPP filter function to traditional OSH hologram recordings begins with the optical experiment to record the 2000×2000 traditional hologram acquired with $\lambda = 532nm$,$f = 10mm$, and $\omega = 0.40319\mu m$. For a three-dimensional Oscillatoria algae specimen as the input object, the intensity of the traditional complex hologram is shown in Figure 127.

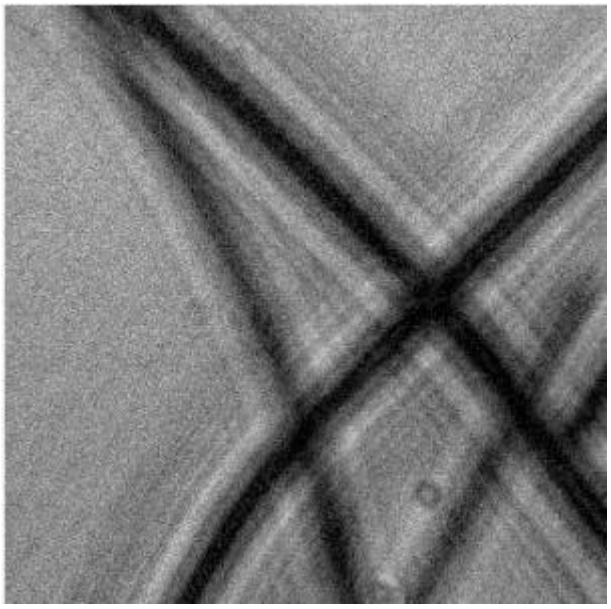

Figure 127 Traditional OSH system recorded algae hologram. [Fair use]

As originally demonstrated by Indebetouw and Zhong (2006) [90], reconstruction of the optical sections are obtained by Fresnel backpropagation using measured pupil functions to the planes in which the different strands are in focus. The results from the backpropagation method using the traditional OSH system and data from Indebetouw and Zhong (2006) [90] are illustrated in Figure 128 (a) where for $z_0 = 130mm$ the strand from the lower left corner to the upper right corner is in focus and (b) where for $z_0 = 160mm$ the strand from the lower center to the upper left corner is in focus.

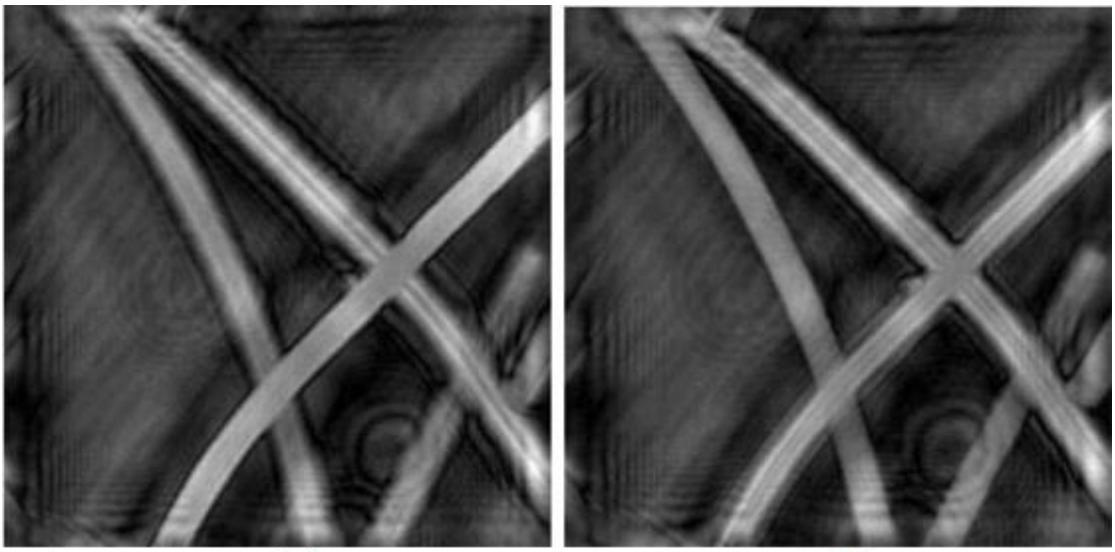

(a) (b)

Figure 128 Reconstruction of traditional hologram (a) for $z_0 = 130mm$ and (b) for $z_0 = 160mm$. [Fair use]

The backpropagation reconstruction process can also be applied to the spiral phase plate OSH system by modulating the measured pupil function with the spiral phase plate transfer function to obtain $\mathcal{F}\{S(\rho,\theta,d)\}\big|_{k_x,k_y} \otimes h(x,y;z)$ in Eq. (147). The results from the backpropagation method using the SPP OSH system are illustrated in Figure 129 (a) where for $z_0 = 130mm$ the strand from the lower left corner to the upper right corner is in focus with enhanced edges and (b) where for $z_0 = 160mm$ the strand from the lower center to the upper left corner is in focus with enhanced edges.

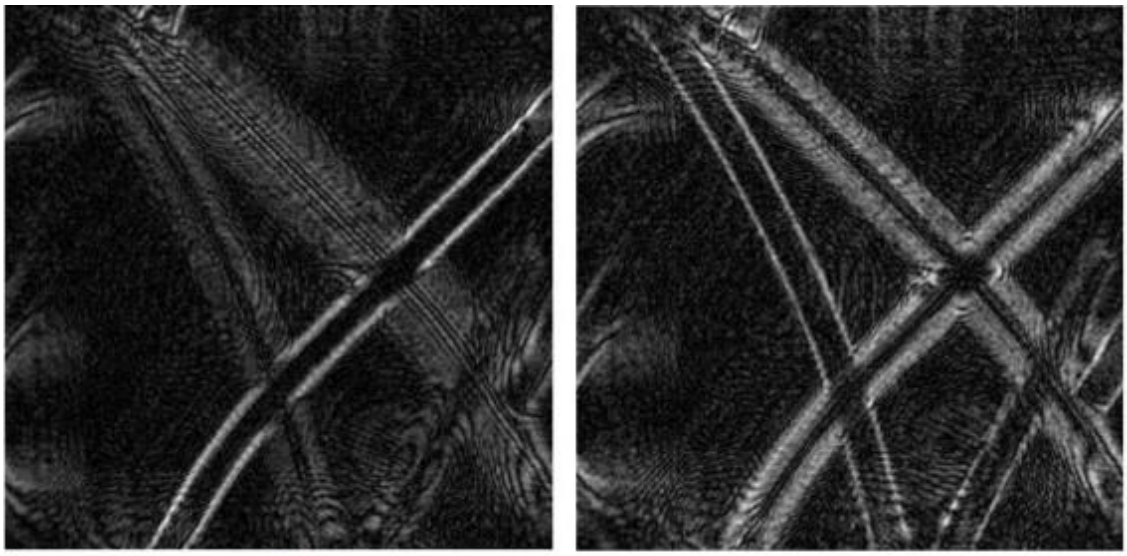

(a) (b)

Figure 129 Reconstruction of SPP OSH hologram for (a) $z_0 = 130mm$ and (b) $z_0 = 160mm$.

These initial results display enhancement of the edges for the portion of the three-dimensional hologram in the in-focus plane and thus illustrate the viability for applying SPP to OSH via the digital reconstruction process of traditionally captured holograms. Investigation into spiral phase filtering isotropic and anisotropic effects for three-dimensional hologram reconstruction via changes to the optical recording system or digital reconstruction remains an area ripe for further exploration.

While the enhancements presented in this dissertation produced visually appealing results, they are specific to the system and parameters as presented. Generalization of these techniques and their effects to other systems and parameters requires additional investigation. This includes investigation into low-coherence or partial-coherence processing, further analysis of phase plate mismatch in optical scanning holography with spiral phase plate, and more optical experiments aimed at application of enhanced optical sectioning realized with spiral phase plate filtering in conjunction with optical scanning holography. As mentioned in the body of the dissertation, the latter could be of particular interest for biological specimens such as cell wall health or other areas where object identification can be aided with more enhanced and pronounced edge structure.

8 CONCLUSIONS

This research set out to explore several techniques for enhancing the reconstruction of a recorded specimen and its optical sections using the concepts of optical scanning holography. While current techniques are able to enhance edges of the recorded specimen and alleviate out-of-focus haze in optical sections, this comes at the expense of bias from self-interference for complicated specimens and computational complexity in inverse filtering techniques due to the need for multiple decoding functions when using 3-D specimens. This research sought to investigate, in simulation and optical experimentation, the effects of adding optical elements to the recording process or modulating the digital reconstruction processing on the reconstructed specimen.

The research proposed and demonstrated, for the first time, using optical scanning holography the ability to reduce out of focus haze in holographic-section reconstruction with circular dammann grating and random-phase coding pupils and the ability to record edge-only information of an object holographically using spiral phase plates. Mathematical simulations and optical experiments demonstrated out-of-focus haze could be reduced by adding either a CDG or RPP to the recording process of a traditional optical scanning holography system. Further analysis investigated the relationship between lateral deviation and pixel changes in the position of the RPP to haze suppression and the quality of the resulting reconstruction. Mathematical simulations were also used to demonstrate isotropic and anisotropic spiral phase filtering by replacing the pupil in the information arm of an optical scanning holography system with a spiral phase plate. These results were then compared to those achieved in optical experiments using the optical scanning holography system with a spiral phase plate inserted during the holographic recording. Simulations were then used to explore the effect of changing parameters, optical system aberrations, using multiple spiral phase plates, and shifting the center of the phase plate on the ability to produce varying degrees of anisotropic edge enhancement. Thus, the research demonstrated in mathematical simulation and optical experiments the ability to modulate the phase or replace pupil functions in a traditional optical scanning holography system and enhance the reconstructed specimen captured via holographic recording.

These enhancements are not generalizable due to the specific system parameters and optical elements used to conduct the simulations and experiments. Therefore, changes to these variables in computer simulations and experimental investigations should be investigated.

This study has contributed to the field of optical scanning holography by exploring enhancements to the reconstruction of holographically recorded specimens both in computer simulation and experimental investigation. The application of several optical coding and phase filtering techniques in conjunction with OSH were motivated and realized for the first time in this field through this research. The resulting reconstruction enhancements have the potential for impact in a number of fields where analysis would be aided with increased resolution and enhanced edge structures such as fingerprint filtering, biological cell analysis, optical character recognition, and nondestructive testing and evaluation.

REFERENCES

[1] T.-C. Poon, *Optical Scanning Holography with MATLAB*, Springer, 2007.

[2] T.-C. Poon and T. Kim, *Engineering Optics with MATLAB*, World Scientific, 2006.

[3] T.-C. Poon, "Scanning holography and two-dimensional image processing by acousto-optic two-pupil synthesis," *J. Opt. Soc. Am. A*, 2, pp. 521-527, 1985.

[4] G. Indebetouw, "Scanning holographic microscopy with spatially incoherent sources: reconciling the holographic advantage with the sectioning advantage," *J. Opt. Soc. Am. A*, 26, pp. 252-258, 2009.

[5] K. Doh, K. Dobson, T.-C. Poon, and P.-S. Chung, "Optical image coding with a circular Dammann grating," *Appl. Opt.*, 48(1), pp. 134-139, 2009.

[6] Y. Shinoda, J.-P. Liu, P.S. Chung, K. Dobson, X. Zhou, and T.-C. Poon, "Three-dimensional complex image coding using a circular Dammann grating," *Appl. Opt.*, 50(7), pp. B38-B45, 2011.

[7] Z. Xin, K. Dobson, Y. Shinoda, and T.-C. Poon, "Sectional image reconstruction in optical scanning holography using a random-phase pupil," *Opt. Lett.*, 35(17), pp. 2934-2936, 2010.

[8] X.-L. Wu, X. Zhou, Q.-H. Wang, T.-C. Poon, Y.-F. Jiang, C-J. Xiao, and K. Dobson, "Deviation influences on sectional image reconstruction in optical scanning holography using a random-phase pupil," *Appl. Opt.*, 52(1), pp. A360-A366, 2013.

[9] Y. Pan, W. Jia, J. Yu, K. Dobson, C. Zhou, Y. Wang, and T.-C. Poon, "Edge extraction using a time-varying vortex beam in incoherent digital holography," *Opt. Lett.*, 39(14), pp. 4176-4179, 2014.

[10] K. Dobson, W. Jia, and T.-C. Poon, "Anisotropic edge enhancement in optical scanning holography with spiral phase filtering," *Chin. Opt. Lett.*, 14, pp. 010006-010010, 2016.

[11] T.-C. Poon and A. Korpel, "Optical Transfer Function of an Acousto-Optic Heterodyning Image Processor," *Opt. Lett.*, 4, pp. 317-319, 1979.

[12] T.-C. Poon. "Scanning Holography and Two-Dimensional Image Processing by Acousto-Optic Two-Pupil Synthesis," *J. Opt. Soc. Am. A*, 2, pp. 621-627, 1985.

[13] G. Indebetouw, P. Klysubum, T. Kim, and T.-C. Poon, "Imaging properties of scanning holographic microscopy," *J. Opt. Soc. Am. A*, 17, pp. 380-390, 2000.

[14] T.-C. Poon, T. Kim, G. Indebetouw, B. Schilling, M.H. Wu, K. Shinoda, and Y. Suzuki, "Twin-image elimination experiments for three dimensional images in optical scanning holography," *Opt. Lett.*, 25, pp. 215-217, 2000.

[15] G. Indebetouw, T. Kim, T.-C. Poon, and B. Schilling, "Three dimensional location of fluorescent inhomogeneities in turbid media by scanning heterodyne holography," *Opt. Lett.*, 23, pp. 135-137, 1998.

[16] A. W. Lohmann and W. T. Rhodes, "Two-pupil synthesis of optical transfer functions," *Appl. Opt.*, 17, pp. 1145-1151, 1978.

[17] G. Indebetouw and T.-C. Poon, "Novel Approaches of Incoherent Image Processing with Emphasis on Scanning Methods," *Opt. Eng.*, 31, pp. 2159-2167, 1992.

[18] J. W. Goodman, *Introduction to Fourier Optics,* McGraw Hill, 1968.

[19] F.T.S. Yu, *Optical Information Processing*, Wiley, 1983.

[20] P.P. Banerjee and T.-C. Poon, *Principles of Applied Optics*, Richard D. Irwin, Inc., 1991.

[21] T. Kim, "Optical sectioning by optical scanning holography and a Wiener filter," *Appl. Opt.*, 45, pp. 872-879, 2006.

[22] H. Kim, S.-W. Min, B. Lee, and T.-C. Poon, "Optical sectioning for optical scanning holography using phase-space filtering with Wigner distribution functions," *Appl. Opt.*, 47, pp. D164-D175, 2008.

[23] X. Zhang, E.Y. Lam, and T.-C. Poon, "Reconstruction of sectional images in holography using inverse imaging," *Opt. Exp.*, 16, pp. 17215-17226, 2008.

[24] T.-C. Poon, T. Kim and K. Doh, "Optical Scanning Cryptography for Secure Wireless Transmission," *Appl. Opt.*, 42, pp. 6496-6503, 2003.

[25] D. Lai, X. Zhou, D.-F. Zhou, and D.-H. Li, "Study on the influence of key errors in the deciphered image in the double random phase encryption system by applying affine cryptography," *J. Mod. Opt.*, 55, pp. 167-176, 2008.

[26] P. Refregier and B. Javidi, "Optical image encryption based on input plane and Fourier plane random encoding," *Opt. Lett.*, 20, pp. 767-769, 1995.

[27] D.S. Monaghan, D.P. Kelly, N. Pandey, and B.M. Hennelly, "Twin removal in digital holography using diffuse illumination," *Opt. Lett.*, 34, pp. 3610-3612, 2009.

[28] Y. Park, W. Choi, Z. Yaqoob, R. Dasari, K. Badizadegan, and M.S. Field, "Speckle-field digital holographic microscopy," *Opt. Exp.*, 17, pp. 12285-12292, 2009.

[29] W. Chien, D.S. Dilworth, E. Liu, and E.N. Leith, "Synthetic-aperture chirp confocal imaging," *Appl. Opt.*, 45, pp. 501-510, 2006.

[30] F. Goudail, B. Javidi, and P. Refregier, "Influence of a perturbation in a double phase-encoding system," *J. Opt. Soc. Am. A*, 15, pp. 2629-2638, 1998.

[31] J. F. Nye and M. V. Berry, "Dislocations in wave trains," *Proc. R. Soc. London Ser. A*, 336, pp. 165–190, 1974.

[32] J. M. Vaughan and D. V. Willetts, "Interference properties of a light beam having a helical wave surface," *Opt. Commun.*, 30, pp. 263–267, 1979.

[33] P. Coullet, L. Gil, and F. Rocca, "Optical vortices," *Opt. Commun.*, 73, pp. 403-408, 1989.

[34] M. Vasnetsov and K. Staliunas, *Optical Vortices*, Nova Science Publishers, Inc., 1999.

[35] A. E. Siegman, *Lasers*, University Science Books, 1986.

[36] M. W. Beijersbergen, R. Coerwinkel, M. Kristensen, and J. P. Woerdman, "Helical-wavefront laser beams produced with a spiral phase plate," *Opt. Commun.*, 112, pp. 321–327, 1994.

[37] G. A. Turnbull, D. A. Roberson, G. M. Smith, L. Allen, and M. J. Padgett, "Generation of free-space Laguerre–Gaussian modes at millimetre-wave frequencies by use of a spiral phaseplate," *Opt. Commun.*, 127, pp. 183–188, 1996.

[38] S. Oemrawsingh, J. van Houwelingen, E. Eliel, J. P. Woerdman, E. Verstegen, J. Kloosterboer, and G.W. 't Hooft, "Production and characterization of spiral phase plates for optical wavelengths," *Appl. Opt.*, 43, pp. 688–694, 2004.

[39] K. Sueda, G. Miyaji, N. Miyanaga, and M. Nakatsuka, "Laguerre–Gaussian beam generated with a multilevel spiral phase plate for high intensity laser pulses," *Opt. Exp.*, 12, pp. 3548–3553, 2004.

[40] R. K. Tyson, M. Scipioni, and J. Viegas, "Generation of an optical vortex with a segmented deformable mirror," *Appl. Opt.*, 47, pp. 6300-6306, 2008.

[41] N. R. Heckenberg, R. McDuff, C. P. Smith, and A. White, "Generation of optical phase singularities by computer-generated holograms," *Opt. Lett.*, 17, pp. 221–223, 1992.

[42] A. Jesacher, C. Maurer, A. Schwaighofer, S. Bernet, and M. Ritsch-Marte, "Near-perfect hologram reconstruction with a spatial light modulator," *Opt. Exp.*, 16, pp. 2597–2603, 2008.

[43] W. Chen and Q. Zhan, "Realization of an evanescent Bessel beam via surface plasmon interference excited by a radially polarized beam," *Opt. Lett.*, 34, pp. 722-724, 2009.

[44] L. Allen, M. W. Beijersbergen, R. J. C. Spreeuw, and J. P. Woerdman, "Orbital angular-momentum of light and the transformation of Laguerre-Gaussian laser modes," *Phys. Rev. A*, 45, pp. 8185-8189, 1992.

[45] M. W. Beijersbergen, L. Allen, H. van der Veen, and J. P. Woerdman, "Astigmatic laser mode converters and transfer of orbital angular-momentum," *Opt. Commun.*, 96, pp. 123-132, 1993.

[46] J.A. Davis, D.E. McNamara, D.M. Cottrell, and J. Campos, "Image processing with the radial Hilbert transform: theory and experiments," *Opt. Lett.*, 25, pp. 99-101, 2000.

[47] R.B. Bracewell, *The Fourier transform and its application*, McGraw-Hill, 1965.

[48] J.A. Davis, D.E. McNamara, and D.M. Cottrell, "Analysis of the fractional Hilbert transform," *Appl. Opt.*, 37, pp. 6911-6913, 1998.

[49] J.A. Davis, D.A. Smith, D.E. McNamara, D.M. Cottrell, and J. Campos, "Fractional derivatives—analysis and experimental implementation," *Appl. Opt.*, 40, pp. 5943-5948, 2001.

[50] N. Baddour, "Optical systems, singularity functions, complex Hankel transforms," *J. Opt. Soc. Am.* A, 57, pp. 207-213, 1967.

[51] M.K. Sharma, J. Joseph, and P. Senthilkumaran, "Selective edge enhancement using anisotropic vortex filter," *Appl. Opt.*, 50, pp. 5279-5286, 2011.

[52] J. A. Davis and M. D. Nowak, "Selective edge enhancement of images with an acousto-optic light modulator," *Appl. Opt.*, 23, pp. 4835-4839, 2002.

[53] A. W. Lohmann, E. Tepichin, and J.G. Ramirez, "Optical implementation of the fractional Hilbert transform for two-dimensional objects," *Appl. Opt.*, 36, pp. 6620-6626, 1997.

[54] G. Situ, G. Pedrini, and W. Osten, "Spiral phase filtering and orientation-selective edge detection/enhancement," *J. Opt. Soc. Am. A*, 26, pp. 1788-1797, 2009.

[55] M. K. Sharma, J. Joseph, and P. Senthilkumaran, "Selective edge enhancement using shifted anisotropic vortex filter," *J. Opt.*, 42, pp. 1-7, 2013.

[56] M. K. Sharma, J. Joseph, and P. Senthilkumaran, "Directional edge enhancement using superposed vortex filter," *Opt. Laser Technol.*, 57, pp. 230-235, 2014.

[57] M. K. Sharma, J. Joseph, and P. Senthilkumaran, "Effect of aberrations in vortex spatial filtering," *Opt. Laser Technol.*, 50, pp. 1501-1507, 2012.

[58] G.-H. Kim, H.J. Lee, J.-U. Kim, and H. Suk, "Propagation dynamics of optical vortices with anisotropic phase profiles," *J. Opt. Soc. Am. B*, 20, pp. 351-59, 2003.

[59] B.G. Sherlock, D.M. Monro, and K. Millard, "Fingerprint enhancement by directional Fourier filtering," *IEEE Proc. – Vision, Image and Signal Processing*, 141, pp. 87-94, 1994.

[60] M.K. Sharma, J. Joseph, and P. Senthilkumaran, "Composite vortex filters," 2013 Workshop on Recent Advances in Photonics (WRAP), 17-18 Dec. 2013 , pp. 1-2.

[61] M. Virendra N., *Optical imaging and aberrations*, Part 1. SPIE Press: 1998.

[62] I.V. Basistiy, V.A. Pas'ko, V.V. Slyusar, M.S. Soskin, and M.V. Vanestov, "Synthesis and analysis of optical vortices with fractional topological charges," *J. Opt. A: Pure Appl. Opt.*, 6, pp. S166-S169, 2004.

[63] V. Y. Bazhenov, M. V. Vasnetsov, and M. S. Soskin, "Laser beams with screw dislocations in their wavefronts," *JETP Lett.*, 52, pp. 429-431, 1990.

[64] A. Y. Bekshaev and A. I. Karamoch, "Spatial characteristics of vortex light beams produced by diffraction gratings with embedded phase singularity," *Opt. Commun*., 281, pp. 1366–1374, 2008.

[65] G.O. Reynolds, J.B. Develis, and B.J. Thompson, *The New Physical Optics Notebook: Tutorials in Fourier Optics*, SPIE, 1989.

[66] S.N. Khonina, V.V Kotlyar, M.V. Shinkaryev, V.A. Soifer, and G.V. Uspleniev, "The phase rotor filter," *J. Mod. Opt.*, 39, pp. 1147-1154, 1992.

[67] A. Jesacher, S. Fürhapter, S. Bernet, and M. Ritsch-Marte, "Spiral interferogram analysis," *J. Opt. Soc. Am. A*, 23(6), pp. 1400-1409, 2006.

[68] Z.S. Saks, D. Rozas, and G.A. Swartzlander, "Holographic formation of optical-vortex filament," *J. Opt. Soc. Am. B*, 15, pp. 2226-2234, 1998.

[69] G. Peele and K.A. Nugent, "X-ray vortex beams: a theoretical analysis," *Opt. Exp.*, 11, pp. 2315-2322, 2003.

[70] S.N. Khonina, V.V. Kotlyar, V.A. Soifer, K. Jefimovs, and J. Turunen, "Generation and selection of laser beams represented by a superposition of two angular harmonics," *J. Mod. Opt.*, 51, pp. 761-773, 2004.

[71] V.V. Kotlyar, A.A. Almazov, S.N. Khonina, V.A. Soifer, H. Elfstrom, and J. Turunen, "Generation of phase singularity through diffracting a plane or Gaussian beam by a spiral phase plate," *J. Opt. Soc. Am. A*, 22(5), pp. 849-861, 2005.

[72] V. V. Kotlyar, S. N. Khonina, A. A. Kovalev, V. A. Soifer, H. Elfstrom, and J. Turunen, "Diffraction of a plane, finite radius wave by a spiral phase plate," *Opt. Lett.*, 31, pp. 1597–1599, 2006.

[73] V. V. Kotlyar, A. A. Kovalev, R. V. Skidanov, O. Y. Moiseev, and V. A. Soifer, "Diffraction of a finite-radius plane wave and a Gaussian beam by a helical axicon and a spiral phase plate," *J. Opt. Soc. Am. A*, 24, pp. 1955–1964, 2007.

[74] W. Jia, K. Dobson, T.-C. Poon, and C. Zhou, "Spiral phase filtering in optical scanning holography," submitted to INDIN 2016.

[75] X. Yang, W. Jia, D. Wu, and T.-C. Poon, "On the differences between single- and double-sided bandpass spatial filtering," submitted to *Amer. J. Phys*.

[76] A. Jesacher, S. Fürhapter, S. Bernet, and M. Ritsch-Marte, "Shadow effects in spiral phase contrast microscopy," *Phys. Rev. Lett.*, 94(23), 233902, 2005.

[77] D.V. Petrov, "Splitting of an edge dislocation by an optical vortex," *Opt. Quant. Elec.*, 34, pp. 759-773, 2002.

[78] I. Freund and N. Shvartsman, "Wave-field phase singularities: The sign principle," P*hys. Rev. A*, 50(6), pp. 5164-5172, 1994.

[79] E. J. Galvez, N. Smiley, and N. Fernandes, "Composite optical vortices formed by collinear Laguerre-Gauss beams," *Proc. SPIE* 6131, pp. 19–26, 2006.

[80] D. M. Kalb and E. J. Galvez "Composite vortices of displaced Laguerre-Gauss beams," *Proc. SPIE* 7227, pp. 1-8, 2009.

[81] M. Ritsch-Marte, "Doing the Waltz with Light," *Optik & Photonik*, 10, pp. 32–37, 2015.

[82] R. C. Gonzalez and R. E. Woods, *Digital Image Processing*, 2nd ed. Prentice Hall, 2002.

[83] J. Xia, D. B. Dunn, T.-C. Poon, and P. P. Banerjee, "Image edge enhancement by Bragg diffraction," *Opt. Commun.*, 128, pp. 1–7, 1996.

[84] D. Cao, P. P. Banerjee, and T.-C. Poon, "Image edge enhancement with two cascaded acousto-optic cells with contrapropagating sound," *Appl. Opt.*, 37, pp. 3007–3014, 1998.

[85] A. Márquez, C. Neipp, A. Beléndez, S. Gallego, M. Ortuño, and I. Pascual, "Edge-enhanced imaging with polyvinyl alcohol/acrylamide photopolymer gratings," *Opt. Lett.*, 28, pp. 1510–1512, 2003.

[86] S. Greenberg and D. Kogan, "Structure-adaptive anisotropic filter applied to fingerprints," *Opt. Eng.*, 44(12), 127004, 2005.

[87] X. Chen, J. Tian, Y. Zhang, and X. Yang, "Enhancement of low quality fingerprints based on anisotropic filtering," *Lect. Notes Comput. Sci.* 3832, pp. 302–308, 2005.

[88] P. Bouchal and Z. Bouchal, "Selective edge enhancement in three-dimensional vortex imaging with incoherent light," *Opt. Lett.*, 37, pp. 2949-2951, 2012.

[89] N. Chen, Z. Ren, A. Chan, X. Sun, and E. Lam, "Depth Enhancement of Optical Scanning Holography with a Spiral Phase Plate," in Digital Holography & 3-D Imaging Meeting, OSA Technical Digest, paper DW2A.3, 2015.

[90] G. Indebetouw and W. Zhong. "Scanning Holographic Microscopy of Three-Dimensional Fluorescent Specimens." *J. Opt. Soc. Am. A*,23(7), pp. 1699–1707, 2006.

APPENDIX A: CITATIONS OF COPYRIGHTED WORKS

Fig. 1 [used with permission]
K. Dobson, W. Jia, and T.-C. Poon. (2016, January). "Anisotropic edge enhancement in optical scanning holography with spiral phase filtering," *Chinese Optics Letters.* [On-line]. 14(1), pp. 010006-010010. Available: https://www.osapublishing.org/col/abstract.cfm?uri=col-14-1-010006 [Accessed 11 January 2016]. Used with permission from the Optical Society of America; 03 May 2016 letter attached.

Fig. 4 [used with permission]
K. Dobson, W. Jia, and T.-C. Poon. (2016, January). "Anisotropic edge enhancement in optical scanning holography with spiral phase filtering," *Chinese Optics Letters.* [On-line]. 14(1), pp. 010006-010010. Available: https://www.osapublishing.org/col/abstract.cfm?uri=col-14-1-010006 [Accessed 11 January 2016]. Used with permission from the Optical Society of America; 03 May 2016 letter attached.

Fig. 13 [used with permission]
K. Doh, K. Dobson, T.-C. Poon, and P.-S. Chung. (2009, January). "Optical image coding with a circular Dammann grating," *Applied Optics.* [On-line]. 48(1), pp. 134-139. Available: https://www.osapublishing.org/ao/viewmedia.cfm?URI=ao-48-1-134&seq=0&html=true&origin=search [Accessed 8 January 2009]. Used with permission from the Optical Society of America; 03 May 2016 letter attached.

Fig. 15 [used with permission]
K. Doh, K. Dobson, T.-C. Poon, and P.-S. Chung. (2009, January). "Optical image coding with a circular Dammann grating," Applied Optics. [On-line]. 48(1), pp. 134-139. Available: https://www.osapublishing.org/ao/viewmedia.cfm?URI=ao-48-1-134&seq=0&html=true&origin=search [Accessed 8 January 2009]. Used with permission from the Optical Society of America; 03 May 2016 letter attached.

Fig. 16 [used with permission]
K. Doh, K. Dobson, T.-C. Poon, and P.-S. Chung. (2009, January). "Optical image coding with a circular Dammann grating," Applied Optics. [On-line]. 48(1), pp. 134-139. Available: https://www.osapublishing.org/ao/viewmedia.cfm?URI=ao-48-1-134&seq=0&html=true&origin=search [Accessed 8 January 2009]. Used with permission from the Optical Society of America; 03 May 2016 letter attached.

Fig. 17 [used with permission]
K. Doh, K. Dobson, T.-C. Poon, and P.-S. Chung. (2009, January). "Optical image coding with a circular Dammann grating," Applied Optics. [On-line]. 48(1), pp. 134-139. Available:

https://www.osapublishing.org/ao/viewmedia.cfm?URI=ao-48-1-134&seq=0&html=true&origin=search [Accessed 8 January 2009]. Used with permission from the Optical Society of America; 03 May 2016 letter attached.

Fig. 18 [used with permission]

K. Doh, K. Dobson, T.-C. Poon, and P.-S. Chung. (2009, January). "Optical image coding with a circular Dammann grating," Applied Optics. [On-line]. 48(1), pp. 134-139. Available: https://www.osapublishing.org/ao/viewmedia.cfm?URI=ao-48-1-134&seq=0&html=true&origin=search [Accessed 8 January 2009]. Used with permission from the Optical Society of America; 03 May 2016 letter attached.

Fig. 19 [used with permission]

K. Doh, K. Dobson, T.-C. Poon, and P.-S. Chung. (2009, January). "Optical image coding with a circular Dammann grating," Applied Optics. [On-line]. 48(1), pp. 134-139. Available: https://www.osapublishing.org/ao/viewmedia.cfm?URI=ao-48-1-134&seq=0&html=true&origin=search [Accessed 8 January 2009]. Used with permission from the Optical Society of America; 03 May 2016 letter attached.

Fig. 20 [used with permission]

Y. Shinoda, J.-P. Liu, P. S. Chung, K. Dobson, X. Zhou, and T.-C. Poon. (2011, March). "Three-dimensional complex image coding using a circular Dammann grating," Applied Optics. [On-line]. 50(7), pp. B38-45. Available: https://www.osapublishing.org/ao/viewmedia.cfm?URI=ao-50-7-B38&seq=0&html=true&origin=search [Accessed 3 March 2011].Used with permission from the Optical Society of America; 03 May 2016 letter attached.

Fig. 21 [used with permission]

Y. Shinoda, J.-P. Liu, P. S. Chung, K. Dobson, X. Zhou, and T.-C. Poon. (2011, March). "Three-dimensional complex image coding using a circular Dammann grating," Applied Optics. [On-line]. 50(7), pp. B38-45. Available: https://www.osapublishing.org/ao/viewmedia.cfm?URI=ao-50-7-B38&seq=0&html=true&origin=search [Accessed 3 March 2011]. Used with permission from the Optical Society of America; 03 May 2016 letter attached.

Fig. 22 [used with permission]

Y. Shinoda, J.-P. Liu, P. S. Chung, K. Dobson, X. Zhou, and T.-C. Poon. (2011, March). "Three-dimensional complex image coding using a circular Dammann grating," Applied Optics. [On-line]. 50(7), pp. B38-45. Available: https://www.osapublishing.org/ao/viewmedia.cfm?URI=ao-50-7-

B38&seq=0&html=true&origin=search [Accessed 3 March 2011]. Used with permission from the Optical Society of America; 03 May 2016 letter attached.

Fig. 23 [used with permission]

Y. Shinoda, J.-P. Liu, P. S. Chung, K. Dobson, X. Zhou, and T.-C. Poon. (2011, March). "Three-dimensional complex image coding using a circular Dammann grating," Applied Optics. [On-line]. 50(7), pp. B38-45. Available: https://www.osapublishing.org/ao/viewmedia.cfm?URI=ao-50-7-B38&seq=0&html=true&origin=search [Accessed 3 March 2011]. Used with permission from the Optical Society of America; 03 May 2016 letter attached.

Fig. 24 [used with permission]

Y. Shinoda, J.-P. Liu, P. S. Chung, K. Dobson, X. Zhou, and T.-C. Poon. (2011, March). "Three-dimensional complex image coding using a circular Dammann grating," Applied Optics. [On-line]. 50(7), pp. B38-45. Available: https://www.osapublishing.org/ao/viewmedia.cfm?URI=ao-50-7-B38&seq=0&html=true&origin=search [Accessed 3 March 2011]. Used with permission from the Optical Society of America; 03 May 2016 letter attached.

Fig. 25 [used with permission]

Y. Shinoda, J.-P. Liu, P. S. Chung, K. Dobson, X. Zhou, and T.-C. Poon. (2011, March). "Three-dimensional complex image coding using a circular Dammann grating," Applied Optics. [On-line]. 50(7), pp. B38-45. Available: https://www.osapublishing.org/ao/viewmedia.cfm?URI=ao-50-7-B38&seq=0&html=true&origin=search [Accessed 3 March 2011]. Used with permission from the Optical Society of America; 03 May 2016 letter attached.

Fig. 26 [used with permission]

Y. Shinoda, J.-P. Liu, P. S. Chung, K. Dobson, X. Zhou, and T.-C. Poon. (2011, March). "Three-dimensional complex image coding using a circular Dammann grating," Applied Optics. [On-line]. 50(7), pp. B38-45. Available: https://www.osapublishing.org/ao/viewmedia.cfm?URI=ao-50-7-B38&seq=0&html=true&origin=search [Accessed 3 March 2011]. Used with permission from the Optical Society of America; 03 May 2016 letter attached.

Fig. 27 [used with permission]

Y. Shinoda, J.-P. Liu, P. S. Chung, K. Dobson, X. Zhou, and T.-C. Poon. (2011, March). "Three-dimensional complex image coding using a circular Dammann grating," Applied Optics. [On-line]. 50(7), pp. B38-45. Available: https://www.osapublishing.org/ao/viewmedia.cfm?URI=ao-50-7-

B38&seq=0&html=true&origin=search [Accessed 3 March 2011]. Used with permission from the Optical Society of America; 03 May 2016 letter attached.

Fig. 28 [used with permission]

Z. Xin, K. Dobson, Y. Shinoda, and T.-C. Poon. (2010, September). "Sectional image reconstruction in optical scanning holography using a random-phase pupil," Optics Letters [On-line]. 35(17), pp. 2934-2936. Available: https://www.osapublishing.org/ol/viewmedia.cfm?URI=ol-35-17-2934&seq=0&html=true&origin=search [Accessed 5 September 2010]. Used with permission from the Optical Society of America; 03 May 2016 letter attached.

Fig. 29 [used with permission]

Z. Xin, K. Dobson, Y. Shinoda, and T.-C. Poon. (2010, September). "Sectional image reconstruction in optical scanning holography using a random-phase pupil," Optics Letters [On-line]. 35(17), pp. 2934-2936. Available: https://www.osapublishing.org/ol/viewmedia.cfm?URI=ol-35-17-2934&seq=0&html=true&origin=search [Accessed 5 September 2010]. Used with permission from the Optical Society of America; 03 May 2016 letter attached.

Fig. 31 [used with permission]

X.-L. Wu, X. Zhou, Q.-H. Wang, Y.-F. Jiang, C.-J. Xiao, K. Dobson, and T.-C. Poon. (2013, January). "Deviation influences on sectional image reconstruction in optical scanning holography using a random-phase pupil," Applied Optics [On-line]. 52(1), pp. A360-A366. Available: https://www.osapublishing.org/ao/viewmedia.cfm?URI=ao-52-1-A360&seq=0&html=true&origin=search [Accessed 1 February 2013]. Used with permission from the Optical Society of America; 03 May 2016 letter attached.

Fig. 32 [used with permission]

X.-L. Wu, X. Zhou, Q.-H. Wang, Y.-F. Jiang, C.-J. Xiao, K. Dobson, and T.-C. Poon. (2013, January). "Deviation influences on sectional image reconstruction in optical scanning holography using a random-phase pupil," Applied Optics [On-line]. 52(1), pp. A360-A366. Available: https://www.osapublishing.org/ao/viewmedia.cfm?URI=ao-52-1-A360&seq=0&html=true&origin=search [Accessed 1 February 2013]. Used with permission from the Optical Society of America; 03 May 2016 letter attached.

Fig. 93 [used with permission]

Y. Pan, W. Jia, J. Yu, K. Dobson, C. Zhou, Y. Wang, and T.-C. Poon. (2014, July). "Edge extraction using a time-varying vortex beam in incoherent digital holography," Optics Letters [On-line]. 39(14), pp. 4176-4179. Available: https://www.osapublishing.org/ol/viewmedia.cfm?URI=ol-39-14-

4176&seq=0&html=true&origin=search [Accessed 22 July 2014]. Used with permission from the Optical Society of America; 03 May 2016 letter attached.

Fig. 105 [used with permission]

Y. Pan, W. Jia, J. Yu, K. Dobson, C. Zhou, Y. Wang, and T.-C. Poon. (2014, July). "Edge extraction using a time-varying vortex beam in incoherent digital holography," Optics Letters [On-line]. 39(14), pp. 4176-4179. Available: https://www.osapublishing.org/ol/viewmedia.cfm?URI=ol-39-14-4176&seq=0&html=true&origin=search [Accessed 22 July 2014]. Used with permission from the Optical Society of America; 03 May 2016 letter attached.

Fig. 107 [used with permission]

Y. Pan, W. Jia, J. Yu, K. Dobson, C. Zhou, Y. Wang, and T.-C. Poon. (2014, July). "Edge extraction using a time-varying vortex beam in incoherent digital holography," Optics Letters [On-line]. 39(14), pp. 4176-4179. Available: https://www.osapublishing.org/ol/viewmedia.cfm?URI=ol-39-14-4176&seq=0&html=true&origin=search [Accessed 22 July 2014]. Used with permission from the Optical Society of America; 03 May 2016 letter attached.

Fig. 127 [fair use]

G. Indebetouw and W. Zhong (2006, July). "Scanning Holographic Microscopy of Three-Dimensional Fluorescent Specimens." Journal of the Optical Society of America A [On-line]. 23(7), pp. 1699–1707. Available: https://www.osapublishing.org/josaa/viewmedia.cfm?URI=josaa-23-7-1699&seq=0&origin=search [Accessed 30 September 2006]. Fair use determination attached.

Fig. 128 [fair use]

G. Indebetouw and W. Zhong (2006, July). "Scanning Holographic Microscopy of Three-Dimensional Fluorescent Specimens." Journal of the Optical Society of America A [On-line]. 23(7), pp. 1699–1707. Available: https://www.osapublishing.org/josaa/viewmedia.cfm?URI=josaa-23-7-1699&seq=0&origin=search [Accessed 30 September 2006]. Fair use determination attached.

VirginiaTech
Invent the Future

Kelly Dobson <kdobson@vt.edu>

Dissertation Copyright Permission

pubscopyright <copyright@osa.org> Tue, May 3, 2016 at 10:12 AM
To: Kelly Dobson <kdobson@vt.edu>, pubscopyright <copyright@osa.org>

Dear Kelly Dobson,

Thank you for contacting The Optical Society.

Because you are the author of the source paper from which you wish to reproduce material, OSA considers your requested use of its copyrighted materials to be permissible within the author rights granted in the Copyright Transfer Agreement submitted by the requester on acceptance for publication of his/her manuscript. It is requested that a complete citation of the original material be included in any publication. This permission assumes that the material was not reproduced from another source when published in the original publication.

Please let me know if you have any questions.

Kind Regards,

Rebecca Robinson

Rebecca Robinson

May 3, 2016

Authorized Agent, The Optical Society

From: Kelly Dobson [mailto:kdobson@vt.edu]
Sent: Wednesday, April 27, 2016 3:47 PM
To: pubscopyright
Subject: Dissertation Copyright Permission
I am completing a doctoral dissertation at Virginia Polytechnic Institute and State University entitled

"Reconstruction Enhancements with Optical Scanning Holography." In accordance with OSA copyright, I would like your permission to reprint in my dissertation excerpts from the following

(1) Yijie Pan, Wei Jia, Junjie Yu, **Kelly Dobson**, Changhe Zhou, Yongtian Wang, and Ting-Chung Poon, "Edge extraction using a time-varying vortex beam in incoherent digital holography," Opt. Lett. **39**, 4176-4179 (2014)

Figure 1, Figure 4, Figure 5

These figures are included in my dissertation as part of a summary of part work. Figure 1 is used to illustrate one of the optical systems in the research. Through the data collected during this experiment I am able to generate Figure 4 and Figure 5 for myself and may look similar to those in the publication.

(2) Zhou Xin, **Kelly Dobson**, Yukitaka Shinoda, and Ting-Chung Poon, "Sectional image reconstruction in optical scanning holography using a random-phase pupil," Opt. Lett. **35**, 2934-2936 (2010)

Figure 3 and Figure 4

These figures are included in my dissertation as part of a summary of part work. Through the access to the simulated data used in this experiment I am able to generate Figure 3 and Figure 4 for myself and may look similar to those in the publication.

(3) Xiu-Ling Wu, Xin Zhou, Qiong-Hua Wang, Yu-Fu Jiang, Chun-Jing Xiao, **Kelly Dobson**, and TingChung Poon, "Deviation influences on sectional image reconstruction in optical scanning holography using a random-phase pupil," Appl. Opt. **52**, A360-A366 (2013)

Figure 4 and Figure 6

These figures are included in my dissertation as part of a summary of part work. Through the access to the simulated data used in this experiment I am able to generate Figure 4 and Figure 6 for myself and may look similar to those in the publication.

(4) Yukitaka Shinoda, Jung-Ping Liu, Po Sheun Chung, **Kelly Dobson**, Xin Zhou, and Ting-Chung Poon, "Three-dimensional complex image coding using a circular Dammann grating," Appl. Opt. **50**, B38-B45 (2011)

Figure 12, Figure 13, Figure 14, Figure 15, Figure 16, Figure 17, Figure 18

These figures are included in my dissertation as part of a summary of part work. Through the access to the simulated and experimental data used in this research I am able to generate Figure 12, Figure 13, Figure 14, Figure 15, Figure 16, Figure 17, and Figure 18 for myself and may look similar to those in the publication.

(5) **Kelly K Dobson**, Wei Jia, and Ting-Chung Poon, "Anisotropic edge enhancement in optical scanning holography with spiral phase filtering," Chinese Optics Letters 14(1),010006 (2016).

Figure 1 and Figure 2

These figures are included in my dissertation as part of a summary of past work and both figures are used to illustrate the optical system used as part of the research in the dissertation.

Thank you for your time and consideration in this matter.

Sincerely,

Kelly Dobson

920 Kabrich Street

Blacksburg, VA 24060

kdobson@vt.edu

VirginiaTech
Invent the Future

Kelly Dobson <kdobson@vt.edu>

Dissertation Copyright Permission

pubscopyright <copyright@osa.org> Tue, May 3, 2016 at 10:13 AM
To: Kelly Dobson <kdobson@vt.edu>, pubscopyright <copyright@osa.org>

Dear Kelly Dobson,

Thank you for contacting The Optical Society.

Because you are the author of the source paper from which you wish to reproduce material, OSA considers your requested use of its copyrighted materials to be permissible within the author rights granted in the Copyright Transfer Agreement submitted by the requester on acceptance for publication of his/her manuscript. It is requested that a complete citation of the original material be included in any publication. This permission assumes that the material was not reproduced from another source when published in the original publication.

Please let me know if you have any questions.

Kind Regards,

Rebecca Robinson

Rebecca Robinson

May 3, 2016

Authorized Agent, The Optical Society

From: Kelly Dobson [mailto:kdobson@vt.edu]
Sent: Thursday, April 28, 2016 11:11 AM
To: pubscopyright
Subject: Re: Dissertation Copyright Permission

I would like to add one additional publication to the consideration as part of inclusion in my doctoral dissertation. In accordance with OSA copyright, I would like your permission to reprint in my dissertation excerpts from the following

Kyu B. Doh, Kelly Dobson, Ting-Chung Poon, and Po Sheun Chung, "Optical image coding with a circular Dammann grating," Appl. Opt. **48**, 134-139 (2009)

Figure 4, Figure 5b, Figure 6b and e, Figure 7, Figure 8, and Figure 9

These figures are included in my dissertation as part of a summary of past work. Figure 4 is used to illustrate the optical system used as part of the research in the dissertation. Through the access to the data used in this experiment I am able to generate the remaining figures (Figure 5b, Figure 6b and e, Figure 7, Figure 8, and Figure 9) for myself and may look similar to those in the publication.

Thank you,

Kelly Dobson

920 Kabrich Street

Blacksburg, VA 24060

kdobson@vt.edu

On Wed, Apr 27, 2016 at 2:46 PM, Kelly Dobson <kdobson@vt.edu> wrote:

I am completing a doctoral dissertation at Virginia Polytechnic Institute and State University entitled "Reconstruction Enhancements with Optical Scanning Holography." In accordance with OSA copyright, I would like your permission to reprint in my dissertation excerpts from the following

(1) Yijie Pan, Wei Jia, Junjie Yu, **Kelly Dobson**, Changhe Zhou, Yongtian Wang, and Ting-Chung Poon, "Edge extraction using a time-varying vortex beam in incoherent digital holography," Opt. Lett. **39**, 4176-4179 (2014)

Figure 1, Figure 4, Figure 5

These figures are included in my dissertation as part of a summary of part work. Figure 1 is used to illustrate one of the optical systems in the research. Through the data collected during this experiment I am able to generate Figure 4 and Figure 5 for myself and may look similar to those in the publication.

(2) Zhou Xin, **Kelly Dobson**, Yukitaka Shinoda, and Ting-Chung Poon, "Sectional image reconstruction in optical scanning holography using a random-phase pupil," Opt. Lett. **35**, 2934-2936 (2010)

Figure 3 and Figure 4

These figures are included in my dissertation as part of a summary of part work. Through the access to the simulated data used in this experiment I am able to generate Figure 3 and Figure 4 for myself and may look similar to those in the publication.

(3) Xiu-Ling Wu, Xin Zhou, Qiong-Hua Wang, Yu-Fu Jiang, Chun-Jing Xiao, **Kelly Dobson**, and TingChung Poon, "Deviation influences on sectional image reconstruction in optical scanning holography using a random-phase pupil," Appl. Opt. **52**, A360-A366 (2013)

Figure 4 and Figure 6

These figures are included in my dissertation as part of a summary of part work. Through the access to the simulated data used in this experiment I am able to generate Figure 4 and Figure 6 for myself and may look similar to those in the publication.

(4) Yukitaka Shinoda, Jung-Ping Liu, Po Sheun Chung, **Kelly Dobson**, Xin Zhou, and Ting-Chung Poon, "Three-dimensional complex image coding using a circular Dammann grating," Appl. Opt. **50**, B38-B45 (2011)

Figure 12, Figure 13, Figure 14, Figure 15, Figure 16, Figure 17, Figure 18

These figures are included in my dissertation as part of a summary of part work. Through the access to the simulated and experimental data used in this research I am able to generate Figure 12, Figure 13, Figure 14, Figure 15, Figure 16, Figure 17, and Figure 18 for myself and may look similar to those in the publication.

(5) **Kelly K Dobson**, Wei Jia, and Ting-Chung Poon, “Anisotropic edge enhancement in optical scanning holography with spiral phase filtering,” Chinese Optics Letters 14(1),010006 (2016).

Figure 1 and Figure 2

These figures are included in my dissertation as part of a summary of past work and both figures are used to illustrate the optical system used as part of the research in the dissertation.

Thank you for your time and consideration in this matter.

Sincerely,

Kelly Dobson

920 Kabrich Street

Blacksburg, VA 24060

kdobson@vt.edu

VirginiaTech
Invent the Future

Kelly Dobson <kdobson@vt.edu>

Dissertation Copyright Permission

pubscopyright <copyright@osa.org> Tue, May 3, 2016 at 3:02 PM
To: Kelly Dobson <kdobson@vt.edu>, pubscopyright <copyright@osa.org>

Dear Kelly Dobson,

Thank you for contacting The Optical Society.

OSA considers your requested use of its copyrighted material to be Fair Use under United States Copyright Law. It is requested that a complete citation of the original material be included in any publication.

Let me know if you have any questions.

Kind Regards,

Rebecca Robinson

Rebecca Robinson

May 3, 2016

Authorized Agent, The Optical Society

From: Kelly Dobson [mailto:kdobson@vt.edu]
Sent: Thursday, April 28, 2016 6:33 PM

To: pubscopyright
Subject: Re: Dissertation Copyright Permission

There is one final publication under consideration as part of inclusion in my doctoral dissertation. In accordance with OSA copyright, I would like your permission to reprint in my dissertation excerpts from the following

Guy Indebetouw and Wenwei Zhong, "Scanning holographic microscopy of three-dimensional fluorescent specimens," J. Opt. Soc. Am. A23, 1699-1707 (2006)

Figure 4 a and b, Figure 5

These are included in my dissertation as part of a future work section. I have used data provided from Dr. Indebetouw to generate results similar to Figure 4 a and b from the captured hologram in Figure 5. I have gone on to modify this for edge enhancement as an extension of my research.

Thank you,

Kelly Dobson

920 Kabrich Street

Blacksburg, VA 24060

kdobson@vt.edu